New frontiers in Gyrochronology

Exploring the evolution of stellar rotation in open clusters and wide binaries

kumulative Dissertation

zur Erlangung des akademischen Grades
doctor rerum naturalium (Dr. rer. nat.)
in der Wissenschaftsdisziplin Astrophysik

David Gruner

eingereicht an der

Mathematisch-Naturwissenschaftlichen Fakultät
der Universität Potsdam

Institut für Physik und Astronomie (Haus 28)
Karl-Liebknecht-Strasse 24/25
14476 Potsdam-Golm

erstellt in Zusammenarbeit mit dem

Leibniz-Institut für Astrophysik Potsdam

An der Sternwarte 16
14482 Potsdam

Datum der Disputation: 07.11.2023

Unless otherwise indicated, this work is licensed under a Creative Commons License Attribution 4.0 International. This does not apply to quoted content and works based on other permissions.
To view a copy of this license, visit:
https://creativecommons.org/licenses/by/4.0/legalcode

Betreuer	Prof. Dr. Klaus G. Strassmeier Dr. Sydney A. Barnes
Mentor	Dr. Christina Chiappini
Gutachter	Prof. Dr. Klaus G. Strassmeier *(Leibniz-Institut für Astrophysik Potsdam & Universität Potsdam)* Prof. Dr. Gibor Basri *(University of California, Berkeley)* Prof. Dr. Terry D. Oswalt *(Embry-Riddle Aeronautical University)*
Prüfungskomission	Prof. Dr. Philipp Richter *(Vorsitz)* Prof. Dr. Terry D. Oswalt *(Gutachter)* Prof. Dr. Tim Dietrich Prof. Dr. Dr. Stefan Geier apl. Prof. Dr. Lida Oskinova

Published online on the
Publication Server of the University of Potsdam:
https://doi.org/10.25932/publishup-61526
https://nbn-resolving.org/urn:nbn:de:kobv:517-opus4-615268

»*Round and round and round it goes – where it stops nobody knows*«

– The Steve Miller Band (Abracadabra, 1982)

Deutsche Zusammenfassung

Sterne mit späten Spektraltypen sind mit Abstand die Häufigsten im Universum und von großem Interesse für verschiedene Bereiche der Astronomie. Dabei sind insbesondere galaktische Archäologie und die Erforschung von Exoplanten zu nennen. Das Problem ist jedoch, dass sich diese Sterne nur sehr langsam entwickeln; ihre Temperatur, Helligkeit und chemische Zusammensetzung ändern kaum während ihrer langen Hauptreihenphase. Daher ist es schwierig für solche Sterne ein Alter zu bestimmen – vorallem wenn sie isoliert sind und es keine anderne Indikatoren (z.B. die Zugehörigkeit zu einem Sternhaufen) gibt. Eine Möglichkeit dieses Problem zu umgehen ist Gyrochronologie. Sterne, wie alle anderen Objekte im Universum, rotieren und die Rate, mit der sie rotieren, beeinflusst viele Aspekte ihrer Evolution. Gyrochronologie nutzt die beobachtete Rotation und ihre Änderung mit der Zeit als ein Mittel zur Altersbestimmung.

Anders als zuvor genannte Parameter ändert sich die Rate, mit der Sterne rotieren, deutlich im Laufe ihrer Hauptreihenentwicklung. Sie verlangsamt sich. Junge Sterne rotieren in wenigen Stunden einmal um sich selbst – ältere brauchen dafür schon einen Monat oder gar bis zu über hundert Tage. Die Tatsache, dass das Abbremsen systematischen Gesetzmäßigkeiten unterliegt, gebar die Idee dies zu nutzen um das Alter eines Sternes zu bestimmen. Das Verhalten junger Sterne wurde ausführlich erfoscht, jedoch für die meisten Sterne älter als 1 Gyr nicht bekannt, wie sich die Rotationsraten entwickeln.

Diese Arbeit fokussiert sich auf die fortgesetzte Erforschung des Abbremsens; insbesondere ob Gyrochronologie auch für ältere Sterne nutzbar ist, ob es universell für alle Sterne (inklusive Feldsterne) ist und darauf weitere Kalibrationspunkte für Abbrems-Modelle bereitzustellen. Dafür habe ich, basierend auf photometrischen Zeitserien (Lichtkurven) von *Keplers K2* Programm, die offenen Sternhaufen Ruprecht 147 (2.7 Gyr alt) and M 67 (4 Gyr) untersucht. Es sind jedoch umfangreiche Schritte in der Datenverarbeitung notwendig um Fehlfunktionen und technischen Limitationen des Teleskops zu begegnen.

Für Ruprecht 147 habe ich aus Literaturdaten eine Liste von 300 Haufen-zugehörigen Sternen erstellt und mit fertig-reduzierte Lichtkurven aus dem *Kepler* Archiv kombiniert. Die gröbsten Datensystematiken wurden in diesen bereinigt, denoch sind problematische Artefakte weiterhin vorhanden. Die Arbeit an Ruprecht 147 hat die Limitationen von archivierten *Kepler* Daten gezeigt. Daher wurde für M 67 mehr Aufwand betrieben. Direkt basierend auf den photometrischen Auffnahmen habe ich eigene Lichtkurven erzeugt, was eine deutlich höhere räumliche Auflösung erlaubt hat. Das hieß jedoch auch, dass ich mich mit all Systematiken in *Kepler* Daten befassen musste. Dafür habe ich eine Methodik konzipiert, die die künstlichen Variation im aufgezeichneten Fluss mit der Position eines Sterns auf dem Detektor korreliert und daraus eine Korrektur bestimmt. Dieser Prozess war so erfolgreich, dass ich Lichtkurven kreiert habe, die in ihrer Qualität an die archivierten Daten heran kommen oder sie gar übersteigen.

Nach entsprechender Korrektur der Artefakte konnte ich Rotationsperioden für 31 (in Ruprecht 147) und 47 (in M 67) Sterne identifizieren. Genau wie zuvor in jüngeren Sternhaufen gesehen, folgen auch die äelteren Sternhaufen einer klaren Sequenz im Farb-Rotations-Raum. Meine Daten schließen direkt an Ergebnisse gleichaltriger Haufen an und erweitern diese zum ersten Mal zu Sternen älter als 1 Gyr und röter als frühe K-Sterne. Meine Ergebnisse zeigen eine deutliche Abweichung von der erwarteten Entwicklung, verkörpert durch eine klare Abflachung der Sequenz für Ruprecht 147, die für M 67 eine sinusförmige Struktur annimmt. Dennoch konnte ich damit zeigen, dass sich das systematische Abbremsen der Rotation von Sterne auch bis 4 Gyr fortsetzt und Sterne sich weiterhin auf eine wohldefinierten Ebene im Farb-Rotations-Alters-Raum befinden. Das heißt auch, Gyrochronologie kann mindestens für bis zu 4 Gyr alte Sterne genutzt werden.

Basierend auf meinen eigenen Ergebnissen und Literaturdaten für jüngere Sternhaufen habe ich einen Vergleich mit Feldsternen durchgeführt. Die Feldsterne für diesen Vergleich entstammen weiten Doppelsternsystemen. Deren gemeinsamer Ursprung erlaubt eine Evaluierung der inneren Konsistenz beider Sterne. Mein Vergleich hat gezeigt, dass Doppelsternsysteme mit sich selbst aber auch mit den Sternhaufen konsistent sind. Ich habe damit erstmalig gezeigt, dass sich die Rotation von Feldsternen und Haufensternen gleich entwickelt. In Konsequenz bedeutet dies auch, dass Gyrochronologie angewandt werden kann, um das Alter von Feldsternen zu bestimmen.

English summary

Late-type stars are by far the most frequent stars in the universe and of fundamental interest to various fields of astronomy – most notably to Galactic archaeology and exoplanet research. However, such stars barely change during their main sequence lifetime; their temperature, luminosity, or chemical composition evolve only very slowly over the course of billions of years. As such, it is difficult to obtain the age of such a star, especially when it is isolated and no other indications (like cluster association) can be used. Gyrochronology offers a way to overcome this problem. Stars, just like all other objects in the universe, rotate and the rate at which stars rotate impacts many aspects of their appearance and evolution. Gyrochronology leverages the observed rotation rate of a late-type main sequence star and its systematic evolution to estimate their ages.

Unlike the above-mentioned parameters, the rotation rate of a main sequence star changes drastically throughout its main sequence lifetime; stars spin down. The youngest stars rotate every few hours, whereas much older stars rotate only about once a month, or – in the case of some late M-stars – once in a hundred days. Given that this spindown is systematic (with an additional mass dependence), it gave rise to the idea of using the observed rotation rate of a star (and its mass or a suitable proxy thereof) to estimate a star's age. This has been explored widely in young stellar open clusters but remains essentially unconstrained for stars older than the sun, and K and M stars older than 1 Gyr.

This thesis focuses on the continued exploration of the spindown behavior to assess, whether gyrochronology remains applicable for stars of old ages, whether it is universal for late-type main sequence stars (including field stars), and to provide calibration mileposts for spindown models. To accomplish this, I have analyzed data from *Kepler* space telescope for the open clusters Ruprecht 147 (2.7 Gyr old) and M 67 (4 Gyr). Time series photometry data (light curves) were obtained for both clusters during *Kepler*'s *K2* mission. However, due to technical limitations and telescope malfunctions, extracting usable data from the *K2* mission to identify (especially long) rotation periods requires extensive data preparation.

For Ruprecht 147, I have compiled a list of about 300 cluster members from the literature and adopted preprocessed light curves from the *Kepler* archive where available. They have been cleaned of the gravest of data artifacts but still contained systematics. After correcting them for said artifacts, I was able to identify rotation periods in 31 of them. For M 67 more effort was taken. My work on Ruprecht 147 has shown the limitations imposed by the preselection of *Kepler* targets. Therefore, I adopted the time series full frame image directly and performed photometry on a much higher spatial resolution to be able to obtain data for as many stars as possible. This also means that I had to deal with the ubiquitous artifacts in *Kepler* data. For that, I devised a method that correlates the artificial flux variations with the ongoing drift of the telescope pointing in order to remove it. This process was a large success and I was able to create light curves whose quality match and even exceede those that were created by the *Kepler* mission – all while operating on higher spatial resolution and processing fainter stars.

Ultimately, I was able to identify signs of periodic variability in the (created) light curves for 31 and 47 stars in Ruprecht 147 and M 67, respectively. My data connect well to bluer stars of cluster of the same age and extend for the first time to stars redder than early-K and older than 1 Gyr. The cluster data show a clear flattening in the distribution of Ruprecht 147 and even a downturn for M 67, resulting in a somewhat sinusoidal shape. With that, I have shown that the systematic spindown of stars continues at least until 4 Gyr and stars continue to live on a single surface in age-rotation periods-mass space which allows gyrochronology to be used at least up to that age. However, the shape of the spindown – as exemplified by the newly discovered sinusoidal shape of the cluster sequence – deviates strongly from the expectations.

I then compiled an extensive sample of rotation data in open clusters – very much including my own work – and used the resulting *cluster skeleton* (with each cluster forming a rip in color-rotation period-mass space) to investigate if field stars follow the same spindown as cluster stars. For the field stars, I used wide binaries, which – with their shared origin and coevality – are in a sense the smallest possible open clusters. I devised an empirical method to evaluate the consistency between the rotation rates of the wide binary components and found that the vast majority of them are in fact consistent with what is observed in open clusters. This leads me to conclude that gyrochronology – calibrated on open clusters – can be applied to determine the ages of field stars.

The building blocks of this thesis

This doctoral thesis is based on three peer-reviewed journal publications. They are reproduced here as individual parts of the thesis. Their texts are preserved and the figures directly taken from the publication. However, some editorial liberties are taken:

- The individual paper appendices are merged into one large appendix for the entire document.
- Individual bibliographies are merged into one at the end of the document.
- Formatting and style are adjusted to match the overall layout of thesis.
- Some minor cosmetic adjustments are done.

The journal publications reproduced here are:

Title	**Rotation periods for cool stars in the open cluster Ruprecht 147 (NGC 6774)**
Published	Astronomy and Astrophysics, Volume 644, id.A16
Authors	**D. Gruner** and S. A. Barnes
DOI	10.1051/0004-6361/202038984
Reproduced in	Part 2 and Appendices A – D

Title	**New insights into the rotational evolution of near-solar age stars from the open cluster M 67**
Published	Astronomy and Astrophysics, Volume 672, id.A159
Authors	**D. Gruner**, S. A. Barnes, and J. Weingrill
DOI	10.1051/0004-6361/202345942
Reproduced in	Part 3 and Appendices E – G

Title	**Wide binaries demonstrate the consistency of rotational evolution between open cluster and field stars**
Published	Astronomy and Astrophysics, Volume 675, id.A180
Authors	**D. Gruner**, S. A. Barnes, and K. A. Janes
DOI	10.1051/0004-6361/202346590
Reproduced in	Part 4 and Appendices H – J

Contents

Page

Deutsche Zusammenfassung **v**

English summary **vii**

Preface **1**

1 The rotation and ages of stars **3**
1.1 Magnetic braking and the evolution of stellar rotation . . . 5
1.2 Exploring stellar rotation in open clusters . . . 6
1.3 The origins and concepts of gyrochronology . . . 9
1.4 Introduction to the presented works . . . 12

2 Rotation periods for cool stars in the open cluster Ruprecht 147 **17**
2.1 Introduction . . . 18
2.2 K2 coverage, cluster membership, and CMD . . . 20
2.3 Analysis of the K2 lightcurves . . . 24
2.4 Rotation periods in the CMD and CPD . . . 28
2.5 Comparison with other empirical cluster period work . . . 29
2.6 Comparison with models . . . 30
2.7 Conclusions . . . 34

3 New insights into the rotational evolution of near solar age stars from the open cluster M 67 **37**
3.1 Introduction . . . 38
3.2 Observational data . . . 39
3.3 Lightcurves and rotation periods from the *K2* superstamp . . . 42
3.4 Results . . . 45
3.5 Discussion . . . 47
3.6 Conclusion . . . 55

4 Wide binaries demonstrate the consistency of rotational evolution between open cluster and field stars **57**
4.1 Introduction . . . 58
4.2 Sample construction and setup . . . 59
4.3 Grouping the wide binaries . . . 63
4.4 Discussion . . . 64
4.5 Conclusion . . . 74

5 The results in context **77**
5.1 Answering the posed questions . . . 77
5.2 Future prospects of gyrochronology . . . 80
5.3 A semi-empirical interpretation of stellar spindown . . . 82

6 Closing remarks and future perspective **89**

Acknowledgments **92**

Bibliography **93**

Appendix **99**

Appendix to Paper I **99**
A Relationship between *Gaia* $G_{\rm BP} - G_{\rm RP}$ and Johnson $B - V$ . . . 99
B Details of the Principal Component Analysis . . . 102
C Lightcurves and phase diagrams . . . 104
D Sample table . . . 107

Appendix to Paper II **109**
E M 67 cluster membership . . . 109
F K2 systematics correction . . . 110
G Supplements . . . 120

Appendix to Paper III **127**
H Issues in the period sample . . . 127
I `gyrointerp` (Bouma et al. 2023) . . . 129
J Sample table . . . 130

Preface

Since prehistoric times, humanity has observed the sky. What our forbears saw in *"the heavens"* has influenced many aspects of their lives – culturally and spiritually. Our earliest ancestors capable of thought have explored the course of the stars, the Moon, the Sun, and comets to find answers to philosophical and religious questions. But also many more practical aspects were shaped by studying the stars. Polynesian seafarers sailed the entire Pacific Ocean navigating by the stars (and ingeniously using oceanic currents) thousands of years before Magellan rounded the globe. But not only spatial awareness was provided by the stars – also temporal awareness. Especially with the advent of agriculture, humans used the stars to identify the right times to plant seeds, to harvest, and estimated how long till the end of winter. This makes astronomy (lit. translated as *"law of the stars"*) one of the oldest sciences systematically explored and applied by humankind, one without humanity may have evolved differently or not even successfully at all. And we have come a long way since those simultaneously humble but resourceful beginnings.

Astronomy, however, differs from other typical scientific fields in one crucial detail. Physicists and chemists can set up experiments in their laboratories to test their hypotheses and explore the nature of things. The same is true for most other natural sciences, for the humanities, and liberal arts – only occasionally limited by ethical considerations. However, controlled experiments are not possible in astronomy. An astronomer cannot take a test star or sample galaxy and put it in the lab to make experiments how it behaves under specific conditions. This comes from three relatively obvious facts.

First, there is no lab large enough to host most astronomical objects. Even the smallest astronomical objects, such as comets, asteroids, or even moons, exceed the size of any lab[1]. However, the size of such an object is crucial to the way it behaves, as for example, planets, moons, and stars are all spherical due to gravity. But gravity is a relatively weak force and only starts to play a role when a lot of mass (and with that a huge object) is considered. While we reach the temperatures and densities and observe the same processes as happen in the core of the sun in the lab, it is impossible to create a *miniature Sun* to be studied here on earth. A workaround – but not a solution – to this problem are model calculations to simulate a star or galaxy on a computer.

Second, astronomical objects are generally very far away. Even the closest object that is not part of the Earth, the Moon, is a whopping 400 000 km away. Not a distance one can easily cross especially considering all the difficulties of interplanetary space flight. Therefore, it was understandably a big deal when the Apollo missions brought back rocks from the surface of the Moon. Today we have visited most bodies in our solar systems with unmanned spacecrafts, either by landing or at least by flying close by. Still, missions like the Mars rovers are peak human ingenuity and dedication and on the edge of what can be done. After being launched in 1977 and decades of flying, the Voyager probes have, in 2012 and 2018, left the solar system and ventured into outer space – the first human-made devices to ever do so. But even after traveling 35 years and about 20 billion kilometers ($\sim$ 150 a.u.), they are only about 0.05 % of the way to the closest star Proxima Centauri, which is about 1.3 pc ($\sim$ 268 000 a.u.) away. Each year, they travel another 3 a.u. but even at this incredible speed[2], they would need another $\sim$ 90 thousand years to reach there. All this does not even mention exploring the Milky Way or even other galaxies. Sometimes, astronomical object arrive at earth and allow us to study them hands-on, but we are understandably uneasy about large asteroids or meteorites coming too close to earth.

Third, the time scales of processes in astronomy can be enormous. Processes span from milliseconds (pulsars), to hours (planetary transits), days (stellar activity), years (Supernovae explosions), and millions and billions of years (stellar evolution). A solar physicist who could, by whatever means, put a test sun into its laboratory would be dead a thousand times over before it would show any measurable changes due to its evolution. This has, of course, its advantages. The fact that the night sky does not change rapidly (aside from the motion caused by the rotation of the earth and the earth orbiting the sun) allowed it to be used by Polynesians for orientation and by Mesopotamians and Egyptians for timekeeping. If we were able to speak to the first modern humans in the African planes some 300 thousand years ago, they may point out that some of the closest stars to us have moved (in the order of a few degrees[3]), some have disappeared (typically the more massive stars exploded in a supernova), or have newly appeared. However, we would need to go back to the emergence of the very first humans, *Homo Habilis*, roughly 2.5 million years ago to see the full life cycles of some of the fasted living stars.

Ironically, one can summarize this by saying that while the firmament has aided us to track time and space throughout human history, but we struggle to assign both to the universe itself. Given those three problems, how are astronomers able to do any research at all? The answer is quantity. As the authors of the Hitchhikers Guide to the Galaxy in Douglas Adams' novel of the same name wrote: *"Space is big. You just won't believe how vastly, hugely, mind-bogglingly big*

[1] An exception to this are meteorites.

[2] Which means they would cover the distance between the Earth and Sun in just four months and the distance from earth to Moon ($\sim$ 0.003 a.u.) in just 8 hours. For comparison: it took the Apollo 11 crew about 3 days.

[3] This motion is large enough that most of the well known stellar constellation – Cygnus, Andromeda, etc – did not exist back then or at least were of notably different shape. Also, the brightest and closest stars to us were different ones throughout the millennia.

it is. I mean, you may think it's a long way down the road to the chemist's, but that's just peanuts to space." And while this is – as explained above – a problem in the exploration of space, it is also our savior seeing that this mind-bogglingly big universe is filled with an equally mind-boggling number of objects. Many of these objects are of similar kind and if we just keep searching long enough, we will find several similar ones. Let us take an example close to home – figuratively as well as literally – the Sun. We can study it in great detail but see nothing of its large-scale and long-term evolution. In fact, even Homo Habilis would not know the sun any differently from today – for that, we would need to go back to the Cambrian Explosion about 550 million years ago and ask a trilobite. Only then are the changes in the sun significant enough to be seen as clearly distinct from its current state. Naturally, this is not a real option as trilobites are very secretive about their observations of the sun (and everything else as well) and we have to explore the evolution of the sun on these timescales in a different way. What can we do? If we observe stars – even those that are relatively close by – we find many very similar to our sun. Most of those are younger, some about equal in age, and a few are older. With that we have our experiment set up, we arrange the stars by age and see how different aspects of them change over time. The universe has provided us with a time series to study.

We are with that, of course, bound to what the universe offers us as objects to explore and we fill the gaps between them with the help of the known laws of nature. It is a long and iterative process to explore the universe in this way. To create above mentioned time series of sun-like stars, we first need to understand that the Sun is a star (something debated since antiquity and only firmly established less than 150 yr ago), work out what differences in appearance are consequences of different evolutionary stages of the same type of object and what differences are indicative of completely different object. It is also possible that the same type of object just looks different to us when observed under different angles. This problem and its solution is inherent to most astronomical research and it is at the core of the work that is presented here – in its motivation but also in its means of exploration. However, there are limitations. The universe, while mind-bogglingly big, can only provide us with objects that *can* exist. For example, the similarly mind-boggling 14 billion years that our universe exists are simply not long enough for some objects to exist. Certain types of stars – M-dwarfs such as aforementioned Proxima Centauri – evolve so slowly that even if they had formed the moment our universe began its existence, they would still be only at around half of their (theoretically estimated) more than 30 billion years long lifetime. We can search as long as we want – we will never find M-dwarfs nearing the end of their life.

Prior remarks about creating a time series of sun-like stars from a set of stars of different ages may have left the inclined reader with the following question:

"How do we know that some stars are younger and some are older than our sun?"

With this, we have arrived at the heart of what this thesis is about. Age dating stars is one of the trickiest endeavours in astronomy and this thesis focuses on one particular method to do that: *gyrochronlogy*. The idea is to correlate the observed changes in the rates with which stars rotate with their age. As they age, stars systematically slow down their rotation. Our hypothetical trilobite discussion partner from earlier could tell us that at its time the sun rotated once every 24 days – slightly faster than today's once every 27 days. If we were to go back to the occurrence of the first life on Earth, commonly assumed to be about 3.5 billion years ago, we would see the sun rotate once every 10 days.

This thesis begins with an introduction in Part 1 that gives a historical perspective on the exploration of stellar rotation in general and gyrochronlogy in particular. Scientific domain-specific terminology is introduced and some fundamental concepts are explained. The aim of this section is to provide a baseline to formulate the posed research questions, construct the framework for the exploration, and motivate the efforts taken. The scientific work this thesis is based on is detailed in three peer-reviewed research papers that are reproduced in Parts 2, 3, and 4. Finally, Part 5 ties the individual works back together and evaluates the outcome of the papers in the grand scheme of things. And with that, let us reach for the stars, use the universe as our laboratory, and dive right into the intricate complexities that are at the core of frontier astronomical research.

Part 1 – An introduction

The rotation and ages of stars

A reliable characterization of stars is crucial for various fields of astronomy and astrophysics. If we find an earth-sized exoplanet around another star, comfortably sitting in the habitable zone, we naturally arrive at the question whether it may harbor life. Crucial in answering this is to figure out how long life on this planet would have had time to evolve, i.e., we need to find out how old the planet is which, in turn, means we have to find out how old its host star is. However, the age of a star is a rather elusive parameter. It cannot be measured directly for it would require us to observe it since its formation with a stopwatch in our hands. Every observation of a star will only reveal a small snapshot of its long life. We have similar problems for objects and processes with characteristic timescales exceeding centuries that occur here on Earth. To find a solution for astronomical objects we can look at how we deal with their more earthly counterparts. Some typical methods to deal with them are:

- Trees live hundreds to thousands of years and we measure their age by counting the rings seen in their stems. Each year a ring forms due to different growth rates throughout the seasons of a year.
- Radiocarbon dating measures the amount of certain carbon isotopes in the (potentially fossilized) remains of an organic life form.
- A human life span is very close to, well, a human life span but still, we can measure the time a human is alive for only very few individuals directly. Still, meeting them on the street, we can estimate the age of a total stranger by looking at how many wrinkles are on their faces and how many gray hairs are on their head.

All those methods have one common concept: they all observe one or more intrinsic parameters (rings, gray hair, ^{14}C) and correlate it with the age of the object from an understanding of its temporal evolution. However, we can see in the examples given above that the individual methods vary widely in aspects of precision (tree rings allow a precision of about a year, wrinkles give more of an old vs. young distinction), reliability (cataclysmic events like volcanic eruptions can stop tree growth entirely making the tree appear younger; humans may have used make-up and hair dye, likewise making them appear younger), and applicability (radiocarbon dating struggles for samples older than 50 thousand years). In a few cases, the correlation between the age and the parameter can be established directly based on some fundamental concepts (one ring per year, dictated by the changing seasons), but for most, we need to establish an empirical calibration as the actual connection between age and parameter is rather obscure and/or complex.

Age dating stars is based on the same concept, we observe a specific parameter and correlate it with its age. The different stellar parameters vary widely in their usefulness, precision, and applicability for age estimates. Let us quickly review some commonly used parameters and methods.

- Classical stellar parameters, such as its temperature $T_{\rm eff}$ or luminosity L_*, are like wrinkles in humans. They change very little throughout large amounts of the stellar lifetime and allow only a rough estimate – whether the studied object is an older or younger specimen. Large-scale surveys tend to employ classical stellar parameters for an age estimate, e.g., VPNEP (Strassmeier et al. 2023) and the Geneva-Copenhagen (Nordström et al. 2004; Casagrande et al. 2011) surveys. However, already the earliest applications have pointed out the inherent uncertainties and limitations when dealing with main sequence stars (e.g., Perrin et al. 1977). Classical stellar parameters can, however, be very useful if we look at an ensemble of coeval stars. In those cases, the association with a more rapidly evolving giant star can allow an age estimate of a barely changing dwarf star. This advantage is leveraged in stellar associations and clusters and is used extensively in astronomy in general and throughout this work in particular.
- The abundances of certain trace elements such as Lithium are like the number of deciduous (*milk*) teeth in a human child. Due to different processes, they deplete over time. They are a very good indicator while the experimentee is young, but cease to be usable at older ages. At some point, no milk teeth and no Lithium is left and all we can say is that our subject is too old to have any. Coincidentally, milk teeth and Lithium are both lost relatively early in

life, limiting both methods to a similarly relatively young subject. Lithium studies typically require detailed work on high-resolution spectroscopy (e.g., Strassmeier & Steffen 2022) and are therefore rather limited in application. There are other trace elements (e.g., Yttrium) whose relative abundance compared to other elements changes with age (e.g., Nissen 2015; Bedell et al. 2018; Jofré et al. 2020). However, the systematics of these are barely explored to date, especially beyond solar-type stars. A related method is Nucleocosmochronometry that employs long-lived radioactive isotopes of, e.g., Thorium and Uranium (e.g., Cowan et al. 1991; Ludwig et al. 2010, and references therein).

- Stars show variability on short timescales. In the sun we know the corresponding effects as sunspots, flares, faculae, and coronal mass ejections. They are summarized under the term of stellar (magnetic) activity and are powered by the stellar dynamo. The amount of activity (meaning, e.g., occurrence rates of spots, their size, or the energy in flares) decreases with age (e.g., Wilson 1963; Wilson & Woolley 1970; Vaughan 1980). However, and we see this directly for the Sun, the amount of activity varies throughout this decline. This is visible in the form of a cycle (like the 11 yr activity cycle for our sun) but also on a day-to-day basis. With that, stellar activity as an age indicator is like gray hair is for a human. If we only observe it at one moment, we only see the current look which can be a bad representation of the age, e.g., when the human just dyed their hair and a star is during a phase of higher activity, both appear younger than they actually are. Humans are also subject to (dis)favorable genetics, causing gray hair to occur earlier or later in life, or may make them lose all hair already at a relatively young age. Stars do not have genes, but changes in stellar metallicity change many aspects of a star, including its activity levels (e.g., Karoff et al. 2018).
- Asteroseismology is a comparably recent addition to the zoo of methods and finds its analogy in ring counting for trees. It uses the frequencies of seismic waves, measured by surface brightness variations, that indicate a star's density structure. From that, one can estimate, e.g., the size of a star's helium core (e.g., Ulrich 1986), which grows over time as the star continues to burn hydrogen – just as the number of rings in a tree. It is explored for decades for giants (e.g., Basu et al. 2011, and references therein), however, the application to dwarf stars is still in its infancy and often leads to conflicting results (e.g., Hall et al. 2021).
- There are *statistical* ages that are somewhat akin to estimating the age of a human based on how recently they had been to a doctor. On average, one will find that the last time of such a visit is longer ago for younger people, but it will not help to narrow down the age of the individual person. For stars one looks at their metallicity content (e.g., Meusinger et al. 1991; Zhao 2005; Sahlholdt & Lindegren 2021) as younger stars tend to be born from more metal-enriched clouds, or the peculiar velocities (e.g., Mihalas & Binney 1981; Newton et al. 2016) because they, on average, increase as stars scatter with massive objects (e.g., clusters, molecular clouds) in the galaxy over time.
- One star is special in this regard as in so many others: the Sun. In terms of age dating, the Sun is like our older sibling, for we know someone who was there when it was born and who we can actually inquire about it. For our sibling, it would be our parents, for the sun it is meteorites. The *Holmes-Houtermans* method compares abundance ratios between different lead isotopes (^{207}Pb/^{204}Pb vs. ^{206}Pb/^{204}Pb, see e.g., Patterson 1956; Dalrymple 1991). The observed ratio is a direct function of the time since the formation of a rock due to the different isotopes being end-products of different radioactive decay chains with well-established half-life times. Studies of meteorites can date the formation of the solar system (and with that of the Sun) to 4.56 Gyr ago (e.g., Tatsumoto et al. 1973; Amelin et al. 2002); and that with systematic uncertainties of ± 1 Myr.

This is only a selection of the most commonly and widely used methods. Other, more niche, methods include *white dwarf cooling ages* (e.g., Salaris 2009, and references therein) and *kinematic expansion ages* (e.g, Blaauw 1964). The zoo of age estimation methods often comes with a distinction into whether methods are empirical (e.g., activity and stellar abundance) or model-dependent (e.g., isochrone fitting and asteroseismology). Model-dependent methods stand and fall with the fidelity and approximations of the input physics for said model. Missing details or insufficient accuracy can lead to systematic errors. Empirical methods are – some more, some less – directly calibrated on observations. With that, they are by design *"accurate"* in describing the observation. However, given that this is often times done without (or with limited) knowledge of the exact causality connecting age with a certain parameter, they lack true predictive power. Independently of being empirical or model-dependent, methods vary widely in their usefulness for different types of stars. Especially for late-type main sequences stars, the most frequent types of stars in the universe, deriving reliable ages using the methods described above – if it is at all possible – requires rather extensive data and cumbersome work while still leaving large uncertainties in an estimate[1]. For an extensive review of age dating methods of stars see Soderblom (2010).

What we need is a method that leverages a stellar parameter that evolves significantly enough throughout the stellar lifetime to allow a well-constrained estimate, one that does not lose applicability prior to or beyond certain age thresholds, and is – at least to some degree – universal for stars. There are more criteria that distinguish a good age dating method – like the degree to which results are model-dependent or how many rungs a corresponding calibration

[1] While being a problem for astronomy and our attempts to derive stellar ages, it is overall a good thing that stars (and their observable properties) evolve so slowly. Life on earth would have had a hard time if the Sun were to evolve over thousands and not billions of years.

ladder has (see e.g., Table 1 in Barnes 2007, or Table 1 in Soderblom 2010). *Gyrochronology* is our way to approach this problem by leveraging the mass-dependent change in a star's rotation rate with age. Its exploration is at the core of this thesis. In the zoo of age estimation methods, gyrochronlogy leans heavily on the empirical side.

1.1 Magnetic braking and the evolution of stellar rotation

It all begins with a simple but consequential observation reported in a paper that today has probably one of the highest ratios of citations to page numbers[2]. On just two pages, Skumanich (1972) reported three findings based on solar-type stars in three open clusters and the sun. Based on measurements in stars in the Pleiades, Ursa Major, and the Hyades stellar open cluster[3], Skumanich (1972) found that (1) with increasing age the Li abundance declines, (2) chromospheric Ca II emission (an indicator for stellar activity) decreases, and (3) the stellar rotation slows down. Relevantly for us, Skumanich (1972) observed that the rotation rate of a sun-like star correlates systematically with its age as

$$v \sin i \quad \propto \quad \frac{1}{\sqrt{t}} \qquad \left(\text{actually: } v \sin i \propto t^{-0.51}\right), \tag{1.1}$$

where $v \sin i$ is the projected rotational velocity of the star and t its age.

This effect is well confirmed today – including for other late-type main sequence stars – and finds its origin in *magnetic braking*, a term likely going back to Alfvén (1942). The charged particles of the stellar wind interact with the magnetic field of the star (see the works of, e.g., Parker (1958) and Weber & Davis (1967) exploring this concept for the sun) and are forced to co-rotate, forming the famous Parker spirals. With that, there is a continuous transfer of angular momentum from the star to the wind, angular momentum that is subsequently lost from the system when the wind particles escape the solar magnetic field beyond the Alvén radius r_A. Alternatively, it is also possible to say that the enforced co-rotation creates a lever that exerts a torque back on the star (e.g., Brandt 1966). The angular momentum loss is significant enough to cause the star's rotation rate to slow down notably – one also calls this the *spindown* – over the cause of its billions of years of lifetime. The strength of magnetic braking is a direct consequence of the coupling between wind and magnetic field and as such is a function of the mass-loss due to the wind and the Alvén radius r_A. The latter depends on the stellar magnetic field and with that on the rotation of the star. This leaves us with an intricate mass-dependent interplay between rotation rate, magnetism, and spindown that causes a systematic evolution in stellar rotation. Before going forward, we need to have two facts in mind.

1. Not all stars spin down. The Kraft break (named after Robert Kraft who was one of the first ones to describe it, e.g., in Kraft 1967) describes an abrupt boundary in stellar rotation rates. Stars cooler than the break at around 6200 K (i.e., $\lesssim 1.3\,M_\odot$) show a wide variety in rotation rates, fast and slow, whereas stars hotter than the break consistently rotate fast. Today, this is associated with the existence of an outer convective envelope in the colder stars which is assumed to be the origin of the stellar dynamo and with that of the magnetic field and activity. Hotter stars do not have such, thus do not experience magnetic braking and remain fast rotating.
2. Magnetic braking reduces the angular momentum of a star. Exploring stellar rotation rates is only meaningful as a measure of the angular momentum when the star does not change its shape (i.e., radial mass distribution, moment of inertia) significantly – the notorious figure skater effect. This is obviously not fulfilled for giant stars which have undergone large changes in their radii and inner structure. In principle, it should be possible to observe angular momentum evolution expressed by the observable rotation rates. However, as of this writing, this has not been done. In any way, giants show rapid evolution and as such do not require gyrochronlogy as a way to determine their ages.

Consequentially, this entire discussion is limited to late-type (FGKM) main sequence stars. Until noted otherwise, when we refer to stars, we will always mean cool dwarfs.

This thesis focuses on its observational and empirical aspects and as such theoretical considerations will be limited to selected opportune moments. To understand stellar rotational evolution, we need to explore the rotation rates that stars of different ages exhibit. Naturally, the exploration of stellar rotation predates Skumanich (1972) and even a variation of stellar rotation rates with age was seen before (e.g., Kraft 1967; Conti 1968; van den Heuvel & Conti 1971). Table 1.1 gives an overview of a selection of open cluster work, including some seminal early work. There is plenty of work done on young open clusters, originally exploring stellar rotation in general and then, later, to establish the connection to stellar activity (e.g., Pallavicini et al. 1981; Noyes et al. 1984, and references therein). The following section details some key aspects of the exploration and measurements of stellar rotation.

[2] Half a century after its publication it has amassed more than 1660 citations for a paper whose content fills two pages, with half a page filled by a figure and another half filled by title and acknowledgments.

[3] The data used by Skumanich (1972) are somewhat outdated – especially the cluster ages – and are reproduced here for completeness: Pleiades ($v \sin i \approx 11\,\mathrm{km\,s^{-1}}$, $t = 40\,\mathrm{Myr}$), Hyades ($v \sin i \approx 7\,\mathrm{km\,s^{-1}}$, $t = 400\,\mathrm{Myr}$), and Sun ($v \sin i \approx 2\,\mathrm{km\,s^{-1}}$, $t = 4.5\,\mathrm{Gyr}$). The $v \sin i$ measurements were taken from Conti (1968). We note that Skumanich (1972) did not have rotation data for Ursa Major stars.

Table 1.1: *Overview of selected works on stellar rotation in open clusters. Not a complete list, but entries have contributed to the systematic exploration of stellar spindown.*

Cluster	t [Myr]	d [pc]	Reference	Method	Observatory
IC 2391	30	151	Patten & Simon (1996)	photometry	ground based (CTIO)
IC 2602	30	152	Barnes et al. (1999)	photometry	ground based (CTIO)
IC 4665	50	345	Allain et al. (1996)	photometry	ground based (Haute-Provence)
α Per	50	170	Randich et al. (1996)	$v \sin i$	
			Prosser et al. (1995)	photometry	ground based (various)
			Prosser & Grankin (1997)	photometry	ground based (various)
Pleiades	150	135	Kraft (1965)	$v \sin i$	
			Anderson et al. (1966)	$v \sin i$	
			Stauffer et al. (1984)	$v \sin i$	
			Stauffer & Hartmann (1987)	$v \sin i$	
			van Leeuwen et al. (1987)	photometry	ground based (Dutch 91 cm)
			Krishnamurthi et al. (1998)	photometry	ground based (various)
			Rebull et al. (2016)	photometry	*Kepler/K2*
M 35	150	885	Meibom et al. (2009)	photometry	ground based (WYIN)
M 50	150	998	Irwin et al. (2009)	photometry	ground based (CTIO)
NGC 2516	150	415	Barnes & Sofia (1998)	photometry	ground based (CTIO)
			Fritzewski et al. (2020)	photometry	ground based (CTIO)
Blanco 1	150	237	Cargile et al. (2014)	photometry	ground based (KELT)
NGC 3532	300	484	Fritzewski et al. (2021)	photometry	ground based (CTIO)
Coma Ber	450	85	Kraft (1965)	$v \sin i$	
			Radick et al. (1990)	photometry	ground based (Lowell)
Hyades	650	47	Kraft & Wrubel (1965)	$v \sin i$	
			Stauffer et al. (1987)	$v \sin i$	
			Radick et al. (1987)	photometry	ground based (Lowell)
			Douglas et al. (2019)	photometry	*Kepler/K2*
Praesepe	700	186	Agüeros et al. (2011)	photometry	ground based (Oschin Schmidt)
			Douglas et al. (2017)	photometry	*Kepler/K2*
			Rampalli et al. (2021)	photometry	*Kepler/K2*
NGC 6811	1000	1150	Meibom et al. (2011a)	photometry	*Kepler*
			Curtis et al. (2019)	photometry	*Kepler*
NGC 752	1300	438	Agüeros et al. (2018)	photometry	ground based (PTF)
NGC 6819	2500	2808	Meibom et al. (2015)	photometry	*Kepler*
M 67	4000	883	Barnes et al. (2016b)	photometry	*Kepler/K2*

1.2 Exploring stellar rotation in open clusters

Originally, estimates of stellar rotation came from $v \sin i$ measurements. The observations are relatively straightforward and its ideas can be traced back to the early days of stellar spectroscopy (e.g., Abney 1877). A spectrum of a star is recorded and $v \sin i$ is measured from the broadening of spectral lines, after accounting for other effects such as temperature broadening and turbulence. This works well for fast-rotating stars – the broadening is huge – and it can be done with a single observation per star. The problems with $v \sin i$ are, however, twofold. (1) slow rotating stars show only a weak broadening and disentangling it from other effects such as temperature and turbulence becomes increasingly difficult. (2) We measure only the projected rotational velocity and the projection angle i is generally unknown. Today's stellar rotation measurements have moved past $v \sin i$ and towards photometric periods.

A photometric rotation period is obtained from periodic brightness variations of a star. Those variations originate in the movement of activity features, generally spots and faculae, across the stellar surface. Where it is known since antiquity that our sun exhibits such activity features[4], it was generally not known if other stars exhibit the same. In a photometric study of eclipsing binaries, Wood (1946) observed *anomalous* brightness variations in time series data of

[4]Solar activity and the behavior of sunspots are systematically observed since centuries (e.g. Arlt 2009; Arlt & Vaquero 2020, and references therein).

AR Lac which could be shown to only originate from one of the stars, and which Kron (1947) interpreted as *"huge light and dark patches"*, moving with stellar rotation. They proceeded to identify the first photometric rotation period; $P_{\rm rot} \approx 2\,$d for the binary's G-type component. The systematic exploration of rotation in stellar open clusters using time series photometry can be traced back to van Leeuwen & Alphenaar (1982, see also van Leeuwen et al. 1987) in the Pleiades and Radick et al. (1987) in the Hyades.

Originally, the recording of stellar photometric time series was as, or even more, tedious as $v \sin i$ measurements. Stars had to be targeted individually (albeit for shorter exposures each), including nearby "constant" stars for calibration, repeatedly over an extended length of time. If one is to identify a periodicity in brightness variability one needs to observe a star for at least twice as long as the period[5]. With the advent of CCD photometry, this problem eased a bit, however, early CCDs were small and often times only captured one star at a time anyway (e.g., Barnes & Sofia 1998).

The exploration of stellar rotation via photometry got a major boost somewhat as a byproduct of different scientific goal. The question of whether we are alone in the universe has concerned humanity likely since it gained consciousness and a major step towards the (far from reached) answer came as do many scientific discoveries: by accident. Mayor & Queloz (1995) studied radial velocity variations of binary stars when they found for one of the stars (51 Peg) a variation that could only be explained by a companion with a mass of a Jupiter-sized planet rather than a star. It was the first detection of an extrasolar planet around a main sequence star[6]. This Nobel Prize-awarded discovery sparked a still ongoing hunt for extrasolar planets and a significant fraction of it is done with photometric time series observations searching for transiting planets.

This meant there were now large-scale programs, dedicated largely but not exclusively to exoplanet hunting, that were planned, commissioned, and launched. And while they discovered thousands of exoplanets (and candidates), they also provided enormous amounts of photometric time series data for field and cluster stars. Data that were used to derive stellar rotation periods. The most significant missions were space-based, i.e., satellites taking uninterrupted (by weather, seasons, and day-and-night cycle) time series with large CCDs of hundreds and thousands of stars at the same time. This work is, as are hundreds of others, based on the legacy of two decades of space-based photometry. Notable among them are:

Microvariability and Oscillations of Stars/Microvariabilité et Oscillations STellaire (MOST, Rucinski et al. 2003) was launched in 2003 and operated by the Canadian Space Agency (CSA). Its mission focused on stellar variation due to pulsations and is only mentioned here as it was the first optical telescope dedicated to long time series data (observed single targets for up to 60 d). The tiny satellite (53 kg) was decommissioned in 2019.

Convection, Rotation et Transits planétaires (CoRoT, Baglin et al. 2006) was launched in 2006 and operated by the French space agency (CNES) and ESA until its decommissioning in 2014. It was the first mission geared towards the detection of exoplanets[7] and also asteroseismology. The *"eyes of CoRoT"*, colloquially referring to the two regions in the galactic plane *CoRoT* observed are indicated in Fig. 1.1 in purple.

Kepler Space Telescope (Kepler, Borucki et al. 2010) is undoubtedly the most impactful space telescope for the exploration of late-type stars. During its almost 10 yr long operation from 2009 to 2019, it provided time series data for several hundred thousand stars which led, among other things, to the discovery of thousands of planets. This work, as so many other contemporary studies, is based on data from the Kepler mission, be it its main mission where it observed one field for 4 yr continuously, or its second light mission *K2* where it observed various fields along the ecliptic for about three months each. Essentially all large samples of rotation periods for cluster and field stars commonly used are based on *Kepler* data. Figure 1.1 displays the locations of the individual *Kepler* fields (green).

BRIght Target Explorer (BRITE, Weiss et al. 2014; Pablo et al. 2016) is a constellation of three (originally 6 planned) microsatellites to photometrically monitor bright stars ($V < 4\,$mag) that was launched in 2013/14. Its mission is geared towards the variability of early-type stars and cool giants.

Transiting Exoplanet Survey Satellite (TESS, Ricker et al. 2014) continues the historic trend of the telescopes from above to be even more geared towards exoplanet detection. It is the intellectual descendant of *Kepler* (operated by many of the same people), began its mission in 2018, and, unlike all others in this list, *TESS* observes almost all-sky (albeit not simultaneously). However, given its large pixels ($20\times20''$) and short baseline for continuous observation ($\approx 25\,$d) it is still open if *TESS* will have a similar impact compared to *Kepler*.

Other noteworthy mentions for this list include the *Gaia* mission (Gaia Collaboration et al. 2016) and the various X-ray telescopes like *Chandra* (Weisskopf et al. 2000), the *X-ray Multi-Mirror Mission* (XMM-Newton, Jansen et al. 2001), or *eROSITA* (Predehl et al. 2010). However, neither of those is dedicated to photometric time series observations, and thus their data is of limited use to us – at least with respect to stellar rotation. The most significant mission

[5] Not continuously, but the individual rotations need to be sufficiently covered.

[6] The very first extrasolar planet was found around a Pulsar by Fruchter et al. (1988) based on timing variations of its pulses.

[7] which it did not long after its launch (Fridlund 2007)

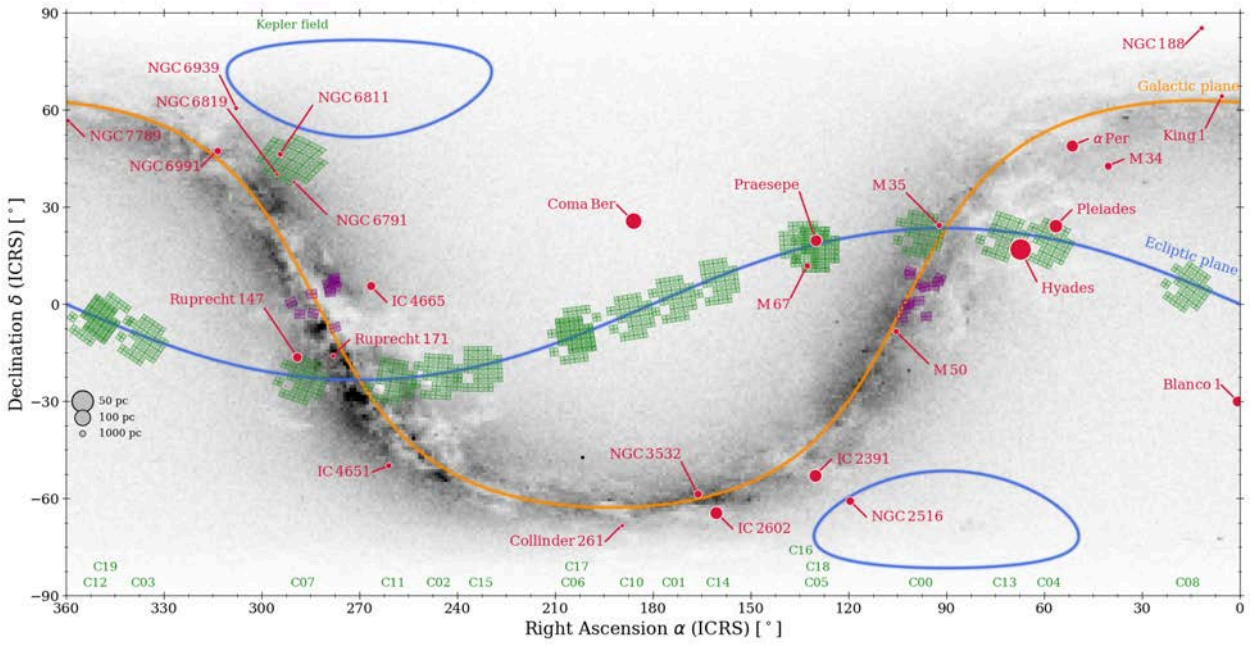

Figure 1.1: *All-sky map of relevant open clusters. Background histogram is created from* Gaia *DR3 (including all stars with* $G \leqslant 13\,mag$*). Overplotted in blue and orange are indications for the ecliptic and galactic planes, respectively. The* Kepler *and* K2 *fields are indicated in green and labeled at the top and bottom of the figure, respectively. Relevant clusters (cf. Table 1.1, and 5.1) are shown in red and their distances are encoded in the symbol size as indicated. Blue encircled areas indicate the* TESS *continuous viewing zones around the ecliptic poles. The* CoRoT *fields are indicated in purple.*

is *Kepler*. In fact, all work in this thesis is based entirely on *Kepler* data. In Table 1.1, we have listed a selection of open cluster work in recent years. A significant fraction – especially regarding older clusters – has been done based on data obtained by *Kepler*.

The original *Kepler* mission pointed at a region in the constellation Cygnus for 4 yrs. Many considerations went into this decision, e.g., the field was moved further away from the galactic plane to reduce the probability of detecting background eclipsing binaries that may mimic planetary occultations in the light curves (Batalha et al. 2006). Figure 1.1 gives an all-sky view of the location of the *Kepler* field in comparison to relevant clusters. Relevantly for us, this field contained the open clusters NGC 6811 (1 Gyr), NGC 6819 (2.5 Gyr), and NGC 6791 (6.7 Gyr). The former two are to this day the most distant and some of the oldest open clusters studied. In general, stars in the *Kepler* field are rather distant and with the relatively large pixels ($\sim 4'' \times 4''$) it is rather difficult to study dense regions (such as clusters). In May of 2013 a second of four reaction wheels failed[8] and the *Kepler* team devised an ingenious method to steer the telescope by using its thrusters and solar wind pressure (see e.g., Van Cleve et al. 2016). This, however, concluded the *Kepler* main mission. In 2014, the telescope saw second light with the start of the *K2* mission, where – instead of one continuous observation of one field – it would now observe various patches along the ecliptic. Also, the scientific focus of the mission shifted, from solar-type stars to M-dwarfs.

Over 4 yr and with 17 different pointings, *Kepler* continued its work – ultimately producing the data that a large fraction of this thesis is built upon. There were, however, problems with the way the telescope was operated now, problems that left their traces in the data.

Large data systematics caused by the perpetual motion of the telescope made handling *K2* data much more difficult. In Part 3 and specifically in Appendix F we address those issues in excruciating detail. In October 2018, after almost nine years and eight months of continuous operation, *Kepler* ran out of fuel and was retired by NASA. It left a legacy of > 2000 planet detections (and several thousand more candidates) and photometric time series data for more than 300 000 stars. The latter enabled the open cluster works listed in Table 1.1.

Similar to photometric rotation periods are those derived from stellar activity. To be clear, this does not refer to estimating a star's rotation period based on its activity level, as done by, e.g., Mamajek & Hillenbrand (2008), typically involving some sort of empirical scaling relation. Those are not measurements in this sense and are subject to the same uncertainties mentioned initially about stellar activity. Therefore, they are not considered here any further. Meant is narrow-band photometric time series data taken around spectral regions very sensitive to stellar activity, such as Ca H&K and the Ca II infrared triplet. Activity periods are therefore closely related to photometric periods in that both methods trace the occurrence of activity features.

Most significant in this regard is the work of Olin Wilson (e.g. Wilson & Vainu Bappu 1957; Wilson 1978) and his

[8] Three are needed to aim the telescope properly. The first had failed in July 2012

intellectual descendants (see Lockwood et al. 2007, and references therein). The essential body of work performed under this umbrella is today typically referred to as the Mt. Wilson (MW) H&K project, named after the employed observatory in Southern California[9]. Over the span of several decades, narrow-band photometry was collected for several dozens of stars[10]. It allowed the first detection of solar-like activity cycles in stars other than the sun by measuring long-term activity changes. Furthermore, by tracing individual activity features similarly to spots as they cross the stellar surface, Baliunas et al. (1996) was able to derive rotation rates for over 100 stars. While this sample was constructed more than half a century ago and many of the stars in it have subsequently been identified as multiples or planet hosts, the Mt. Wilson stars are still the best-studied sample in all of stellar activity. Notably, due to their proximity various Hyades stars are among the MW sample and their overlap are the same stars used in the original work by Skumanich (1972), albeit Skumanich did not use the MW data but independent $v \sin i$ measurements.

The availability of rotation data for vast numbers of stars – especially those within clusters and thus with secure age estimates – has enabled a systematic exploration of rotational evolution and the proposition of gyrochronology.

1.3 The origins and concepts of gyrochronology

At this point, I want to quickly introduce another concept that is important going forward, the *color-period diagram* (CPD, see Fig. 1.2). As the name suggests, it is not unlike its famous cousin the *color-magnitude diagram* (CMD). However, it uses the central stellar parameter of this work: the rotation period $P_{\rm rot}$. We will see below, that stellar spindown is mass-dependent and a CPD allows us to trace this mass dependence easily. The color acts as a proxy for the stellar mass M_* in this case. For main sequence stars, there is a direct (albeit non-trivial and metallicity-dependent) relationship between mass and color. The color is – unlike the mass – an observable, and thus preferred here. Figure 1.2 indicates an additional axis for mass and temperature each to indicate the relationship to the color.

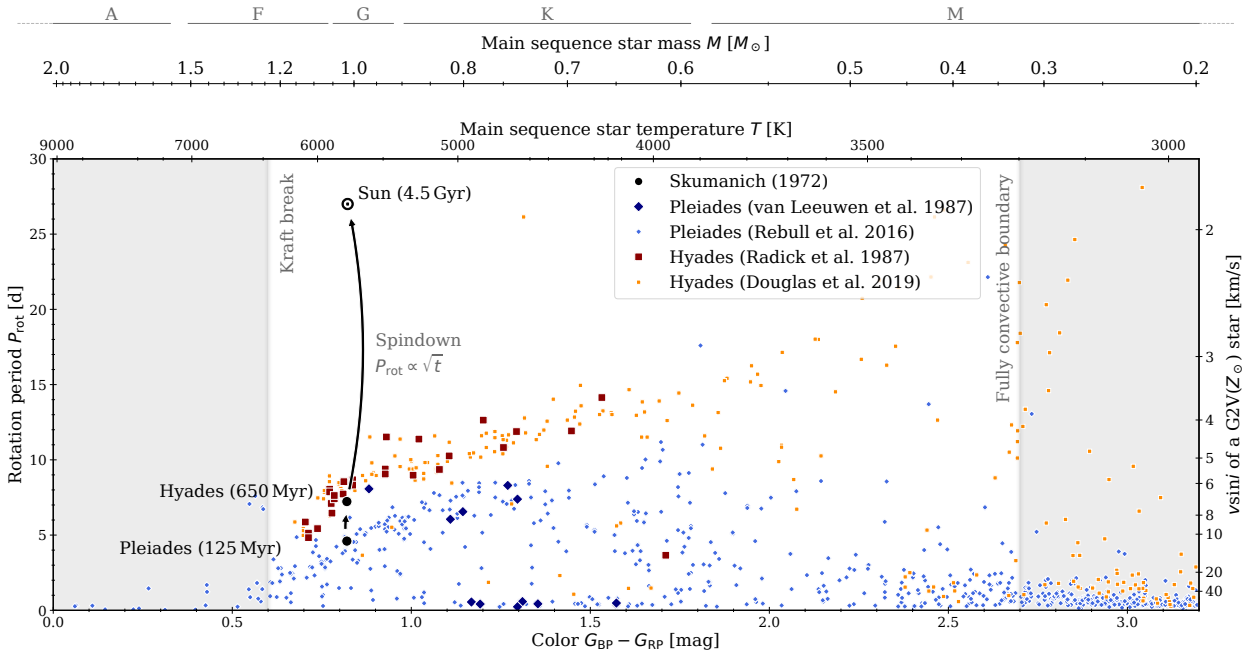

Figure 1.2: *The fundamental concepts of a color-period diagram (CPD). The figure recreates some relevant aspects from Skumanich (1972, see footnote 3), albeit using the rotation period P_{rot} instead of $v \sin i$ (red). Overplotted are rotation period measurements for the Hyades (red, Radick et al. 1987; Douglas et al. 2019) and Pleiades (blue, van Leeuwen et al. 1987; Rebull et al. 2016) from later ground-based (large symbols) and space-based (small symbols) photometry for comparison giving an idea of the historical progress in the observations and the mass-dependence. Note that the Skumanich (1972) data originates from a mean $v \sin i$ of the studied stars at the time whereas all other points denote individual stars. Additional axes are given to illustrate the connection between mass, color, $T_{\rm eff}$, and spectral type of a star (estimated based on solar metallicity). The $v \sin i$ scale refers to a sun-like (G2V) star with solar metallicity (i.e., $R_* = R_\odot$ is fulfilled) and is generally not valid for any other type of star.*

[9]Historical note: The similarity in name between the Mt. Wilson observatory (lending its name to the survey) and the observer Olin C. Wilson is purely coincidental. The observatory is named after the mountain (Mt. Wilson), which itself was named after Benjamin Davis Wilson, who (in 1852) created a trail following his ultimately unsuccessful search for wood suitable to make casks out of for his nearby vineyard. It was the first recorded exploration of the mountain; however, archaeological findings suggest that the native Tongva people and Spanish explorers had surveyed the mountain before. In fact, B. D. Wilson's trail followed an older route created by the natives (Collins 2000). The observatory itself was built from 1905 to 1907 and named after the mountain. Olin Wilson moved there from San Francisco/UC Berkeley in 1932 for his Ph.D. thesis and proceeded to spend most of his research career there (Abt 2003). His biography by Abt does not contain an indication whether or not the naming coincidence had an impact on this decision.

[10]see details at `nso.edu/data/historical-data/mount-wilson-observatory-hk-project/`

Stellar rotation periods were gathered plentiful since the 1960s, exploring many young and nearby open clusters. The quality of data and the precision of measurements improved steadily. And it all led to Barnes (2003), who to took the gathered puzzle pieces and revealed the emerging picture a little more than three decades after the original work of Skumanich (1972). Barnes (2003) took the aforementioned data for the open clusters and viewed them as a series of steps in the temporal evolution of open clusters and the stars within them and identified the formation and evolution of two distinct substructures (see their Fig. 2).

The formation of substructures was nothing new; similar sightings had been report by, e.g., Stauffer & Hartmann (1987) and Soderblom et al. (1993b). However, what was new was bringing all the clusters together, giving shape to the substructures, recognizing their temporal evolution, and ultimately proposing the idea to invert the observed principles to use stellar rotation rates directly as an age indicator. And with that Barnes (2003) gave rise to a new age dating method which is the central aspect of the work in this thesis. Barnes (2003) coined the term *gyrochronology* for the proposed methodology, inspired by the term *dendrochronology* by A. E. Douglass (1928, for dating trees from their ring growth; from the Greek *dendron* meaning "tree")), as a combination of the Greek words *gŷros* ("round", lit. "to turn"), *khronos* ("times") and *logia* ("the study of")[11].

In homage to its 20th anniversary (and to illustrate the concept), we have reproduced some key aspects of Fig. 2 and 3 of Barnes (2003) here in Fig. 1.3, based on updated photometry and rotation data for the some of same clusters and with the original empirical description (their Eq. (1) and (15)).

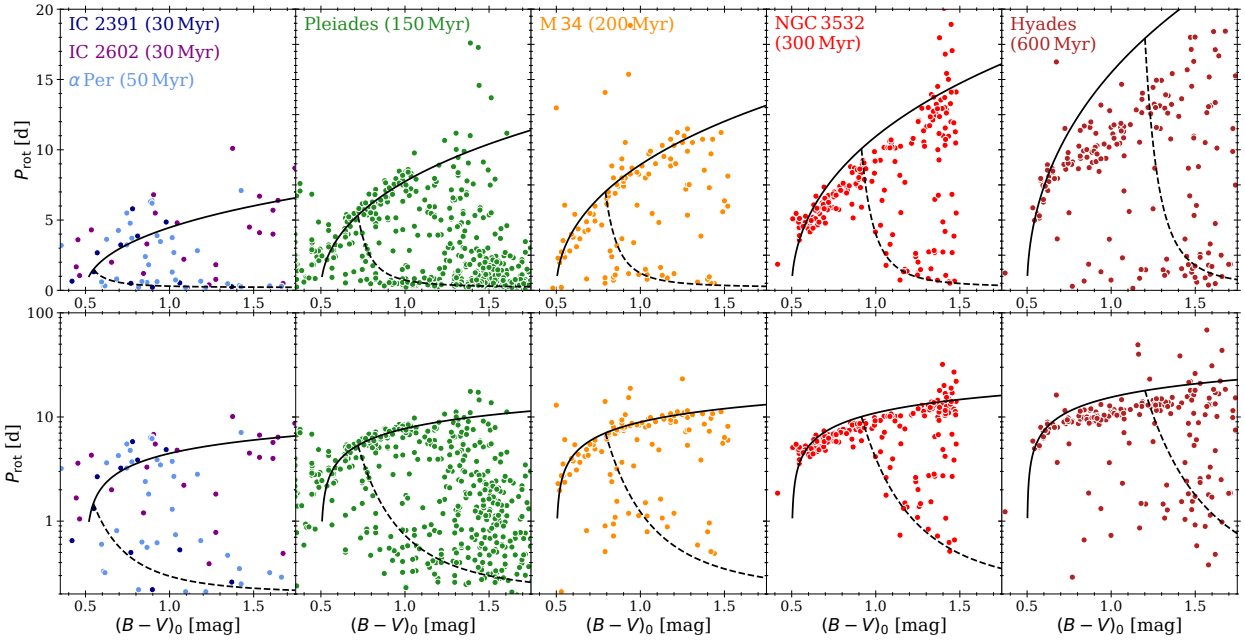

Figure 1.3: *Recreation of some key aspects of Fig. 2 from Barnes (2003). The color-period diagrams (CPD) show the distribution of stellar rotation periods measured for selected young open clusters. The open cluster data is taken from the references listed in Table 1.1.*

What exactly did Barnes (2003) – and now us – find? Two structures emerge for all clusters, formed out to varying degrees of definiteness, and roughly traced by the overplotted lines in the figure. The solid line indicates a somewhat diagonal band across the CPD, from rapidly rotating stars in the blue to slower rotating stars in the red. With increasing age, the band moves to slower rotation rates and the faction of stars on this band increases. This band was dubbed *Interface* (*I*) sequence by Barnes (2003). Entirely below in a color-dependent sense, we find what Barnes (2003) has called the *convective* (*C*) sequence (indicated by the dashed line). Between those two sequences, we find a *gap*, albeit a somewhat populated one. Barnes (2003) has actively refrained from naming the sequences the *slow* and *fast rotator* sequences. Thou the naming may be intuitive it is obviously not an accurate description as it is not the rotation rate alone that separates the sequences. Nevertheless, the terminology of fast[12] and slow rotator sequences has found its way into the vernacular of the community and we will adopt it here as well[13].

The focus of this work is with regard to the evolution of rotation for stars much older than the clusters in Fig. 1.3 and concerns almost exclusively the slow rotator sequence. As such, we limit ourselves to a brief overview of some

[11] Although it should be noted that *gyrochronlogy* refers with its name to the property of the object (rotation) and not to the object itself as does *dendrochronology* (tree). However, the term *astrochronology* (which would be the direct equivalent) is already used in geology for dating sediments with regards to astronomical timescales and processes (e.g., Krijgsman et al. 1999).

[12] sometimes also referred to as *rapid rotator*

[13] *I* and *C* sequences derive their naming from assumption towards the dominating dynamos in each star, i.e., one created at the *interface* (*I*) between radiative core and convective envelope (at the tachocline) and one created in the *convective* (*C*) zone.

general understandings regarding early evolution and the fast rotator sequence.

The generally accepted interpretation of Fig. 1.3 is that stars upon formation are fast rotating. And they have to be, owing to the fact the angular momentum of the (huge) molecular cloud a star is formed from has to be conserved in the comparably tiny star. Some of the angular momentum of the proto-stellar gas cloud can be stored in a forming planetary system but that is not sufficient to create slow-rotating young stars.[14]

Upon formation, stars have rotation periods ranging from a few hours – near break-up velocity – to a few days. The origin of this initial spread is not fully established but discussed explanations involve, e.g., disk-locking (e.g. Edwards et al. 1993; Matt & Pudritz 2005; Gehrig & Vorobyov 2023). Hereby, the stars do not occupy a continuous range but form two distinct groups, rotating either fast ($P \leqslant 2$ d) or slow ($P \geqslant 3$ d), i.e., the sequences from above. During their early main sequence lifetime, stars from the fast rotator sequence gradually converge into the slow rotator sequence, eliminating the former over time. The details of this evolution are intricate[15] and not fully understood. See Fritzewski et al. (2021, and references therein) for a more extensive discussion of the evolution of fast rotators.

Once stars have converged to the slow rotator sequence, they all evolve (i.e. spin down) in the same manner. The fundamental idea for this lies in the origin of magnetic braking. Two stars of the same spectral type and with the same rotation rate will show the same (average) level of magnetic activity. As such, the braking provided by the stellar wind coupling to the magnetic field will be the same on long timescales. And it is the existence of this sequence, evolving (in a mass-dependent way) towards slower rotation as the stars age, that provides us with the opportunity for gyrochronlogy. However, to establish gyrochronlogy as a valid age indicator we have to investigate the following aspects of stellar rotation:

Universality: Do all (late-type main sequence) stars spin down due to magnetic braking? Are there certain types of stars that despite having a convective envelope do not experience spindown? Is there a difference between stars at different locations (galactic core, disk, halo) or in different environments (cluster stars, field stars)?

Single-valued: Will a combination of rotation period and mass provide a unique age? We know already of a limitation in this regard due to the existence of the fast-rotator sequence. The existence of slow and fast-rotator sequences means there are at least two possible rotation periods for a star of specific mass and age. The intersection of fast rotator sequence of one age and slow rotator sequence of another (younger) age means that a combination of mass and period will provide two different ages. Are at least the slow and fast rotator sequences among their kin mutually exclusive?

Precision: What precision in age can be reached with an estimate via a star's mass and rotation period? Is there a point when magnetic braking is so weak that the rotation of the star is not notably changing anymore?

To do this, spindown has to be explored further, especially beyond the few young open clusters. Following the original proposition of the possibility of gyrochronlogy by Barnes (2003), further investigations were undertaken (cf. the more recent works listed in Table 1.1). Despite the decades long effort, only a small fraction of rotational evolution is explored (see Sect. 1.4.1). In fact, only four open clusters are sufficiently enough explored that they extend our knowledge reliably beyond the range originally investigated by Barnes (2003): Praesepe, NGC 6811, NGC 6819, and M 67. And all of them with ages $\leqslant 1$ Gyr, we only know about the rotation of G and early-K-type stars. However, all open cluster data obtained to this point support the idea of a universal spindown for late-type main sequence stars and that the slow rotator sequence represents a unique relation between mass, rotation period, and age. Furthermore, Otani et al. (2022) has shown that gyrochronlogy can be used to obtain age with uncertainties ranging from 5 – 20 %, depending on the color of the star. This means that, at least in the explored parameter regime, gyrochronlogy is shown to be a valid age determination method with superior precision and applicability compared to some of the classical methods listed above. The next step is now to expand the range of applicability and calibration by exploring spindown beyond what the current state. This is, however, not a simple task and some recent results have unearthed curious aspects of stellar rotation.

The vastness of the *Kepler* results is not limited to open clusters. As such, large quantities of rotation periods were derived for field stars. McQuillan et al. (2013, 2014) and Santos et al. (2019, 2021) produced rotation period for tens of thousands of stars from the *Kepler* field and Reinhold & Hekker (2020) and Gordon et al. (2021) did likewise for *K2* data. Unlike cluster stars, we generally do not know much about the individual stars for which periods were reported. However, their sheer vastness can allow certain conclusions based on the populations as such. In Fig. 1.4, we have reproduced some of those results. Reinhold & Hekker (2020) has identified a gap in the distribution, best seen in panel (a) of the figure, which spans from around 5000 K to 3000 K following a somewhat diagonal path from 10 d to 20 d. The existence of this gap is debatable as the underlying data are subject to systematic effects. There are the selection effects of the *Kepler* mission itself (see the difference in populations between *Kepler* (panels a and b) and *K2* (panel c) data in the figure), detectability issues within certain period regimes (see the various vertical and horizontal structures in the figure), and systematics in the light curves themselves (see below for more details).

[14] We recall that there is 100 times more angular momentum in the orbit of Jupiter as it is in (current) solar rotation. For the young sun, however, this ratio was close to unity.

[15] As evidenced by the gap population that does not seem to adhere to a similar mass-dependence seen in slow and fast rotator sequences

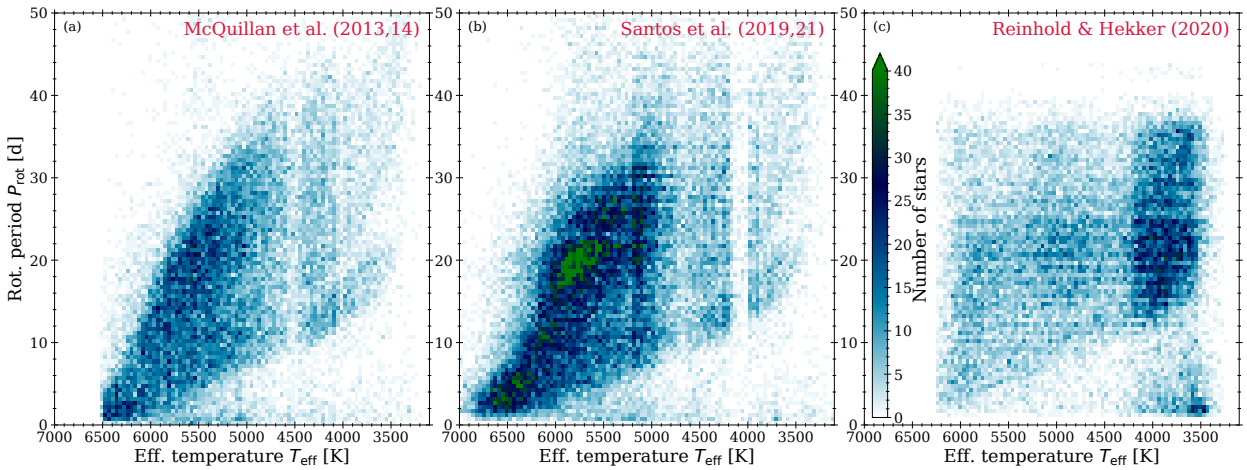

Figure 1.4: *Rotation period samples of stars in the* Kepler *and* K2 *fields. The individual panels show histograms of the samples of the references as indicated. Panel (a) shows the data from McQuillan et al. (2013, 2014, 34k stars), panel (b) those from Santos et al. (2019, 2021, 55k stars), and (c) those from Reinhold & Hekker (2020, 32k stars). Thus, panels (a) and (b) depict data from the 4 yr long* Kepler *primary mission and panel (c) from data from the 17 individual fields of* Kepler*'s* K2 *extension – each was observed for about 80 d.*

Assuming the gap to be real, reasons for its existence brought up include (1) the existence of two distinct populations in the *Kepler* field (e.g., Davenport & Covey 2018), (2) reduced detectability due to a transition from spot to faculae-dominated phases (Reinhold et al. (2019), see also Vaughan-Preston gap: Vaughan & Preston 1980), and (3) a temporary reduction in spindown (e.g., Curtis et al. 2020; David et al. 2022)[16]. Whether or not it is real, it is not visible for fully convective stars ($T_{\rm eff} \leqslant 3200$ K, Lu et al. 2022, based on ZTF data).

These are, however, not the only aspects of stellar rotational evolution that are debated in the community. Asteroseismology has opened a completely new realm of possibilities in exploring late-type stars, including stellar rotation and age dating. The details of the methodology are beyond the scope of this work (for more details see, e.g., Aerts et al. 2010). Asteroseismology can provide a (strongly model-dependent) estimate for the age and the rotation period of a star. Early attempts using this, however, have collided with established knowledge. Generally speaking, the results always showed stars rotating faster than they are supposed to given their age. Exploring sun-like stars (supposedly) beyond solar age, Hall et al. (2021) suggested a complete ceasing of spindown due to older stars showing rotation rates similar to that of the sun. Metcalfe et al. (2022) argues that this is due to a change in morphology in the stellar magnetic field in sun-like stars around solar age.

However, scrutinizing those and similar results often reveals some general flaws in the interpretation. As, e.g., Barnes et al. (2016a) have pointed out, many of the stars used by van Saders et al. (2016) to argue for breakdown of gyrochronlogy around solar age are not at all suitable for the purpose of exploring stellar rotation. Many of their field stars sample were somewhat evolved or of highly non-solar metallicity. Both of which make it difficult to interpret stellar rotation periods in the context of gyrochronlogy. Similarly, the results by Hall et al. (2021) fail to reproduce the clear relation we see in sun-like stars younger than the Sun. According to their data, stars around the age of NGC 6819 (2.5 Gyr) rotate systematically faster than the stars in said cluster. This hints at an underlying calibration issue in asteroseismology for dwarf stars and any related results should be viewed with appropriate caution.

Independently of the interpretation of above-mentioned results, it is clear that there is a lot about stellar rotational evolution we do not understand yet. And only continued exploration of stellar rotation will reveal the answers to us, as it is the stars themselves who know best whether or not (and to which degree) they evolve systematically and they will reveal it to us if just investigate them carefully.

1.4 Introduction to the presented works

When I started with this thesis, gyrochronology felt like exploring the ruins of an ancient, long-forgotten town in an overgrown and dense jungle. A first explorer (Barnes 2003) has identified patterns in the streets (the open clusters and their sequences) of our metaphorical metropolis. These patterns, if read correctly, allow us to gain insights into the life of its inhabitants (stellar evolution), understand the concepts behind its construction (spindown and magnetic braking), and navigate the townscape (apply gyrochronlogy). However, with the uncovering of more and more buildings (i.e., stars with rotation periods, cf. Sect. 1.2) the picture became blurry and the concepts questionable (cf. Sect. 1.3). The

[16]The author of this thesis considers only the second explanation as plausible but is doubtful about the existence of the gap for the mentioned reasons. (1) is largely refuted in the other works mentioned above and (3) appears rather unlikely in the light of the recent results for Ruprecht 147 and M 67 obtained as part of this thesis.

existence of town squares where none should be was claimed (e.g., the gap observed by Reinhold & Hekker 2020) and streets uncovered where they do not belong (van Saders et al. 2016). However, looking closer, some of the streets turned out to be only large hallways, unsuitable for understanding and navigating the town (Barnes et al. 2016a). Ultimately, this confusion led to claims that our way of navigating falls apart when we reach, e.g., the suburbs (i.e., older ages, Metcalfe et al. 2019). It is now on us to take a step back and focus on the large streets and boulevards once more, to map out the roads in the city center as well as in the suburbs, and tackle this confusion head-on.

Three peer-reviewed publications form the core of this thesis and are dedicated to the continued exploration of stellar rotation and the prospects of gyrochronlogy. I am the principal author for all three papers and conducted the majority of the work described in each. After a collaborative discussion with the co-authors about the individual goals, I conceived the main approach to each posed research project, carried out the related work regarding data handling and analysis, wrote the first draft of the papers, and then gathered feedback from the co-authors. Below, I will give an overview of the principal ideas, what motivated the individual steps taken, the work that was done, and a brief summary of the results as they lead directly to the subsequent project.

1.4.1 Open questions

There seems to be a recent trend to go to larger and larger samples. While there is always some confidence in big numbers, huge samples come with the disadvantage that there cannot be attention to individual stars. But to map a pattern, establish a relation, and understand large-scale concepts, we need to trust our calibrators, our mileposts along the way: the stars. As such, for the work at hand, we focus back on the reliable calibrators: open cluster stars with well-established ages and periods. The former are available and the latter we set out to derive. Let us first have a look again at what was done and what is out there. Figure 1.5 provides an overview of what part of the rotation period-age-mass space is explored.

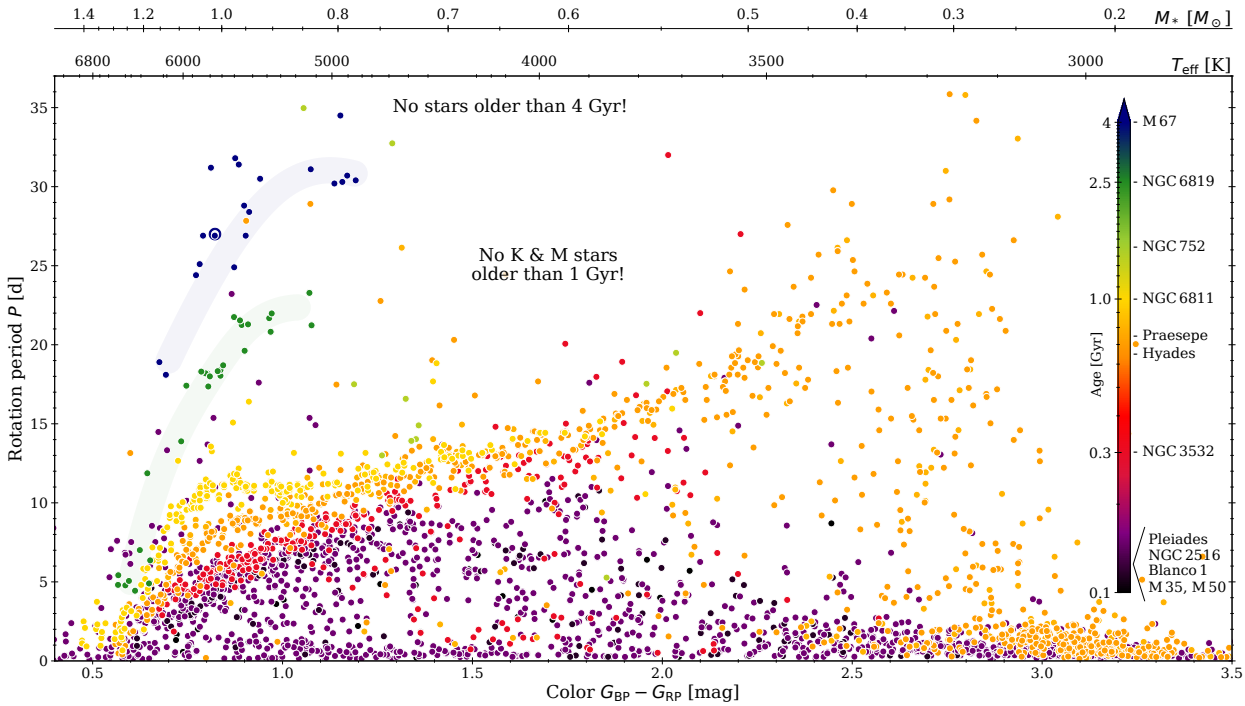

Figure 1.5: *Rotational evolution of stars as explored with open clusters. The CPD shows selected open clusters with their age color coded. The data is compiled from the sources listed in Table 1.1 and the individual clusters are indicated. The sun is shown with its usual symbol. We have highlighted the sequences of NGC 6819 and M 67 due to them being rather inconspicuous compared to the other, more populated cluster samples.*

We recall that the ultimate aim is to create a description of stellar spindown that enables an estimate of the stellar age, i.e, apply gyrochronlogy. Even for an empirical calibration, we need a sufficiently complete picture of the evolution of stellar rotation to describe the relationship between mass, age, and rotation period. As we can see in Fig. 1.5, there is a lot to be desired. Only a fraction of the rotational evolution is explored. Sun-like stars have their rotation mapped out up to the age of the sun. Several open clusters can be used to describe the evolution $\leqslant 1$ Gyr. Beyond that, however, we have only 2 clusters and the sun as mileposts. This means only about half of the lifetime of the sun is currently explored rotation-wise. For stars redder than the sun, the situation is even worse. No cluster has been explored beyond 1 Gyr. With that, the rotational evolution of K and M-type stars older than 1 Gyr is entirely unconstrained. All stars rotationally explored in those regions so far were only weakly characterized field stars (cf. the debated results in prior

section) and have created confusion. We seek to remedy this by exploring the following questions in this thesis:

- *How do non-solar-like stars spindown beyond 1 Gyr?*
- *Can we bridge the gap between cluster and field stars?*
- *Can we address some of the conflicts and inconsistencies pointed out in prior work?*

There are of course more open questions – such as the one about the spindown of sun-like stars older than 4.5 Gyr – but not everything can be answered in the course of one thesis.

From the works of, e.g., McQuillan et al. (2013, 2014) and Reinhold & Hekker (2020), we know that *Kepler* and *K2* data allow the identification of rotation periods in what we suspect is the relevant regime (cf. the region in Fig. 1.5 devoid of clusters). Therefore, as many before us, we turn to *Kepler* data. There is not much left for us to work with, but a few worthwhile targets remain, especially in the age regime relevant to our science goals. The fact that the questions above are yet unanswered but with suitable data available for answering them is caused by the difficulties inherent to the handling and evaluation of said data. This can be seen in the differing results by the works of Barnes et al. (2016b), Gonzalez (2016a), and Esselstein (2018) for M 67 – all based on the same *K2* data. However, we are not deterred by those difficulties and aim to bring some order to the chaos and confusion. We begin this exploration with one of the nearest open clusters, one fortunately situated in one of *Kepler/K2* fields, and hitherto largely unexplored regarding stellar rotation: the 2.7 Gyr-old open cluster Ruprecht 147. And such is the story of paper I.

1.4.2 Paper I: Rotation periods for cool stars in the open cluster Ruprecht 147

In this publication, we present our work on *Kepler K2* data for stars of the 2.7 Gyr old open cluster Ruprecht 147. We investigated yet unexplored photometric time series. For that, I have compiled a sample of cluster stars from the literature and investigated archived light curves. Realizing that the data is tainted by the presence of data systematics, I performed a correction based on a Principal Component Analysis that involved the entirety of the data from the relevant *Kepler K2* campaign (C07).

The full work is detailed in Part 2, but let us briefly summarize what we found. We were able to derive rotation periods for 33 stars and the 21 most reliable, effectively single main sequence stars form a clear sequence in the color period diagram. The cluster sequence is where it is supposed to be, but not in the exact locations we have expected. In a color-dependent sense, Ruprecht 147 sits above the younger cluster NGC 6811 and below the older cluster M 67. It connects directly to the almost coeval NGC 6819 in the region the sequences overlap. However, here the cluster leaves the path of expected behavior and ventures into unmapped territory.

It is not straightforward to say what the expectations had been at this point with regards to behavior of the cluster redder than $B - V = 1.0$ mag. But it is safe to say that what we found for Ruprecht 147 was not it. It contradicts the expectation of a monotonous increase in rotation rate with color at a given age and shows even indications of a slight downturn. However, it also shows a clear continuation of spindown, and it crosses the proposed gap – existing partly above and below it. With that, the work on Ruprecht 147 has brought up more questions than it has answered.

One thing is certainly clear at this point: The spindown descriptions embedded in the models – be it the original more empirical ones or the more recent and more physically sophisticated ones – all struggle or fail outright in their ability to describe and predict the observed sequence of Ruprecht 147. Therefore, it is, for now, opportune to leave the models a little behind in our work and focus on the empirical work.

With this in mind, we decide to follow the empirical path in exploring stellar rotational evolution. However, easier said than done. *Kepler* has provided vast amounts of data for this purpose but we are slowly running out of it. What is left is not easily accessible, everything easy has been harvested. But, so we believe, there are answers to the questions in front of us in the remaining data, lending value and motivation to the difficult work required to reach there. Our work described in the coming section will ultimately prove this belief to be true.

So, what is it exactly we are looking for and what data do we have left to explore it? Ruprecht 147 shows us a clear continuation of the spindown to the age 2.7 Gyr for stars of all relevant masses. It also shows us a cluster sequence that deviates strongly from expectations. However, this conclusion is not held up by many stars. Therefore, we decide to explore this behavior further, bolster it with additional measurements of stars in this age regime and track it to older ages.

Here, we face a problem. Old and accessible stellar open clusters are few and far between. But there is one notorious one, one which was studied so much that all the literature on it would fill books: M 67. This open cluster is of almost solar age, sparking huge interest in various fields of stellar astrophysics. Its special place was already hinted at by Johnson & Sandage (1955), and history has ultimately proven them right as there are more than 2000 publications in the literature that focus more or less directly on the cluster.

This includes gyrochronlogy. To this day, M 67 remains the oldest open cluster ever studied with respect to the rotation of late-type main sequence stars. There are the three studies mentioned above with this focus, which, when taken together, are all but conclusive on the matter. Therefore, we take on this cluster with the goal to extend it to

hitherto unexplored regions and to clear up the confusion created. One more thing we have learned from our work on Ruprecht 147: we are reaching the limit of what can be done with the present (pre-processed) data. If we hope to gain valuable insights from M 67, we have to go above and beyond on the available observations, squeezing every bit of information from them. And such is the story of paper II.

1.4.3 Paper II: New insights into the rotational evolution of stars from M 67

Our work on the 4 Gyr-old open cluster M 67 is a direct continuation of the work on Ruprecht 147, but with some significant changes informed by what we found there. Instead of using archived light curves – which are very limited – we take the observations directly and create our own light curves. In this publication we present our work on one of the *Kepler/K2 superstamps*, a continuous region observed for ~ 80 d during the extended *Kepler* mission. This hitherto untapped data for M 67 covers the rich cluster center but suffers from systematics inherent to *K2* data. However, only in this data, we can explore the cluster's K and M-dwarfs. I devised a complex algorithm that performs photometry on the data and deals with those systematics. This allowed me to construct lightcurves for hundreds of M 67 stars and to measure rotation rates from photometric variability. I combined this with a membership analysis based on *Gaia* astrometry and created a cluster CPD that extended far beyond all prior work. I then went on to use the gained knowledge on stellar rotation but also on *K2* data systematics to re-evaluate the somewhat contradictory nature of said prior work.

The full work is detailed in Part 3, but let us again briefly summarize what was found. The found rotation periods define a sequence for M 67 continuously spanning from early G to early-M type stars for the first time. This confirms that the fundamental assumptions of gyrochronlogy hold even at ages as old as M 67. The deviating shape, only suggestively seen in Ruprecht 147, is now very much confirmed by my results. This brings us back to some of the problems with gyrochronlogy raised by the community over the years. One objection arises from the observed mismatch between gyrochronlogy predictions and a sample of (unfortunately not always) well-studied field stars. Generally speaking, stars seem to rotate faster than their age would have suggested. If this holds, a fundamental assumption of gyrochronlogy – the universality of an age and mass-dependent spindown for all late-type main sequence stars – falls apart. However, now we have seen that also old open clusters do not agree with what gyrochronlogy models calibrated on younger clusters predict at those older ages. This means one point is irrefutable: current spindown descriptions do not work. Furthermore, partially simultaneously to this work Fritzewski et al. (2020) have shown strong indications for this universality by demonstrating the rotational equivalence in the coeval clusters NGC 2516, Blanco 1, M 50, and the Pleiades. Therefore, we have good reason to believe that also field stars follow the same spindown – a universal spindown at that – and the deviations are of different origins. Thus, it is opportune to leave the spindown descriptions fully aside and explore the universality of stellar spindown in a direct comparison of open clusters and field stars. And such is the story of paper III.

1.4.4 Paper III: Wide binaries demonstrate the consistency of rotational evolution between open cluster and field stars

In this publication, we present our comparison of the rotation rates in wide binary and open cluster stars. The components of wide binaries have the same origin and as such they are coeval and of the same composition. In some sense, they can be considered the smallest possible open cluster. However, they are still as diverse as field stars and not associated with clusters – allowing us to use them to bridge the gap between clusters and field stars. The consistent (albeit generally unknown) age between the components allows us to explore whether or not the rotation rates (as an indication for the spindown) are also consistent.

This evaluation is done with a direct comparison to the available open cluster data. I compiled a sample of wide binaries from the literature and supplemented them with rotation periods from *Kepler* and *K2*. Based on the experience gathered in the works on Ruprecht 147 and M 67, I dedicated substantial effort to the vetting of the rotation data. For the comparison, I constructed an open cluster sample, explicitly including our own results from papers I and II.

We found a striking agreement between the open cluster and the wide binary stars. The vast majority of wide binary systems made up of 2 main sequence stars behave indeed like miniature open clusters. They either agree outright with the cluster sequences or fall consistently in the gaps between them. Furthermore, we were able to show that main sequences stars in systems containing evolved components, i.e., (sub)giants or white dwarfs, have rotation rate-based ages consistent with the evolved state of said evolved component. The wide binary systems that do not agree with the open clusters are to a large degree hierarchical. This support once more the observation in paper II that it is more likely than not that stars that show signs of binarity are unsuitable for gyrochronlogy due to past angular momentum transfer. The corresponding work is detailed in Part 4.

○ ○ ○

Part 2 – Paper I

Rotation periods for cool stars in the open cluster Ruprecht 147[†,‡]

D. Gruner *and S. A. Barnes*

Abstract

Gyrochronology allows the derivation of ages for cool main sequence stars based on their observed rotation periods and masses, or a suitable proxy thereof. It is increasingly well-explored for FGK stars, but requires further measurements for older ages and K – M-type stars.

We study the nearby, 3 Gyr-old open cluster Ruprecht 147 to compare it with the previously-studied, but far more distant, NGC 6819 cluster, and especially to measure cooler stars than was previously possible there.

We constructed an inclusive list of 102 cluster members from prior work, including *Gaia* DR2, and for which light curves were also obtained during Campaign 7 of the *Kepler/K2* space mission. We placed them in the cluster color-magnitude diagram and checked the related information against appropriate isochrones. The light curves were then corrected for data systematics using Principal Component Analysis on all observed K2 C07 stars and subsequently subjected to periodicity analysis.

Periodic signals are found for 32 stars, 21 of which are considered to be both highly reliable and to represent single, or effectively single, Ru 147 stars. These stars cover the spectral types from late-F to mid-M stars, and they have periods ranging from 6 d – 33 d, allowing for a comparison of Ruprecht 147 to both other open clusters and to models of rotational spindown. The derived rotation periods connect reasonably to, overlap with, and extend to lower masses the known rotation period distribution of the 2.5 Gyr-old cluster NGC 6819.

The data confirm that cool stars lie on a single surface in rotation period-mass-age space, and they simultaneously challenge its commonly assumed shape. The shape at the low mass region of the color-period diagram at the age of Ru 147 favors a recently-proposed model, which requires a third mass-dependent timescale in addition to the two timescales required by a former model, suggesting that a third physical process is required to model rotating stars effectively.

[†] *The contents of this chapter have been published in Astronomy and Astrophysics, Volume 644, id.A16*
Reproduced with permission ©ESO.
[‡] *Table 2.2 and the processed light curves of the sample stars as plotted in Appendix C are available in electronic form at the CDS.*

2.1 Introduction

Studies that require coeval groups of stars older than 1 Gyr are often hindered by their distance. The younger Hyades (46 pc; ∼600 Myr) and Pleiades (130 pc; ∼150 Myr) are the nearest open clusters and, consequently, have been extensively studied, including with respect to the rotation periods of their cool stars (Radick et al. 1987; van Leeuwen et al. 1987; Rebull et al. 2016; Douglas et al. 2019). The closest open cluster of near-solar age (∼4 Gyr) is M67 at a distance of roughly 900 pc (Kharchenko et al. 2005, see also Johnson & Sandage (1955)); a fortuitous proximity that provides valuable samples of solar analogs and many other cluster stars of non-solar mass, enabling detailed studies (e.g., Sandage 1957; Racine 1971; Demarque et al. 1992) including of its rotational properties (Barnes et al. 2016b).

At intermediate ages, say 2 – 3 Gyr for instance, the closest open cluster that has been well-studied with respect to stellar rotation is the 2.3 kpc-distant cluster NGC 6819. This object fortuitously was in the field observed by the *Kepler* satellite, permitting a careful rotational study despite its relative distance by using data acquired over the 4yr *Kepler* observational baseline (Meibom et al. 2015)[1]. The study of another cluster of a similar age would permit the independent verification of the NGC 6819 rotation results (if the results were similar); and additionally, if that cluster were substantially closer than NGC 6819, this would also allow the derivation of rotation periods for lower mass cool stars than was possible in NGC 6819. Observations of the nearby (305 pc), ∼ 3 Gyr-old open cluster Ruprecht 147 (= NGC 6774) with the *K2* reincarnation of the *Kepler* satellite permit exactly this type of work, as described in this paper.

A key motivation for our work is to examine whether Ruprecht 147 can be used as an additional benchmark for "gyrochronology," the technique for deriving the age of a main sequence star from its (measured) rotation period and mass, or a suitable mass proxy such as color (e.g., Barnes 2003, 2007; Mamajek & Hillenbrand 2008; Barnes 2010; Spada & Lanzafame 2020). The spindown of stars of solar mass was famously described by Skumanich (1972)[2] and is now well-known as originating in angular momentum loss caused by magnetized stellar winds (Parker 1958; Weber & Davis 1967; Kawaler 1988). However, its generality and applicability to stars of non-solar mass, the basis of gyrochronology, are by no means assured.

Fritzewski et al. (2020, Fr20 hereafter) have recently shown that the measured rotation period distributions of the well-studied Zero Age Main Sequence (ZAMS) open clusters Pleiades, M 35, M 50, Blanco 1, and NGC 2516 are indistinguishable (with data from Rebull et al. 2016; Meibom et al. 2009; Irwin et al. 2009; Cargile et al. 2014; Fritzewski et al. 2020, respectively). This fact suggests that the ZAMS cool star rotational distribution is indeed identical in otherwise identical clusters, that such a distribution is a natural outcome of pre-main sequence evolution, and perhaps of the star formation process itself. However the paucity of suitable cluster data at older ages has not allowed such a corresponding check to date for older stars. Ruprecht 147 allows such a comparison to be made for 3 Gyr-old stars by comparison with the similarly-old NGC 6819 cluster, previously studied by Meibom et al. (2015).

Data for late-F to mid-K-type stars, in a series of clusters of increasing age; for Hyades (625 Myr; Radick et al. 1987; Douglas et al. 2019), NGC 6811 (1 Gyr; Meibom et al. 2011a), NGC 6819 (2.5 Gyr; Meibom et al. 2015), and M 67 (4 Gyr; Barnes et al. 2016b) show that the spindown for those stars follows the generalized Skumanich relationship $P(m) \propto \sqrt{t}$, where P, m, and t represent a cool star's rotation period, mass, and age respectively. Such models are called "separable" because the dependence of P on m and t is factorized into separate functions $f(m)$ and $g(t)$, of stellar mass and age respectively.

However, data for lower-mass stars in the Praesepe (Agüeros et al. 2011) and NGC 6811 open clusters (Curtis et al. 2019) indicate deviations from the simple $P(m) \propto \sqrt{t}$ spindown relationship. Certain deviations are expected because, as has been clearly explained in Barnes (2010, Ba10 hereafter) and Matt et al. (2015, see also Barnes et al. (2016a), BSW16 hereafter), second-generation (i.e., non-separable) gyrochronology models (e.g., Ba10) only require that $P(m) \propto \sqrt{t}$ hold in the asymptotic limit of large Rossby Number, Ro. The rotational evolution at small Ro is both intrinsically different and also modulated by the initial rotational distribution, resulting in different predicted shapes for rotation period distributions as a function of stellar mass and age[3]. Regardless, non-separable models are also believed to have deficiencies and the data mentioned above have prompted Spada & Lanzafame (2020) to develop a model with one additional degree of freedom as compared with Ba10[4]. This enters via the parameter p, which specifies the power law in the mass dependence of the internal coupling in their two-zone rotational model, which otherwise follows the Ba10 spindown formulation. The Matt et al. (2015), Garraffo et al. (2018), and Amard et al. (2019) models allow several more degrees of freedom, with varying success in describing the observations. (A detailed summary comparison of these models in connection with Zero Age Main Sequence (ZAMS) open clusters can be found in Fr20.)

From a field star viewpoint (as opposed to the cluster viewpoint above), van Saders et al. (2016) and Metcalfe & Egeland (2019) have used asteroseismic ages for field stars to claim significant deviations of theoretical gyrochronology models from observations, originating in a drastic decrease of angular momentum loss when stars

[1] This rotational study was itself built upon extensive prior work on the cluster in the literature, including a near-decade-long radial velocity survey for cluster membership and multiplicity, and also a ground-based proper-motion study (Platais et al. 2013).

[2] A power law was fitted to the averaged $v \sin i$ values of solar mass stars in a limited number of open clusters.

[3] Observed rotation period distributions are of course not completely homologous and display patterns that are a combination of intrinsic differences and also observational sensitivity.

[4] These models have a pedigree that dates back to MacGregor & Brenner (1991) in mathematical form.

reach middle age, initially broadly interpreted as the main sequence career beyond 2 Gyr; and more recently as the point where stars reach a rotation period such that $Ro \approx 2$. However, as noted by, for example, do Nascimento et al. (2013, 2014), BSW16, and Beck et al. (2016), there appear to be a number of problems and disagreements regarding the ages, metallicities, and binary status of many of these field star samples, where determination of a star's evolutionary status and stellar parameters is inherently far more challenging than that in open cluster member stars. Indeed, Lorenzo-Oliveira et al. (2020) have recently published a secure 35 d rotation period determination for the 8 Gyr-old solar twin star HD 197027 (= HIP 102152, see also Lorenzo-Oliveira et al. 2019; Schmitt & Mittag 2020). These results appear to refute the proposal that stars stop spinning down in middle age. Ongoing large scale surveys like *Gaia* and TESS provide increasingly large samples of field stars for gyrochronology (e.g. Lanzafame et al. 2018; Canto Martins et al. 2020, respectively) and future studies, such as PLATO (Rauer et al. 2014), will further expand the amount of available data.

Wide binaries bridge the gap between field stars and open clusters; to a certain extent, they could be considered the smallest open clusters. Rotational studies of such systems in the *Kepler* field (e.g. Janes 2017; Oswalt et al. 2017) have also provided some intriguing evidence for deviations. Approximately 60% of the systems in Janes (2017) appear to agree with rotational isochrones calculated using the Ba10 models. However, the remaining systems display partial-to-significant disagreements, with the secondary star rotation periods largely located below the rotational isochrone for the primary component. This result modulates the original result from Barnes (2007, Ba07 hereafter), where the three wide binary systems with measured rotation periods for both components then known (α Cen A/B, 16 Cyg A/B, and ξ Boo A/B) all agreed within their uncertainties with their respective rotational isochrones. The discrepant systems have not to date been investigated carefully for tertiary components or other pathologies[5].

With the present study on Ruprecht 147, we approach the above mentioned problems from the open cluster perspective. Ruprecht 147 (also known as NGC 6774) was originally discovered by Herschel (1833), who designated it as GC 481 (Herschel 1863), and has been mentioned occasionally since then in various catalogs (e.g. Dreyer 1888; Alter et al. 1958; Ruprecht 1966; Lynga & Palous 1987). However, it has recently attracted significant interest because of the combination of its relative proximity ($\sim$ 300 pc) and age. In fact, Ruprecht 147 is the oldest nearby open cluster with 2 – 3 Gyr age (Curtis et al. 2013, Cu13 hereafter). Several other recent studies have identified member stars and derived cluster properties using a variety of techniques including photometry, astrometry, and radial velocities (e.g. Conrad et al. 2017; Cantat-Gaudin et al. 2018; Bragaglia et al. 2018; Gaia Collaboration et al. 2018a; Olivares et al. 2019). The combination of all of the above-mentioned information with additional results from astrometric surveys such as Gaia DR2 (Gaia Collaboration et al. 2018b, see also Gaia Collaboration et al. (2016)) provides extensive information about the cluster's membership, stellar multiplicity, and other fundamental properties.

[5]The faintness of the systems in the *Kepler* field is an obstacle to detailed spectroscopic investigation.

Table 2.1: *Astrometric and physical parameters adopted for Ruprecht 147.*

Parameter	Unit	Value	Reference
Ra	deg	289.087	1
Dec	deg	-16.333	1
$\mu_{\rm Ra}$	mas/yr	-0.939	1
$\mu_{\rm Dec}$	mas/yr	-26.576	1
parallax π	mas	3.250	1
$v_{\rm rad}$	km s^{-1}	41.79	2
distance d	pc	305.0	3
[Fe/H]		+0.08	4
[Fe/H]		+0.12	5
Age	Gyr	2.7	6
$E_{G_{\rm BR}-G_{\rm RP}}$	mag	0.1	7
A_G	mag	0.2	7

References. *(1) Cantat-Gaudin et al. (2018); (2) Gaia Collaboration et al. (2018a); (3) Conrad et al. (2017); (4) Bragaglia et al. (2018); (5) Donor et al. (2020); (6) Torres et al. (2019); (7) this work.*

Additional studies have focused on individual objects within the cluster, such as eclipsing binaries (Torres et al. 2018, 2019, 2020), brown dwarfs (Nowak et al. 2017), and exoplanets (Curtis et al. 2018). Finally, Yeh et al. (2019) have suggested that Ruprecht 147 is imminently likely to dissolve into the galactic disk.

We take advantage of all relevant prior work and combine it with detailed analysis of high-precision time series photometry acquired using the *Kepler*/*K2* mission to measure the rotation periods of cool stars in Ruprecht 147. Unfortunately, the *Kepler*/*K2* data for Ruprecht 147 both have an abbreviated observing baseline as compared with the original *Kepler* data for NGC 6819 and are of significantly lower photometric quality. These observational realities will require special efforts to overcome, as described below. In short, we use Principal Component Analysis (PCA), reprising a technique that our group used successfully in our analysis of similar *Kepler*/*K2* data for the 4 Gyr-old open cluster M 67 (Barnes et al. 2016b). Ruprecht 147 also presents a peculiar difficulty. Because of its proximity and perhaps its imminent dissolution, it is spread out over a large area on the night sky, making it operationally difficult to obtain the detailed membership analysis required to distinguish the cluster stars from non-members. Fortunately, the cluster has offsets with respect to the surrounding field stars in both radial velocity and proper motion, allowing member identification when such data are actually available. Gaia DR2 is particularly helpful in this regard. We rely on a combination of prior work from the literature for this membership and other basic cluster information. An overview of the adopted parameters of Ruprecht 147 is provided in Table 2.1.

This paper is structured as follows. In Sect. 2.2, we describe the construction of the sample of stars for detailed study, including the construction of Color-Magnitude Diagrams (CMDs) in multiple relevant colors. The issues with *K2* lightcurves and our treatment of those using Principal Component Analysis, followed by period analysis, are outlined in Sect. 2.3, while the resulting periods are discussed in Sect. 2.4. We compare our results to data from other comparable clusters in Sect. 2.5, and to widely-used stellar spindown relations in Sect. 2.6. Section 7 outlines our conclusions, and there are also four Appendices containing ancillary information, together with all relevant light curves.

2.2 K2 coverage, cluster membership, and CMD

We now describe the sample selection based on the archival data, the *K2* coverage, and the construction of the cluster color-magnitude diagram. For our analysis of Ruprecht 147, we use light curves obtained during Campaign 7 (C07) of the *Kepler*/*K2* mission, during which a part of Ruprecht 147 was monitored over the 82.5 d interval from Dec 26th, 2015 to Apr 20th, 2016. 15085 lightcurves were recorded during C07 of *K2*. Of those, 13483 correspond to individual sources listed in the EPIC catalog (Huber et al. 2017). These are used as the starting point for our study, hereafter called the "full sample"[6].

2.2.1 Source catalogs

The EPIC catalog uses the 2MASS[7] (Cutri et al. 2003) and the UCAC4[8] (Zacharias et al. 2012) catalogs as inputs and, therefore, contains identifiers from those two catalogs for a large number of targets. Consequently, it conveniently lists J, H, K_s, g, and r magnitudes for most stars. The cross-match by Marrese et al. (2019) of the Gaia DR2 catalog with other large scale surveys, among them the 2MASS point source catalog (PSC, Skrutskie et al. 2006), is also helpful to us and facilitates identification.

The identification of members, their evolutionary status and possible multiplicity is crucial to our analysis and interpretation of results. Therefore, we adopt the *Gaia* photometry (G, $G_{\rm BP}$, $G_{\rm RP}$; Evans et al. 2018, Ev18 hereafter) and parallax (π, Lindegren et al. 2018). We initially use the extinction and reddening parameters (A_G, $E(G_{\rm BP} - G_{\rm RP})$ Andrae et al. 2018) from the Gaia DR2 catalog, before coming up with an alternative.

2.2.2 Cluster membership

Fortunately, several studies of Ruprecht 147's cluster membership have been carried out over the years. Notable ones are the membership analysis of Curtis et al. (2013, Cu13 hereafter), based on pre-*Gaia* astrometry and spectroscopic data, and *Gaia*-related work by Gaia Collaboration et al. (2018a, GC18 hereafter) and Cantat-Gaudin et al. (2018, CG18 hereafter), both using Gaia astrometry to identify cluster members. The most recent census of Ruprecht 147 was performed by Olivares et al. (2019, Ol19 hereafter) using all information then available in the literature. Consequently we need not carry out our own membership analysis and can simply adopt the results of these four prior studies as inputs. It is important to note that these studies have by no means identified the same set of stars as members. However, there is a large degree of overlap between the candidates found; see Fig 2.1. We begin by adopting all stars that are identified as members in at least one of the studies for our sample, that is to say we work with the union of the prior data sets. We will review the membership and multiplicity information again, after the rotation period work in our study has been completed. For a summary of the details regarding the differences between the four membership studies see Ol19.

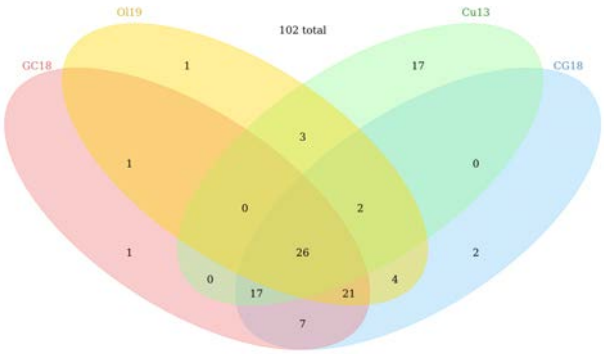

Figure 2.1: *Venn diagram of the 102 cluster members observed by* Kepler/K2*. The numbers indicate the quantity of stars in each corresponding subset. Stars included from the individual studies are: all those listed by Gaia Collaboration et al. (2018a, GC18), those labeled P or Y by Curtis et al. (2013, Cu13), and those listed in Cantat-Gaudin et al. (2018, CG18) or Olivares et al. (2019, Ol19) with membership probability greater than 0.5.*

An operational difficulty is that of these four studies, only Ol19 and CG18 list an actual membership probability. Cu13 assigns stars to one of the three categories: "non-member", "very-likely-member", and "member", while GC18 only list members according to their own analysis. We match stars to Cu13 based on their 2MASS IDs; to GC18 and CG18 based on their *Gaia* IDs; and to Ol19 based on their EPIC and *Gaia* IDs. For our analysis we adopt a star as a possible member if it is identified as such in at least one of the four above-mentioned catalogs. From Cu13, we take all stars labeled as "very-likely-member" and "member". We also include all stars listed by GC18, and all stars from CG18 and Ol19 with $P \geqslant 0.5$. We emphasize that this selection includes stars that are listed as members in one study, but that are labeled as non-members in another. Whenever this occurs, we break the impasse by prioritizing the four studies in the order

$$\text{Ol19} > \text{CG18} > \text{GC18} > \text{Cu13}, \qquad (2.1)$$

and where two studies of the set $\{\text{GC18}, \text{CG18}, \text{Ol19}\}$ may overrule the third in case of disagreement. This procedure enabled us to identify 310 unique cluster members, of which 102 were also observed by *Kepler*. Figure 2.2

[6] The others correspond to special targets that require a different pixel mask for each cadence. Those can be identified by their EPIC IDs (2000#####) and correspond to Pluto, and Trojan and Hilda asteroids.

[7] CDS: II/246/out

[8] CDS: I/322A/out

provides an overview of the coverage of *Kepler*/*K2*, including a comparison with numbers of stars represented in each member list. While the cluster center does indeed lie within the region covered by C07 of *K2* (cf. Fig. 2.2 panel (b)), a large fraction of the Ruprecht 147 stars is located outside the *K2* field of view. In fact, as the numbers above show, fewer than a third of the identified members from the four studies, as provided by our procedure above, were actually observed as part of the *K2* C07 target sample.

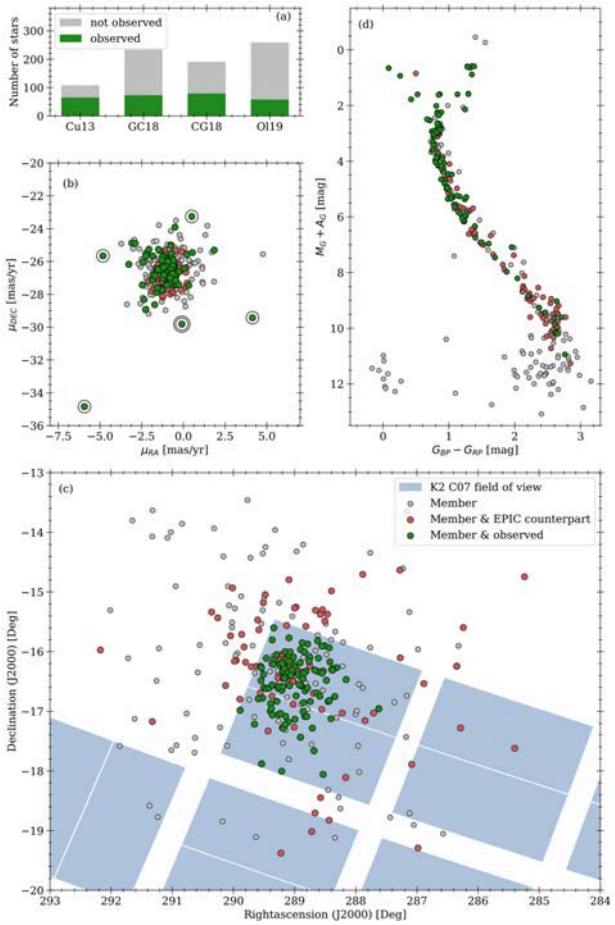

Figure 2.2: *Overview of the identified Ruprecht 147 cluster members in* K2*. The histogram in panel (a) shows the fraction of stars in each membership catalog that was observed during* K2 *as compared with the total number of identified stars. Panel (b) shows the* Gaia *vector point diagram for our compiled member list. We note that certain observed stars (encircled: EPIC 219665632, 219515762, 219560884, 219437560, and 219855372) are apparent outliers. However, with the exception of EPIC 219515762 (encircled twice), none are in our final sample, and 219515762 itself is discarded from the interpretation of the results since it is clearly past the cluster turnoff. Panel (c) shows a map of the sky centered on Ruprecht 147, with all member stars from our merged sample, assimilated from Cu13, CG18, GC18, and Ol19 (gray). Red symbols indicate those stars which have a counterpart in EPIC while the green ones are those that were actually observed. The shaded regions indicate the approximate layout of the CCDs in the* Kepler/K2 *field of view. Panel (d) shows a distance-corrected (but not reddening-corrected) CMD of Ruprecht 147 cluster members with the color coding as in panel (b).*

In Fig. 2.2, we also display a (distance-corrected) color-magnitude diagram (CMD) in *Gaia* $G_{\rm BP} - G_{\rm RP}$ color for context. This CMD shows that despite minor issues with Gaia DR2 photometry at the faint end, there is good consensus between the membership and photometry. Correspondingly, we see a well-defined cluster main sequence, turnoff, giant branch, red clump, blue stragglers, and even several white dwarfs.

We note that the crossmatch between Gaia and 2MASS does not cover all targets in *K2* C07. However, all targets relevant to our rotation period work are covered. Furthermore, we also independently cross-matched the EPIC and Gaia DR2 catalogs based on astrometry and magnitudes, finding the same matches as in Marrese et al. (2019) for the Ruprecht 147 stars. In summary, our procedure has identified 102 cluster members from the four membership studies discussed above that have been observed by *Kepler*/*K2*.

2.2.3 Cluster reddening, extinction, and color transformation

To verify this combined membership information and also the age of Ruprecht 147 in light of it, we have plotted a number of color magnitude diagrams of the member stars and the field, including distance-calibrated and dereddened ones. While so doing, we noticed a suspicious trend with the reddening and extinction parameters provided in Gaia DR2. As can be seen in Fig. 2.3, panels (a) and (b), various problems become evident when photometry is dereddened using the reddening and extinction parameters provided by *Gaia* DR2. Firstly, suspicious horizontal structures are introduced in the CMD for the late-type dwarfs, secondly, Ruprecht 147 loses definition near the cluster turn-off, and, thirdly, barely any stars are located above the zero age main sequence.

We infer that the machine learning approach (Apsis) advocated and described by Andrae et al. (2018) in dealing with the Gaia DR2 data is biased toward stars in highly populated regions such as the Main Sequence and the Red Clump. This approach appears to simply *de-redden every star* in low-stellar-density regions of the CMD back onto the main sequence. The strongly varying (and sometimes very large) extinction values between the individual cluster stars (cf. Fig. 2.3 panel (c)) are improbable and thus another telling indicator. Yet another suspicious trend is that the majority of stars with reddening estimates (gray in Fig.3) are already situated close to densely populated regions in the CMD. While these issues could potentially be resolved with improved spectrophotometry in the future Gaia DR3 data release, we dismiss these reddening and extinction parameters as unreliable for the purposes of this work.

Instead, we see (e.g., panel (a) in Fig. 2.3), that only a small uniform reddening for all Ruprecht 147 stars is required to bring a 3.0 Gyr isochrone into agreement with the observed colors (Fig. 2.3 panel (b)). Consequently, guided by the linear relationship between Apsis (Andrae et al. 2018) reddening and extinction estimates, that is, the ratio of selective to total extinction (cf. Fig. 2.3 panel (d)),

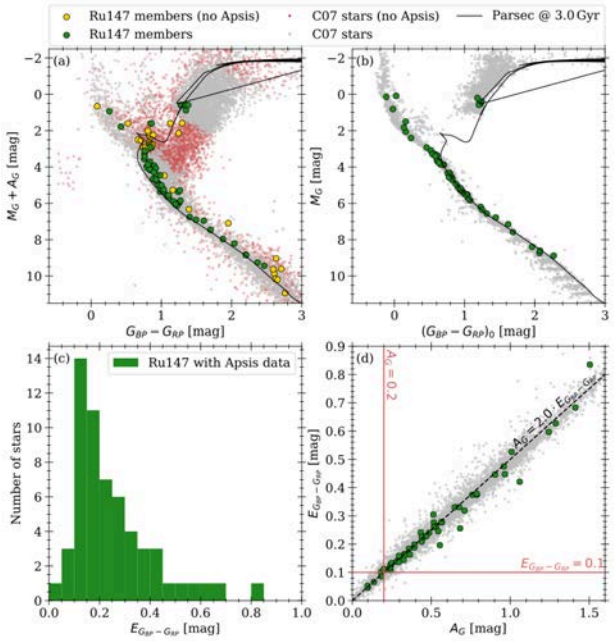

Figure 2.3: *Reddening-related aspects of Ruprecht 147.* Top: *Color-magnitude-diagrams for all* K2 *C07 objects (pale symbols); (a) only distance corrected according to their parallax and (b) additionally corrected for both distance and reddening according to Gaia DR2. The gray symbols refer to the subset of stars with reddening parameters provided and red to those without. Ruprecht 147 members (green for stars with reddening parameter, yellow for those without) are superimposed in both panels (a) and (b), the latter corrected for reddening $E(G_{BP} - G_{RP})$ according to Gaia DR2. A* PARSEC *isochrone for 3 Gyr is overplotted.* Bottom: *The panels show that while the reddening values are greatly divergent (c), there is a strong (and unsurprising) correlation between reddening and extinction (d). The ratio between $E(G_{BP} - G_{RP})$ and A_G allows us to set A_G for Ruprecht 147 based on our $E(G_{BP} - G_{RP})$ estimate. This is indicated by the red lines in panel (d).*

the values $E(G_{\rm BP} - G_{\rm RP}) = 0.1$ and $A_G = 0.2$ were adopted[9]. A small change in the adopted reddening parameters does not impact the results of our main study in any significant way.

The availability and quality of parameters for the individual cluster stars varies strongly across the sample. Optical and IR photometry are not available for all stars, with especially uncertain B and JHK magnitudes for the red, faint stars in the sample. Fortunately, most stars have extensive (and relatively well-constrained) magnitudes from *Gaia*. However, the relation between Gaia and Johnson colors is non-trivial. The relationship between magnitudes and colors provided by Evans et al. (2018), itself calibrated on standard stars, fails for late-type stars. The region with $B - V > 1.4$ is especially problematical. Therefore, we create our own empirical color transformation based on photoelectric photometry of Hyades and Pleiades stars in the literature and those of Pecaut & Mamajek (2013, and continuously updated afterwards, PM13 hereafter)[10]. We note that the PM13 results do not list individual stars but averaged results for various intrinsic stellar parameters of local dwarfs ($\leqslant 30$ kpc) as a function of the spectral type. We are gratified that both approaches provide similar results, thereby verifying one another's results. The derivation of the relationships is described in detail in Appendix A. However, readers are cautioned that this relation is only valid on the main sequence and generally fails for giants. (A related disagreement is highlighted in Fig. 7.1.)

2.2.4 Color Magnitude Diagram

The final CMD is shown in Fig. 2.4 in both *Gaia* and other commonly used colors. Stars with available *K2* light curves are highlighted with colored symbols, while the remaining cluster members are displayed in the background. We see a significantly more realistic cluster sequence, as compared with the versions in Fig. 2.3. In particular, we now see a well-defined cluster turnoff, a tight blue hook region, and additional stars populating the giant branch, the red clump, and even the blue straggler regions. A number of photometric binaries are also clearly present here, in contrast with the CMD that uses the Gaia DR2 extinction and reddening values. This CMD is more compelling than the earlier versions, in our opinion, and provides the confidence needed to place stars effectively in the color-period diagram later.

Reddening and extinction in Johnson colors are calculated using the mean extinction coefficient from Casagrande & VandenBerg (2018) as

$$E(B-V) = E(G_{\rm BP} - G_{\rm RP})/1.339 = 0.075\,{\rm mag}$$

and $A_V = 3.1 \cdot E(B-V) = 0.23$ mag. From the latter we calculate $E(V-K) = 0.21$ according to Johnson (1968, their Table 12). We note that despite the fact that all extinctions are calculated rather than fitted, they agree very well with the observations. No dereddening is applied to the 2MASS $(J-K)$ CMD.

We also display two sets of 3.0 Gyr isochrones in Fig.2.4, in both *Gaia* and other colors. We show isochrones from the PAdova and TRieste Stellar Evolution Code[11] (PARSEC: Bressan et al. 2012; Tang et al. 2014; Marigo et al. 2017; Pastorelli et al. 2019) and the Yale-Potsdam-Isochrones[12] (YaPSI: Spada et al. 2017). We note that the YaPSI isochrones were transformed into *Gaia* colors using the transformations we derived, as described above, and detailed in the Appendix. The PARSEC isochrones provide *Gaia* colors based on the revised passbands from Weiler (2018). We observe a generally satisfactory agreement between the finally-selected cluster members and the isochrones.

During this comparison, we found that our relationship between $G_{\rm BP} - G_{\rm RP}$ and $B-V$ and that constructed from the colors provided in the PARSEC isochrones are incom-

[9] These values are not intended to provide a definitive estimate for the cluster reddening and are only a consistiency check, motivated by our interest in the rotational properties of Ruprecht 147 cluster members observed with *Kepler*/*K2*.

[10] "A Modern Mean Dwarf Stellar Color and Effective Temperature Sequence", Version 2019.3.22, pas.rochester.edu/~emamajek/EEM_dwarf_UBVIJHK_colors_Teff.txt.

[11] stev.oapd.inaf.it/cgi-bin/cmd

[12] astro.yale.edu/yapsi/

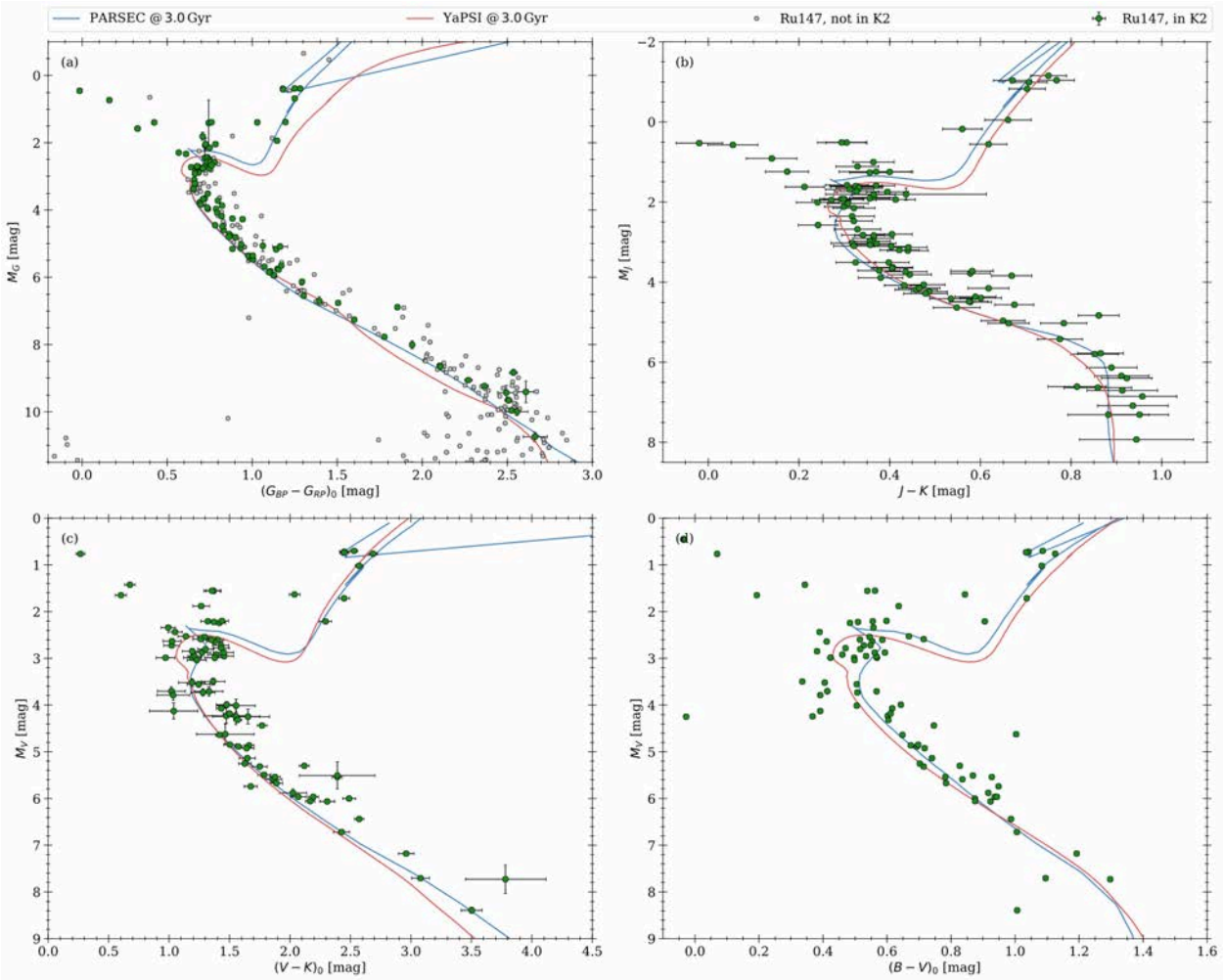

Figure 2.4: *Color-magnitude diagrams in* Gaia*,* 2MASS*, and Johnson photometry for the Ruprecht 147 member stars, both observed in* K2 *(green) and not (gray). Main sequence stars, photometric binaries, the turnoff, giant branch, and also blue stragglers are clearly distinguishable.* `PARSEC` *and* `YaPSI` *isochrones for 3.0 Gyr, are overplotted for comparison. Agreement is largely better than satisfactory, especially in the (most comprehensive)* Gaia *CMD. The stellar samples differ in each panel because of varying levels of completeness in the member photometry for the relevant color. The uncertainties in* $B - V$ *photometry are suppressed for visibility reasons. The individual stellar positions in the* Gaia *CMD are distance-corrected using the Gaia parallaxes; reddening and extinction-corrected uniformly with* $E(G_{BP} - G_{RP}) = 0.1$ *mag and* $A_G = 0.2$ *mag, in preference to the* Gaia *reddening and extinction values. (For additional corrections, see text.) The* `PARSEC` *isochrones use the* Gaia *colors provided within the isochrones; for the* `YaPSI` *isochrones we use our empirical color transformation from* $B - V$*. This causes the redward displacement of the giant branch in the* `YaPSI` *isochrones, because our transformation is not valid on the giant branch and tends to predict too red* Gaia *colors (cf. the encircled region in Fig. 7.1).*

patible with each other for stars redder than $B - V > 1.5$. The `PARSEC` isochrones fail to reproduce the observed color distribution of the Hyades and Pleiades (see Appendix Fig. 7.1). We are unable to explain this difference in the colors and proceed as follows: For the CMD we always display both `YaPSI` with our transformed colors and `PARSEC` with their provided colors. Whenever we need to transform *Gaia* colors of the cluster stars to $B - V$ (or vice versa), we use our derived relation. We see later that all stars for which we find rotation periods have $G_{\rm BP} - G_{\rm RP} < 2.3$ ($B - V \approx 1.4$) and for these stars the difference is small, posing no problem for this study.

The metallicity of Ruprecht 147 is generally reported to be [Fe/H] $\approx$ 0.1, with values ranging from [Fe/H] $= +0.08 \pm 0.07$ (Bragaglia et al. 2018, $Z \approx 0.017$) to [Fe/H] $= +0.12 \pm 0.03$ (Donor et al. 2020). We adopt [M/H] $= 0.08$ for the `PARSEC` isochrone, corresponding to $Y = 0.28$ and $Z = 0.0175$, and [Fe/H] $= 0.0$ and $Y = 0.28$ (corresponding to solar metallicity and $Z = 0.0162$)[13] for `YaPSI`, aiming to be as close to Ruprecht 147 as is feasible.

Although we display only 3.0 Gyr isochrones, we find that both the 2.5 and 3.0 Gyr `PARSEC` and `YaPSI` isochrones provide plausible fits to the cluster data, as commonly suggested in the literature, all the way from the lowest-mass stars to the clump stars on the giant branch. Neither isochrone is completely satisfactory in the blue hook region past the turnoff, where the convective core appears. We tend to favor the higher age because it requires lower values of extinction and reddening when matching

[13] The next higher metallicity available is [Fe/H] = 0.3

the cluster data with the isochrone in Gaia colors. This is reasonable for a cluster as close as Ruprecht 147 is. Torres et al. (2019) have suggested an isochrone age of 2.7 ± 0.61 Gyr, based on a PARSEC model fit to eclipsing binary systems in the cluster. We have no objection to this result, noting that both 2.5 Gyr and 3.0 Gyr are well within the uncertainties.

2.3 Analysis of the K2 lightcurves

We determine the rotation periods of stars by measuring the modulation of the stellar flux caused by the carriage of surface inhomogeneities such as star spots or plage across the stellar disk as the star rotates. When the orientation of the stellar rotation axis is sufficiently favorable, and the asymmetries are large enough and stable enough, periodicity can be observed and measured, even visually in the best cases, by counting the number of pattern repetitions over the time baseline available.

2.3.1 Basic K2 lightcurve information

The 82.5 d observational baseline, while long by the standards of most ground-based campaigns, still limits the detectability of long periods, potentially problematic for the late type stars in Ruprecht 147. To identify a period reliably based on spot motion, we typically need to recognize three occurrences of the spot. Therefore, the observational baseline needs to be longer than double the period. It is, however, possible to identify periods with a shorter baseline when more than one spot is visible in the light curve, so that their individual signatures can be assigned unambiguously and yield similar periods. Differential rotation and spot evolution often further complicate the period analysis. The reduced amplitude of smaller spots in old stars, combined with the limited (82 d) window of observation, makes the detection of long periods in old stars a matter of good fortune. (Ground-based studies (e.g. Strassmeier et al. 1994; Henry et al. 2013; Radick et al. 2018; Mallonn et al. 2018) often monitor stars for multiple years, and occasionally even decades, before they are able to detect a large-enough spot group to derive the rotation period.)

The *K2* field of C07 would initially have missed the cluster were it not for a community-driven effort that led to a change in the telescope pointing to include the center of the cluster at the edge of the field of view (cf. lower panel in Fig. 2.5). The related *K2* observing program "K2 survey of Ruprecht 147 - the oldest nearby star cluster" (GO7035[14]) added about 1000 stars of interest to the *K2* target list distributed over 60 target pixel files (TPFs). As described above, we find that 102 member stars of Ruprecht 147 (by our determination, integrating prior membership determinations) actually have *K2* light curves. Because of data transmission limitations during the *K2* mission, only target pixel files containing predefined pixel masks for selected stars are available, that is, no full frame images (FFIs) are available.

[14] keplerscience.arc.nasa.gov/data/k2-programs/GO7035.txt

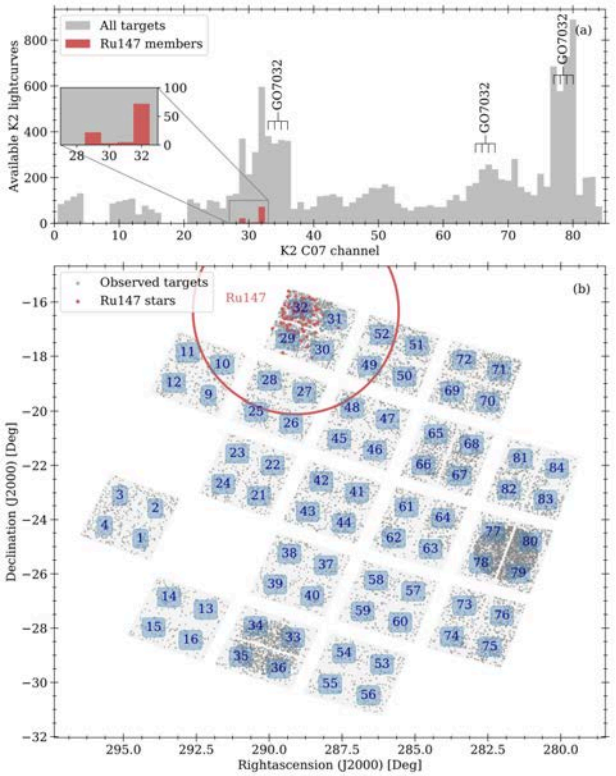

Figure 2.5: *Overview of* K2 *campaign 07. Panel (a): Histogram displaying the C07 target distribution over the channels (enumerated as displayed) that constitute the* K2 *CCD array. Ruprecht 147 targets (red) are mainly in channels 29, 31, and 32, while the others (gray) are everywhere. Panel (b): Sky map displaying the spatial coverage of all* K2 *C07 targets. Ruprecht 147 (encircled) is located at the northern edge. The footprints of a galactic archaeology campaign (GO7032) are prominent in both panels.*

Figure 2.5 (upper panel) shows the channel distribution for all C07 targets over the *K2* field. Ruprecht 147 is located in the northern portion (channels 29, 31, and 32). Although our scientific interests are here confined to Ruprecht 147, we also make use of data from other channels for light curve corrections, as discussed further below. Notably, a galactic archaeology campaign (GO7032) observed > 4000 targets whose footprints are also visible in the lower panel. (GO7012, which observed Pluto and GO7025, which observed Trojan and Hilda asteroids, is already removed in this overview.) Two *Kepler* modules became dysfunctional early in the *Kepler* mission and account for the blank spaces in both panels of Fig. 2.5.

For the acquired TPFs, various attempts have been carried out to extract de-trended light curves that are free of systematics in the observations and to correct, for example, the image drift during the observation. We do not attempt to perform this very-specialized data extraction process ourselves; instead, we use the Everest light curves (Luger et al. 2016) as our basic input. These were extracted using a pixel level de-correlation function (PLD, Deming et al. 2015). Other methods, for example, k2sc (Aigrain et al. 2016), are useful primarily for exoplanet search and use purely mathematical approaches on *K2* lightcurves extracted using simple aperture photometry

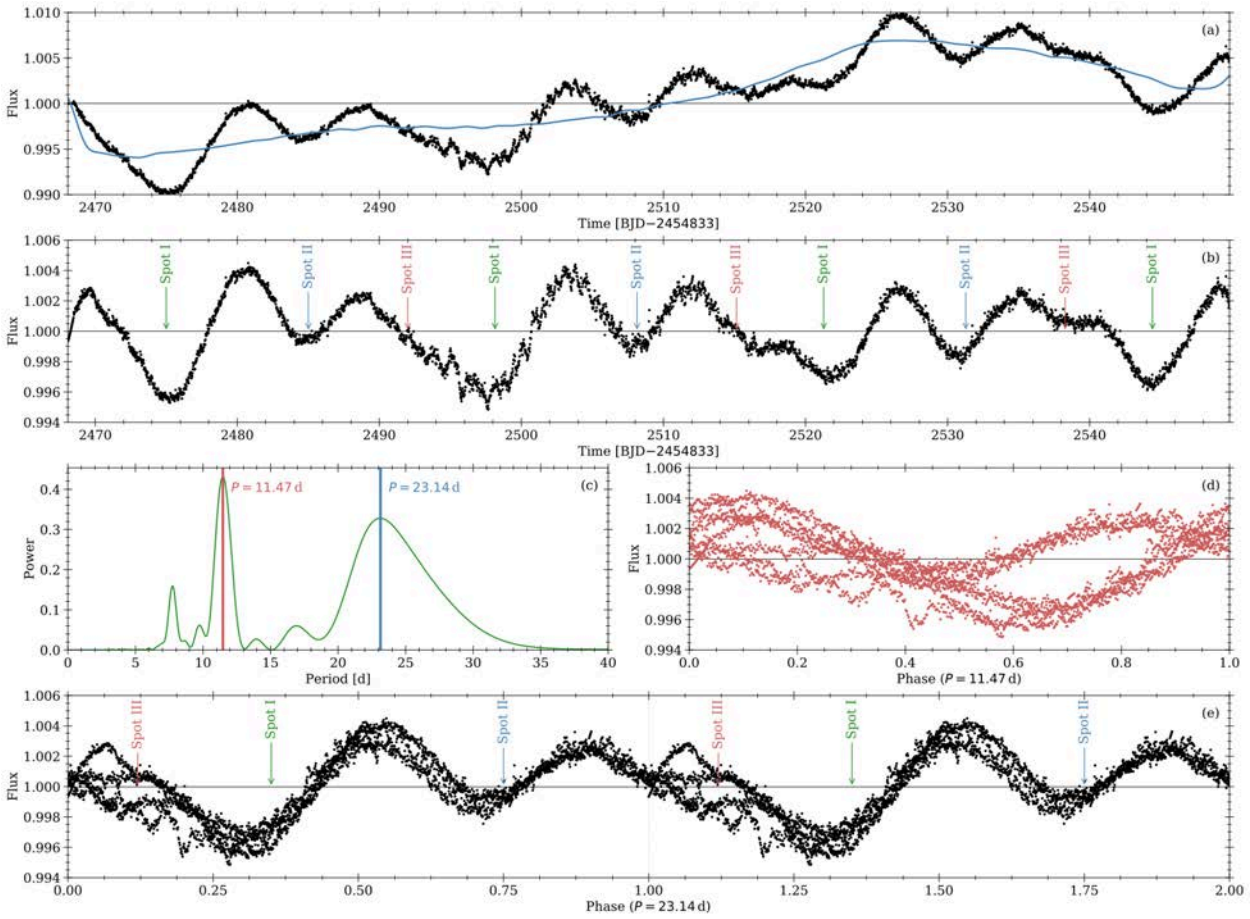

Figure 2.6: *Light curve processing and period analysis for EPIC 219297228. The light curve exhibits a complex structure from multiple spot groups and spot evolution; panel (a) shows the* `Everest` *lightcurve (black) and the reconstruction from the PCA (blue). Panel (b) displays the PCA-corrected lightcurve (black) with large spot features marked. Panel (c) shows the result of a Lomb-Scargle analysis with the maximum in the power spectrum indicated in red and the period determined by manual inspection of the light curve in blue. Panels (d) and (e) show the light curve phase folded with the periods obtained from the Lomb-Scargle and the manual inspection, respectively. For this particular light curve, the Lomb-Scargle analysis preferentially picks out half the true period despite the clearly different shapes of the recognizable spot features.*

(SAP) to correct for common trends in the data. These latter methods generally overfit the lightcurves and eliminate all traces of intrinsic, long-term, stellar variability. As a result, such lightcurves are unsuitable for our purposes; hence our usage of the `Everest` lightcurves.

2.3.2 Light curve detrending

Despite the sophistication of the method employed by Luger et al. (2016) to extract the `Everest` light curves, various trends and correlations are still apparent. We are unable to determine the origin of such trending conclusively, but it could plausibly be attributed to instrumental systematics which appear to become more pronounced in the lightcurves after the extraction by Luger et al. (2016). In any case, the lightcurves, as provided, are unsuitable for analysis of periodicity, and must be reworked. To ameliorate the trending in the curves, we perform a Principal Component Analysis (PCA) on sets of lightcurves.

The technical and procedural details of the PCA are described fully in Appendix B. We also display the 32 individual light curves and their PCA corrections in the Appendix (Fig 7.6). The upper panel (a) in each figure shows the `Everest` light curve and the reconstruction used, while the lower panels show the corrected and phased light curves. We note that our correction is superior to that with, for instance, a simple, higher order polynomial. While both approaches involve some level of subjectivity in the fitting process, that subjectivity is strongly reduced for the PCA. This is achieved via the dominant role played by the common trends in the PCA components, in opposition to a polynomial fit which only acts on the individual light curve, ignoring prior knowledge of shared systematics. Consequently, a polynomial fit is prone to overfit stellar signal with a long baseline and to ignore short baseline systematics. This can, in principle, be overcome by a manually fine-tuned fit of a higher order polynomial ($\geqslant$5) but this only replaces the identification of systematics using the PCA with a more subjective one that varies from star-to-star. The PCA correction provides us with detrended light curves for subsequent periodicity analysis. We believe that these light curves (See Fig. 2.6 and Appendix C) are far more representative of the underlying astrophysical reality than are the `Everest` light curves.

Table 2.2: *Periodicity and related information for the 32 sample stars. (This table is available in electronic form at the CDS via anonymous ftp to cdsarc.u-strasbg.fr (130.79.128.5) or via cdsweb.u-strasbg.fr/cgi-bin/qcat?J/A+A/644/A16/).*

EPIC	$(G_{\rm BP}-G_{\rm RP})_0$ [mag]	$(B-V)_0$[a] [mag]	P [d]	ΔP [d]	Components	Category	Flag[b]	Final sample[c]
218933140	0.87	0.69	20.4	2.5	9	1	MS	yes
219037489	0.99	0.80	22.8	1.5	6	1	MS	yes
219141523	2.27	1.50	26.9	1.8	4	1	MS	yes
219238231	*0.78*	*0.61*	*28.1*	*0.9*	*3*	*2*	*MS*	*no*
219275512	*0.88*	*0.70*	*20.4*	*0.5*	*6*	*2*	*BIN*	*no*
219280168	1.15	0.95	23.0	0.8	5	1	MS	yes
219297228	1.13	0.93	23.1	0.4	6	1	MS	yes
219306354	0.98	0.79	22.8	0.8	5	1	MS	yes
219333882	*1.16*	*0.95*	*11.6*[f]	*0.5*	*11*	*2*	*MS*	*no*
219341906	*0.75*	*0.58*	*1.6*	*0.1*	*14*	*1*	*TO*	*no*
219353203	2.1	1.48	21.6	0.7	5	1	MS	yes
219388192	0.86	0.69	12.5	0.2	8	1	MS[d]	yes
219404735	*0.79*	*0.62*	*24.4*	*1.1*	*5*	*1*	*BIN*	*no*
219409830	*0.83*	*0.66*	*9.6*	*0.4*	*7*	*2*	*MS*	*no*
219422386	1.01	0.81	22.6	1.3	5	1	MS	yes
219479319	1.6	1.31	20.1	0.7	4	1	MS	yes
219489683	1.78	1.40	19.0	0.5	5	1	MS	yes
219515762	*0.57*	*0.43*	*5.7*	*0.1*	*8*	*1*	*TO*[e]	*no*
219545563	0.93	0.75	22.2	1.6	4	1	MS	yes
219551103	1.0	0.81	22.0	1.8	5	1	MS	yes
219566703	1.51	1.25	23.2	1.5	5	1	MS	yes
219610232	*1.17*	*0.97*	*5.6*	*0.2*	*5*	*1*	*BIN*	*no*
219610822	1.11	0.91	23.1	1.5	5	1	MS	yes
219619241	2.11	1.48	22.1	1.5	5	1	MS	yes
219634222	1.29	1.08	27.3	3.5	5	1	MS	yes
219646472	*0.61*	*0.47*	*22.1*	*2.0*	*3*	*1*	*TO*	*no*
219683737	1.07	0.88	21.7	1.0	5	1	MS	yes
219721519	1.1	0.90	21.9	1.5	2	1	MS	yes
219722212	0.94	0.75	22.7	2.1	5	1	MS	yes
219722781	1.39	1.16	21.4	0.5	7	1	MS	yes
219755108	*0.94*	*0.76*	*29.4*	*0.5*	*4*	*1*	*BIN*	*no*
219800881	*0.9*	*0.72*	*32.7*	*8.1*[f]	*5*	*2*	*MS*	*no*

Notes. *(a) Calculated from $(G_{\rm BP}-G_{\rm RP})_0$ with our derived transformation; (b) MS = Main sequence, TO = Turn-off, BIN = (possible) binary? (c) Star used for detailed comparison in Sect. 2.5 and 2.6; (d) Spectroscopic binary (G+M star) and eclipsing Brown Dwarf companion (e.g. Beatty et al. 2018); (e) Suspicious proper motions, cf. Fig 2.2, and only mentioned in Cu13, cf. Table 7.3, thus likely not a member; (f) Ambiguity in the matching of visible spot features.*

2.3.3 Analysis of periodicity

Our principal targets from the point of view of rotation are the cooler stars among the *K2* targets that are on the cluster main sequence. Nevertheless, we have inspected all 102 member stars in *K2* for possible periodicity. We eliminated most stars in evolutionary states past the turnoff (TO) from our sample. Stars at the turnoff (i.e., Spectral type G0; $(G_{\rm BP}-G_{\rm RP})=0.7$) and even somewhat cooler ones display no discernible periodicity. However, we retained some bluer stars near the core-convection hook in the isochrone, one star blueward of the giant branch, and a number of photometric binaries. (These are flagged accordingly below.) We also eliminated lightcurves that clearly show features from eclipsing binary/planetary systems and those that are essentially featureless.

As one can see from the example of EPIC 291722781 in Fig. 7.4 and from the light curves constructed by our PCA procedure for the final sample, and displayed in the Appendix (Figs. 7.6 – 7.6), periodicity is visually recognizable for all the light curves retained[15]. One can typically read off the approximate rotation period of the star in question by inspection, with the proviso that in most cases, more than one spot group is present. The periodicity analysis discussed below simply serves to quantify the visually observed periodicity.

The periodicity in the processed light curves is measured by subjecting each one to Lomb-Scargle analysis (Lomb 1976; Scargle 1982). The algorithm is run for peri-

[15] Such a choice could be considered overly conservative, and others might have chosen inclusivity, but we prefer to retain an exclusive sample in this work.

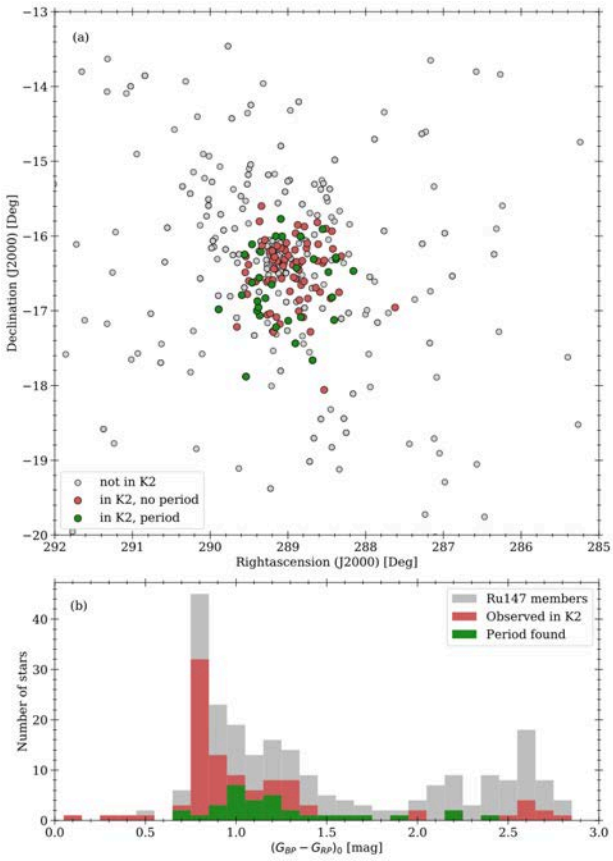

Figure 2.7: *Fraction of stars with detected periods. Panel (a) shows the spatial distribution of the cluster stars, color coded to indicate both coverage in* K2*, and whether a periodic signal was identified (green) or not (red). Panel (b) shows a histogram of the stars identified as Ruprecht 147 members and its coverage in* K2*. Gray depicts all stars identified as Ruprecht 147 members in Sect. 2.2.2. Stars for which we found periodic signals are displayed in green, while red symbols indicate the remaining stars observed by* Kepler/K2*. Red and green that denote stars that were observed during* K2 *C07 and green are the stars for which we found a periodic signal.*

ods in the range $0.2\,\mathrm{d} \leqslant P \leqslant 40.0\,\mathrm{d}$[16], with a logarithmic spacing of $\Delta \log P = 0.001$ dex. For a minority of lightcurves that show periodic variations over the complete duration of C07, this approach is able to identify the correct periods without further intervention. However, most of our lightcurves display spot evolution and/or multiple spot groups. This requires that we inspect all lightcurves manually to identify the correct period. The lightcurves are then phase-folded to match features.

This process is illustrated in Fig. 2.6, but for EPIC 219297228 which exhibits signals of at least three clearly distinct spot groups. In fact, we observe multiple spot features for the majority of our stars. And with the exception of EPIC 219353203, it is only the fastest rotating stars in our sample that show only one (large) feature. This observation is consistent with the findings of Basri & Nguyen (2018), where the incidence of multiple spot groups was found to increase with rotation period.

The identification of rotation periods from starspot features can be hindered by both differential rotation, which yields slightly different periods for each spot, and also spot evolution, which occasionally makes spots (dis)appear. We estimate the period error from the phase-folded light curve. We do this by examining the above-mentioned effects and the extent to which they allow period changes that still result in an acceptable phase folded light curve. If no such effects are present, the period error is found to be generally small $\sim$3%, owing to the photometric precision and the short cadence of *Kepler* data. In the worst case, the error is on the order of $\sim$25%.

More difficulties arise in noisy data, or when the degree to which the PCA is performed results in ambiguities. Therefore, we assign each period found to one of two categories based on the reliability of the signal found. Category 1 denotes periods in which we have great confidence, while category 2 periods are those where doubts can reasonably be entertained. By this classification, we aim to reduce the impact of possible false-positives. Because we aim for the greatest confidence in the final sample of rotation periods, we have been relatively conservative in accepting light curves as periodic and more so when assigning Cat. 1 to it. For the time being, and for the convenience of researchers interested in non-rotational variability, we retain evolved stars, binaries, etc., but we will mark or remove them in due course. The results of the periodicity analysis are summarized in Table 2.2.

We note that our derived periods display a visually similar distribution to the one found by Curtis & Agüeros (2018) (hitherto unpublished, but see below), with the exception of a handful of stars in the vicinity of $G_{\mathrm{BP}} - G_{\mathrm{RP}} \approx 0.6$, which is not present in our sample. The lower (b) panel in Fig. 2.7 displays an overview in *Gaia* color that depicts the fraction of member stars by color for which a period was ultimately found in the *K2* data. The upper (a) panel of Fig. 2.7 shows the spatial locations of these stars. It is rather obvious in Fig. 2.7 that late-type stars are vastly underrepresented. The total number of stars with $G_{\mathrm{BP}} - G_{\mathrm{RP}} > 1.5\,\mathrm{mag}$ is probably much higher and a large number of stars is likely simply missing in our sample. Furthermore, *K2* targets are clearly biased towards solar type stars. Aside from the obvious predominance of solar type stars, the faintness of M-dwarfs also contributes to this bias.

A parallel and independent study of this cluster has been carried out by Curtis et al. (2020), with whom we have exchanged periodicity data (but no other information, to preserve independence) after both publications were essentially complete. This exchange allows us to compare the periods for all 26 stars in common to both studies, as shown in Fig. 2.8. We are pleased to report very good agreement between their periods and ours, with the exception of one outlier (EPIC 219333882, encircled in Fig. 2.8).

This outlier is assigned Cat. 2 by us because of an ambiguity that, in principle, allows to double or even triple the associated period and still obtain a reasonable phased

[16]The *K2* baseline of 82.5 d does not permit secure identification of any periodicity longer than this.

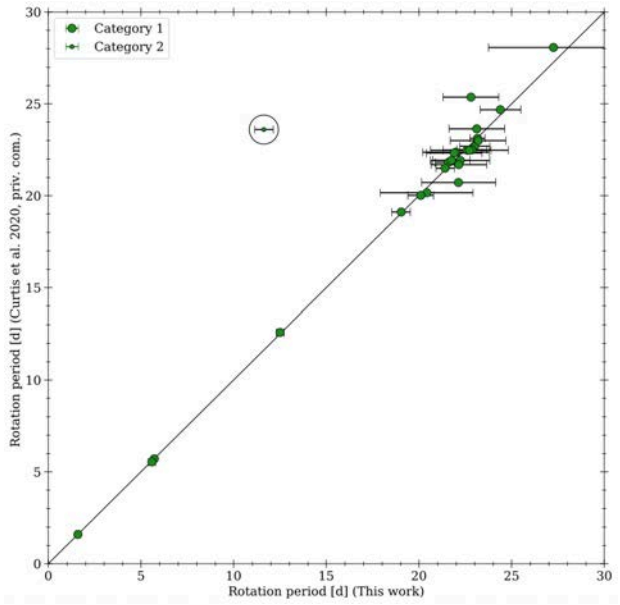

Figure 2.8: *Comparison of our periods with those found by Curtis et al. (2020) for the 26 stars common to both samples. The encircled outlier (EPIC 219333882, which does not make it into our final 21-star sample) has an ambiguous light curve that permits multiples of the period listed.*

curve (cf. Fig. 7.6). Doubling our period would put it in good agreement with the distribution observed for the other stars and suggests that that we have likely identified half the true period. However, we have decided to list the star as is, because our light curve by itself evinces no preference for the longer period[17]. We also note that of our final 21 star sample (see below), 20 stars are common to both studies, 19 of which have periods that agree within $\leqslant 2\,\%$; only EPIC 219037489 is more discrepant than the errorbar[18] ($\approx 10\,\%$).

2.4 Rotation periods in the CMD and CPD

The near-final sample of periodic stars that constitute the result of our analysis contains 32 stars in which a periodic signal could be identified and plausibly attributed to stellar rotation. For the time being (and for the convenience of other researchers), we retain various objects unsuited to our main sequence rotation interests such as evolved stars, binaries, and stars as blue as spectral type F3V, the last clearly stars without surface convection zones. The cross-identifications and other basic properties of these stars are summarized in Table 7.3.

In addition to the derived period and the number of components required, this table lists the assigned category of reliability as described before[19]. We also flag stars in Table 2.2 to indicate their evolutionary and binary status. The latter criterion is given when a star sits above the main sequence but is clearly redder then the turn-off (undetected multiplicity), or when the stellar environment suggests light contamination due to crowding.

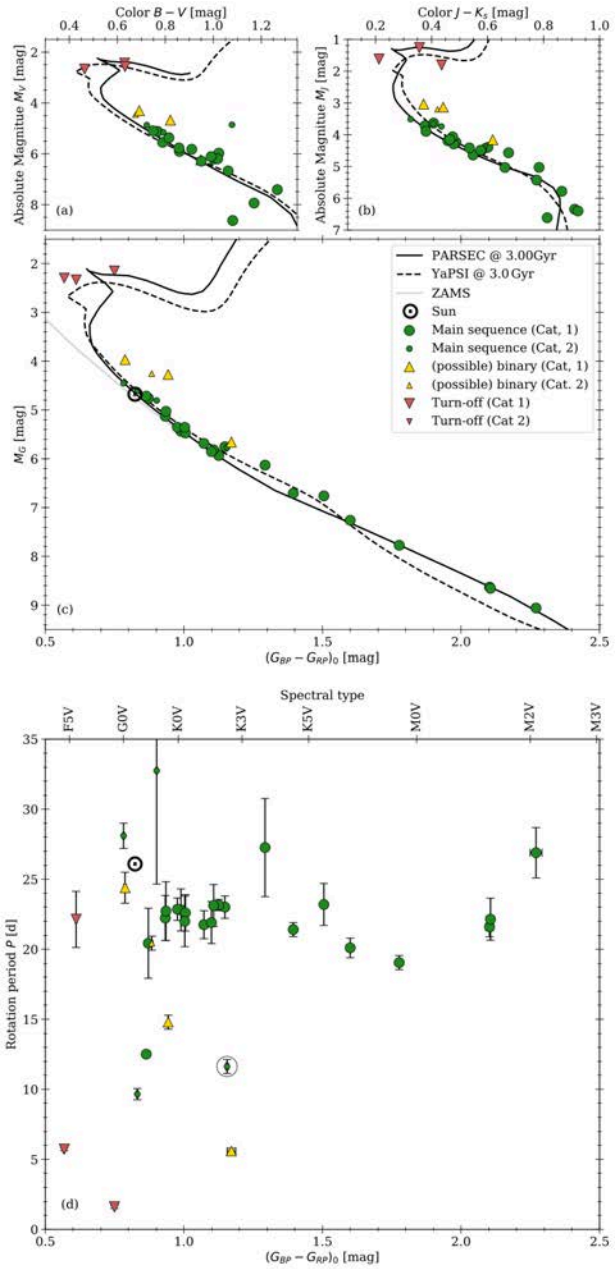

Figure 2.9: *CMDs in various color systems (upper panels (a), (b), and (c)) for the 32 periodic Ruprecht 147 cluster members. The bottom panel (d) shows the corresponding color-period diagram (CPD) for the same stars. The 3 F-type stars past the cluster turnoff are marked with red symbols, single main sequence cluster members are in green, and yellow symbols indicate known binaries. The plot symbols also encode both object type and period category (large symbols for Cat. 1 periods, small for Cat. 2) as indicated in the legend. The sun is marked with its usual symbol in both the CMD and CPD and is displayed only as a reference point. The encircled star is EPIC 219333882, for which multiples of our period are equally plausible (see text).*

[17] In fact, we have taken some care in our work to compartmentalize each star and not to let the results of neighboring stars affect periodicity judgements. This makes our work comparable to field star studies, where the occasional multi-spotted star could potentially be assigned a submultiple of the true period and hence provide a significantly younger rotational age than the real one.

[18] We infer from this that our uncertainties are likely reasonable.

[19] For various reasons, we err on the side of caution, so it is quite possible that future work on the same data could yield a larger sample of acceptable periods.

Table 2.3: *Reddenings used for the individual clusters in Fig. 2.10. Calculated reddenings use the relationship* $1.339 \cdot E_{B-V} = E_{G_{\rm BP}-G_{\rm RP}}$ *(Casagrande & VandenBerg 2018) and the arrow indicates the direction of the calculation.*

Cluster	E_{B-V}		$E_{G_{\rm BP}-G_{\rm RP}}$	Ref	[Fe/H]	Ref
NGC 6819	0.15	$\Rightarrow$	0.201	Meibom et al. (2015)	0.05	Donor et al. (2020)
NGC 6811	0.048	$\Rightarrow$	0.065	Curtis et al. (2019)	-0.05	Donor et al. (2020)
Hyades	0.027	$\Rightarrow$	0.036	Joner et al. (2006)	0.13	Netopil et al. (2016)
M 67	0.04	$\Rightarrow$	0.054	Barnes et al. (2016b)	0.03	Casamiquela et al. (2017, 2019)
Ruprecht 147	0.075	$\Leftarrow$	0.1	this work	0.12	Donor et al. (2020)

These periodic star results are displayed in color-magnitude diagrams (CMDs) in panels (a) – (c) of Fig. 2.9 and in a color-period diagram (CPD) in panel (d) of Fig. 2.9. We see that three of the F-type stars (red triangles in the figures), indeed some of the bluest stars of our periodic sample, are clearly evolved past the turnoff and are in the vicinity of the blue hook. Two of their rotation periods are below 6 d, while one is far higher, at ∼22 d. Four additional stars (yellow triangles) are photometric binaries which are located significantly above the single star sequence in the CMD. Their rotation periods also have a wide range, from 5.6 d to 29.4 d, with all but one being clear outliers also in the CPD.

The remaining 25 periodic stars (green circles) are all plausibly on the cluster's single star main sequence in the CMDs. As can be seen in the corresponding CPD, these stars also display a wide range of rotation periods, ranging from under 10 d to almost 33 d. However, the majority (19 out of 25) of these GKM-type main sequence stars occupy a horizontal band between 19 d and 27 d periods across the GKM spectral range. These are all stars for which we have great confidence in the periods determined (Category 1). The remaining 6 stars are outliers, based both on the measured distribution itself and prior expectations from studies of other open clusters.

We now trim our dataset down to those periodic stars that are on the main sequence, for which no contaminating flux is evident and for which we have a high degree of confidence (category 1) in the rotation periods. This leaves us with 21 stars, cf. the *Final sample* column in Table 2.2, which will be the only ones we use for the remainder of this paper.

2.5 Comparison with other empirical cluster period work

Before comparing our measured periods with models we wish to show the context of, and continuity with, other work in the literature. There are three other relevant open clusters for which rotation periods are available, all of which are based on work with *Kepler* or its *K2* reincarnation. These are the 4 Gyr-old open cluster M 67 (Barnes et al. 2016b), the 2.5 Gyr-old open cluster NGC 6819 (Meibom et al. 2015), and the 1 Gyr-old cluster NGC 6811 (Meibom et al. 2011a; Curtis et al. 2019). The measured rotational distributions for their cool stars are also displayed in Fig. 2.10. In order to avoid any possible color-related inconsistencies, we associate the stars with measured rotation periods with their *Gaia* colors (the most uniform currently available), which we subsequently deredden appropriately. The reddening parameters used are listed in Table 2.3. We also transform this $G_{\rm BP} - G_{\rm RP}$ color into $(B - V)_0$ color to display the same information in $B - V$ color in an additional panel for the reader's convenience.

The M 67 data display the greatest dispersion in rotation period, likely a consequence of the difficulty of determining rotation periods in this relatively old cluster, and the result of its having been observed for only one *K2* quarter. The rotation periods are taken from the study of Barnes et al. (2016b), where the large rotation period uncertainties can be appreciated. Despite this dispersion, it is clear that all the M 67 stars are located *above* the Ruprecht 147 stars in a mass-dependent way, as expected. This fact informs us that Ruprecht 147 is younger than the 4 Gyr-old M 67 cluster.

Conversely, all the rotation periods measured in NGC 6811 are located below those of Ruprecht 147, again in a mass-dependent way. This tells us that Ruprecht 147 is clearly older than the 1 Gyr-old NGC 6811 cluster. We display the rotation period determinations of both Meibom et al. (2011a), based on a single *Kepler* quarter, and those of Curtis et al. (2019), based on the entire 4 year *Kepler* dataset. We note the good agreement of the majority of the rotation periods between the two studies and especially the very well-defined sequence of NGC 6811 in the CPD. The latter is likely the result of NGC 6811's relative youth, which manifests itself in relatively large flux variations from starspots and the fact that NGC 6811 was located in the *Kepler* field itself, allowing for it to be observed over the entire 4yr baseline.

We also show the rotation periods measured by Radick et al. (1987) in the younger (∼ 625 Myr-old) Hyades open cluster. This sequence of rotation periods was the first to be measured, and provided the first significant clue to the mass dependence of stellar rotation in cool stars. As expected, they are located below the NGC 6811 data, except in the mid-K spectral type region, where there is some overlap with the NGC 6811 data. For completeness, we also display rotation periods from the recent *Kepler*/*K2* study of Douglas et al. (2019), which seem to be marginally below the NGC 6811 values.

The comparison with the 2.5 Gyr-old NGC 6819 cluster is perhaps the most revealing. In the region of the spectral types G-K, the rotation periods of the two clusters overlap one another significantly enough that they could almost be merged. This fact confirms that Ruprecht 147 is roughly the same age as the 2.5 Gyr-old NGC 6819 cluster. Our Ruprecht 147 rotation periods also extend the

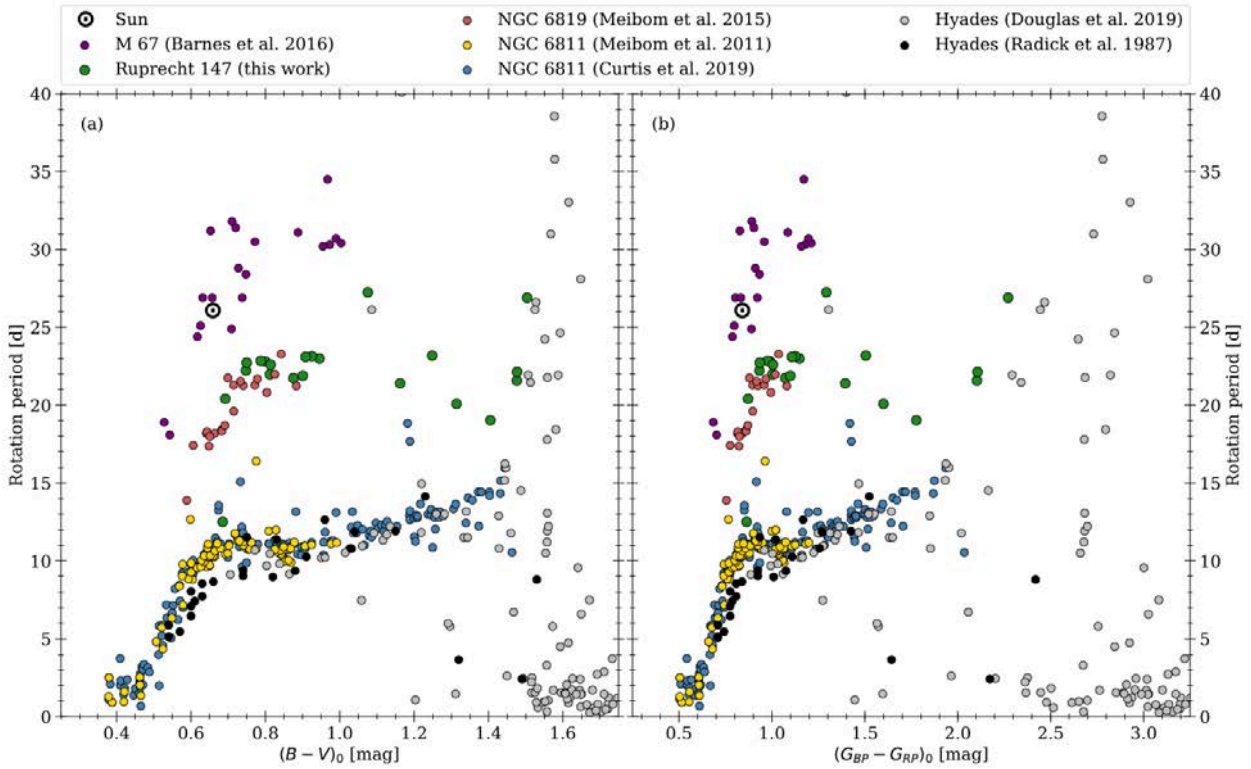

Figure 2.10: *Color-Period-diagrams in Johnson $B-V$ and Gaia colors for Ruprecht 147 in relation to those for other relevant clusters. We see that Ruprecht 147 stars (green) are sandwiched between the 4 Gyr-old cluster M67 (purple), and the 1 Gyr-old cluster NGC 6811 (yellow, blue), as expected. The Ruprecht 147 rotation periods also connect smoothly to the rotation period data for the 2.5 Gyr cluster NGC 6819 (red), overlapping well in the G-K spectral range. We also display the distribution(s) for the younger (∼625 Myr) Hyades open cluster (black, gray). (See legend and text for references.)*

empirical rotational isochrone for $(2.5-3\,\mathrm{Gyr})$ towards much lower masses. These rotation periods for the lower mass stars are somewhat shorter than those of the G-K stars in the cluster. This is somewhat unexpected and will be discussed further in Sect. 2.6. We have unfortunately been unable to derive rotation periods for early G-type stars in Ruprecht 147, to confirm any possible overlap with NGC 6819 in this mass range. This could be the result of one of more of the following: (a) our study using overly strict requirements in accepting periodicity, (b) the relatively small amplitudes of spot variability for such 2.5 Gyr-old stars, and (c) the relatively poor quality and shorter baseline of the *K2* Ruprecht 147 light curves, as opposed to the 4yr baseline of the higher-quality *Kepler* NGC 6819 data. The NGC 6819 periods and $(B-V)_0$ colors are taken from Extended Data Table 1 in Meibom et al. (2015).

We conclude from this empirical comparison that all extant cool star rotation period data for open clusters between 1 and 4 Gyr, including the current ones for Ruprecht 147, are compatible with all these data lying on a single surface in color-rotation period-age space, as originally proposed by Barnes (2003) and as emphasized by Meibom et al. (2015) in connection with rotation periods in the 2.5 Gyr-old open cluster NGC 6819. The period determinations for Ruprecht 147 herein extend this surface towards lower-mass stars at this important intermediate age. However, the detailed shape of the surface proposed appears to require revision for lower-mass stars, as argued by Curtis et al. (2019), when they extended the NGC 6811 (1 Gyr) rotation period data of Meibom et al. (2011a) to the low mass range.

2.6 Comparison with models

Another aim of our study is to examine the predictions of stellar spindown models in a region of parameter space (lower mass, combined with higher age stars of well-defined age) than has not been possible thus far, as can be appreciated in Fig. 2.10. The goal of such efforts is of course to construct an empirically-constrained model of stellar rotational evolution across the largest-possible parameter range. Such models could be used to derive stellar ages via gyrochronology if the relationship between the underlying variables is suitably well-behaved, and more generally, to understand the physics of magnetic braking.

The first of such mass-dependent models was that proposed by Kawaler (1988), subsequently implemented in the Yale Rotational stellar Evolution Code (YREC; Pinsonneault et al. 1989), following a method for computing rotational stellar models first explicated by Endal & Sofia (1978). This method of modeling rotating stars has also been implemented in the Geneva code (e.g. Maeder & Meynet 2000) which, although it is generally used for modeling hot stars, has been updated for usage in particular cool star contexts (Eggenberger et al. 2012; Amard et al. 2019). Rotational evolution in all extant stellar mod-

els is overlaid on non-rotating stellar models (so-called "standard models"), using a number of additional parameters unique to the rotational aspect of the modeling (see Pinsonneault et al. 1989), with various tradeoffs between their number and the fidelity of description of the data (e.g. Barnes & Kim 2010). We note that relevant data prior to the mid-1990s typically consisted of measured $v \sin i$ values, with notable exceptions being the rotation period work of van Leeuwen et al. (1987, Pleiades) and Radick et al. (1987, Hyades).

The advent of large-format CCDs allowed increasingly large numbers of rotation periods to be measured for both pre-main sequence stars (e.g. Attridge & Herbst 1992; Bouvier et al. 1993, 1995) and for main sequence stars (e.g. Prosser et al. 1993; Irwin et al. 2006; James et al. 2010), with corresponding steady pressure on models. Barnes (2003) collected the open cluster rotation periods then available for cool main sequence stars and identified color- and age-dependent patterns in the rotation period data that could be described by a simple empirical relationship between rotation period, color, and age using only three fitted numerical constants. The possibility of deriving the age (otherwise hard to measure) from the measured periods and colors led to his proposing the neologism gyrochronology for the associated age-determination procedure. A subsequent publication (Barnes 2007) showed that the associated uncertainties in the derived stellar age ($\sim 15-20\%$) for cool main sequence stars were indeed small enough to be useful and similar empirical relationships have been been subsequently proposed by Mamajek & Hillenbrand (2008) and Angus et al. (2020), among others.

The undesirability of constructing separate relationships with new fitted parameters for each relevant color prompted Barnes & Kim (2010) and Barnes (2010) to formulate an empirical spindown relationship that captures the fact that cluster stars appear to have a bimodal rotation period distribution of fast- and slow rotators at the ZAMS, that subsequently erodes into a unimodal slow rotator distribution in older clusters. The fast- and slow asymptotic rotation period behaviors were formulated mathematically symmetrically, using the convective turnover timescale, τ, in stars as the mass variable, to describe the two mass-dependent timescales in the problem. The usage of τ allowed the model to be translated into any relevant observed color as necessary, and arguably more importantly, connected to stellar magnetic activity and dynamo theory, where the convective turnover timescale, or equivalently the Rossby Number $Ro = P/\tau$ (or its inverse, the Coriolis Number, Co) has long been recognized as an important variable (Durney & Latour 1978; Durney et al. 1993; Noyes et al. 1984; Patten & Simon 1996; Brandenburg 2018). This (Symmetric Empirical) Model[20] requires only two dimensionless constants, k_C and k_I, to describe rotational evolution on the main sequence, and will also be shown below, unmodified from its original, now 10 yr-old formulation. A key feature of the Barnes (2010) model is that the morphology of the predicted cluster rotation period distributions changes with cluster age (as seen in the observations) and in contrast to the Ba07 model and a number of other subsequent ones.

These proposed models all have additional degrees of freedom. They include the ones of Spada & Lanzafame (2020), Matt et al. (2015), Garraffo et al. (2018), and Amard et al. (2019), in order of increasing number of degrees of freedom. (See Fr20 for an inter-comparison of these models in the context of an extensive rotation period dataset for the Pleiades-age southern open cluster NGC 2516.) Of these models, we also display our Ruprecht 147 data against the model of Spada & Lanzafame (2020) because it appears to come closest to describing them with a minimum of parameters and to the Amard et al. (2019) models, which in principle have enough degrees of freedom to enable them to describe the observations with greater fidelity. For an alternative perspective on this subject, one that emphasizes the magnetic braking perspective and uses scaling relations and associated parameters liberally, see the recent work of Ahuir et al. (2020).

2.6.1 The Barnes (2010) model

Our first detailed comparison is with the model of Barnes (2010, Ba10 hereafter), which uses the relationship listed in Barnes & Kim (2010, their Table 1) to convert between stellar mass, temperature, and U, B, V, R, I, J, H, K colors. This fact permits us to use the dimensionless scaling constants k_C and k_I unchanged from that work. Equation (32) from Ba10, explicit for the age,

$$t = \frac{\tau}{k_c} \ln\left(\frac{\mathrm{P}}{\mathrm{P}_0}\right) + \frac{\mathrm{k_I}}{2\tau}\left(\mathrm{P}^2 - \mathrm{P}_0^2\right) \tag{2.2}$$

also provides an implicit function for the rotation period P for any given age, t, in terms of the convective turnover timescale, τ and the initial period P_0, adequately represented by the 1.1 d value for stars of sufficiently advanced ages[21].

For computational convenience, we transform the above expression into an explicit one for the rotation period P. (For this particular use, we actually began with the explicit solution for τ in Eq. (22) from Ba10, which itself uses the fact that Eq. (2.2) above is quadratic in τ, and hence, solvable.) Solving this equation yields

$$P = \sqrt{\frac{a \cdot \mathcal{L}(w, 0)}{2b}} \tag{2.3}$$

with

$$w = \frac{2 \cdot \exp\left(2 \cdot (b \cdot P_0^2 + t)/a\right) bP_0^2}{a},$$
$$a = \frac{\tau}{k_c}, \text{ and } b = \frac{k_i}{2\tau}$$

[20] The name was coined by Brown (2014), who advocated a "Metastable Dynamo Model", where the shape of the slow rotator sequence does not change over time.

[21] For young stars, the full range of possible ZAMS rotation periods ought to be considered.

where $\mathcal{L}$ is the Lambert W function[22], and $k_c = 0.646\,\mathrm{d\,Myr^{-1}}$, $k_i = 452\,\mathrm{Myr\,d^{-1}}$, exactly as in Ba10. (We note that for small τ, solving Eq. (2.3) can lead to numerical instabilities; this is only relevant for stars bluer than those considered here. In such cases, it may be necessary to solve the explicit function for t from Ba10 and reproduced in Eq. (2.2), numerically.)

The convective turnover timescale, τ, is obtained from Barnes & Kim (2010, Table 1), which in turn relied on the $T_{\rm eff}$-color transformations of Lejeune et al. (1997, 1998). Both Johnson and 2MASS colors are provided there as a function of convective turnover timescale, stellar mass, effective temperature, etc. The conversion to $G_{\rm BP} - G_{\rm RP}$ is effected using the transformation from $B-V$ as described earlier, in Sect. 2.2.3. The solution of Eq. (2.3) returns a range of periods for a given age and color that is bounded by the spread permitted in the initial periods P_0. Cool stars span a range of periods at the ZAMS, from near-breakup rotation periods at 0.12 d and up to 3.4 d, the latter appearing to be longest rotation period found in very young clusters at the relevant mass range (Barnes 2010). Following Ba10, we use the intermediate $P_0 = 1.1$ d as a representative reference value for solar-type stars in each range. The result can be seen in Fig. 2.11, where we show the Ba10 rotational isochrones for three different ages, 3.0, 2.5, and 1.6 Gyr (top to bottom).

In Fig. 2.11, we also display the most reliable of our rotation periods, defined as such if they are both in category 1 and also if the star is on the main sequence. These are all redward of $(G_{\rm BP} - G_{\rm RP})_0 = 0.86$ ($(B-V)_0 = 0.68$). Unfortunately, as the reader may see by glancing back at Fig. 2.7, very few stars bluer than solar color were observed in *K2*, and of these we have been able to determine rotation periods for no normal ones. Consequently, we supplement our Ruprecht 147 rotation periods with those in NGC 6819 (also believed to be of similar age) that were determined by Meibom et al. (2015) to enable a full comparison.

The comparison between the data and the models shows that there is a reasonable match between the isochrone for 2.5 Gyr for all the NGC 6819 data (as was also found by Meibom et al. 2015) and the Ruprecht 147 rotation periods for stars warmer than spectral type K2V (i.e., $(G_{\rm BP} - G_{\rm RP})_0 \sim 1.2$; $(B-V)_0 \sim 0.95$). However, while the models for all ages predict a steady rotation period increase with redder color at a given age up to early M stars, our rotation period data show a much more horizontal, even slightly declining trend for the cooler (mid-K and early-M) stars. Consequently, for the 8 cooler stars with measured rotation periods, there appears to be a significant mismatch between the measurements and the Ba10 model, with the data points mostly accumulating in the region corresponding to the 1.6 Gyr isochrone rather than that for 2.5 Gyr. This behavior was first pointed out by Curtis & Agüeros (2018) where it was entitled the "puzzle of K dwarf rotation".

[22] see `docs.scipy.org/doc/scipy-0.14.0/reference/generated/scipy.special.lambertw.html` for the python implementation used.

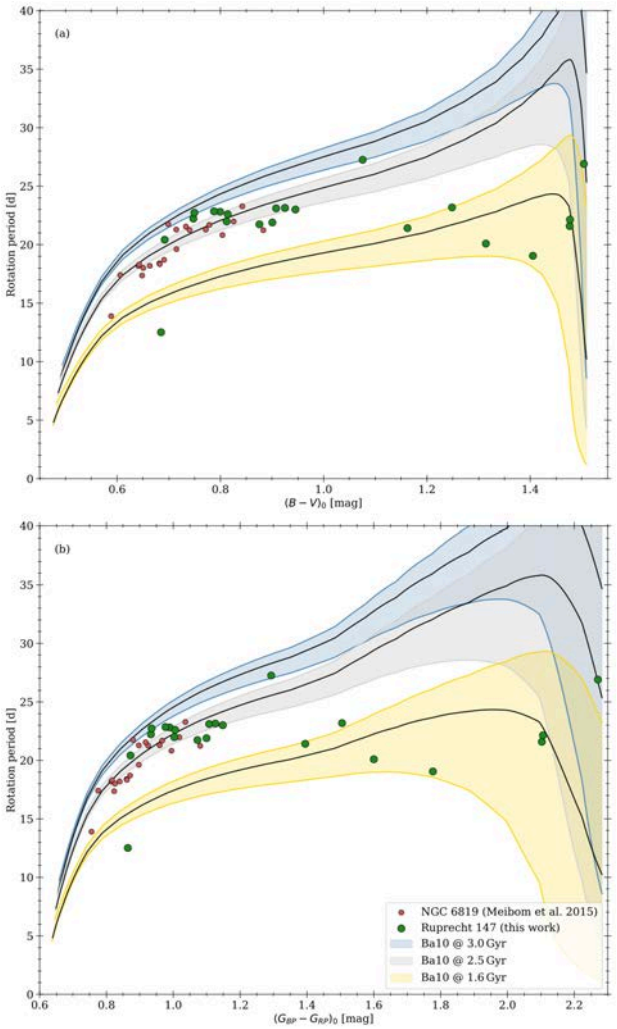

Figure 2.11: *Color-Period-Diagrams in both Johnson $B-V$ (a) and Gaia (b) colors. Both show our Ruprecht 147 stars (green) and those from NGC 6819 (red; Meibom et al. 2015), compared with the Ba10 models. We only display stars that are neither evolved nor suspected binaries, and only those with periods classified as Category 1 (unambiguous). The rotational isochrones from the Ba10 model are also displayed for ages of 3.0, 2.5, and 1.6 Gyr using blue, gray and yellow corridors respectively. (See text for details.) The central black lines within each corridor correspond to $P_0 = 1.1$ d for the relevant age.*

We also find a group of Ruprecht 147 stars located in the late-G and early-K region [$(G_{\rm BP} - G_{\rm RP})_0 \sim 0.85 - 1.1$]. These appear to overlap well with their counterparts in NGC 6819, and to be consistent with a rotational isochrone for 2.5 Gyr, the age of Ruprecht 147 (e.g., Cu13; see also Torres et al. (2018), which uses eclipsing binaries and PARSEC models to propose a 2.7 Gyr age.). However, they are clearly inconsistent with an older 3.0 Gyr rotational isochrone. In fact, we consider this region of the Ruprecht 147 color-period diagram to be populated well enough to have conclusive significance.

We note that there is one outlier rotation period at 12.5 d. We have been unable to convince ourselves that we have grossly underestimated its rotation period, or that we have only identified a period submultiple and that it should instead be recorded as a star with 25 d period (cf. the

light curve of EPIC 219388192 in Fig. 7.6 in the Appendix). The star has been reported to be a (gravitationally bound) wide binary composed of G and M dwarfs, with the primary G star itself having an eclipsing brown dwarf companion with a 5.3 d orbital period (Curtis et al. 2016; Nowak et al. 2017; Beatty et al. 2018), whose transits are visible in our corrected lightcurve (c.f. appendix Fig. 7.6). This configuration could be responsible for the unexpected and discrepant rotational period. We exclude it from further consideration for this reason.

Finally, of the 8 late-K and M-type stars that show a decidedly horizontal rotation period distribution, there is one star (EPIC 21963422, c.f. its light curve in Fig. 7.6) with a significantly longer period of 27 d [$(G_{\rm BP}-G_{\rm RP})_0 = 1.29$; SpT K4V] that appears to follow the model predictions for 2.5 Gyr, but appears as a long-period outlier, as compared with neighboring data points. No peculiarities about this star are known at the time of this writing that may contribute to its atypical (compared the rest of Ruprecht 147) rotation. Given that this star is the only long period one in the present sample, we may not assign too much significance to its apparent agreement with the model predictions.

2.6.2 Other models

We now compare the measured distribution of rotation periods in Ruprecht 147 and NGC 6819 to other models of stellar spin down proposed over the last decade. A careful inter-comparison between these has been published in Fr20, in connection with measured rotation periods in the ZAMS open cluster NGC 2516. Consequently, the description here will be abbreviated.

2.6.2a The Spada & Lanzafame (2020) model

The Spada & Lanzafame (2020, SL20 hereafter) isochrones incorporate a two zone model of internal stellar coupling in addition to implementing the (2-parameter) braking formulation of Ba10. The additional parameter is the index of the power-law describing the mass dependence of the coupling. The angular momentum previously stored in the radiative core of the star is released to the surface convection zone on the related mass-dependent timescale, delaying the spindown of the star's surface, and potentially even spinning it up briefly[23]. In principle, two additional parameters describe the initial period and effect of disk locking (Koenigl 1991) during the pre-main sequence phase; both lose relevance as the star gets older. Finally, it should be noted that the SL20 models are technically formulated only for the slow rotators, that is, the fast rotators are not directly addressed.

As can be seen in Fig. 2.12, in the region of the CPD that represents Sun-like and warmer stars, their model is essentially indistinguishable from the Ba10 one, as expected because of the identical braking formalism. However, for cooler regions in the mid-K to mid-M spectral range, the SL20 isochrone is able to resist the spindown seen in the Ba10 and other comparable models and clearly comes the closest to describing the Ruprecht 147 rotation period data, including an increase in the rotation periods of mid-M stars. We presume that a small adjustment in the coupling parameter could push the models closer to the Ruprecht 147 data points, but we are not in a position to speculate whether such a change would also be compatible with the rotation period distributions of younger open clusters.

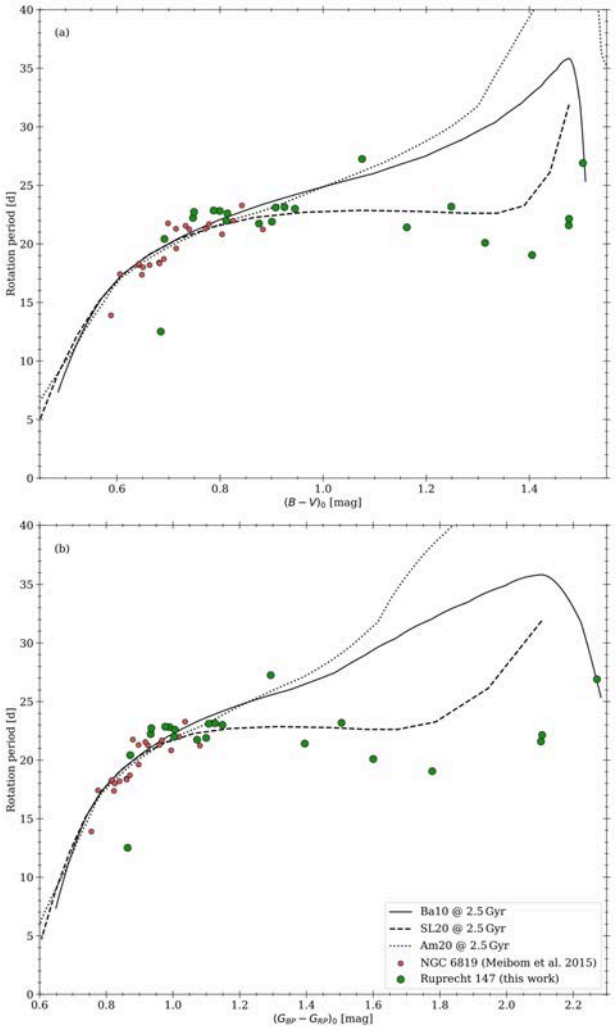

Figure 2.12: *Comparison between the rotation period distributions in Ruprecht 147 (green) and NGC 6819 (red) and rotational isochrones for 2.5 Gyr from Amard et al. (2019, dotted), Barnes (2010, solid), and Spada & Lanzafame (2020, dashed). The Spada & Lanzafame (2020) models come closest to the measured Ruprecht 147 rotation periods in the mid-K to mid-M region, with a relatively flat morphology in the K star region and an upturn among the early M stars.*

2.6.2b The Amard et al. (2019) model

The Amard et al. (2019, Am19 hereafter) model has the largest number of degrees of freedom of the major models, in principle allowing for the most faithful reproduction of the data. It implements the spindown formulation of the Matt et al. (2015) model, itself a modified version of the

[23] Models invoking decoupling (and subsequent recoupling) have been a steady presence in angular momentum evolution, most notably MacGregor & Brenner (1991). We find this version to be more convincing than prior ones, partly because the time-scale for recoupling is transparently stated.

Ba10 model with more degrees of freedom, onto the stellar models of the Geneva-Montpelier group. However, the threshold for magnetic saturation has been modified from that in Matt et al. (2015) and certain other choices have been made made both in the main sequence and pre-main sequence phases[24]. It should also be noted that this model provides a competitive description of the ZAMS rotation period data, as shown in Fr20, even if all features of those data are not reproduced.

As can be seen in Fig. 2.12, the Am19 isochrone for 2.5 Gyr is located in approximately the same region as both the observations and the other models for Sun-like and warmer stars. However, it begins to diverge from the data at spectral type K0V and is significantly above the Ruprecht 147 rotation periods for later spectral types. The spindown formulation of this model is clearly over-aggressive in the K-M region, even more so than the Ba10 model. We note that the isochrones published by Am19 incorporate the slightly older color transformation for *Gaia* colors from Evans et al. (2018). This is not to blame here, because we instead recalculate these for $G_{\rm BP} - G_{\rm RP}$ from $B-V$ using our own transformation, as described above. Finally, it should be mentioned that we do not display separable models, such as those of Barnes (2007), Mamajek & Hillenbrand (2008), or Angus et al. (2020) for the detailed reasons given before. In particular, the fact that all of these lead to a mass dependence that does not change with age is a serious challenge in view of the observed time-varying morphology of open cluster CPDs.

2.6.3 Implications for the modeling of rotating stars

In summary, we find that the new Ruprecht 147 rotation periods create significant challenges for theoretical rotational evolution models in the K-M spectral region that were not anticipated when only warmer middle-aged stars were measured in NGC 6819 (Meibom et al. 2015) and M 67 (Barnes et al. 2016b). Rotational isochrones for 2.5 Gyr from the models of Ba10 and Am19 which are in reasonable agreement with the data for stars bluer than early K-type stars appear to predict significantly longer rotation periods than actually measured in Ruprecht 147 among the mid-K to M stars. The isochrones of SL20, which include a parameterized 2-zone model with associated angular momentum exchange, appear to perform considerably better (see Fig. 2.13) with respect to the K-M stars in both Ruprecht 147 and prior measurements. We also show their isochrones for younger and older ages in Fig. 2.13, so that the overall behavior of these models vis-a-vis other cluster measurements can be appreciated. It is possible that small adjustments to the parameters in their model might result in an even closer match to the observations.

More generally, our work here appears to confirm the existence of a single surface in rotation period-mass-age space that is occupied by "effectively single" non-pathological rotating stars of roughly solar metallicity. The warmer (Sun-like) part of this surface appears to be asymptotically Skumanich-like in its behavior against age, although with a strong mass dependence, and can likely be modeled reasonably using just two or even one mass-dependent timescales, depending on the degree of fidelity desired, and whether or not fast rotators are included in the description. The cooler (K-M) part of this surface appears to exhibit more complex behavior and seems to require an additional (strongly) mass-dependent timescale to model it. Describing the spindown of cool stars on the main sequence therefore seems to require the invocation of three distinct physical processes.

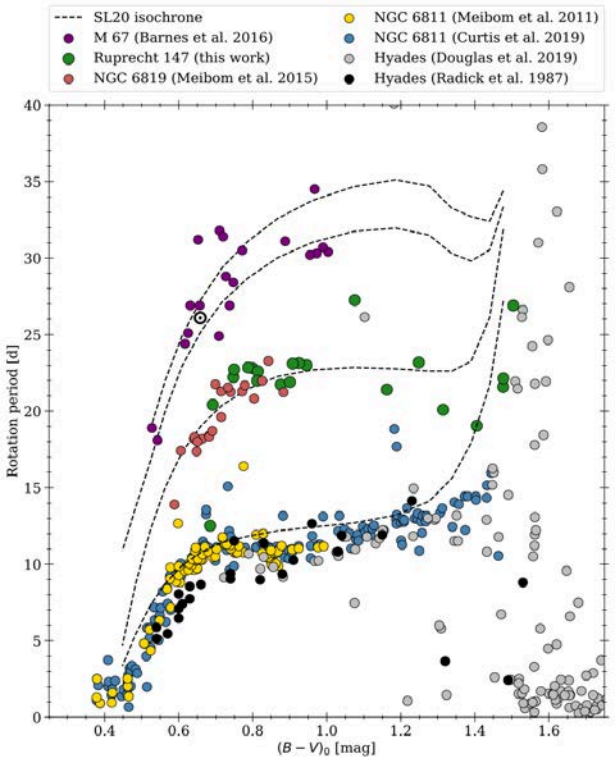

Figure 2.13: *Color-Period Diagram displaying the same cluster rotation period data as Fig. 2.10, compared with rotational isochrones (dashed lines) rotational isochrones from Spada & Lanzafame (2020, SL20) for younger- and older ages. The ages, from top to bottom, correspond to those of the Sun (4.57 Gyr, shown with its usual symbol), M 67 (4.0 Gyr), NGC 6819 & Ruprecht 147 (both 2.5 Gyr), NGC 6811 (1.0 Gyr), and the Hyades (600 Myr).*

2.7 Conclusions

We have studied space-based photometric data from Campaign 7 of the *Kepler*/*K2* satellite for the 2.5 Gyr-old open cluster Ruprecht 147 in combination with prior membership work, to examine the calibration of gyrochronology for middle age stars, especially in the previously unexplored $K - M$ star region. We have identified 102 cluster member stars that were observed by *K2*. That target selection appears to be biased towards solar type stars, rather than being broadly representative of the entire Ruprecht 147 population. There are also certain technical issues with the nature of the *Kepler*/*K2* light curves

[24] See Fr20 for a summary.

and the Campaign 7 data from *K2* that require additional efforts, as compared with those from the original *Kepler* field. Nevertheless, we have identified periodic behavior for 32 of these objects that can plausibly be associated with star spot modulation.

Twenty one of these periods correspond to single stars and are unambiguous enough for a comparison with both previous open cluster studies and widely used rotational evolution models. We find that our results connect reasonably to prior measurements by Meibom et al. (2015) in NGC 6819, a cluster of very similar age, verifying the behavior of 2.5 – 3 Gyr rotating stars. Our data extend the measured rotation period sample to the previously unexplored K- and M-star region. We find that the Ruprecht 147 rotation periods are compatible with the idea that it, M 67 (4 Gyr), NGC 6819 (2.5 Gyr), NGC 6811 (1 Gyr), and the Hyades (625 Myr) clusters all lie on a single surface in color-rotation period-age space. This surface apparently extends to the ZAMS, where the ($\sim 130-150$ Myr-old) Pleiades, NGC 2516, M 35, M 50, and Blanco 1 open clusters appear to have identical rotation period distributions (Fritzewski et al. 2020). However, the Ruprecht 147 and NGC 6811 data for $K-M$ type stars suggest that it has a a revised shape as compared with the original form proposed by Barnes (2003) and succeeding models.

A comparison with the predictions of rotational evolution models shows that most models fail to predict the observed distribution of stars redder than spectral type K3. We find that the best current description of the spindown of stars beyond 1 Gyr is provided by the model of Spada & Lanzafame (2020), invoking a third mass-dependent timescale in addition to the two timescales in the model of Barnes & Kim (2010) and Barnes (2010). Consequently, it appears that models describing the rotational evolution of solar metallicity cool main sequence stars need to include three distinct physical processes if they are to account for the fast, slow, and low mass rotators observed in open clusters to date.

○ ○ ○

Appendix

The Appendix to this paper begins on page 99 as Appendix Sections A – D.

Acknowledgements

We are grateful to the referee, Gibor Basri, for a timely response and helpful suggestions to improve readability. We thank Jason L. Curtis for the provision of period data from his team's independent study prior to final publication, enabling the relevant comparison.

Part 3 – Paper II

New insights into the rotational evolution of near solar age stars from the open cluster M 67[†,‡]

***D. Gruner**, S. A. Barnes, and J. Weingrill*

Abstract

Gyrochronology allows the derivation of ages for cool main sequence stars from their observed rotation periods and masses, or a suitable proxy of the latter. It is increasingly well explored for FGK stars, but requires further measurements for older ages and K – M-type stars.

Recent work has shown that the behavior of stellar spindown differs significantly from prior expectations for late-type stars. We study the 4 Gyr-old benchmark open cluster M 67 to explore this behavior further.

We combined a *Gaia* DR3 sample with the *Kepler K2* superstamp of Campaign 5 around M 67 and created new light curves from aperture photometry. The light curves are subjected to an extensive correction process to remove instrumental systematics and trending, followed by period analysis to measure stellar rotation.

We identify periodic signals in 136 light curves, 47 of which are from the rotation of effectively single main-sequence stars that span from early-G to mid-M type. These results connect well to prior work on M 67 and extend it to much later spectral types.

We find that the rotation periods of single stars of age 4 Gyr define a tight relationship with color, ranging from spectral types F through M. The corresponding surface of rotation period against age and mass is therefore well-defined to an older age than was previously known. However, the deviations from prior expectations of the stellar spindown behavior are even more pronounced at 4 Gyr. The binary cluster members do not follow the single star relationship. The majority are widely scattered below the single star sequence. Consequently, they do not seem to be suitable for gyrochronology at present.

[†] *The contents of this chapter have been published in Astronomy and Astrophysics, Volume 672, id.A159*

[‡] *Table 7.8 is available in electronic form at the CDS.*

3.1 Introduction

A key issue in cool star science is to understand the extent to which the rotation rate of a star can be used to infer its age. While empirical data are available in a series of young open clusters, they are lacking for cooler spectral types in older clusters. Here we confirm related prior results and extend the empirical knowledge of this extent to K- and M-type stars of age 4 Gyr by presenting measured rotation periods in the open cluster M 67.

The fact that the rotation rate of a star depends on its age was originally proposed by Skumanich (1972) following $v \sin i$ measurements for stars of solar mass in open clusters. Older stars were found to rotate slower than younger ones, that means the stars spin down as they age, approximately as a power law. This relationship was later extended to other late-type stars by Barnes (2003) who showed the existence of a mass-dependence of the spindown rate and suggested that the age of a star can be inferred from its measured rotation period and mass (or a suitable proxy of the latter, such as color). This marks the onset of what is now known as gyrochronology.

Using stellar rotation for age estimates of late-type main sequence stars opens up new possibilities in age dating for stars whose classical parameters change only very little over the course of billions of years (e.g., temperature and luminosity), which can only be used reliably in young stars (e.g., Li abundance), or which change as long-term averages but vary significantly on short timescales (e.g., activity). However, to be able to use gyrochronology reliably, it needs to be first established if and how stellar rotation changes systematically with age for stars of different masses. Now, if the rotation periods of stars change systematically with age, then regardless of the details of the dependencies on stellar mass and age, appropriate measurements of open cluster stars of known ages can be used to set up a series of "mileposts" at suitable ages to derive stellar ages from their measured rotation periods. This has led to the exploration of accessible open clusters of differing ages to construct the sequence of spindown empirically as a function of mass and age. Open clusters are the preferred means to explore the spindown as they provide sets of stars of different masses with well-established ages and metallicities.

Fortunately, the relationship has so far been found to be single-valued as a function of mass at least for clusters older than the Hyades (∼600 Myr). Unfortunately, only a small number of such clusters are readily available. Outstanding among them is M 67; with its sun-like age of 4 Gyr, it is the oldest cluster explored in this regard today. However, only two distinct groups have been measured reliably to date: F- and G-type stars by Barnes et al. (2016b) and mid to late M-type stars by Dungee et al. (2022). Here we present new measurements for stars spanning from early-G to early-M types, overlapping with the prior work and bridging the gap between them. Crucially, we find that the rotation periods of single cluster members in M 67 continue to define a single-valued relationship with stellar mass at this age. Consequently, we claim that rotation is usable as an age indicator even though its mass and age dependencies are likely more complex than was thought earlier.

The systematic exploration of rotation in stellar open clusters using timeseries photometry can be traced back to van Leeuwen & Alphenaar (1982, see also van Leeuwen et al. (1987)) in the Pleiades (∼125 Myr) and Radick et al. (1987) in the Hyades. However, $v \sin i$ measurements were typical at that time and, despite the ambiguity introduced by the unknown inclination i, showed traces of the patterns we observe today (e.g., Stauffer et al. 1984; Soderblom et al. 1993a; Queloz et al. 1998). Subsequently, CCD photometry from ground-based facilities and, later, the onset of space-based CCD photometry (mostly thanks to the *Kepler* mission) has allowed large-scale studies of various readily available open clusters. Photometric rotation periods, that means measuring the periodic brightness variations induced by activity features traversing the stellar disk, remove the ambiguity of unknown inclination.

Numerous ground-based, and more recently, space-based photometric studies have together constructed a set of mileposts with open clusters, including the Pleiades (125 Myr, van Leeuwen et al. (1987), revisited by Rebull et al. 2016), the Hyades (650 Myr, Radick et al. (1987), revisited by Douglas et al. 2019), Praesepe (700 Myr, Agüeros et al. 2011), NGC 6811 (1 Gyr, Meibom et al. 2011a; Curtis et al. 2019), NGC 6819 (2.5 Gyr, Meibom et al. 2015), and Ruprecht 147 (2.7 Gyr, Gruner & Barnes 2020; Curtis et al. 2020). Fritzewski et al. (2020) have also recently shown that the distribution of stellar rotation periods in the 125 Myr-old clusters NGC 2516, Pleiades, M 35 (Meibom et al. 2009), M 50 (Irwin et al. 2009), and Blanco 1 (Cargile et al. 2014) are indistinguishable. For additional work, and especially for rotation in the wider context of stellar activity, readers may refer to chapter 5 in Basri (2021).

Recent work has advanced to large field star samples (e.g., Reinhold & Hekker 2020; David et al. 2022; Distefano et al. 2022) which provide a much more extensive parameter space than the clusters alone, especially with respect to metallicity but lack the definitive nature of clusters to allow their usage for calibration. Furthermore, especially concerning slower rotating stars, the detection and identification of accurate stellar rotation periods is somewhat problematical. As Tan & Basri (2020, see also Basri & Nguyen (2018)) have pointed out, a significant fraction ($\approx 10\,\%$) of the widely used McQuillan et al. (2014) sample is likely listed with only half the actual period due to double-dipping. Field stars require more rigorous and extensive vetting than cluster stars, which have uniform metallicity, age, and distances among them. If not, unaccounted non-solar metallicities, binarity, or an evolutionary state even marginally past the main sequence are prone to lead to flawed conclusions. Given those shortcomings, open clusters remain the primary calibrators for the evolution of stellar rotation, and provide the main motivation for this work.

M 67, also known as NGC 2682, has long been of great interest because it is one of the oldest open clusters known,

Table 3.1: *Basic properties of M 67*

Parameter		Value	Ref.
Ra	[h min s]	08 51 18	1
Dec	[° ′ ″]	+11 48 00	1
$\mu_{\rm Ra}$	[mas/yr]	-10.97	2
$\mu_{\rm Dec}$	[mas/yr]	-2.94	2
$v_{\rm rad}$	[km/s]	33.92	3
Age t	[Gyr]	4.0	4
Parallax ϖ	[mas]	1.1325	1
Distance d	[pc]	883	from parallax
Distance mod.	[mag]	9.6	from distance
$E(B-V)$	[mag]	0.04	5
A_V	[mag]	0.124	from $E(B-V)$
[Fe/H]		0.028	6

References. *(1) Cantat-Gaudin & Anders (2020); (2) Gaia Collaboration et al. (2018a); (3) Carrera et al. (2019); (4) Bellini et al. (2010): (5) Taylor (2007); (6) Casamiquela et al. (2019).*

has an age near that of the sun and is located close enough to allow extensive study. In Table 3.1, we give an overview of some of the fundamental parameters of M 67. Apart from the work on stellar rotation in M 67 by Barnes et al. (2016b) and Dungee et al. (2022) there have been the studies of Gonzalez (2016b,a) and Esselstein (2018) whose findings challenge not only the prior work on M 67 but also those for other clusters and one bedrock principle of gyrochronology: the single-valued nature of the spindown relation. We also investigate and make some sense of their findings below.

This paper is structured in the following way. In Sect. 3.2, we describe the observations that this work is based on, as well as the stellar content of the *Kepler K2* superstamp. This section includes a membership analysis based on GDR3 data which is detailed in Appendix E. Section 3.3 addresses the creation of lightcurves from the *K2* data. The section gives a short overview of the steps carried out while Appendix F describes all the details regarding the difficulties of *K2* data and our ways of overcoming them. The lightcurves thus constructed are subjected to a period analysis which is described in Sect. 3.3.2. The results of the analysis are presented in Sect. 3.4. There, we construct a Color-period diagram (CPD) for M 67 after scrutinizing each and every star in the sample. We then go on to discuss our findings and their implications in the contexts of prior work on open cluster and the modeling of rotational evolution in Sect. 3.5 before we finish with some conclusions in Sect. 3.6.

3.2 Observational data

In this section we describe the photometric data we use throughout this work: the *Kepler K2* Campaign 05 superstamp. We obtain the stellar content of the field of view from the *Gaia* catalogs and carry out a membership analysis. The cluster sample constructed is then used to reconfirm the age of M 67 and estimate reddening parameters in different colors.

3.2.1 The K2 superstamp

Our goal is to explore the cluster center of M 67 to its fullest. Therefore, we ignore the few *Kepler K2* light curves supplied by the mission itself, and construct our own based on a new, more extensive target list. This allows us to use the richness of the cluster center without being bound by the preselection of targets in the *K2* program. We show in Appendix F.9 the meager extent of the original *K2* program, especially when it comes to the superstamp. However, this also means that we now have to solve by ourselves the problems addressed by the mission itself when it provided the *K2* light curves.

After the conclusion of its primary mission, the *Kepler* telescope started its *K2* program. Between 2014 and 2019, the telescope was pointed at 19 different fields along the ecliptic for approximately 80 d each (denoted as campaigns, C## hereafter). Prior to and during this long observation run several parts of the telescope ceased to function. However, *Kepler* was able to continue its mission until it ultimately ran out of coolant in 2019, long after its originally designated lifetime. Some of the defects make *K2* data problematic to use if not properly addressed.

M 67 was in the field of view during three of those campaigns, namely C05, C16, and C18. Special attention was paid to the cluster during C05 and data for an extended region around the cluster center were collected. This *superstamp* covers the central part of the cluster (cf. Fig. 3.1) from April to July in 2015 and is the basis for the present work. The coverage during C16 (Dec. 2017 to Feb. 2018) and C18 (May 2018 to Jul. 2018) may provide additional opportunities for future explorations.

During C05, *Kepler* obtained 3663 images in its slow-cadence mode. These span a baseline of approximately 70 d. Because of data transmission limitations, *Kepler* did not transmit full frame images, but only certain preselected regions. These are stored and made available as target pixel files (TPF). For C05, TPFs were selected such that they cover a continuous region around the center of M 67. Cody et al. (2018) used those TPFs to create a continous region, the *superstamp*, around the cluster, measuring 400 by 400 pixels in size ($\approx 0.5^\circ \times 0.5^\circ$). The coverage of the cluster region in the superstamp and its location in the *Kepler* FOV are illustrated in Fig. 3.1. Additionally, they created a new, time dependent astrometric calibration for each individual image, overwriting the default, time independent *K2* pipeline results to account for the jitter of the targets. We note that this astrometric solution turns out to be both very good and useful, and it is of fundamental importance for this work. We note further that Cody et al. (2018) omitted a small number of cadences, resulting in only 3620 superstamp images for M 67.

3.2.2 Stellar content of the superstamp

The superstamp covers a region of about $0.25\,\mathrm{deg}^2$, aligned with the cluster center. The most consistent and extensive catalogs for any random region of the sky are from the *Gaia* mission and thus we use *Gaia* DR3 (Gaia Collaboration 2022, GDR3 hereafter) as a foundation for

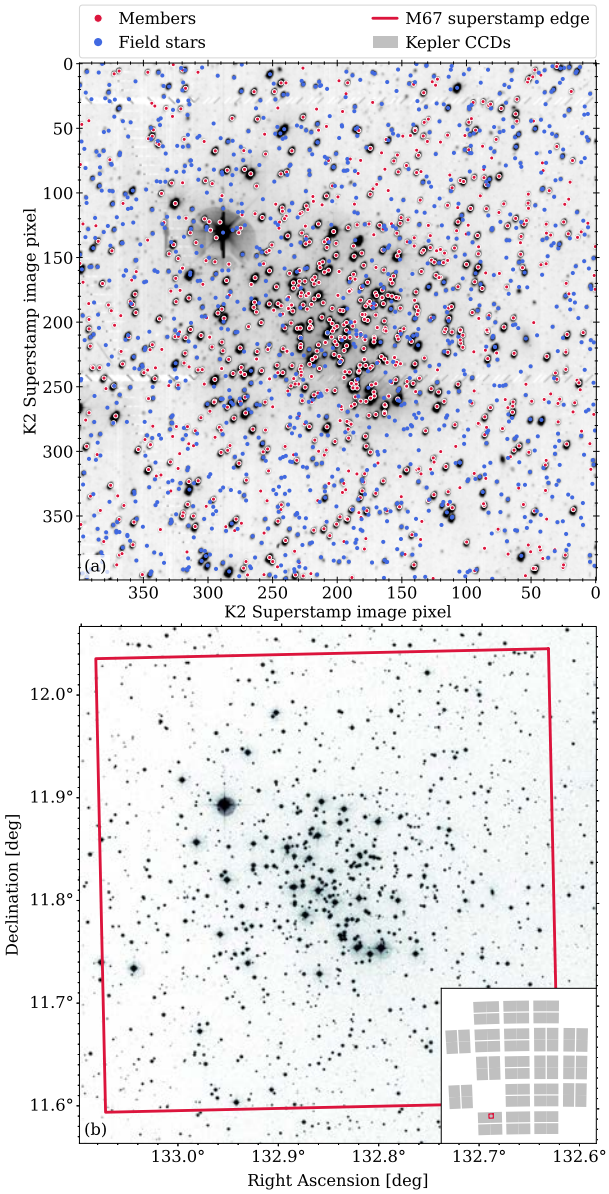

Figure 3.1: *Overview of the* K2 *C05 superstamp coverage of M67. The upper panel shows one superstamp image on a logarithmic gray-scale. Stars recognized by GDR3 are overplotted, color-coded according to our membership evaluation (see Sect. 3.2.2 and Appendix E for details). The lower panel shows a DSS2 (red channel) image of the same region. The extent of the superstamp is indicated in red. The small inset in the corner shows the location of the superstamp in the Kepler FOV C05. Both panels are shown such that their orientations are as similar as possible (see coordinates in panel b).*

our work. We obtain a subset of GDR3 data for the region covered by the superstamp. This subset contains about 2000 stars, but the *K2* mission only provided light curves for 96 of these. Due to the motion of the telescope, individual targets on the edges may shift in and out of the field of view. Here, we did not limit the stars by brightness or any other parameter. However, we note that, as expected, the parameter coverage of the individual stars varies widely in the sample, generally becoming more sparse toward the faint end. We note further that the spatial resolution of *Gaia* greatly exceeds that of *Kepler*[1], while on the other hand *Gaia* omits certain significantly brighter sources[2]. This requires us to carefully assess which star's light we are analyzing.

M 67 is obvious in the field-of-view (FOV) sample in both photometry and astrometry (see Fig. 3.2). In a color-dependent sense, the brightest stars in the field belong to M 67, with the exception of a few very bright foreground stars. We complement the GDR3 sample with data from the *Two-micron All Sky Survey* (2MASS, Cutri et al. 2003; Skrutskie et al. 2006), *US Naval Observatory B catalog* (USNO, Monet et al. 2003), *Guide Star Catalog 2.4.2* (GSC, Lasker et al. 2008), and the *Ecliptic Plane Input Catalog* (EPIC, Huber et al. 2017, via their 2MASS IDs, where available) and the SIMBAD database[3]. This cross-match provides us with multiband photometry and radial velocity information for a large number of stars. Most of the radial velocity measurements are from groundbased surveys by Geller et al. (2015, 2021) and Donor et al. (2018). We note that these surveys prioritized cluster stars and, as such, the availability of radial velocities is strongly biased toward member stars and is brightness limited, with the cutoff being approximately $G = 17$ mag. We supplement those radial velocities with additional ones provided in GDR3. Based on this, admittedly heterogeneously available information, we designate each star in the field either as a *member*, or as *field star*. Details about this designation are described in Appendix E. Figure 3.3 depicts the resulting cluster sample which amounts to 971 *members* and 1042 *field stars*. Around 80 % of the *members* can be assumed to be main sequence stars, spanning a brightness range from $G = 13$ mag down to $G = 21$ mag.

We also include a designation for stars displaying signs of binarity. Those are derived either from the extensive information present in the SIMBAD archive or from a star's position in the CMD indicating a photometric binary. The former leads to a star being assigned binary status if it is listed in SIMBAD as an eclipsing binary (`EB*`), spectroscopic binary (`SB*`), or cataclysmic variable (`RSCVn` or `CataclyV`). Their designations are based on various catalogs and studies, too numerous to be listed here, do not include all actual binaries in the sample, or could misidentify a single star as a binary. However, judging from the overall picture that emerges, we find this designation to be relatively reliable and consistent. An identification of binaries is crucial because multiplicity can lead to a number of issues, for example, tidal interactions or mass exchange may change the stellar angular momentum and as such disqualify a star for our purposes. Those stars need to be discarded from our final sample.

Henceforth, we will use $G - G_{\rm RP}$ as the color parameter for the stars. This has the advantage that it is essentially independent of *Gaia* $G_{\rm BP}$, which is either very uncertain or unavailable for the faint and red stars. The disadvantage of this choice is the unavailability of a mea-

[1] *Kepler* had 4″pixels.

[2] e.g., those with problematic astrometric solutions, i.e., very active stars or binaries.

[3] `simbad.u-strasbg.fr/simbad`

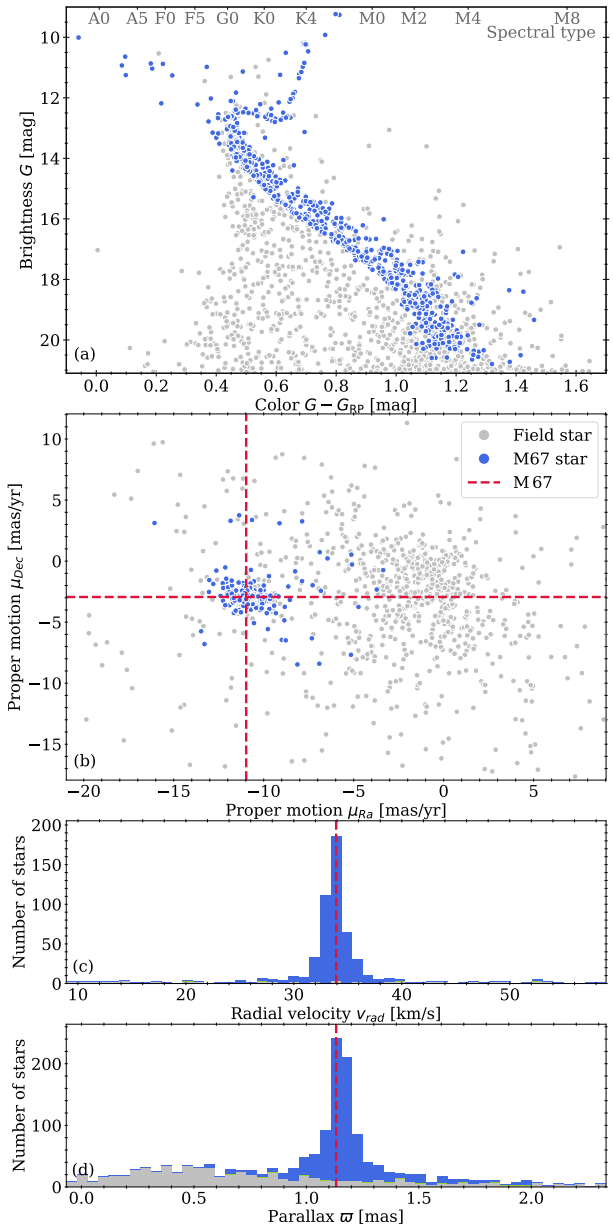

Figure 3.2: *Overview of GDR3 stars in the field of view and their M 67 membership status (following Sect. 3.2.2 and Appendix E). In all panels, blue stars denote* members *while non-members are gray. Panel (a) shows a color-magnitude diagram in* Gaia $G - G_{RP}$ *color, panel (b) the proper motions, panel (c) a histogram of radial velocities, and panel (d) a histogram of the stellar parallax. Dashed red lines indicate the position of M 67.*

sured reddening parameter in this color. We will address this issue below. Plots in other colors (such as $B - V$, $V - K$, or $G_{BP} - G_{RP}$) that are potentially useful to the community are provided either parallel to the main plot or as supplementary plots in Appendix G.3. We will not use the individual parallaxes of the stars to obtain absolute magnitudes. Stellar photometry is much better constrained and more widely available. As such, for a subsequent isochrone fit to the cluster, we will apply the cluster parallax (and reddening, cf. Table. 3.1) to the isochrone to match the cluster data instead.

3.2.3 Color magnitude diagram of M 67

To reconfirm the age of the cluster and to determine the $E(G - G_{RP})$ reddening and extinction A_G, we proceed with an isochrone fit to the cluster sample (cf. Fig. 3.3). We opt for an empirical determination of $E(G - G_{RP})$ for M 67 based on the offset observed between a distance-corrected isochrone and the observed cluster sample. We work with the isochrones from the Padova and Trieste Stellar Evolutionary Code (PARSEC[4] Bressan et al. 2012; Chen et al. 2014, 2015). In principle, the isochrone fit has four free parameters: the cluster metallicity, cluster age, reddening, and extinction. However, we can constrain some of them. The cluster metallicity has been measured repeatedly in the past, with values ranging from [Fe/H] $= -0.01$ to [Fe/H] $= 0.03$. Thus M 67 is essentially of solar metalicity. We adopt [Fe/H] $= 0.03$ (Netopil et al. 2016) and note that changes within the range described above do not change the result below in a significant way.

Following the method described in Gruner & Barnes (2020), we use the coefficients obtained by Casagrande & VandenBerg (2018) for the relation between the extinction in *Gaia* $G_{BP} - G_{RP}$ and Johnson $B - V$ colors. We adopt $E(B-V) = 0.04$ mag[5] (Taylor 2007) and calculate

$$E(G_{BP} - G_{RP}) = 1.339 \cdot E(B-V) = 0.054\,\text{mag} \quad (3.1)$$

and combine it with the relation that we already used for Ruprecht 147 (Gruner & Barnes 2020) for extinction

$$A_G = 2.0 \cdot E(G_{BP} - G_{RP}) = 0.107\,\text{mag}. \quad (3.2)$$

With A_G constrained, we adjust $E(G - G_{RP})$ to best reproduce the observed cluster sequence and find

$$E(G - G_{RP}) = 0.03 \pm 0.005\,\text{mag}. \quad (3.3)$$

This fit uses the the distance modulus listed in Table 3.1. As a byproduct of this calculation, we have obtained $E(G_{BP} - G_{RP})$. We note that this value also produces a consistent fit between the isochrone and the cluster in $G_{BP} - G_{RP}$ (see panel (b) of Fig. 3.3). Below, we also provide $V - K$ as a *Gaia*-independent color that omits the issues of blue bands. For the corresponding reddening, we use the prescription by Martin & Whittet (1990) to obtain

$$E(V - K) = \frac{A_V}{1.1} = \frac{3.1 \cdot E(B-V)}{1.1} = 0.11\,\text{mag}. \quad (3.4)$$

M 67 is generally believed to be about 4.0 Gyr old, somewhat younger than the sun. In the process of fitting isochrones to the cluster sequence, we notice that the isochrones suggest a slightly younger age for the cluster, namely $t = 3.6$ Gyr. This is mostly caused by the shape of the turn-off point and the subgiant sequence (see zoomed plots in Fig. 3.3). However, a 4 Gyr PARSEC isochrone still provides a reasonably good fit to the cluster stars.After all, isochrone fitting is not the purpose of this paper. We note that in no color do the isochrones reproduce the faint red

[4] stev.oapd.inaf.it/cgi-bin/cmd
[5] $A_V = 0.124$ mag

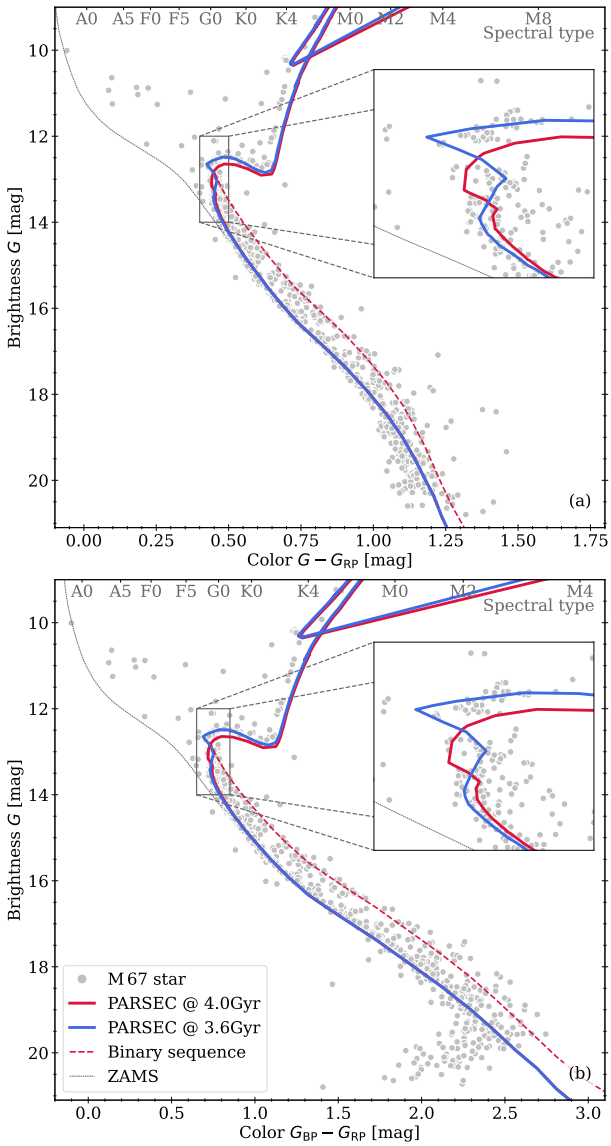

Figure 3.3: *Isochrone fit to the identified cluster members in two different* Gaia *colors. The PARSEC isochrone G-band magnitude is adjusted for the parallax ϖ and extinction A_G using Eq.* (3.2)*. The PARSEC $G_{\rm BP} - G_{\rm RP}$ color is reddened by $E(G_{\rm BP} - G_{\rm RP})$ from Eq.* (3.1)*. The dashed line indicates the nominal position of the equal-mass binary sequence (main sequence stars only). An alternative version using $B - V$ and $V - K$ is shown in Fig 7.25.*

end of the main sequence completely satisfactorily. We note further that the observed red giant branch is slightly bluer than the isochrone prediction. This seems to point to an underlying problem in the isochrones (or the input physics) rather than the photometry as it is also visible in other, non-*Gaia* colors (cf. Fig. 7.25).

3.3 Lightcurves and rotation periods from the *K2* superstamp

In this section we describe the creation and correction of stellar light curves from the *K2* superstamp. We lay out briefly the problems inherent to *K2* data and our approach to dealing with them. A more thorough explanation of all the technical details is provided in Appendix F.

During the *K2* mission, some vital parts of the *Kepler* telescope became dysfunctional. The loss of certain parts of the detector (see missing CCDs in panel (b) inset in Fig. 3.1) does not affect us. However, the well known pointing problems of the telescope do. Essentially, the telescope was in a constant state of drift throughout the observations, causing the stars to move slowly across the detector. This drift was periodically corrected (i.e., at $\approx 6\,$h intervals) by firing the telescope's thrusters (Van Cleve et al. 2016). Consequently, stars move across the detector during the run. The movement is small for individual exposures and as a result there are no noticeable star trails on the images. Between the thruster firings, however, a star moves up to two pixels ($\lesssim 8''$) across the detector. There are also significant sensitivity variations between the pixels and within the individual pixel. This means that due to the changed positions of an otherwise constant star on the detector, the recorded flux varies from image to image. Those changes, while systematic, are unique for each pixel and its environment. As such, there is no general way to correct for those systematics in a simple, wholesale manner. However, those variations are rather fast and there have been approaches to correct those systematic effects (e.g., K2SC and EVEREST programs by Aigrain et al. 2016; Luger et al. 2016, respectively) with varying levels of success and usability of the resulting corrected light curves for various purposes.

Unfortunately, none of these prior light curves are very well suited for our purpose. The main reason is their availability for only a limited number of targets. K2SC and EVEREST (and essentially all other works in this regard) operate on the EPIC catalog and the sample of stars *observed* by *Kepler*[6]. The list of observed stars originates from the original proposals that shaped the *Kepler K2* mission. However, for the superstamp there are only 96 individually designated targets with light curves whereas the field contains more than 2000 stellar sources. Therefore, we create our own light curves, directly based on the superstamp FFI and a list of sources obtained from *Gaia* DR3 rather than the EPIC catalog. This means that we have to perform the photometry and corrections thereof from scratch. Below, we lay out the principal ideas and steps that we employ to create the light curves we subsequently investigate for rotation signals.

3.3.1 Lightcurve extraction and correction

We have constructed a procedure aiming to extract light curves and to remove the artificial variations introduced by the effects mentioned above. The plan is to create an empirical model that captures the systematic position dependence of the flux in order to remove it. The position dependence turns out to be of a very complex nature and requires special attention to the individual stars. As such, it is rather labor intensive and requires iteration between different steps until the best result is achieved. Ultimately, we are able to create light curves that are sufficiently free of systematics for a large number of stars.

In Appendix F, we provide a detailed explanation of the

[6] see *Kflag* column in the EPIC catalog

extraction and correction process applied to the data in order to create the light curves. There we include all the technical details and illustrate them on a sample star. Here, we only describe the general steps taken.

First, we introduce a naming convention that we will use throughout this work. The *total flux variation* of an extracted light curve for a star is the combination of three things. First there is the *intrinsic astrophysical variability* of the star, which is the variation we are actually seeking. This flux is modified by the motion of the star across the detector in combination with the detailed pixel sensitivity. We will refer to the changes caused by this effect as the *instrumental systematics*. Superimposed on those are quasi-systematic, long-term patterns in the data which are common between similar stars, and which we will refer to as *trending* or *trends*. We illustrate the correction steps for an example star in Fig. 3.4.

We define an aperture mask for each star on the superstamp and create the raw light curve by simply summing up the enclosed flux. The aperture mask is defined manually and adjusted individually for each star to provide the best (i.e., cleanest, low noise, best systematics removal) light curve possible. Depending on the star being considered, the instrumental systematics appear to introduce flux variations up to a few tenths of a magnitude (cf. panel (a) of Fig.3.4). We correlate the flux with positional changes of the star on the detector. The time-dependent position is obtained from the world coordinate system (WCS[7], Greisen & Calabretta 2002) which is part of the superstamp FFI data for each individual image and was created by Cody et al. (2018). We proceed to model this behavior (flux as a function of position) with a fifth-order polynomial in order to remove it. Here, we also need to handle jumps in the data that do not allow us to process the light curve as a whole but only in chunks as described in Appendix F. This is probably the most intricate step and provides us with a set of light curves *largely* free of the instrumental systematics (cf. panel (b) of Fig.3.4).

The processed light curves still contain *trending* at this point, which we then correct using Principal Component Analysis (PCA). For this, we select a subsample which excludes all stars with obvious intrinsic variability. For any given star that is to be corrected we select all similar stars (in terms of brightness and position) from this subset as the basis for the PCA. This procedure needs such selectivity as there are significant differences between the stars in the trends with respect to those parameters. And with an 80 d light curve, expected rotation periods of 20 – 30 d and trends of similar length, there is a limited time baseline available for the light curve to express those variabilities. Degeneracy between them is a real issue and it again requires attention to the individual stars to identify. From the individually tailored PCA basis we calculate a correction based on two components and apply it to the light curves. This results in the final light curve product (cf. panel (c) of Fig.3.4) that we provide and use in the subsequent period analysis.

This process is not successful for all stars; faint stars and

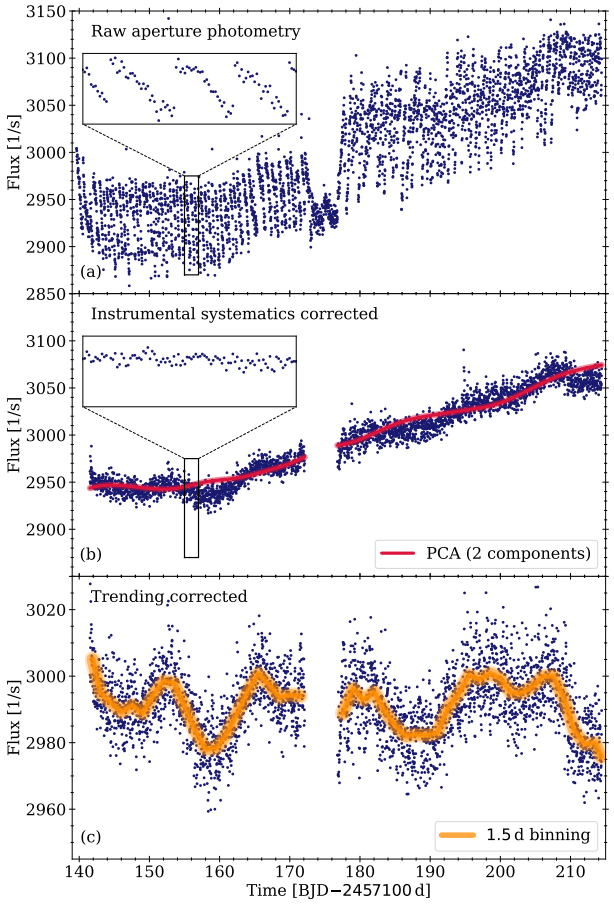

Figure 3.4: *Example of the light curve reduction process using* Gaia DR3 604971466769552128. *Panel (a) shows the raw light curve (blue dots), Panel (b) shows an intermediate light curve after the systematics correction (blue dots) together with the PCA correction (red) that is applied to the create the final reduced light curve that is shown in panel (c). The orange line in panel (c) shows the reduced light curve with 1.5 d binning to highlight the now visible intrinsic stellar variability. The insets in (a) and (b) zoom in on a 2 d span of the light curve. The drift-induced flux changes and the jumps caused by the realignment of the telescope are readily visible in panel (a), while their disappearance can be seen in panel (b).*

those in particularly crowded areas cannot be processed satisfactorily. In fact, most light curves still show remnants of systematics and trends. However, those are now typically small compared with the stellar signal itself and as such more of a nuisance than a real stumbling block. We remove all stars for which we cannot obtain light curves of reasonable quality. This includes stars that are located in problematic areas on the detector, that is, those where large systematic effects impact groups or rows of pixels. Some of these regions are visible in the upper panel of Fig. 3.1 (horizontal and vertical structures, e.g., around $y = 245$). Our usage of aperture photometry, does not allow us to separate heavily blended sources. Furthermore, the correlation between location and flux cannot be adequately reproduced and removed for every star. This is especially true for stars which show very rapid intrinsic variability (i.e., variability similar to the systematics). We are also forced to remove the first 2 d of the light curves

[7] See also `fits.gsfc.nasa.gov/fits_wcs.html`

and a central part (172 – 178 d) as those simply defy any correction attempt with our approach.

The resulting light curves show a wide variety of signals in addition to the rotation signals we seek. We also identify pulsations and eclipsing binaries (some of them with secondary eclipses). Traces of the instrumental systematics remain for a number of stars; however, those are often minor compared with the observed intrinsic signal. We note that we do not (and cannot) attempt to extract and fine tune each and every star in the field of view. Each target apparently requires individual attention, from the design of the pixelmask to the evaluation of the resulting light curve. Given our science goal, we limit ourselves only to M 67 members, together with a sufficient number of non-members to provide a good basis for the PCA.

We also emphasize that the light curves we produce with this method are not intended to rival large scale correction endeavors such as Everest or K2sc. Our light curves are purpose-built, with assumptions made in the creation that are invalid for other purposes (e.g., astroseismology). However, we include a comparison between our results and light curves provided in the larger endeavors in Appendix F.9 to validate our results. We will provide all light curves of stars for which a signal was identified as part of the auxiliary data to this publication. Figure 7.28 displays the light curves for those 47 stars that are single M 67 main-sequence stars and where we were able to identify a periodic rotational signal.

3.3.2 Period analysis

For the period analysis, we continue with a hands-on approach for the individual light curves. Unlike the case of most ground-based data, space-based data are both well-sampled and, for the most part, equally sampled. Owing to that, a long-period signal can usually be identified by eye easily when present (cf. panel (a) in Fig. 3.5). Manual inspection also permits the identification of a periodic signal when spot evolution or remnants of systematics or trends are present. Automated algorithms often struggle or fail outright in such cases. However, we subject all light curves to an array of algorithms to verify and quantify a generally obvious signal (panel (b) in the figure). We run period finding algorithms employing a Lomb-Scargle (LSC, Scargle 1982) periodogram[8], a Clean analysis (CA, Roberts et al. 1987), and phase dispersion minimization (PDM, Stellingwerf 1978).

Whenever the results of the individual algorithms are inconsistent, a manually determined period supersedes the algorithms. Typically, the algorithms agree among each other, with the one most prone to failure being LSC, and the most consistently reliable being PDM. This is to be expected as the spot-induced features in the light curve appear to deviate strongly from a sinusoidal shape for the stars we are most interested in. We provide the derived power spectra together with the light curve data in the auxiliary files. Fig. 7.28 includes plots of the phase folded light curves.

[8] Based on the `astropy` v5.1 implementation (VanderPlas et al. 2012; VanderPlas & Ivezić 2015).

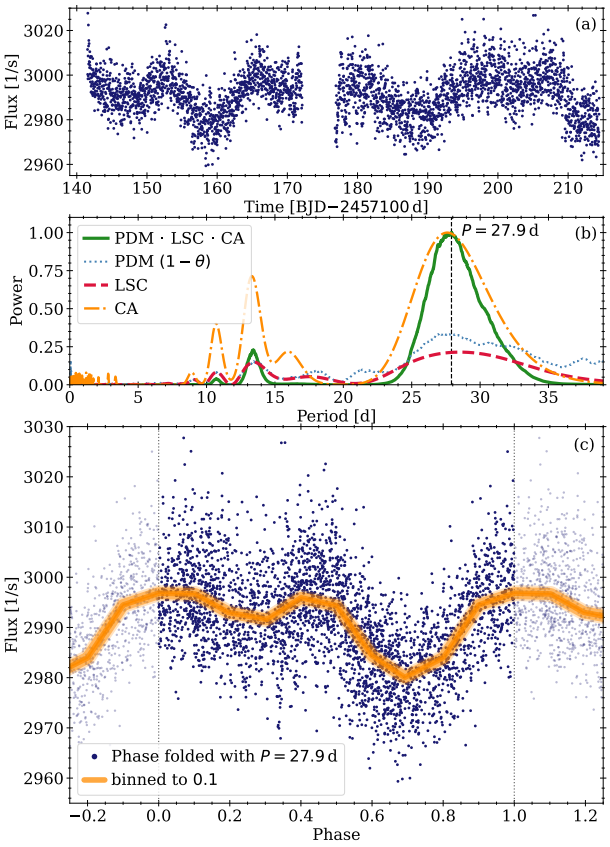

Figure 3.5: *Result of period analysis on the light curve for* Gaia DR3 604971466769552128. *Panel (a) shows the light curve produced, one which exhibits a clear periodic signal. The power spectra in panel (b) are obtained using multiple methods as indicated. The Clean (CA) and Combined power spectra are normalized to their maxima and the PDM spectrum is shown as* $1 - \theta$. *Panel (c) shows the phase-folded light curve, folded with* $P = 27.9\,d$, *corresponding to the peak in the combined spectrum.*

Period errors are derived in much the same way as the periods themselves. The presence of data systematics and spot evolution makes the usage of an automated algorithm for error determination problematical. Therefore, we decided to determine errors manually based on the phase folded light curve. We folded the light curve with different periods and set the error range such that for every period covered a phase folded light curve provides a reasonable result in matching the spot-induced features. The uncertainty arises from a number of factors: (1) the number of periods covered, that is, how many repetitions of the features we observe in the *K2* C5 baseline, (2) the general signal-to-noise of the variation, and (3) the amount of spot evolution, together with the remaining systematics. Generally, this results in errors that are in the order of ± 5 – 10 %. This procedure is supported during the comparison between our derived periods and those from the literature (see below in Sect. 3.5 and particularly Table 3.2.) Furthermore, ignoring the three outliers, 37 of the 44 remaining stars of our sample overlap with the trend line (see Fig. 3.9 below), suggesting that our uncertainties are on the order of 1.5σ.

3.4 Results

In this section we present the stars for which periodic signals were identified. We investigate outliers, construct a Color-Period diagram (CPD) for M 67 of single MS-stars to be used in the subsequent discussion, and present the final CPD for M 67.

3.4.1 The raw Color-Period Diagram

We identify 136 stars in the FOV that exhibit periodic signals of which 96 are M 67 *members* which exhibit signals that can be attributed to stellar rotation and 83 of which are MS stars. Apart from the few stars that do not have a convective envelope (namely the blue stragglers with spectral types earlier than mid-F), the sample covers spectral types from early-G to mid-M. Figure 3.6 gives an overview of the stellar rotation period distribution found. The detected periods range from a few hours up to 38 d, the latter abutting the detection limit of *K2* C05. A significant fraction of the cluster sample (53 stars, 43 on the MS) are binaries; those are typically both fast rotating and among the bluer stars of the sample.

To enable the usage of this sample as a calibration set for gyrochronology, we also remove all stars that detract from this purpose. We define these as any that violate one of the following statements:

1. The stars are M 67 cluster members.
2. Their colors are a valid proxy for their mass i.e. they are unevolved.
3. They are not likely to have experienced angular momentum transfer that has caused *externally induced* changes in their rotation rate, and have spun down over time based on the processes described above.

Adherence to the first statement is simply addressed through our membership analysis. Figure 7.26 in the appendix shows that the field stars (red symbols there) are scattered all across the CPD, corresponding to a wide range of (unknown) ages. Accordingly, we remove them from our sample.

The second statement is violated by evolved stars. Stellar evolution causes stars to change their colors as well. Changes on the main sequence are small enough to be a nonissue here. However, when stars leave the main sequence they become significant. This means that the color ceases to be a valid proxy for mass for all stars that have left the main sequence and have undergone drastic changes in their colors (typically turning redder toward the red giant branch). We will address those stars separately below in Sect. 3.5.5 with respect to what happens when we forgo color and revert to assess the stars directly via their masses. For now, we omit them from our sample by removing all stars brighter than $G = 13.2$ mag (red symbols in Fig. 3.6).

The third statement is violated by stars that have experienced angular momentum transfer in the past. Prime candidates for this are stars in close binary systems. Angular momentum is typically transferred from orbit to rotation, causing a spin up (rejuvenation of the rotation rate). Consequently, removal of binaries from studies like ours

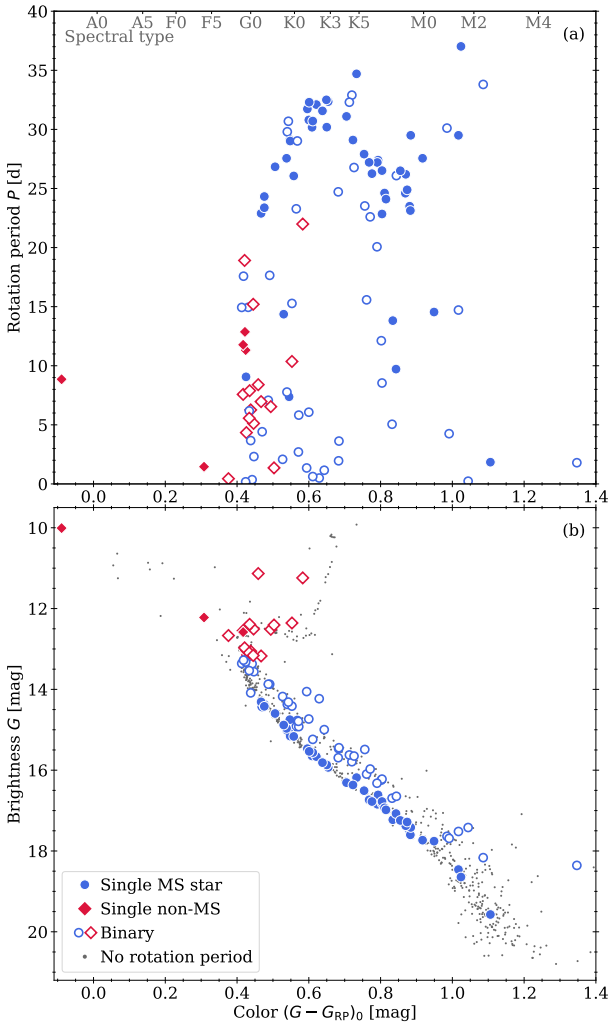

Figure 3.6: *Stars for which we have identified rotation periods. Panel (a) shows a color-period diagram (CPD) and panel (b) the corresponding color-magnitude diagram (CMD). Stars belonging to M 67 according to our membership analysis are shown as blue circles (the main sequence stars) and red squares (post-MS stars). Open symbols (in all of the above) mark those that show signs of binarity. Error bars are suppressed here for visibility reasons.*

is performed almost habitually. Here we see the effects of binarity clearly thanks to our sample size. A significant fraction of the cluster sample (53 stars, 43 on the MS) are binaries; and those are both fast rotating and typically among the bluer stars of the sample. Examination of Fig. 3.6 shows that whereas the single cluster members are concentrated at the long-period end of the distribution, already suggesting a sequence against color, the binaries are scattered over the entire rotation period range, with almost all having shorter periods than the single stars.

To our knowledge, this phenomenon has not been observed as starkly before. After an extensive radial velocity and photometric survey of the young open clusters M 35 (∼150 Myr) and M 34 (∼200 Myr, Meibom et al. 2009), Meibom et al. (2011b) noticed that the rotational distribution of binaries beyond the influence of tides was marginally skewed toward faster rotation. Other work in young open clusters (e.g., in NGC 2516 and NGC 3532 by

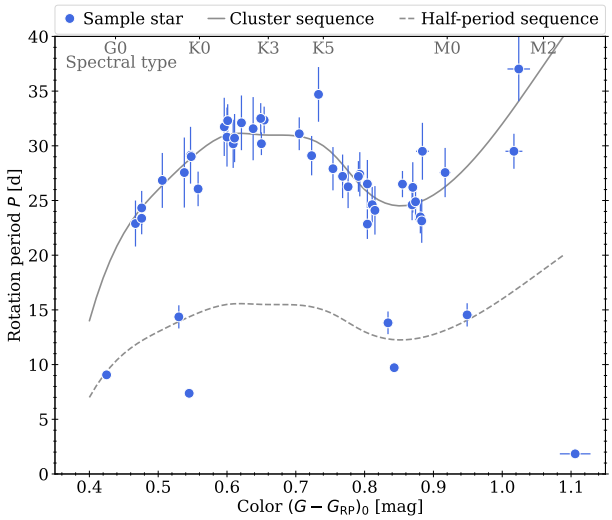

Figure 3.7: *Color-period diagram for our sample, now including rotation period uncertainties. Only* member *stars on the main sequence, and with no indications of binarity are displayed. An approximation of the emerging cluster distribution (solid gray line) is overplotted, together with its half-period counterpart (dashed line).*

Fritzewski et al. 2020, respectively) found that while certain (presumably very close) binaries were anomalous, the vast majority of the photometric binaries were rotationally indistinguishable from the single stars. In the far older (2.5 Gyr) but much sparser cluster Ruprecht 147 Gruner & Barnes (2020) noted that three of the four binaries therein were off the single star sequence. However, that is too few stars to be able to draw conclusions. In contrast, the situation here is obvious. 34 out of the 43 main sequence stars with signs of binarity exhibit slightly to considerably faster rotation than the single star sequence.

In fact, the scatter is so great that it seems unlikely that photometric or tighter binaries of this age are suitable for gyrochronology. Their ages will have to be determined by other means. Although we only have indications for photometric binarity for many of our stars (increasingly toward the fainter end), this already appears to be enough to identify a star as unsuitable. We stress that binarity does not mean that a star does not agree with the rotation of a similar single star per se; however, it is obvious in our results that *it is considerably more likely than not* that rotation is affected. Consequently, we remove all stars with signs of binarity from our sample, including the nine binaries whose positions agree with the single star sequence.

The above pruning leaves us with the 47 stars that are displayed in Fig. 3.7, enabling a closer look at the emerging period distribution and its features. We find a group of slower rotating stars with rotation periods between 15 and 35 d, spanning from early-G to early-M. They follow a somewhat sinusoidal shape, with a maximum at $(G - G_{\rm RP})_0 \sim 0.65$ and a local minimum at $(G - G_{\rm RP})_0 \sim 0.85$. We identify this with the classical *slow rotator* sequence. We have indicated this group with a simple trend line (cf. solid line in the figure). It is created from a simple cubic interpolation to points listed in Table 7.6. We stress that this line is drawn solely to guide the eye and indicate the cluster sequence. We will employ similar indications in color-period diagrams for other clusters below. Another group of stars apparently follows the same distribution but at half the period. This *half-period* sequence is formed by double dipping stars which feature two spots whose signals in the light curve are indistinguishable and as such appear to have only half the actual period.

3.4.2 Double dipping stars

Stars can exhibit more than one significant star spot (or group). In fact, as Basri & Nguyen (2018, see also Tan & Basri (2020)) have shown, it is more likely for stars with longer rotation periods to exhibit more than one spot at a given time. We recall that we use the term *spot* as a simple handle for any coherent activity (combination of) features on the stellar surface that is visible as a significant modulation in our light curves. This explicitly includes faculae, which are assumed to be the dominant flux-altering feature at the age of M 67 (e.g. Reinhold et al. 2019). Following the results of Basri & Nguyen (2018), at the rotation rates we find for M67 it is up to ten times more likely. We indeed find that about half of the stars in our sample exhibit signs of more than one surface feature. This may create an additional problem. If those features are sufficiently similar in shape and close to a phase shift of 0.5, they may become indistinguishable. This means that we are likely to find a number of stars whose determined rotation periods will be half of their actual periods. Sufficient numbers of such stars will form a sequence at half the actual period, a *half-period sequence*.

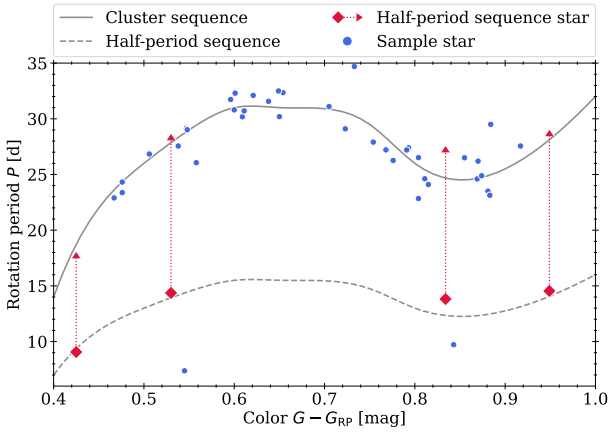

Figure 3.8: *CPD for our M 67 sample emphasizing stars on the* half-period sequence. *The cluster sequence, approximated by an interpolated line, is overplotted in gray. The dashed line shows its half-period counterpart. Stars for which we double the measured periods (red) are connected to their new positions by dashed lines.*

Indeed, we do observe this behavior (cf. Fig. 3.8). 43 stars define a long-periodic sequence with periods between 15 and 38 d, while four stars follow the *half-period sequence*. Following Basri & Nguyen (2018) and the distribution of other cluster stars, it is a reasonable assumption that those four stars have rotation periods that are ac-

tually twice the identified ones. Therefore, we adopt final rotation periods for those four stars that are twice the measured ones. We note that such light curves are also visible in the prior rotation period work on warmer stars in the M 67 work of Barnes et al. (2016b).

3.4.3 Color-period diagram for M 67

With the half-period sequence stars accounted for and with binaries and evolved stars eliminated, we can construct a color-period diagram for M 67 that can be compared with other clusters and with spindown models. The final emerging CPD contains 47 stars and is shown in Fig. 3.9. Appendix Table 7.8 lists these stars.

The emerging distribution of rotation periods, spanning from early-G to mid-M stars, shows a clear sinusoidal sequence. It rises from around 18 d periods for G0 stars, the earliest type stars at the age of M 67 that is still on the MS, to periods around 30 d for K3 stars. Following the distribution redward, the periods decrease again to around 25 d at M0 only to rise again to 30 d and longer for mid-M. This distribution will be compared with prior work and discussed in more detail in the next section, following a discussion of the outliers immediately below.

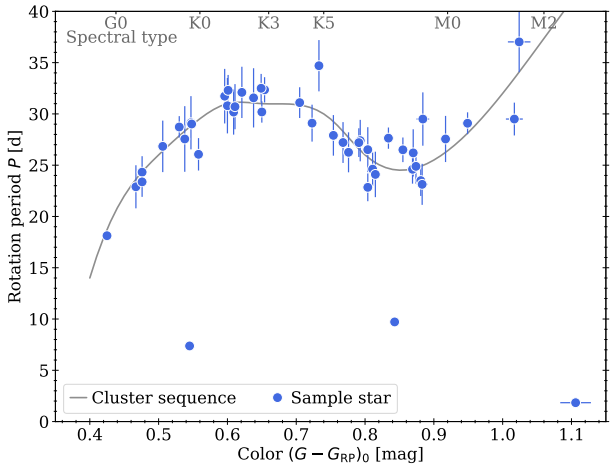

Figure 3.9: *Final CPD of M67 based on our study. The corresponding data are displayed in Table 7.8*

3.4.4 Outliers

Our sample contains three fast rotating stars with periods $P \leqslant 10$ d that deviate strongly from the slow rotator sequence occupied by all other stars. We suspect that the likely origin of this deviation is undiscovered binarity impacting the stellar angular momentum evolution. The stars in question are actually inconspicuous among the sample as regards their *renormalized unit weight error* (RUWE) in GDR3. (A larger than average RUWE value can indicate an underlying issue with the astrometric solution, which itself may originate in undiscovered multiplicity.)

Gaia DR3 604911204083987584 ($P = 7.4$ d, $(G - G_{RP})_0 = 0.55$ mag) sits right within the area of the CPD that is typically occupied by binaries (cf. Fig. 3.6). It does have two very close companions (0.5 and 4.3 magnitudes fainter) within 5″. Those cannot be separated during light curve extraction; however, it is clear from an investigation with different pixelmasks that the star itself is the source of the observed variability. Geller et al. (2015) actually designate the star as a non-member based on radial velocity work but *Gaia* astrometry indicates a high probability member. Consequently, we retain it in the CPD.

Gaia DR3 604922229264424448 ($P = 9.7$ d, $(G - G_{RP})_0 = 0.84$ mag) could potentially be part of the *half-period sequence*. However, closer inspection shows that it lies significantly below, a deviation even more pronounced if one were to double its period. Furthermore, its light curve shows clear signs of continuous spot evolution which would mean both spots evolving identically, if it were a double-dipping star. This seems unlikely.

For those two objects, angular momentum exchange (e.g., in a binary system) appears to be the most likely explanation. The third outlier is the reddest and simultaneously fastest rotating star of our sample *Gaia DR3 604969061592133376* ($P = 1.8$ d, $(G - G_{RP})_0 = 1.11$ mag). It could still be part of the fast rotator sequence, similar to what can be observed in other, younger clusters. It would be the first known star that is part of the fast rotator (denoted *convective* in Barnes 2003) sequence at a confirmed age older than 1 Gyr. However, it may also simply be a star with hidden binarity.

3.5 Discussion

In this section our results for M 67 are placed in the larger context of the rotational evolution of stars. First, we compare our results with findings in past studies and investigate deviations and inconsistencies. In the process, we address certain issues with prior work. We then build a sample of combined knowledge for rotation data from M 67 and compare it with the few old open clusters studied to date and also with the predictions of rotational spindown models.

3.5.1 Comparison with prior work on M 67

There have been three prior studies of M67 using *K2* light curves from C05: Barnes et al. (2016b, B16 hereafter), Gonzalez (2016b, with a followup in Gonzalez (2016a), G16 hereafter), and Esselstein (2018, see also Esselstein et al. (2018), E18 hereafter). Those studies were performed on the *presearch data conditioning* (PDC) light curves provided in the *K2* archive[9]. These light curves were created from aperture photometry and include a correction that, to a certain degree, accounts for systematics and trending. However, as pointed out by Barnes et al. (2016b), the light curves are not free of either problem. E18 made additional use of self-extracted light curves from the C05 superstamp and C16 light curves. All studies operated on the low spatial resolution given by the EPIC catalog. For this comparison we match their samples with GDR3. In addition to the work mentioned above, a recent study by Dungee et al. (2022) created light curves from 3 years worth of ground-based observation. This latter work is limited to M-dwarfs.

[9] archive.stsci.edu/missions-and-data/k2

Barnes et al. (2016b, 20 stars) and Gonzalez (2016b,a, 98 stars) operated on the light curves provided by the *Kepler* mission itself; only a few of those were from the superstamp region (cf. Fig. 7.21). Thus, the overlap with our sample is small. Esselstein (2018, 30 stars) includes parts of the superstamp, but the overlap is still small. We also have some overlap with Dungee et al. (2022). Table 3.2 shows the stars that are common between the samples. The agreement in derived rotation periods is very good, with period differences typically $\lesssim 2$ d. The only star with a significant difference is EPIC 211397501[10], for which Gonzalez (2016a) reported the half-period. (It is identified as a half-period sequence star by us.) In the comparison with Dungee et al. (2022) we find that seven rotation periods (including three that were nominally rejected from their sample) are in good agreement with our periods.

Table 3.2: *Overlap between our sample, those based on* Kepler *data by Barnes et al. (2016b, B16), Gonzalez (2016b,a, G16), and Esselstein (2018, E18), and that of ground-based data from Dungee et al. (2022, D22). D22 periods in parentheses were rejected as outliers in their sample.*

Gaia DR3	P [d]	$P_{\rm B16}$ [d]	$P_{\rm G16}$ [d]	$P_{\rm E18}$ [d]	$P_{\rm D22}$ [d]
598899796057231616	—	31.8	31.7	—	—
598902716634970240	—	30.7	30.4	—	—
598903678707639296	32.4	30.3	30.1	—	—
604895948360165888	24.2	—	12.4	—	—
604896051439391104	—	25.1	28.3	—	—
604896498115959296	23.5	—	—	—	25.9
604896635554924672	32.5	34.5	—	—	—
604896837417607808	12.9	—	24.9	—	—
604897631987337600	—	28.4	26.8	—	—
604897833850019328	24.3	26.9	26.3	—	—
604900651348634240	23.1	—	—	—	(25.3)
604903331408222208	29.5	—	—	—	31.6
604903438783070208	37.0	—	—	—	(826)
604906531159503616	4.4	—	—	4.3	—
604906840397139584	29.1	—	—	—	(28.2)
604917354477131392	6.1	—	—	6.4	—
604917698074587136	7.8	—	—	8.0	—
604920549932807296	24.6	—	—	—	(442)
604922229264424448	9.7	—	—	—	(9.8)
604923848467470976	26.2	—	—	—	26.0
604930544320911744	—	18.1	—	19.8	—
604930681760054656	27.6	—	—	—	(63.9)
604960235430488960	—	26.9	26.8	—	—
604969267746267520	26.5	—	—	—	26.1
604970131035099008	24.1	—	—	—	(237)
604973635728426752	—	24.9	—	25.3	—
604996106997219712	—	31.1	29.2	—	—

3.5.1a Barnes et al. (2016b)

Given that instrumental systematics and trending are still present in the data, Barnes et al. (2016b) subjected their sample to a PCA to remove trending and, partially, systematics. They identified 20 stars with a rotational signal, shown with red squares in panel (a) of Fig. 3.10, together

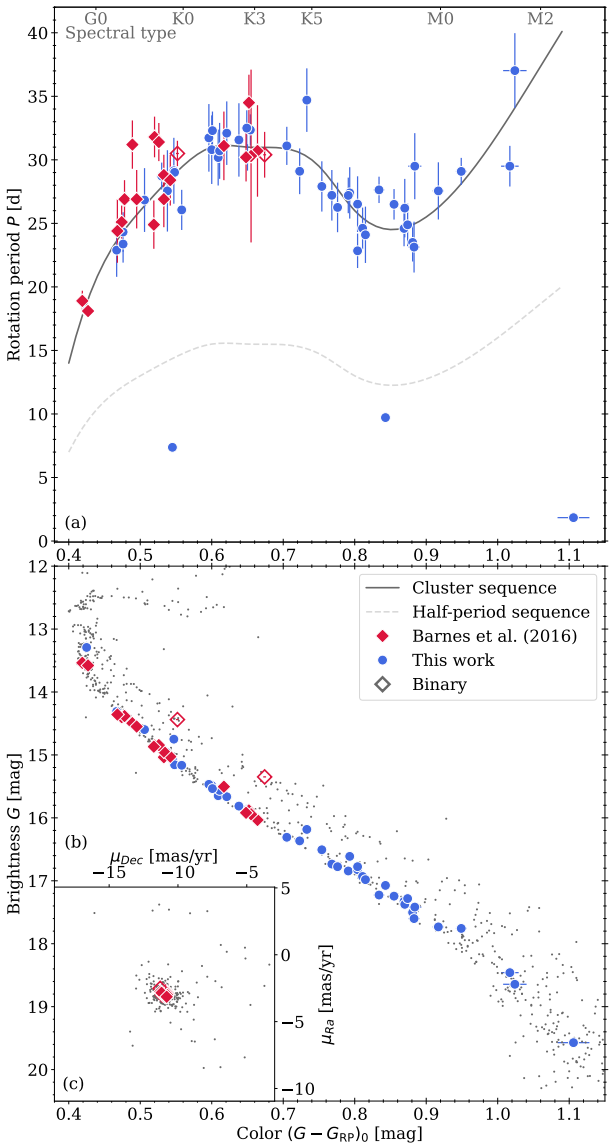

Figure 3.10: *Comparison of our results with those of Barnes et al. (2016b). Panel (a) shows a CPD as in Fig. 3.9 and overplotted in red are the measurements by Barnes et al. (2016b). The gray lines, solid and dashed, are our indication of the cluster and half-period sequences, respectively. Panel (b) shows a CMD of the same stars and the inset (panel c) the proper motions centered on M 67. Gray dots in panels (b) and (c) are* members *without period determinations.*

with our sample. Generally speaking, they subjected each light curve to the same vetting that we performed, and for the common stars, found periods in agreement with ours to within the uncertainties.

The Barnes et al. (2016b) sample forms a sequence spanning from early G stars with rotation rates around 18 d to mid-K stars with rotation rates around 30 d, and with a continuous, but non-linear, increase in period in that range. The derived distribution of stars was in very good agreement with the models of the time (that only had the sun as anchor point before) and is still in agreement with the ones today, given that it is used as a calibrator for said models. The crossmatch with GDR3 reveals that two stars included in the B16 sample are likely photomet-

[10] Gaia DR3 604895948360165888

ric binaries (cf. CMD in Fig. 3.10 panel (b)). However, they are not deviant in any way in the CPD. An inspection of panel (c) in Fig. 3.10 shows that sample stars are all well-constrained cluster members.

Our sample connects well to the B16 sample, overlaps with theirs in the G0 to K3 range of spectral types, and extends it in a continuous fashion to early M stars. It is notable that the B16 sample has its reddest stars right at the point where the range of monotonically increasing rotation with color ends (at K4).

3.5.1b Gonzalez (2016b)

G16 has carried out an extensive analysis on de-trended *K2* C05 light curves as provided in the *K2* archives, subsequently refined in Gonzalez (2016a) with a larger sample but with a more restrictive selection of rotational signals. Similar to Barnes et al. (2016b), they used the PDC light curves for their analysis.

The sample includes 98 stars between early G and early M spectral types, spanning periods from 12 d to 40 d. The sample distribution found by G16 is atypical as compared with the sequences of known clusters (cf. panel (a) in Fig. 3.11). The distribution resembles a double wedge shape with a pinch point around mid-K and large period spreads for both warmer (early-G) and cooler (early-M) stars. As such, it spans an area rather than a sequence in color-period space, unlike any other measured cluster. The lower boundary of this area overlaps with the Barnes et al. (2016b) results and with our data in the respective color ranges. The region of lowest period spread in the G16 data (around mid-K) coincides with the red limit of the Barnes et al. (2016b) data, and where our present distribution slopes down toward shorter periods. Additionally, G16 has a group of faster ($P \approx 14$ d) late-K stars that fall on our identified half-period sequence.

If the rotation periods found by G16 are to be truly representative for M 67, they, and the stars that they have been derived from, must satisfy certain criteria. Firstly, they need to be bona-fide cluster members. G16 worked in the pre-*Gaia* era, but we now have the advantage of *Gaia* astrometry. We match their targets to their GDR3 counterparts and find that that the member selection is good, although certain stars have deviating proper motions. It includes some subgiants and, like Barnes et al. (2016b), a few photometric binaries. Neither of these are responsible for the deviations observed.

We then inspect the light curves used. G16 used the PDC light curves from the *K2* archive, subjected them to removal of flux outliers and used the result for the period analysis. And here we find the source of the problem. G16 assumes the PDC light curves to be free of systematics and trends. This is emphatically not true. Although apparently corrected for these effects, the light curves are riddled with them. We have taken the light curves from the archives and followed their steps (see Sect. 2 in Gonzalez 2016a) to recreate the same input data. Their period analysis goes on to identify periodic signals in the light curves where there are clearly (from a manual inspection) none present. Those misidentified signals are generally

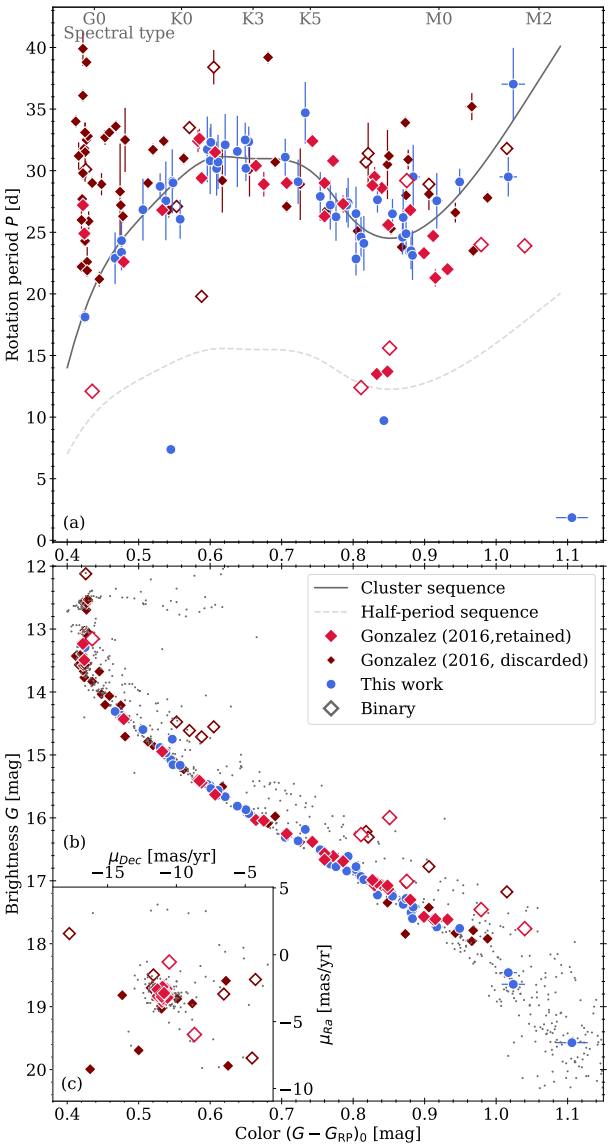

Figure 3.11: *Same as Fig. 3.10 but with a comparison to results of G16 (red), showing both retained and discarded stars from that sample.*

a combination of low level, somewhat random, intrinsic variation paired with remnants of systematics and trends. Neither of those can be used for the reliable derivation of a rotation period. The maxima in a PDM power spectrum of those light curves is generally low, which supports the picture of misidentifications.

We therefore manually inspect the light curves of all 98 stars of their sample and select those stars for which a periodicity is obvious in the light curve. For this selection we uses the PDC and `k2sc` light curves and prepared them in the same way as G16.In our selection, we err on the side of caution, similar to the selection of our own sample, and identify 33 stars whose periods we adopt. We do not derive a period ourselves for those stars but adopt the ones reported by G16, even though we may disagree slightly on the assigned period for individual stars. Our selection is purely based on the shape of the light curve. Those 33 light curves are generally those with the greatest variability amplitude, because they dominate the light curve over

the systematics and trends and are easy to pick out. We list these 33 stars in Table 7.7.

We now compare this subset with our findings. This new subset reduces the G16 sample from an *area* to a *sequence* in the CPD. A particular improvement is seen for the bluest stars of the G16 sample, where we now exclude almost all of the long period G-type stars. This improvement is also visible in the comparison with our data shown in Fig. 3.11. The agreement is now much better than with the entire sample. The largest part of the subset occupies the downward sloping section of our sequence, starting at the period maximum at early-K stars and going toward the minimum at early-M, thereby matching our distribution well. However, the downward sloping section appears slightly red-shifted ($\Delta(G - G_{\rm RP})_0 \approx 0.1$ mag). It also connects well to the Barnes et al. (2016b) sample and extends it toward redder stars with a small range of overlap. Interestingly, all five stars of the G16 sample that lie on the half-period sequence made it into our vetted subset.

Finally, we note that G16 adopted 998 light curves and identified rotational signals in 441 ($\approx$ 44 %) for their M 67 study. This is a very high fraction, even for a much younger, more active cluster, where stellar rotation periods are far easier to identify. For comparison, we identified rotation signals in $<$ 10 % of the sample and Gruner & Barnes (2020) identified rotation periods in 21 out of 102 ($\approx$ 20 %) stars for the 2.7 Gyr-old open cluster Ruprecht 147. We therefore conclude that the results of G16 represent an overly inclusive set of stars (unfortunately including misidentifications) in addition to those with true rotational periodicity. Our sample is far more exclusive in comparison. When systematics and instrumental trends are excluded, the two distributions can be seen to be substantially similar.

3.5.1c Esselstein (2018)

The study of Esselstein (2018, E18 hereafter, see also Esselstein et al. (2018)) had a slightly different focus than the ones before. Their main objective was to assess the detectability of rotation signals from light curves of stars as old and inactive as in M 67. They devised a sophisticated methodology around the artificial injection of variability signals into real *Kepler* data. Mostly as a byproduct, they identified rotation periods from archived light curves (SAP) and self-extracted data.

E18 provides rotation periods for 30 stars (their Table A.13) that span from the turn-off point to early K-stars (cf. panel (a) in Fig. 3.12). Their sample includes a large number of fast rotators while the slow rotators show significant scatter. As before, we scrutinize the sample by identifying binaries and also subject their light curves to manual inspection. E18 lists identifications for *binaries* and *probable binaries* which we complement with a photometric binary designation from *Gaia* photometry. We come up with a list of 11 binaries. Additionally, three of their stars are clearly evolved past the main-sequence. All fast rotators in the E18 data either show signs of binarity or are post-MS.

The E18 slow rotators agree reasonably well with our

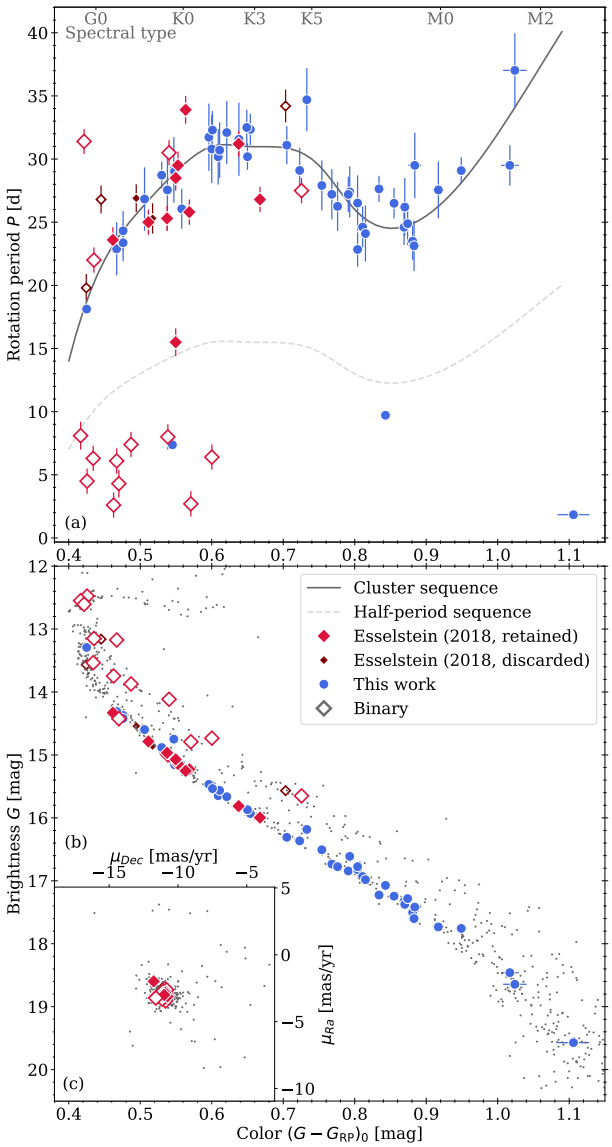

Figure 3.12: *Same as Fig. 3.10 but with a comparison to results of Esselstein (2018) (red), again identifying retained, discarded, and binary stars.*

distribution (as verified with B16 and G16). However, theirs shows significantly greater scatter than the other studies. Similar to our investigation of the G16 sample, we inspect the light curves to look for inconsistencies. This, however, is more difficult than before as their light curves are largely only available to us in plotted form (see their Appendix Sect. B). We identify five stars for which we cannot verify the rotation signal. However, their elimination from the sample does not change the overall picture. As before, we adopt their period as is even though we may disagree about the derived value for individual stars. One star of the sample (EPIC 211404554) sits arguably on the half-period sequence.

This scrutiny suggests that E18 does agree reasonably well with the overall picture of M 67 constructed here. Inconsistencies can largely be explained through binarity and post-MS evolution. However, the slow rotator sequence has greater scatter than other results. We argue that this originates in the detection method used. E18 used

a Lomb-Scargle analysis. While that is a good choice for fast rotating stars, it ceases to be for slow rotators. This is because the sine wave that is assumed in the LSC becomes less and less suitable for slow rotators due to the occurrence of multiple spots and significant spot evolution between consecutive rotations. Phase dispersion and autocorrelation are much better suited for this period regime. As such, we treat the results of E18 with caution.

3.5.1d Dungee et al. (2022)

A recent study by Dungee et al. (2022) has used ground-based data acquired over a 3 yr baseline to investigate the rotation of M dwarfs in M 67. They have obtained periods for 383 stars and applied iterative outlier rejection leading them to adopt 64 of the M 67 M-dwarfs as their cluster sample. The full sample spans a huge range in rotation periods, from a few to several hundred days. After outlier rejection the remaining sample (dubbed as *converged*), a clear sequence appears to emerge, starting around 28 d periods for late-K stars and showing an increase in period at mid-M to almost 60 d. Figure 3.13 shows their periods together with ours.

We find very good agreement between our results and those of Dungee et al. (2022). Their sample has its blue boundary at late K-stars and extends toward mid-M. This connects directly to a well populated area in our sample and extends it redward where our data is thinning out but is still in direct agreement with theirs. They have included a photometric cut to their data, eliminating photometric binaries and consequently, we do not find any problematic binary systems in the sample.

We do not have access to the light curve data from Dungee et al. (2022) (only plotted images) to inspect them in similar fashion as we did with the other samples. However, we also see no reason to do so as the agreement between our results and theirs is excellent and their long-baseline ground-based data is not subject to the problems specific to *Kepler* data.

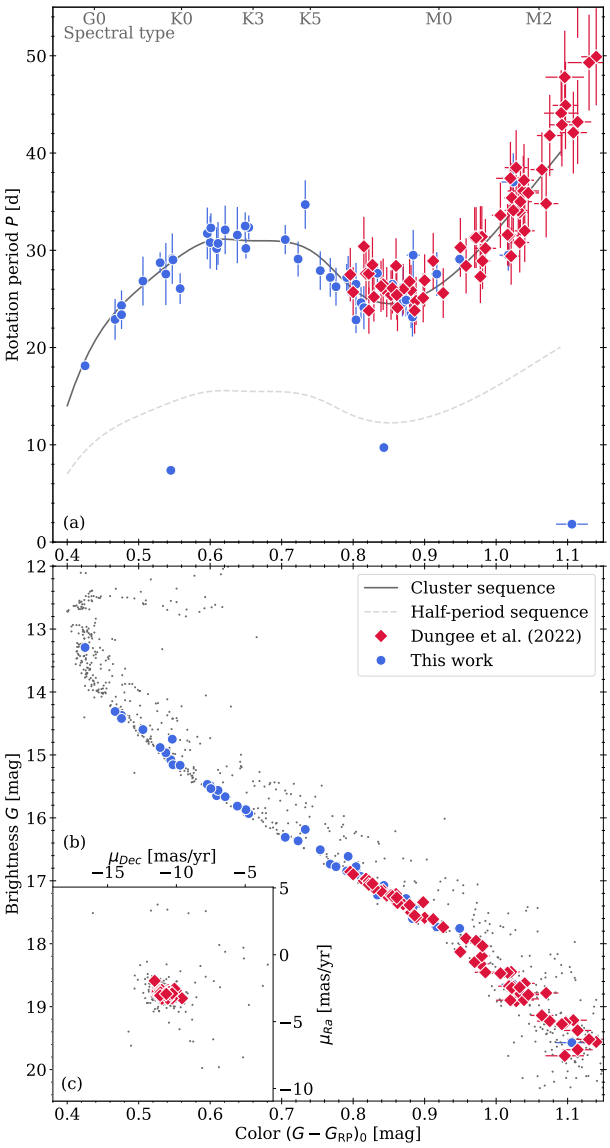

Figure 3.13: *Same as Fig. 3.10 but comparing with the results of Dungee et al. (2022) (red). Dungee et al. (2022) assume a flat period error of 10 %.*

3.5.1e A lesson from prior studies

Based on the above comparisons, we emphasize the need for a very careful approach in the identification of rotation periods from space-based data, especially in the present period regime. Trending and systematics could mask or mimic spot-like variability in a light curve and spot evolution may further complicate period identification. Despite concerns about objectivity, it appears to be essential to supplement all algorithmic period determinations with manual inspection and judgment. We suggest far more exclusivity with similar rotation period derivations generally, but especially in the presence of systematics and when operating with a rather limited observation baseline.

3.5.2 Assembly of final sample

Before comparisons with models and to work in other clusters can be performed, we need to assemble a final sample. This consists of the following steps:

1. We accept all stars of our sample that are both on the MS and that are not identified as binaries.
2. We assume that the stars occupying the half-period sequence are in fact double-spotted stars and as such we double those observed periods. (This assumption is valid to the extent that at the rotation rates we observe, stars tend to be in the double spotted domain. Furthermore, we have several stars among our sample that are clearly double spotted, but with the spot shape and phase shift such that they cannot be mistaken as being single spotted.)
3. We add the stars from the Barnes et al. (2016b) sample, but omit the binaries therein.
4. We omit the Gonzalez (2016b) and Esselstein (2018) samples entirely.
5. We include the 64 stars marked as *converged* from the Dungee et al. (2022) sample.
6. We do not remove stars that are common between the samples.

Table 3.3: *Reddening parameters used for the individual clusters in Fig. 3.15. Calculated reddening use Eqs.* (3.2) *and* (3.5) *for* $E(G_{\rm BP}-G_{\rm RP})$ *and* $E(G-G_{\rm RP})$*, respectively. The Ref. column refers to source of* $E(B-V)$*.*

Cluster	$E(B-V)$	$E(G_{\rm BP}-G_{\rm RP})$	$E(G-G_{\rm RP})$	Ref.
NGC 6811	0.048	0.065	0.035	Curtis et al. (2019)
NGC 6819	0.15	0.201	0.11	Meibom et al. (2015)
Ruprecht 147	0.075	0.1	0.055	Gruner & Barnes (2020)
M 67	0.04	0.054	0.03	Taylor (2007)

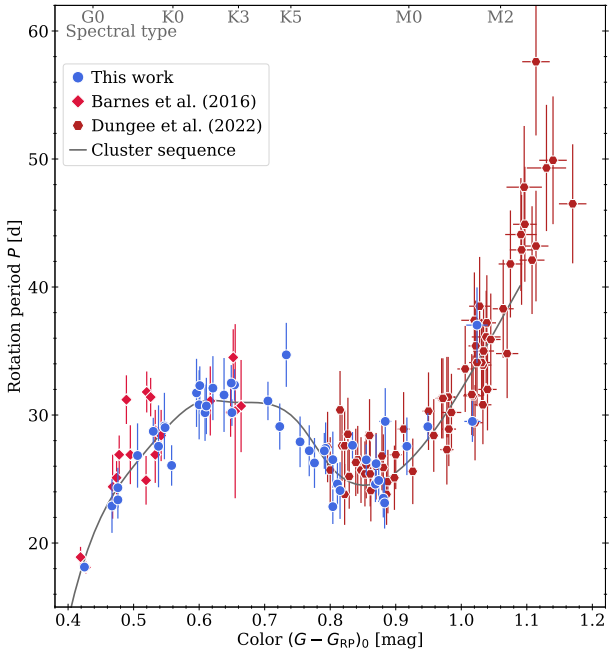

Figure 3.14: *Color-period diagram for our final assembled sample (combined with the results of Barnes et al. 2016b), now including only main sequence stars with no indications of binarity. Only the slow rotator sequence is shown.*

The addition of stars from Barnes et al. (2016b) significantly strengthens the emergent distribution and bolsters the region around mid-G type stars, while adding the D22 stars completely defines the M-dwarf region.

We match the sample to the 2MASS, USNO, and GSC catalogs to obtain a large set of measured stellar colors for each star. The availability of particularly blue bands is understandably sparse toward fainter stars. We also extend this search to non-M 67 stars, namely those included in rotational studies for other clusters (cf. overview in Sect. 3.1). Those will allow a more reliable comparison between the different cluster sequences that emerge later. The final assembled sample, offering as complete a view of the rotational distribution of M 67 is shown in Fig. 3.14.

3.5.3 Empirical comparison with observations of other clusters

We now compare our rotational distribution for M 67 with those of certain other open clusters. For this comparison we use data for NGC 6819 (Meibom et al. 2015, 2.5 Gyr), Ruprecht 147 (Gruner & Barnes 2020; Curtis et al. 2020, 2.7 Gyr), and NGC 6811 (Meibom et al. 2011a; Curtis et al. 2019, 1.0 Gyr) as they are the only open clusters equal or older than 1 Gyr for which rotation periods have been determined. We crossmatch their individual catalogs analogously to what was done in Sect. 3.5.2 to obtain a broader and more equally described sample. This requires accounting for the individual reddenings. We obtain $E(B-V)$ for each cluster and calculate $E(G_{\rm BP}-G_{\rm RP})$ from that. We use the following prescription to obtain $E(G-G_{\rm RP})$: As the transformation from $E(B-V)$ to $E(G_{\rm BP}-G_{\rm RP})$ can be obtained with a simple multiplicative factor (as an approximation) it is reasonable to assume the same works for the transition from $E(G_{\rm BP}-G_{\rm RP})$ to $E(G-G_{\rm RP})$. To determine the relevant factor we use our empirical result for $E(G-G_{\rm RP})$ in Eq. (3.3) (namely $E(G-G_{\rm RP})=0.03\pm0.005$) for M 67 and the calculated $E(G_{\rm BP}-G_{\rm RP})$. We find

$$E(G-G_{\rm RP}) = 0.556\cdot E(G_{\rm BP}-G_{\rm RP}). \qquad (3.5)$$

We use this to calculate $E(G-G_{\rm RP})$ for all clusters. The results are listed in Table 3.3.

M 67 is the oldest open cluster with reliable rotation periods available. It is therefore unsurprising, indeed expected, that its sequence lies above all other clusters in a color dependent sense (cf. Fig. 3.15). Similar to Ruprecht 147 and NGC 6811, M 67 shows a flattening of its sequence around early-K spectral type, although this feature appears to move to the red with increasing age. The cooler stars (later than mid-K) in Ruprecht 147 indicated a slight downturn of the sequence, with a minimum around late-K/early-M and a steep increase in period with redder color. However, given the small sample size in that range, the existence of the downturn was uncertain. Our new data for M 67 now confirms the existence of this downturn and validates the distribution seen for Ruprecht 147.

It is visually apparent that M 67 displays the greatest scatter in rotation period. This fact may be surprising in that the stars are expected to have all converged to the slow rotator sequence. The scatter is, however, a consequence of the difficulty of the period measurement and not an intrinsic property of the distribution. Additionally, the relatively short baseline of the space-based observations, combined with differential rotation results in significant uncertainties on the periods. To help visualize the cluster distributions and unclutter subsequent plots, we have created rough approximations of the cluster sequences (based on cubic interpolations to the points listed in Table 7.6) as shown with colored lines in Fig 3.15.

3.5.4 Comparison with rotation models

The long-term goal of studies like ours is to understand the rotational evolution of stars and the physics of mag-

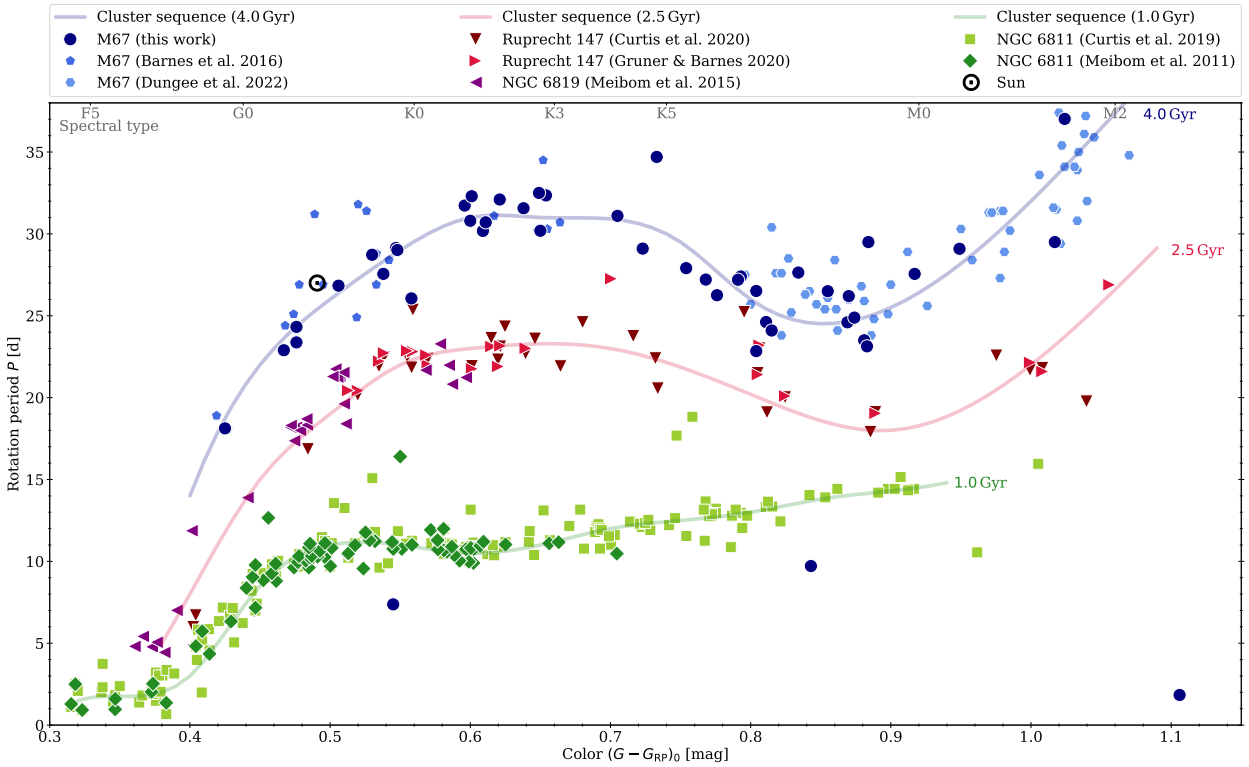

Figure 3.15: *CPD of the three open clusters 1 Gyr or older. Shown are NGC 6811 (Meibom et al. 2011a; Curtis et al. 2019) at 1 Gyr, NGC 6819 (Meibom et al. 2015) and Ruprecht 147 (Gruner & Barnes 2020; Curtis et al. 2020) at 2.5 Gyr, and M 67 (Barnes et al. 2016b; Dungee et al. 2022, and this work) at 4 Gyr. The color coding groups cluster data by age. Overplotted is a simplified representation of the emerging cluster sequences by age (solid lines color coded by age). The sun is shown with its usual symbol. Figure 7.27 shows equivalent plots in the colors* $(G_{\rm BP} - G_{\rm RP})_0$, $(B-V)_0$, *and* $(V-K)_0$.

netic braking, to describe the evolution in an empirically constrained model, and to use it to derive stellar ages via gyrochronology. Numerous stellar spindown models have been created over the years with varying levels of detail in their physical descriptions. As our new data extends the knowledge of stellar rotation rates into a parameter space that has not been explored before (lower mass and higher ages), we go on to examine how well the models perform against our new findings.

We know from prior work in Ruprecht 147 (e.g., Curtis et al. 2020; Gruner & Barnes 2020) that models of rotational evolution do not reproduce well the observed distributions of cluster stars at higher ages. Any lingering doubts about discrepancies between the models and the data are removed now. The deviating shape shown by Ruprecht 147 is also present in M 67, and is more pronounced. We know now that rotational evolution deviates significantly from model predictions. As such, we limit this section to comparison up to this conclusion and omit a longer discussion on the intricate model details. For a more detailed discussion see the comparison to Ruprecht 147 in Sect. 6 of Gruner & Barnes (2020).

We also limit ourselves to a comparison with the spindown descriptions of Barnes (2010) and Spada & Lanzafame (2020). These are chosen among the numerous models available as they are related in their descriptions and exemplify the difference based on the inclusion of an additional parameter. This comparison is essentially similar to the one performed in Gruner & Barnes (2020), but the observed deviations there are even more pronounced here, and the larger sample allows a stronger conclusion. We note that the models are only available in certain colors and for particular ages. Spada & Lanzafame (2020) published a few time steps (notably 2.5, 4.0, and 4.57 Gyr in the relevant age range) and are available only in $(B-V)_0$ color. Barnes (2010) offers a mathematical prescription that we use similarly to Gruner & Barnes (2020) (see their Sect. 6.1) which intrinsically allows any given age and a variety of Johnson and 2MASS colors. $B-V$ is especially problematic with respect to reliability and availability for stars as red and faint as we deal with here. As such, an examination based on a more reliable and consistent set of colors is preferred. We opt for *Gaia* $G - G_{\rm RP}$ as it omits the problems of *Gaia* $G_{\rm BP} - G_{\rm RP}$ in the blue and is accessible from one consistent source (unlike e.g., $V-K$). However, we do include those colors below to offer a complete picture.

To perform the comparison in $G - G_{\rm RP}$, we do need the models in said color. We employ a color transformation that is constructed from stellar models in the PARSEC isochrones by comparing the different synthetic colors for stars of the same mass, age, and metallicity. This approach has its weaknesses, for example it is problematic toward the very red, but it is sufficient for our comparison. The comparison that is shown in Fig 3.16 is now based on the following: (1) all stellar colors are measured, that is, obtained from one of the above mentioned catalogs and dereddened according to the description in Sect. 3.2.3, (2)

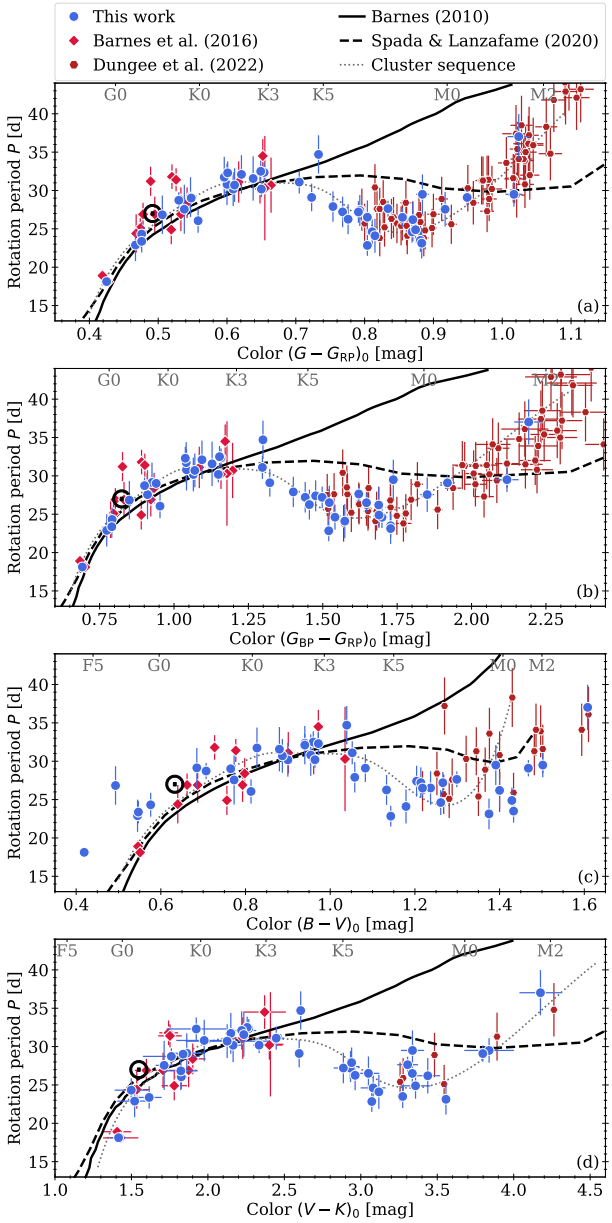

Figure 3.16: *Comparison between our final sample of measured rotation periods (this work combined with the results of Barnes et al. (2016b) and Dungee et al. (2022)) and the stellar rotation models of Barnes (2010) and Spada & Lanzafame (2020). Each panel performs the comparison in a different color system: (a) $G - G_{RP}$, (b) $G_{BP} - G_{RP}$, (c) $B - V$, and (d) $V - K$. The errors on $B - V$ are suppressed for visibility reasons.*

both models in $B-V$ and Barnes (2010) in $V-K$ are obtained directly from the sources, and (3) $V-K$ for Spada & Lanzafame (2020) and both models in *Gaia* colors are obtained via the transformations. We use the same color transformation on our empirical cluster sequence which was originally constructed in $G - G_{RP}$ (see Table 7.6).

3.5.4a The Barnes (2010) model

We find good agreement between our results and the Barnes (2010) model prediction for stars earlier than K5 (in the overlap region with the Barnes et al. (2016b) data). Redward of K5, the model predicts a steady increase in rotation period with color which is not seen in the data. Instead, the observed stars turn significantly downward toward shorter rotation periods. After this point, the model diverges away from the observed stellar distribution. Similar behavior was observed in Ruprecht 147 by Gruner & Barnes (2020) but the effect is stronger here, and thanks to the larger sample, can now be stated with much more certainty. It is to be noted that the period increase for the reddest stars in the sample is much steeper than predicted in the model. This leads to an apparent reconvergence between model and observations for mid-M stars. As has now been seen with multiple clusters, the Barnes (2010) model fails to predict the stellar rotation rates for older stars later than mid-K. Additional physics is apparently required to describe the spindown adequately.

3.5.4b The Spada & Lanzafame (2020) model

The model of Spada & Lanzafame (2020) incorporates the Barnes (2010) description for magnetic braking and adds a two-zone model where an additional parameter describes the coupling between those two zones and the angular momentum exchange between them. Generally speaking, angular momentum from the radiative core is transferred to the convective envelope, reducing the stellar spindown to the point where a star may even spin up slightly. This effect is mass-dependent. It should be noted that the Spada & Lanzafame (2020) model only describes stars of the slow rotator sequence, in contrast to the Barnes (2010) model. However, this is not directly relevant here, since at the age of M 67, all stars have converged to the slow rotator sequence.

Similar to the Barnes (2010) model, the Spada & Lanzafame (2020) model provides good agreement for stars bluer than mid-K. For later spectral types, it is closer to the data than the Barnes (2010) model, but still does not appear to be able to reproduce the observations in detail. Both the model and observed cluster sequence show first a flattening of the distribution followed by a subsequent downturn in the CPD and eventually a steep increase from blue to red. However, those features appear not to be aligned. The Spada & Lanzafame (2020) model predicts a flattening of the distribution and a potential downturn around M0, whereas the observations show said downturn already at mid-K. Furthermore, the amplitude of this downturn in the model is much shallower than observed. Given that the model incorporates a mass-dependent coupling that is responsible for the observed downturn, it is possible that a recalibrated model that incorporates our findings and the recent results for Ruprecht 147 could improve the level of reproduction of the data and increase the predictive power of the model.

3.5.4c Implications for modeling of rotating stars

The new M 67 rotation periods thus continue to challenge theoretical rotational evolution models. No rotational evolution model to date is capable of reproducing the observed behavior for old cool stars later than mid-K. This

is unsuprising, as the calibration of the models for a long time could only rely on warmer stars. And it is only recently that we have started to see that the behavior for cool stars differs strongly from that anticipated. This discovery began with the work of Curtis et al. (2019) on NGC 6811, whose behavior in the red sparked the idea of a (temporarily) stalled spindown, found further indication in the works of Gruner & Barnes (2020) and Curtis et al. (2020) for Ruprecht 147, and is now confirmed by the new data on M 67. The best results are achieved by the Spada & Lanzafame (2020) parameterized two-zone model and small adjustments to the model could potentially provide a better match to the observations.

3.5.5 Stars at and around the turn-off point

In contrast to younger clusters where all stars redward of the Kraft break are still on the main sequence, M 67 is old enough that this becomes an issue. For those evolved stars, their colors (and temperatures) are no longer a valid proxy for the stellar mass. Consequently, we need to return to the mass as the relevant indicator, and examine the stars omitted above. We estimate the stellar masses of our sample stars from an isochrone fit with a `PARSEC` isochrone of 3.6 Gyr age (cf. panel (a) of Fig. 3.17). The uncertainty for this mass estimate is typically on the order of $\Delta M \lesssim \pm 0.05\,M_\odot$.

Plotting the rotation periods against mass (panel c) instead of color (panel b) unclutters the region around the turn-off point. It also demonstrates that those stars appear to populate a direct extension of the cluster sequence toward the blue. Panel (d) of the same figure projects the stars back to their zero-age main sequence (ZAMS) color, estimated from a 100 Myr isochrone and the derived stellar masses. For this comparison, we have included binaries whose type does not suggest a tight system, that means, excluding eclipsing and cataclysmic systems, and those whose CMD position makes a mass estimate difficult, that is, photometric binaries. As expected, eclipsing and cataclysmic systems show much faster rotation rates than comparable stars of the same mass/ZAMS color.

The impact of post-main sequence expansion of the star's envelope is likely to be a small effect on their current rotation periods as their radii have not increased significantly ($\lesssim$ 2 %, cf. panel (c) of the figure). This is estimated from a comparison of the radii of ZAMS stars and those at the age of M 67.

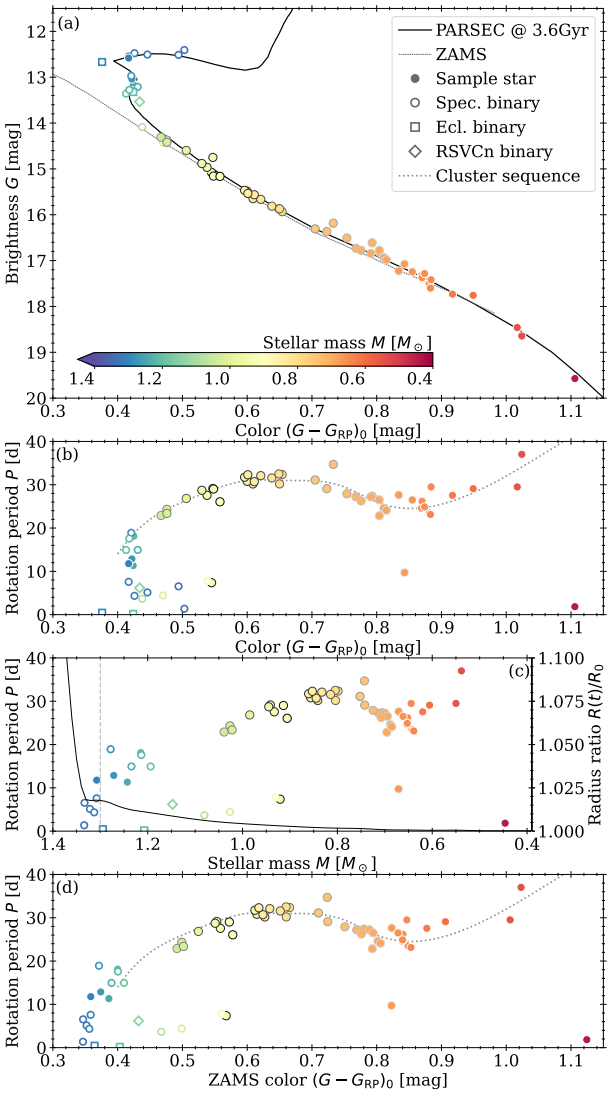

Figure 3.17: *CMD and three CPDs highlighting M 67 sample stars evolved beyond the Main sequence. Panel (a) shows a CMD of our sample with the stars color coded according to their masses. Differing symbols distinguish different types of binaries. Panel (b) shows a corresponding CPD in Gaia colors and identical symbols. Panel (c) plots the rotation periods of the stars against their estimated masses. An approximate indication of the position where stars cease to have an outer convective zones (i.e., the Kraft break) is overplotted with a dashed gray line. The solid black line corresponds to the scaling on the right and denotes the ratio between current ($R(t)$) and ZAMS stellar radius (R_0). Panel (d) shows an inferred CPD with stars assigned colors they had when on the ZAMS.*

3.6 Conclusion

We have studied space-based photometric data from *Kepler*'s *K2* mission for the 4 Gyr open cluster M 67 to examine this key object in its role as a gyrochronology calibrator and to extend our knowledge of the evolution of stellar rotation. We used the *K2* superstamp created from Campaign 5 target pixel files together with a stellar sample based on *Gaia* DR3 and performed membership analysis. We constructed light curves of stars in the superstamp region based on aperture photometry and devised a correction algorithm to deal with the well known *K2* systematics. We identified periodic signals in 128 of these light curves, and created a color-period diagram using the 47 stars which are believed to be effectively single main-sequence stars. Those span spectral types from early-G type stars to mid-M and as such reach a region hitherto unexplored.

Our data connect well to prior studies on M 67, especially Barnes et al. (2016b). Most of the data of Dungee et al. (2022) lies redward of ours but their results agree with ours in the overlap region and extend it smoothly toward the very red. The work of Gonzalez (2016b) and Esselstein (2018) is also shown to be consis-

tent with our work if they are suitably pruned of binaries and light curves with remaining instrumental effects. Despite the current extension toward significantly later-type stars, open cluster rotation period data remains compatible with the idea that effectively single stars populate a unique surface in rotation period-mass-age space. However, the suggestion of a diminishment of spindown for K-type stars by Curtis et al. (2019) based on NGC 6811 data, and subsequently supported by Gruner & Barnes (2020) and Curtis et al. (2020) for Ruprecht 147 now appears to be secure. The shape of the rotation period surface is more complex than originally envisaged, and deviates strongly from the classical Skumanich-style, mass-dependent predictions. A comparison with models of rotational evolution shows that the models appear to be inadequate for stars redder than mid-K. We find that the model of Spada & Lanzafame (2020) currently provides the closest description of the spindown by invoking a third mass-dependent timescale that parameterizes internal angular momentum transport. We conclude that future models likely need to include three distinct physical processes to account for slow, fast, and low-mass rotators if they are to accurately describe stellar spindown.

One fact about stellar rotation appears to continue to hold in the aftermath of the newly-obtained data. *Single stars continue to occupy a unique surface in rotation period-mass-age space.* However, its shape is now found to be more complex than was indicated schematically in Meibom et al. (2015). The warmer part of the sequence appears to behave mostly Skumanich-like, albeit with a strong mass dependence. Current models already reproduce this behavior reasonably, and it is likely that a good description can be found using only one or two mass-dependent timescales. But it is not true for the cooler part of the surface where the behavior becomes more complex. It is likely, and the transition from the Barnes (2010) model to the Spada & Lanzafame (2020) model strengthens this thought, that the description of the cooler part requires the inclusion of at least a third parameter, an additional distinct mass-dependence of stellar spindown. Finally, it appears that even photometric binary stars of M 67 age are so diverse in their rotational behavior as compared with single stars that they seem to be unsuitable for gyrochronology at present.

○ ○ ○

Appendix

The Appendix to this paper begins on page 109 as Appendix Sections E – G.

Acknowledgements

We are grateful to an anonymous referee for insightful suggestions that helped to improve the quality of this paper.

Part 4 – Paper III

Wide binaries demonstrate the consistency of rotational evolution between open cluster and field stars[†,‡]

***D. Gruner**, S. A. Barnes, and K. A. Janes*

Abstract

Gyrochronology allows the derivation of ages of late-type main sequence stars from their rotation periods and a mass proxy such as color. It has been explored in open clusters, but a connection to field stars has yet to be established successfully.

We explore the rotation rates of wide binaries, representing enlightening intermediaries between clusters and field stars, and their overlap with those of open cluster stars.

We investigate a recently created catalog of wide binaries, match them to observations by the *Kepler* mission (and its *K2* extension), validate or rederive their rotation periods, identify 283 systems where both stars are on the main sequence and have vetted rotation periods, and compare them with open cluster data.

We find that the vast majority of these wide binaries (236) line up directly along the curvilinear ribs defined by open clusters in color-period diagrams or along the equivalent interstitial gaps between successive open clusters. The parallelism in shape is remarkable. 12 additional systems are clearly rotationally older. The deviant systems, a minority, are mostly demonstrably hierarchical. Furthermore, the position in the color-magnitude diagram of the evolved component in the additional wide binary systems containing one is consistent with the main sequence component's rotational age.

We conclude that wide binaries, despite their diversity, follow the same spindown relationship as observed in open clusters, and find that rotation based age estimates yield the same ages for both wide binary components. This suggests that cluster and field stars spin down in the same way and that gyrochronology can be applied to field stars to determine their ages provided that they are sufficiently distant from any companions to be considered effectively single. The results also suggest that the impact of metallicity variations on the spin down is likely not to be a major concern.

[†]*The contents of this chapter have been published in Astronomy and Astrophysics, Volume 675, id.A180*

[‡]*The complete Table 7.10 is only available in electronic form at the CDS.*

4.1 Introduction

Wide binary systems are unique in the sense that they combine aspects of both field stars and cluster stars in an advantageous way. With field stars, they share the diversity regarding their formation and composition, the continuous and vast range of their ages, and their scattered locations across the Galaxy. And just as with cluster stars, the shared origin and coevality of the components furnishes insights not gained from an isolated star, especially with respect to stellar evolution. Thus, they provide us with an opportunity to connect the behaviors of cluster and field stars by asking whether an assertion that is true for one component treated as a field star is also true for the other. This duality allows us to probe beyond the limited parameter space spanned by cluster stars while still benefiting from the intrinsic consistency of the individual components. In this paper, we demonstrate an underlying connection between the rotation/age behaviors of clusters and wide binaries, thereby strengthening the possibility of deriving ages through rotation (gyrochronology) for appropriately characterized cool field dwarfs.

Reliable characterization of stars is essential to various fields of astronomy. From exoplanet hosts to stars in larger populations, understanding the star is key to understanding the system. However, a crucial parameter involved in such characterization is the rather elusive stellar age. But deriving reliable ages requires rather extensive data and cumbersome work, especially for late-type main sequence stars, the most frequent types of stars in the universe. The methods employed typically involve the observed correlation of one or more stellar parameters with age. However, classical stellar parameters either change only very little over the course of billions of years (e.g., temperature, luminosity), can only be used reliably in young stars (e.g., Li abundance), or change as long-term averages while varying significantly on short time scales (e.g., activity). This imposes various limits on their applicability, especially during the long main sequence careers of cool stars, during which the classical parameters are almost constant. For an extensive review of age dating methods see Soderblom (2010).

Gyrochronology offers an age dating method that alleviates some of these problems, particularly on the main sequence. It exploits the observed decline in stellar rotation with age. The idea of this spindown goes back to the work of Skumanich (1972) and scattered antecedents. Subsequently, it was found that the spindown is systematically mass dependent (Barnes 2003, see also Barnes 2007). Numerous studies of stellar open clusters have since explored the spindown relationships further, including (but not limited to) the Pleiades (125 Myr, van Leeuwen et al. (1987), revisited by Rebull et al. 2016), the Hyades (650 Myr, Radick et al. (1987), revisited by Douglas et al. 2019), Praesepe (700 Myr, Agüeros et al. 2011, revisited by Douglas et al. 2017 and Rampalli et al. 2021), NGC 6811 (1 Gyr, Meibom et al. 2011a; Curtis et al. 2019), NGC 6819 (2.5 Gyr, Meibom et al. 2015), Ruprecht 147 (2.7 Gyr, Gruner & Barnes 2020; Curtis et al. 2020), and M 67 (4 Gyr, Barnes et al. 2016b; Dungee et al. 2022; Gruner et al. 2023).

Taken together, the defined mass dependence of rotation at the age mileposts provided by clusters defines a skeleton of rotational evolution, enabling the ages of non-cluster stars to be read off by comparison with that skeleton, regardless of the details of spindown of stars of differing mass. For additional context, readers may refer to Chap. 5 in Basri (2021).

Although such studies have shown that the underlying spindown relation is more complex than originally thought to be, it has remained true that all (late-type main sequence) stars populate a single surface in mass-age-rotation period space, a fundamental underpinning for gyrochronology. Recently, Fritzewski et al. (2020) have provided some evidence for the universality of the relation by finding that the rotational distributions of five roughly coeval (125 Myr) clusters NGC 2516, Pleiades, M 35 (Meibom et al. 2009), M 50 (Irwin et al. 2009), and Blanco 1 (Cargile et al. 2014) are essentially indistinguishable. Such similarity was also observed at around 2.5 Gyr for NGC 6819 and Ruprecht 147 by Gruner & Barnes (2020).

What is now missing is a robust connection to field stars. As a first step, we need to establish that the spindown relation we observe in open clusters holds for much more diverse field stars as well. While this appears to be likely it still requires verification. Exploring this with individual field stars returns us to the original problem that field star ages are difficult or even impossible to derive by other methods. But we can investigate a different option – one that embodies the middle ground between open clusters and individual field stars – wide binaries.

In certain significant ways, genuine wide binaries constitute the *smallest possible open clusters*. They are composed of stars born at the same time from the same molecular cloud[1].As such they have the same age and metallicity, the very advantage leveraged by cluster work, although the precise values may not be known to us. Furthermore, their spindown should have (in a mass-dependent sense) progressed to an equivalent point. Unlike stars in close binaries, the two components of a wide binary are distant enough to be spatially resolved and not to interfere mutually with their individual evolution (e.g., by tidal interactions). The rotation periods of cluster stars have already been shown to define certain mass-dependent patterns, with each cluster forming the rib of a skeleton that defines how rotation changes with both mass and cluster age. We show here that wide binary stars follow the *same skeleton* defined by cluster rotational evolution, thereby allowing an important rotational connection between clusters and field stars to be recognized. Interestingly, while we compare wide binaries with open clusters, wide binaries are generally not present within clusters (Deacon & Kraus 2020).

This idea has been explored before, although perhaps not as definitively as we are able to do in this pa-

[1] It has been suggested that certain wide binaries could be formed via gravitational capture (Dhital et al. 2013, and references therein); our results below do not broadly support such a claim for our sample, although it might still be true for the occasional rare system.

per. Barnes (2007) demonstrated that the components of the wide binaries ξ Boo AB, 61 Cyg AB, and α Cen AB have consistent gyro ages while finding deviations for 36 Oph ABC. Mamajek & Hillenbrand (2008) expanded this list with wide binaries whose rotation periods were estimated from their activity level to compare them with their proposed spindown description. Overall, they found reasonably good agreement between their predictions and the measured periods. However, there were numerous deviations, enough to cast reasonable doubt on the validity of the fundamental assumptions. Nearly a decade later, Janes (2017) used *Kepler* data for wide binaries to compare their rotational behavior with extant spindown descriptions. His findings echoed those of Mamajek & Hillenbrand (2008); the overall trends appeared to be plausible but a significant number of binaries deviated from the predictions. This work identified a number of 'complexities' such as the redder stars rotating faster, something unexpected at the time. Updated samples (Janes 2018, 2019) did not help to overcome these difficulties. Recently, Silva-Beyer et al. (2022) have followed-up with another comparison that traced similar steps based on different, more recent, spindown descriptions and again arrived at similar, albeit generally more optimistic, conclusions.

Taking wide binary coevality and the validity of gyrochronology somewhat at face value, Deacon et al. (2016) briefly touched on the topic based on the Mamajek & Hillenbrand (2008) description, finding their own results in the same ballpark of agreement (see their Fig. 11). Similarly, Otani et al. (2022) devised a method to compare the accuracy of commonly used spindown models regarding their ability to estimate ages for stars in wide binaries. Finally, Pass et al. (2022) have explored fully-convective M-dwarfs with the help of wide binaries to constrain their spindown evolution.

The prevailing impression conveyed by prior wide binary work is that while a large fraction of wide binaries confirm expectations, a substantial fraction does not. The latter creates doubt about the generality of spindown and the validity of gyrochronology. However, there is a common denominator in these studies; all of them compared wide binaries to prescriptions of spindown models rather than directly to open cluster observations. (To a certain extent, they had no choice since relevant observations were either sparse or unavailable, especially towards older ages.)

We argue that such a comparison is flawed in principle, as recent open cluster studies (Gruner & Barnes 2020; Curtis et al. 2020; Dungee et al. 2022; Gruner et al. 2023) have shown that the spindown of older cluster stars deviates strongly from the predictions (which were extrapolated from younger ones). And even among younger clusters the degree to which the models reproduce the observations is questionable. Consequently, comparing a model that is not able to describe the clusters at a given age to wide binaries is not particularly instructive. Therefore, we here present a study that mitigates the effects of inadequate spindown models by directly comparing observations alone – open clusters to wide binaries.

This paper is structured as follows. In Sect. 4.2, we describe the construction of our wide binary sample, the open cluster data used, and the framework for the subsequent comparison. This part includes the (re)derival or validation of rotation periods, with illustrative examples of identified issues detailed in Appendix H. The comparison between wide binaries and clusters is carried out in Sect. 4.3 and the results are further dissected in Sect. 4.4, followed by some conclusions in Sect. 4.5.

4.2 Sample construction and setup

This section describes the assembly of the relevant data and the manner of preparing them for the subsequent analysis. Our approach has been enabled by three developments: (1) the availability of the cluster skeleton for FGKM stars out to 4 Gyr (the age of the M 67 cluster), (2) the availability of a large sample of wide binaries from *Gaia* astrometry, and (3) the availability of space-based photometry from the *Kepler*/*K2* space mission (Borucki et al. 2010; Howell et al. 2014), enabling the rotation periods of many of these wide binaries to be determined. The base data consists of a sample of wide binaries with vetted rotation periods, a significant number of them rederived, and of a set of open cluster stars with known rotation period measurements.

4.2.1 Wide binary sample

We begin with the wide binary (WB) catalog of El-Badry et al. (2021, EB21 hereafter). They have assembled a list of 1.3 million WBs based on Gaia EDR3 (Gaia Collaboration 2020) astrometry of stars within 1000 pc. This sample overlaps to varying degrees with those of Mamajek & Hillenbrand (2008), Janes (2017, 2018, 2019), and Silva-Beyer et al. (2022). They have followed a cautious approach in their assembly, dismissing doubtful systems from their sample, and providing a list with only high probability WB pairs. EB21 also removed stars appearing in multiple binaries, together with a dedicated search for, and elimination of stars in clusters and groups. This ensures that there will be no overlap between our WB sample and open cluster stars. (A significant part of the open cluster sample we make use of in our work below is based on *Kepler* and *K2* data). However, this also means that we lose genuine resolved triple systems; they may benefit from a similar separate future investigation to that performed here. Furthermore, the sample has also likely lost a certain number of genuine binaries that have suffered chance alignments with more distant tertiaries. Overall, this precaution has reduced the sample size, depriving us of a number of genuine systems. However, we ourselves favor a rather exclusive approach to an inclusive one in constructing our sample, for which we require excellent reliability. Therefore, we are fully aligned with the approach of EB21.

The step-by-step process of assembling our sample is illustrated in Fig. 4.1 and detailed below. We updated the stellar parameters of the EB21 sample with Gaia DR3 (GDR3, Gaia Collaboration et al. 2022) measurements. Because the faintest stars often do not have $G_{\rm BP}$ and

$G_{\rm RP}$ magnitudes, we dismissed those stars from the sample. Furthermore, we remove stars whose CMD positions, based on $G_{\rm BP} - G_{\rm RP}$ and $G - G_{\rm RP}$, are inconsistent to avoid stars with problematic photometry. GDR3 includes a match to *The Two Micron All Sky Survey* (2MASS, Skrutskie et al. 2006) catalog which we adopt in addition. We note that the GDR3 match to 2MASS is not perfect. There are numerous binaries where both component GDR3 sources have been matched to the same 2MASS source; again we dismissed such binaries from our sample.

Based on the 2MASS identifiers, we looked up the stars in the Kepler Input Catalog (KIC, Kepler Mission Team 2009) and the K2 Ecliptic Plane Input Catalog (EPIC, Huber et al. 2017). Those in turn were used to match stars to their *Kepler* and *K2* archive light curves and to find them in the rotation period samples of McQuillan et al. (2014, ∼34 000 rotation periods from *Kepler*, MQ14 hereafter) and Reinhold & Hekker (2020, ∼30 000 rotation periods from *K2*, RH20 hereafter). We note that while RH20 report individual periods for each *K2* campaign a particular star was observed in, those periods can be inconsistent[2]. In case of multiple reported periods for a given star we adopt the one with the highest normalized peak[3]. Here we only retain WBs for which at least one star has an associated light curve. This procedure provides us with a sample of 12202 WBs (24404 stars, with 9126 from *Kepler*, and 15278 from *K2*). Only a minority of these stars (3334, with 1869 from *Kepler* and 1465 from *K2*) have a reported period. They belong to 3124 wide binaries, with 210 of them being systems for which both stars have an identified rotation period.

One of the criteria we demand for this work is the validity of the rotation periods used. This encouraged us to inspect them in some detail. It soon became obvious that a certain fraction of the rotation periods reported in MQ14 and RH20 are not as reliable as we had hoped. We identified problems that render a reported rotation period unusable. These appear to originate in one of two sources: (1) From light curve creation – here there is cross-contamination from nearby stars (removes 131 periods), and (2) from period detection – here there is misidentification of non-periodic variability and/or remaining data systematics as a periodic signal (removes 65 periods). We illustrate these problems in more detail in Appendix Sect. H. These issues lead us to manually inspect all stars, together with their on-sky surroundings, their periods, and light curves in our sample to either verify ($\Delta P_{\rm rot} \leqslant 10\,\%$, 3086 stars), adjust ($\Delta P_{\rm rot} > 10\,\%$, 52 stars), or altogether dismiss (196 stars) the previously reported rotation periods. This inspection involves a comparison with light curves from similar[4] stars in the surroundings to identify common trends. *K2* targets are particularly affected by this issue. For this process, we have downloaded the *Kepler* and *K2* light curves for all relevant stars. Where available, we used the *K2 Systematics Correction*[5] (`k2sc`, Aigrain et al. 2016) and *EPIC Variability Extraction and Removal for Exoplanet Science Targets*[6] (`Everest`, Luger et al. 2016, 2018) light curves for additional validation.

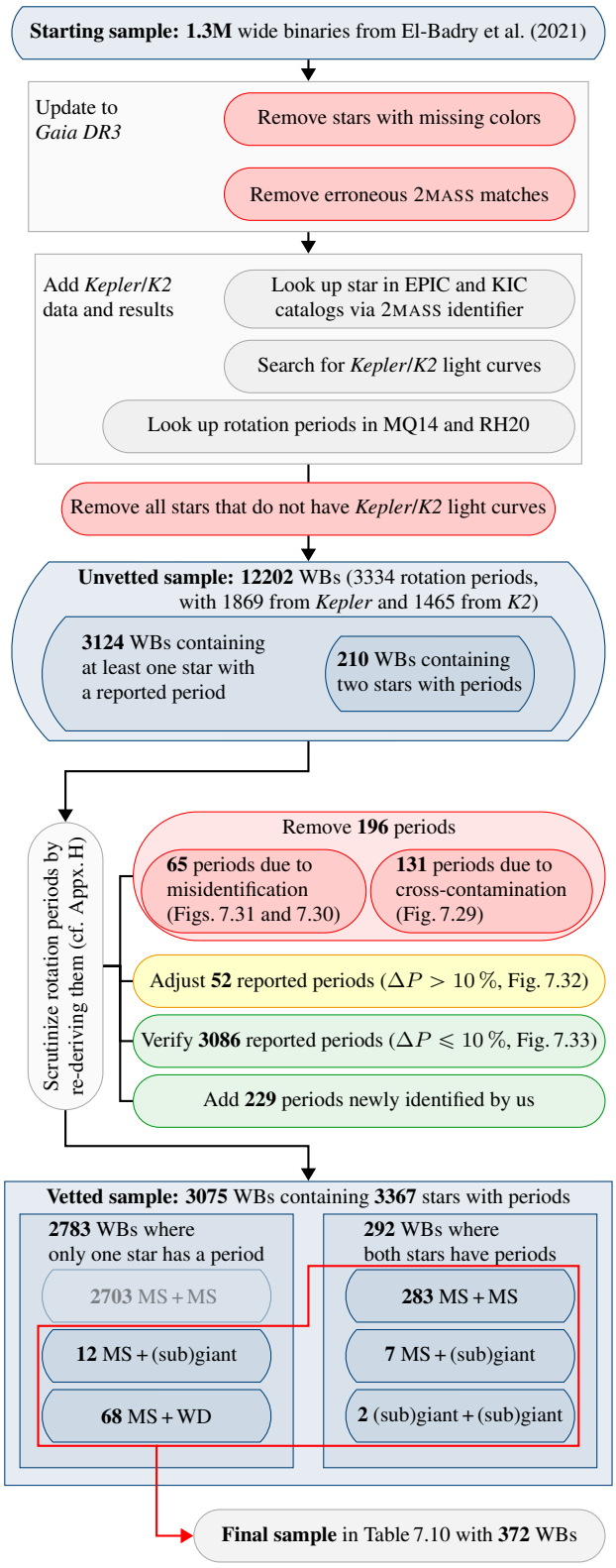

Figure 4.1: *Flowchart visualizing the steps of the wide binary sample selection process as detailed in Sect. 4.2.1.*

[2] e.g., EPIC 211638150, for which RH20 reports $P_{\rm C05} = 26.8 \pm 4.8$ d, $P_{\rm C16} = 20.6 \pm 2.2$ d, and $P_{\rm C18} = 22.7 \pm 2.9$ d

[3] see *Hpeak* column in their catalog at `J/A+A/635/A43/table2`

[4] i.e., comparable in color and brightness

[5] `archive.stsci.edu/prepds/k2sc/`

[6] `archive.stsci.edu/hlsp/everest`

We also inspected the immediate surroundings of a star for crowding relative to the comparatively low spatial resolution of *Kepler*. When the origin of the observable variability was in doubt, we rejected the star from our sample.

We were also able to add rotation periods that have not been identified in MQ14 or RH20 for an additional 229 stars (127 from *Kepler* and 102 from *K2*). These were derived using procedures described in detail in Gruner et al. (2023, GBW23 hereafter). Note that we suppress the period errors in all figures for visibility reasons. However, these are listed in Table 7.10. Typically, the error is $P_{\rm err} \sim 0.1 P_{\rm rot}$.

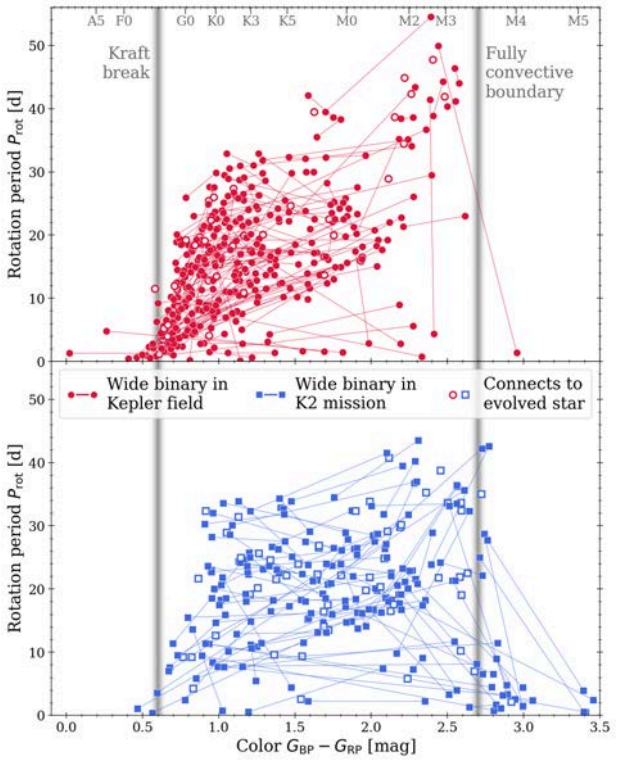

Figure 4.2: *Our wide binary sample, split into the Kepler field and K2 subsamples. The two components of each binary are connected by straight lines. The Kraft break (beyond which more massive stars lack an outer convective envelope and thus do not experience significant magnetic braking) and the boundary between partially-convective and fully convective stars are marked. Unfilled symbols indicate the main sequence components of WBs that contain evolved stars. (The latter typically do not have measured periods).*

We thus arrive at a sample of 3367 stars with rotation periods, belonging to stars in 3075 WBs. 283 wide binaries are composed of two main sequence stars where both have rotation periods. Figure 4.2 illustrates their distribution in the color-period diagram, and Table 7.10 lists an excerpt of our full sample. The figure helps to visualize the different emphases of the *Kepler* and *K2* missions; *Kepler* favored G-type stars whereas *K2* emphasized redder spectral types. However, in all subsequent matters we do not distinguish between *Kepler* and *K2* targets and treat them as equivalent.

There are of course a large number (2783) of additional wide binaries for which only one of the component stars has a measured rotation period. The majority of these are composed of two main sequence (MS) stars. The periods for these stars lie in the same regions of the CPD as our sample, but the absence of a companion period prevents us from making an effective comparison between the two[7]. Accordingly, we do not consider them further in this work. However, there is a certain type of WB system with only one period which retains interest for us, namely those where the star without a period is somewhat evolved. Those components have left the main sequence and their positions in a Color-Magnitude diagram (CMD) correlate strongly with their ages. This means that the evolved component in these systems can help us verify the (rotation period based) age of the non-evolved MS component. We will address those 89 systems separately below. For 7 systems the evolved stars have rotation periods in addition to the main sequence components, but we lump them together with the rest here. The process described above leaves us with 372 WBs for further investigation in Sect. 4.4.

We note that we do not have a consistent source of reddening estimates for the WB stars, the values reported in GDR3 also being rather unreliable. Therefore, we are left to use the reddened colors and carry out the comparison below with this caveat in mind. Curtis et al. (2020) have shown that the median reddening for the *Kepler* field stars is $E(B-V) = 0.04$ mag/kpc. Given that our sample is fully within 1 kpc it is unlikely that reddening is a significant issue here.

4.2.2 Open cluster data

We now construct a comparison sample based on the open cluster (OC) work currently available. The rationale for this is our desire to be guided by the data alone where possible, instead of performing a comparison between the wide binaries and models of rotational evolution, as has been typical in prior work. Our task is enabled by recent work, including our own, in older open clusters, that was unavailable before. In particular, we ask the following question:

> *If one component of a wide binary has a rotation period that places it on the rotational sequence of a cluster, is it likely that the other component is also on the cluster sequence?*

Curiously, this appears to be extremely likely. This motivates us to create a set of groups that roughly trace out the cluster sequences and allow the binaries to each be associated with a particular cluster, a group of clusters, or the inter-cluster regions between them[8].

We selected a number of open clusters, ranging in age from the zero age main sequence (ZAMS) to 4 Gyr as our comparison sample. These are listed in Table 4.1. This sample is intended to cover the age and color range rather

[7] While we use evolved stars where an isochrone can be used to constrain the system age reasonably, the uncertainty on a main sequence isochrone age is too large to be useful. In fact, this is the fundamental motivation for gyrochronology itself.

[8] This is parallel to the usage of the 'group' terminology in geological stratigraphy.

Table 4.1: *Overview of the open cluster sample*

Age group	Cluster	Age [Gyr]	[Fe/H]	Sample ref.	N_{star}
1	Pleiades	0.15	0.032	1	759
	Blanco 1	0.15	-0.016	2	127
	NGC 2516	0.15	-0.008	3	308
	M 35	0.15	-0.123	4	441
	NGC 3532	0.3	0.050	5	279
2	Hyades	0.65	0.149	6	23
				7	237
	Praesepe	0.7	0.196	7	743
	NGC 6811	1.0	0.032	8	71
				9	171
3	NGC 752	1.4	-0.037	10	12
4	NGC 6819	2.5	0.093	11	30
	Ruprecht 147	2.7	0.089	12	32
				13	35
5	*No open clusters for* $2.7 < t < 4$ *Gyr*				
6	M 67	4.0	0.072	14	20
				15	64
				16	47

Notes. *Age groups refer to the rough age classification set in Sect. 4.3. [Fe/H] and A_V for all clusters is taken from Dias et al. (2021).*

References. *(1) Rebull et al. (2016); (2) Gillen et al. (2020); (3) Fritzewski et al. (2020): (4) Meibom et al. (2009); (5) Fritzewski et al. (2021); (6) Radick et al. (1987); (7) Douglas et al. (2019); (8) Meibom et al. (2011a); (9) Curtis et al. (2019); (10) Agüeros et al. (2018); (11) Meibom et al. (2015); (12) Gruner & Barnes (2020); (13) Curtis et al. (2020); (14) Barnes et al. (2016b); (15) Dungee et al. (2022); (16) Gruner et al. (2023)*

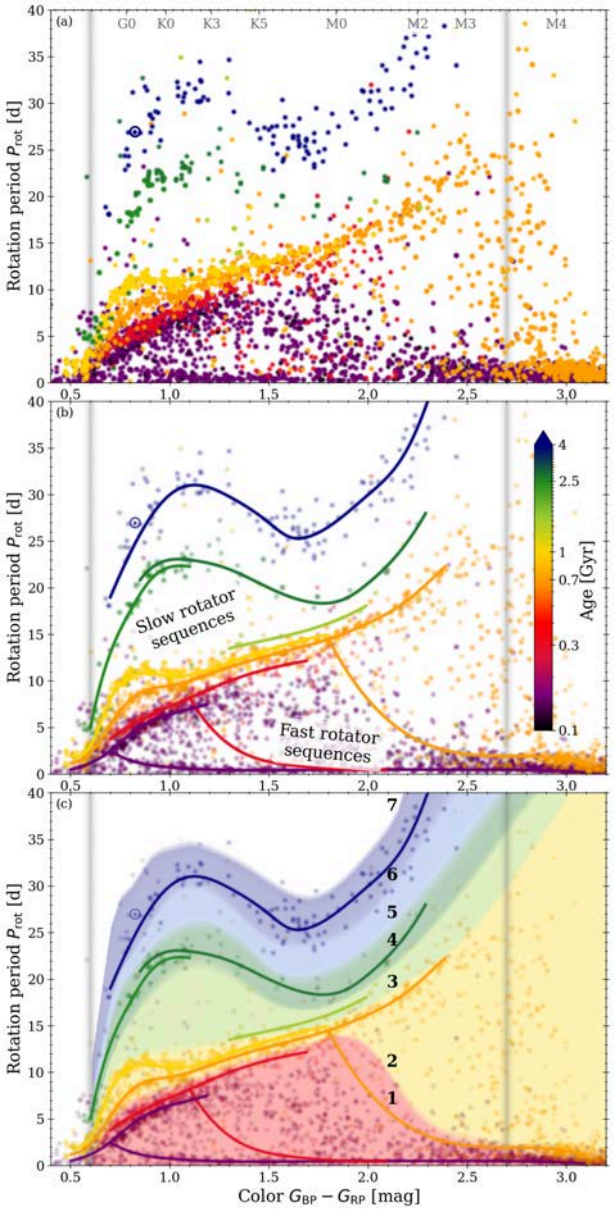

Figure 4.3: *Color period diagrams for our sample of open cluster stars. Panel (a) shows all the stars from our open cluster compilation (cf. Table 4.1). Panel (b) shows the same stars overplotted with a manual indication of the sequences followed by stars of the same age (the cluster sequences), with slow and fast rotator sequences where available. Panel (c) shows how the cluster sequences and inter-cluster gaps are used to divide the continuous space of the CPD into groups 1–7 (cf. Sect. 4.2.3). Stars, sequences, and groups are all color coded by age (see colorbar in panel (b), based on the cluster ages in Table 4.1). The sun is shown with its usual symbol. As in Fig. 4.2 vertical gray lines indicate the Kraft break and the fully-convective boundary.*

than to be complete with respect to the specific OCs covered or to studies of the listed clusters. However, it is sufficient to illustrate the cluster sequences at a given age to the extent of current availability in the literature. Overlap between different studies on the same OC are permitted, and we do not remove stars that occur more than once in the sample. From each source catalog, we only adopt the rotation period and the identifiers used for the stars and match all to GDR3. This results in a consistent set of photometry for all WBs and OCs. The accumulated data for 12 open clusters is shown in panel (a) of Fig. 4.3. We obtain the $E(B-V)$ reddening for each cluster from the compilation of Dias et al. (2021) and calculate the reddening in Gaia colors, that is $E(G_{BP}-G_{RP})$, via the prescription of Casagrande & VandenBerg (2018),

$$E(G_{BP}-G_{RP}) = 1.337 \cdot E(B-V). \quad (4.1)$$

In all matters, we always use dereddened colors for the cluster stars.

We note that we do not subject stars from the OC sample to the same scrutiny as the WB stars. There are outliers in the individual cluster samples but the very fact that we can identify them as outliers is already telling, as the clusters are defined well-enough that outliers are actually visible. And it is those sequences themselves that we ultimately compare our WBs to.

In panel (b) of Fig. 4.3 we have drawn fiducial lines by eye through the cluster sequences. Keeping in mind that there is a continuous color-period space (or color-age space), we have distinguished the cluster age groups with different colors in this figure (cf. panel c) and in the following ones. Groups 1, 2, 4, and 6 are associated directly with the open cluster sequences, see Table 4.1 and Sect. 4.2.3 for the details. Because of the large age gap between the clusters,

we have inserted additional groups there. Group 3 is placed in the gap between Praesepe/NGC 6811 (2) and NGC 6819/Ruprecht 147 (4), whereas group 5 is placed between NGC 6819/Ruprecht 147 (4) and M 67 (6). Finally, we have added a group (7) for WB systems older than M 67. The result is effectively a stratification of what is actually a continuous distribution of stars in the color-period space (cf. panel c of Fig. 4.3). However, as with certain other groupings of continuous distributions into discrete bins[9], there seems to be a distinct benefit to the grouping, as we show below.

4.2.3 Grouping of the open cluster distribution

We define the set of seven age groups in the CPD whose mass-dependent range is dictated by the OCs, including the sequences themselves and the intervening gaps. Here, we define the following groups:

1. Group 1 contains main sequence clusters younger than 500 Myr. These clusters contain significant numbers of stars occupying the fast rotator sequence. The group incorporates the ZAMS clusters, Pleiades, Blanco 1, NGC 2516, M 35, and the roughly 300 Myr-old cluster NGC 3532.
2. Group 2 includes clusters with ages ranging from 0.5 Gyr to 1 Gyr, thereby containing the Hyades, Praesepe, and NGC 6811. The fast rotators in these clusters (with the exception of M-dwarfs) have converged to the slow rotator sequence.
3. Group 3 ranges from (above) 1 to (below) 2.5 Gyr, and marks the first inter-cluster gap in the cluster distribution. Only NGC 752 is available for this group, but it barely contains any stars with known periods to define a sequence[10].
4. Group 4 covers the 2.5 Gyr to 2.8 Gyr region, and contains the more evolved clusters NGC 6819 and Ruprecht 147.
5. Group 5 spans the age range from (above) 2.8 Gyr to (below) 4 Gyr, and marks the second inter-cluster gap. No open cluster study in this age range is currently available.
6. Group 6, around an age of approx. 4 Gyr, is formed solely by the oldest open cluster studied with respect to rotation – M 67.
7. Group 7 includes all wide binaries likely older than 4 Gyr, where no open cluster has been explored to date.

Panel (c) of Fig. 4.3 shows the (approximate) ranges covered by these groups in comparison with the open cluster data. We acknowledge some leeway in the group stratification. For instance, age group 6 is set around 4 Gyr but also includes the sun (4.56 Gyr, Amelin et al. 2002, cf. also the CPD position of the sun in comparison with the width of M 67 sequence). There is also some overlap in the color-period diagram among the fast-rotating stars.

[9] The colors assigned to different segments of the rainbow and demographic cohorts (generations) are obvious examples.

[10] Curtis et al. (2020) have noted that of the 12 rotators reported in Agüeros et al. (2018) 4 are non-members post Gaia DR2, and many of the rest are binaries.

4.3 Grouping the wide binaries

In this section we compare the distribution of rotation periods as seen in the wide binaries with the age groups we have defined based on the open clusters. We wish to investigate the consistency between the WB components with respect to the groups and explore the agreements and deviations. There is one caveat in this comparison; while the colors of the clusters are dereddened, the colors of the binary stars are not and are subject to an unknown amount of reddening. This effect is likely small for most stars, but could affect the grouping of the more distant or the bluest stars in our sample (due to the strong color-dependence of the cluster rotational sequences for $G_{\rm BP} - G_{\rm RP} < 0.8$ mag). The comparison below is carried out with this in mind, occasionally permitting equal reddening for both binary components to be considered consistent.

First, we assign each WB to one of our age groups. For this procedure, we designate the stars of the individual WBs as the *leading* (L) and *trailing* (T) components. The L component is placed in the color-period diagram (CPD) and assigned to a group based on its $G_{BP} - G_{RP}$ color and period $P_{\rm rot}$. With that we essentially use gyrochronology and assign it a *gyro age*, an age based on its rotation period and color, albeit a rather rough one. The choice of which star in a particular WB is designated L is based on which star's CPD position allows for a better estimation of the age (group). Furthermore, we avoid stars in a somewhat evolved state and, when possible, very fast rotating stars. Typically, this means that we adopt the star whose color is in the range $0.8 < G_{\rm BP} - G_{\rm RP} < 1.8$ since the age groups allow the best distinction in that region. Crucially, we avoid late-F and early G-stars as leading components because of the strong color-dependence in this region and the (likely small) uncertainties arising from the unknown reddening.

Figure 4.4 illustrates this process on a few selected WB pairs. Encircled stars mark the L component for the selection process. We note that WB systems are selected for the figure to allow good visualization, that means L components of similar colors, spanning several age groups and connecting to different areas of the CPD, essentially covering the diversity of the systems we find.

With all L components set, we now take the T components, place them in the CPD, and see how their locations compare with the age groups assigned to the L components. Depending on the result of this comparison, we classify the wide binary pair itself as either S, F, or C, depending on the content[11]. The classification of binary systems composed of two MS stars, each with a listed rotation period, follows these criteria:

- If T falls reasonably well on the slow rotator sequence in the same age group as L, we mark the whole system as S. Such systems are shown with connected red circles in the figure.
- If T is located where the OCs matching L's age group

[11] Naming derived from S = slow rotator, F = fast rotator, C = contradicting, E = evolved, and W = white dwarf.

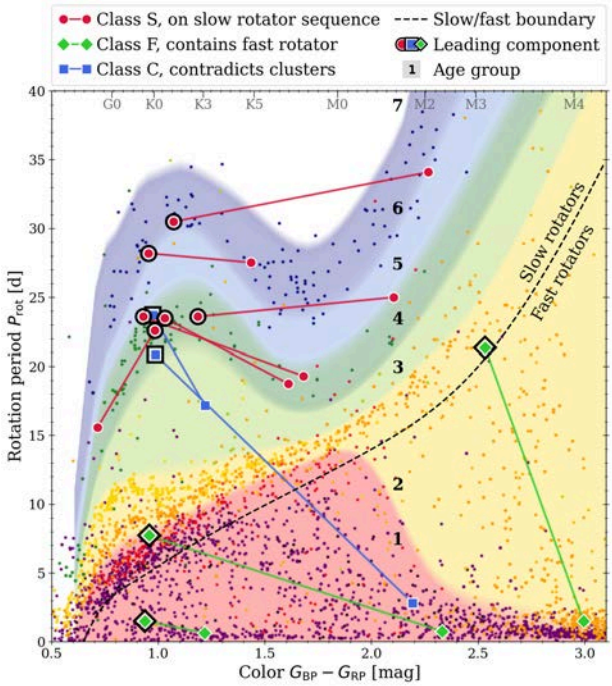

Figure 4.4: *Color period diagram defining age groups (colored regions) and illustrating of the classification of our wide binaries. Color coding roughly follows Fig. 4.3 and corresponds to the cluster stars plotted in the background (small dots). Age group numbers (1 – 7) correspond to Table 4.1. 11 sample wide binaries are overplotted. Red circles indicate binaries agreeing with the slow rotator sequences, green squares are those containing a fast rotator, and blue boxes mark those altogether disagreeing with the cluster behavior. Stars of each wide binary that were preferentially used to assign them to an age bin, i.e., the* L *components are outlined in black. The dashed line denotes the approximate boundary used to distinguish between fast and slow rotators (cf. the sequences indicated in panel (b) of Fig. 4.3). The systems plotted are listed in Table 7.10.*

see figure on facing page ▸

Figure 4.5: *Color period diagrams for six age groups shown in order of age (left to right, top to bottom). Gray dots are open cluster stars, and cluster stars of the same age group are highlighted. Components of wide binaries are connected by lines and overplotted. Red circles indicate those agreeing with the slow rotator sequences (S), green squares are those connecting to a fast rotator (F), and blue boxes are those altogether disagreeing with the cluster behavior (C). Open symbols denote* doubles*, i.e., WB components identified as binaries themselves. Numbers in the upper left corner of each panel enumerate the binaries in that age group, distinguished by class (see color coding). Numbers in parentheses indicate how many of these are hierarchical, i.e., where the component itself is a binary. The sun is shown with its usual symbol. As in Fig. 4.2 vertical gray lines indicate the Kraft break and the fully-convective boundary.*

indicate a fast rotator population, then we classify the system as *F*. All of these binaries are from age groups 1 and 2 because only such clusters have a population of fast rotators. Such systems are shown with (connected) green squares in the figure.

- All other systems, that means those whose *T* components are main sequence stars and do not fall in a region that is populated by cluster stars of *L*'s age group, are classified as *C*. They are indicated with connected blue boxes in the figure.
- Age group 7 is special in this regard as there are no cluster predictions and it contains all systems that are arguably older than age groups 6 (4 Gyr). Since we cannot fully classify systems in this groups, we adopt all systems there as *S*, but investigate those later separately in Sect. 4.4.3a . An exception to this are obvious contradicting systems that contain one star in age group 7 and one in another group. Those are accordingly classified as *C*.
- Several systems in age groups 1 and 2 are composed of two fast rotators and are as such classified as *F*.

We note that it is more difficult to identify rotationally deviant component stars in WBs as compared with clusters where the sheer numbers of other stars on the slow rotator sequences make outliers stand out.

Systems whose *T* component is not a main sequence star but has evolved past it are classified based on *T*'s state. If *T* is a (sub)giant of any kind, the system is marked as *E* and if *T* is a white dwarf (WD) it is marked as *W* (cf. footnote 11). Neither is displayed in the figure. With that, we classify MS+MS systems (which are the interesting ones for a direct cluster comparison) based on the CPD positions of the components, whereas we classify all other systems based on the CMD positions of the components.

Table 4.2 gives an overview of the numbers of WB systems that fall into all the aforementioned classes, also resolved by age group. Table 7.10 correspondingly includes a column that lists the class assigned to each wide binary system. Following our definition of the classes, all systems now labeled as *S* or *F* agree with the open clusters (except those in age group 7 which are beyond), and those labeled *C*, which are contradictory. Figure 4.5 displays the distribution of wide binaries separated into the individual age groups 1 – 7, also distinguished by class. Below in Sect. 4.4, we will explore the emerging patterns and distributions in detail. The commonalities are illustrated in Sect. 4.4.1, whereas the disparities are investigated in Sect. 4.4.2. Age group 7 and classes *E* and *W* and will be discussed separately in Sect. 4.4.3 below.

4.4 Discussion

In this section, we examine how our binary sample compares with the open clusters (Sect. 4.4.1). We investigate outliers and identify probable causes for any deviations (Sect. 4.4.2). Generally, a remarkable agreement between WBs and OCs is found. We follow up (Sect. 4.4.3) with a closer look at the WBs that either exceed the age range of the open clusters or for which one component is an evolved star.

4.4.1 Systems in agreement with open clusters

We find that the vast majority (193 *S* and 43 *F*) of the wide binary systems agree with the cluster sequences. Only a small fraction (38 *C*) does not. This means that 236 out of 274 total (MS+MS, excluding group 7) WB systems

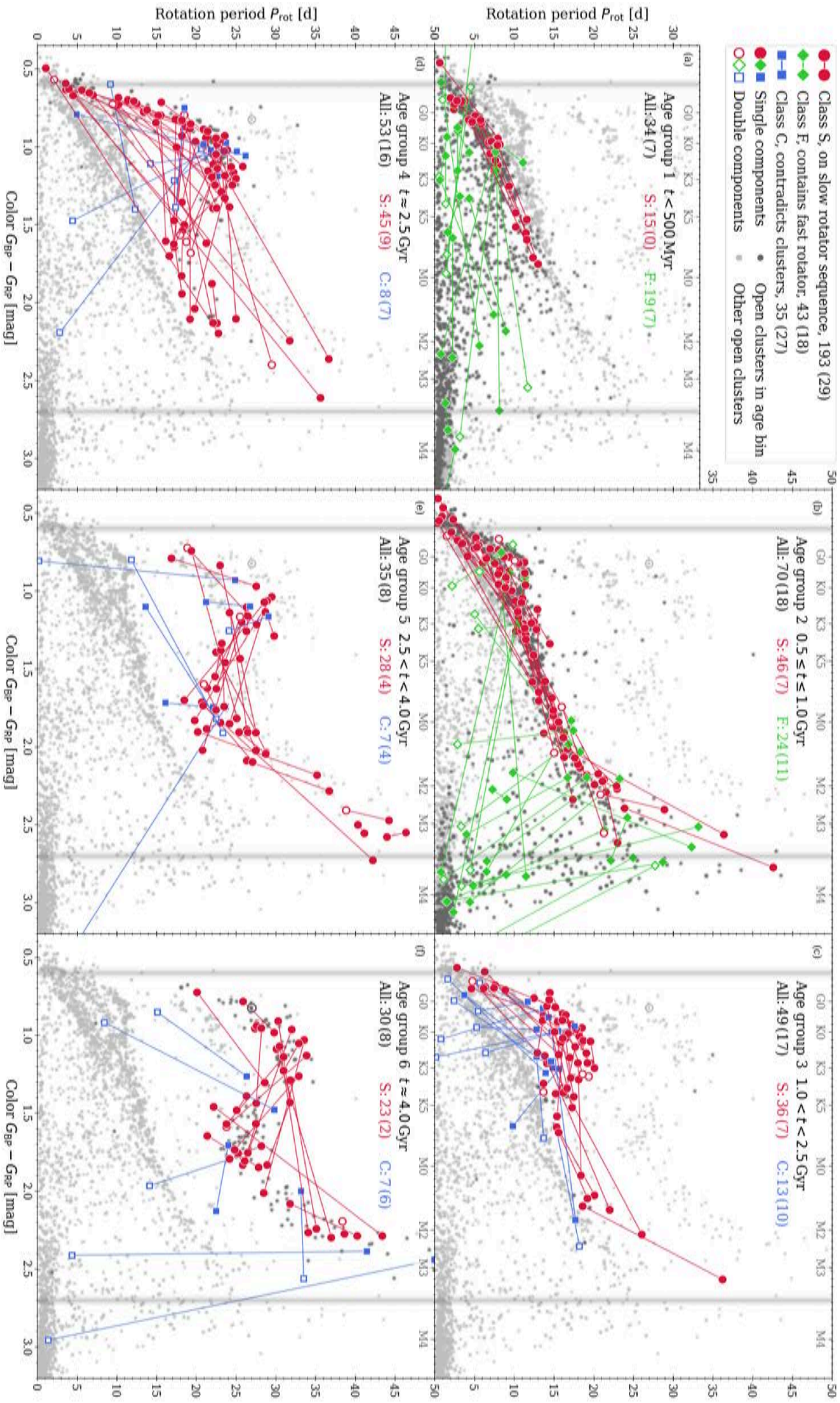
Class S, on slow rotator sequence, 193 (29)
Class F, contains fast rotator, 43 (18)
Class C, contradicts clusters, 35 (27)
Single components
Open clusters in age bin
Double components
Other open clusters
(a)
Age group 1 t < 500 Myr
All: 34 (7) S: 15 (0) F: 19 (7)
(b)
Age group 2 0.5 ≤ t ≤ 1.0 Gyr
All: 70 (18) S: 46 (7) F: 24 (11)
(c)
Age group 3 1.0 < t < 2.5 Gyr
All: 49 (17) S: 36 (7) C: 13 (10)
(d)
Age group 4 t ≈ 2.5 Gyr
All: 53 (16) S: 45 (9) C: 8 (7)
(e)
Age group 5 2.5 < t < 4.0 Gyr
All: 35 (8) S: 28 (4) C: 7 (4)
(f)
Age group 6 t ≈ 4.0 Gyr
All: 30 (8) S: 23 (2) C: 7 (6)
Rotation period P_{rot} [d]
Color $G_{BP} - G_{RP}$ [mag]
G0 K0 K3 K5 M0 M2 M3 M4

Table 4.2: *Population of wide binary systems within the individual age groups, also distinguished by class.*

Class	1	2	3	4	5	6	7[b]	Total
S	15	46	36	45	28	23	9	202
F	19	24	–	–	–	–	–	43
C	0	0	13	8	7	7	3	38
MS[a]	34	70	49	53	35	30	12	283
E	0	1	4	7	3	4	2	21
W	4	17	13	8	15	8	3	68
All	38	88	66	68	53	42	17	372

Notes.[a] *Class* MS *is simply the sum of all WBs composed of two main sequence stars (i.e., excluding classes E and W).* [b] *Age group 7 includes three systems classified as C based on the analysis in Sect. 4.4.3a .*

agree well with the cluster predictions. They agree even to the extent that they follow the sinusoidal shapes of the sequences from the old clusters; *they connect along and often across the peaks and troughs in the color dependence*. The fact that the WBs agree with the clusters holds both for two very similar component stars (which tend to have very similar periods) and for two very different components (which may or may not have two very different periods). The above statements hold across all the age groups, from the youngest to 4 Gyr (and likely beyond). The number of contradictory systems is relatively constant across the groups. Except for age groups 1 and 2 where there is not really one sequence and deviations are not apparent.

Age group 2 contains the largest number of WB systems here. This is likely a consequence of its youth and the presence of the fast rotators, as both make it relatively easy to detect rotation periods. There is a clear transition from group 1 to 2, seen both in open clusters and in WBs, of the fast rotator population moving redward. The remaining blueish ($G_{\rm BP} - G_{\rm RP} < 2.0$) fast rotators in group 2 are low in number and all of them show signs of binarity.

Age group 3 lies in the gap region between clusters of ages 1 Gyr and 2.5 Gyr. It is notable that the WBs here seem to slot in perfectly between these two cluster populations, with a certain amount of (understandable) overlap only among the bluest stars where distinguishing age groups is inherently difficult.

Age group 4 is the most striking of our sample. It contains WB systems that are directly comparable with the 2.5 Gyr-old clusters NGC 6819 and Ru 147. Its stars range in color from close to the Kraft-break to early M-dwarfs, in certain cases even within the same WB system. Here we find the most impressive agreement between WBs and OCs; stars connect across large color ranges and fall on the same cluster sequence.

Age group 5 lies in the unpopulated region between clusters of age 2.5 Gyr and 4 Gyr. As such, it resembles systems in group 3. It is relatively sparsely populated as compared with younger groups, and shows a significant amount of scatter. However, this feature is partially by design. This group includes all the binaries that cannot be clearly associated with groups 4 or 6.

There is an apparent shift in population from the younger to the older groups regarding the color range populated by the corresponding WBs. With increasing age, the numbers begin to favor K-type stars instead of G-type stars. This is likely a consequence of the reduced variability shown by aging G-type stars which makes them more difficult to detect in comparison with K and M spectral types.

To summarize, we find that the vast majority of MS + MS wide binary systems agree with the individual cluster sequences and our corresponding age groups. The age groups represent a series that changes with age, albeit a rather rough one. We can now display the data of Fig. 4.5 in a single color-period diagram to fit the groups back together. We reduce the systems plotted to the 236 agreeing ones (i.e., classes *S* and *F*) and add the 9 systems from group 7. These are shown in Fig. 4.6. The WBs form a clearly layered structure[12]. Despite the significant scatter in certain regions of the CPD, the individual age groups are clearly separated in our WBs.

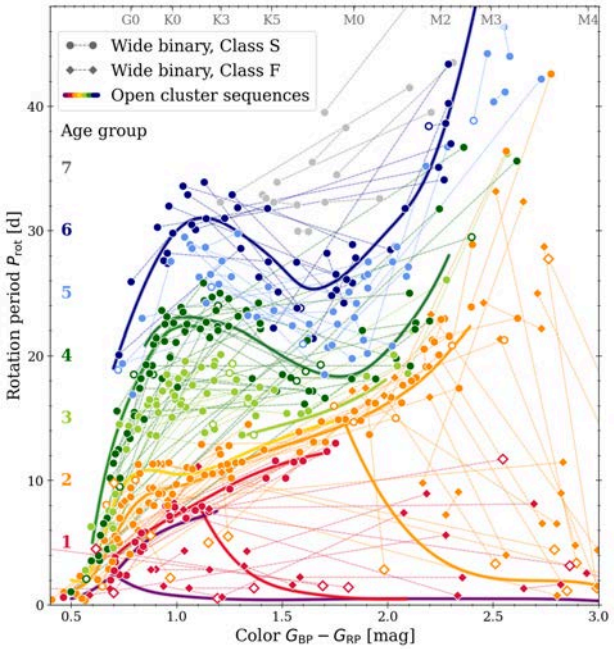

Figure 4.6: *Color period diagram (CPD) showing the close agreement between the open cluster sequences and the wide binaries split into distinct age groups. The color coding follows the designation of the groups in Fig. 4.3 (see also* Age group *labeling). The open cluster sequences are overplotted with relevant colors. Only systems classified as S and F are shown. Again, open symbols denote stars identified as* doubles.

A recent study by Bouma et al. (2023) recommends interpolating directly between clusters to estimate ages for stars in a slightly different but related way. They use the effective temperature $T_{\rm eff}$ and rotation period $P_{\rm rot}$ to estimate an age probability distribution. In Appendix I, we apply their software to our WB sample by estimating $T_{\rm eff}$ from the stars' $G_{\rm BP} - G_{\rm RP}$ color. The calculated ages (including errors) and the temperature estimates are included

[12] Again, we note the parallels to stratigraphy in geology.

in the electronic version of Table 7.10. We find reasonable agreement between the calculated ages and our group affiliations despite the fact that we might sort a given binary into another group based on either the joint behavior or preference for the *leading* companion in the system (cf. upper panels of Fig. 7.35). In fact, the ages for the components of our systems consistently on the slow rotator sequence (i.e., class *S*) both correlate strongly ($r = 0.94$) and have a relatively small dispersion $1\sigma = 0.28$ Gyr (cf. lower panel of Appendix Fig. B1). This corroborates the assumed coevality of wide binary stars and demonstrates that age estimates based on a star's color and rotation period can provide consistent results when used carefully. To a good approximation, one may adopt the mean age for the class *S* wide binary components as the age of the system.

4.4.2 Systems contradicting the open clusters

A big obstacle to definitive conclusions in prior work was the larger number of systems that did not behave as expected. Therefore, we take a closer look at our outliers – those systems where components do not agree with what the open clusters define. But before that, we remark about the quantity and distributions. In our total sample of 274 wide binaries (MS + MS, excluding group 7) we find 38 pairs (∼14 %) that do not agree with the OCs. This fraction is already lower than that seen in the works of, e.g., Mamajek & Hillenbrand (2008) and Silva-Beyer et al. (2022). Furthermore, unlike Silva-Beyer et al. (2022), we do not see an increase in disagreement for the (presumably) older systems. We believe that this difference is a consequence of the nature of the comparison (observations vs. observations, rather than observations vs. models, because the models get worse for older ages, see e.g., their Fig. 2).

4.4.2a Hierarchical systems

GBW23 has shown that at the age of M 67 it is exceedingly more likely than not that a star that shows signs of binarity (even only photometric binarity) is not suitable for gyrochronology as it is likely to exhibit a contradictory rotation period in the sense that the rotation period lies recognizably distant from the single-star cluster sequence in the CPD. Interacting binaries transfer angular momentum from the binary orbit to stellar rotation via tidal interactions. Thus they are in a sense rejuvenated, and rotate faster than their compatriot single stars. These rejuvenated stars are not useful for gyrochronology – whether for its calibration or for its application. GBW23 concluded that gyrochronology breaks down almost entirely for stars like this, and in their sample only about 20 % of the stars with signs of binarity behave like single stars.

This means that signs of binarity are a very good indicator that a star's rotation rate differs from the normal spin-down (typically too fast). Conversely we can say that if a star shows a rotation rate that does not fit its age group and we find signs of binarity for it, it is very likely (the more so the older the system is) that this binarity is responsible for that misfit.

All this, of course, specifically refers to close binarity. Systems as distant as our wide binary components are not affected in this way. However, the individual components themselves may be much closer binary systems as well. These *doubles* are subject to the consideration above and such a WB system is called *hierarchical*.

After constructing our sample, we queried every star in the SIMBAD database[13] and marked it as binary if it was listed there as such (e.g., as spectroscopic or eclipsing binary). We complemented this with an annotation if GDR3 photometry suggests a photometric binary. We find that 76 of our MS + MS wide binary systems are hierarchical (i.e., contain a double). Table. 7.10 flags hierarchical WBs and individual stars suspected as doubles accordingly and we highlight them in the relevant figures.

Looking back at our outliers, we find that 29 of the 38 systems are hierarchical. They are displayed in Fig. 4.7. In agreement with our hypothesis of rejuvenation, we find all but one hierarchical system to exist in a configuration where the double component exhibits rotation that is too fast for the age predicted by the non-binary component.

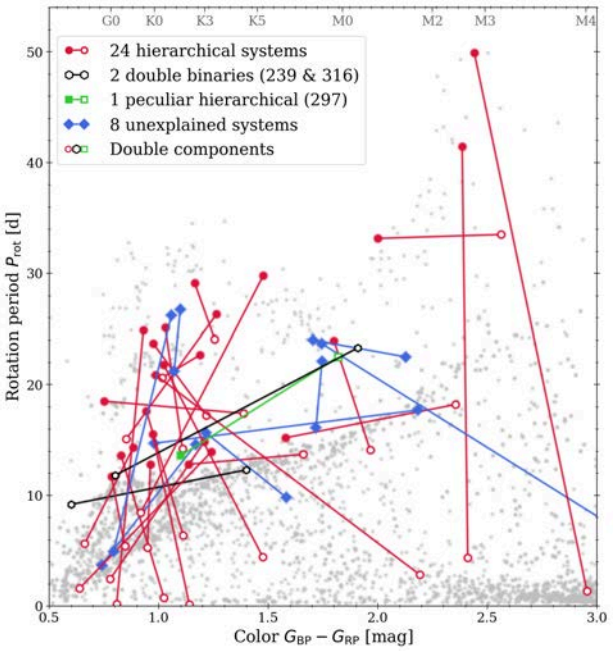

Figure 4.7: *Color period diagram (CPD) for the wide binary outliers. Open symbols indicate* doubles*, those WB components with binarity signs themselves (i.e., the WB system is hierarchical). Such hierarchical systems are displayed in red, while WBs in blue indicate those where we cannot identify an obvious reason for not following the cluster sequences. Binary 297 (shown in green) is hierarchical, but is the only system in our sample where the hierarchical component is not the one with younger gyro age.*

The only exception to this pattern is binary 297 whose secondary is KIC 2442084, an eclipsing binary (K-star + K-star) in a highly eccentric, relatively long-periodic[14] orbit ($e = 0.599$, $P_{\rm orbit} = 47.9$ d, Kjurkchieva et al. 2017). The high eccentricity of this long-period orbital configu-

[13] simbad.u-strasbg.fr/simbad

[14] We mean long as compared with the expected rotation period

ration is likely the reason for the inverted rotation in the wide binary as the slow periastron passage is prone to decelerate a faster rotating star.

It is also the case that a certain number of hierarchical systems lie uncontroversially on the rotational sequences we have defined. 29 binaries (out of 193 in age groups 1 – 6) in the *S* class and 18 binaries in the *F* class are hierarchical. However, this fraction is much smaller ($\lesssim 20\,\%$ of the systems per group, cf. Fig. 4.5) than the $29/38 \approx 76\%$ in class *C*, more along the lines of what was found by GBW23. We further note that the hypothesis of GBW23 that the impact of binarity increases with age finds its confirmation here. While the fraction of hierarchical systems in our wide binary sample is relatively constant throughout the age groups, the fraction of those that do not agree with the cluster sequences increases with age (cf. counts listed in Fig. 4.5; none in groups 1 and 2, about half in groups 3 – 5, and nearly all in group 6). However, we stress that our sample only allows a conclusion based on relatively low number statistics in this regard.

Our sample also contains two systems in which both stars are identified as binaries. Generally speaking their position as a whole in a CPD (cf. black symbols in Fig. 4.7) is likely meaningless. Any assigned age group in such a case has to be viewed with commensurate caution.

Where does this leave us regarding close binarity of stars and their rotational evolution? There is likely a (complicatedly-shaped) boundary beyond which a close binary system remains rotationally unremarkable (i.e., both components evolve without interactions). This boundary likely depends on the orbital configuration (separation, component masses, eccentricity, etc) but may not be such that we encounter multiple unresolved systems (i.e., likely relatively close) that are inconspicuous. Future efforts will have to explore this boundary, for example on samples like ours, to identify the differences between the affected and unaffected systems. One point, however, is already abundantly clear – whether the rotation periods of close binary components will be affected is likely determined already during the system's formation. Gravitational encounters during the system's lifetime tend to drive close systems closer and wide system wider (often summed up in the distinction between *hard* and *soft* systems, see e.g., Binney & Tremaine 1987). What remains is to evaluate the amplitude of the effect that angular momentum exchange has, and to identify the boundary beyond which it loses significance. Until such understanding is attained, close binaries (and with that hierarchical systems like we discussed here) will remain inconclusive in the pursuit of exploring the rotational evolution of stars. And of course all of this still leaves out two more aspects regarding unresolved binaries – the (combined) color may cease to be a valid proxy for the mass and the origin of an observed rotational signal is somewhat ambiguous.

4.4.2b Other outliers

After removing the hierarchical systems, there are 9 outlier WBs remaining. We are unable to identify an obvious source for their contradictory behavior. However, there are a range of possible explanations for their apparent non-conformity:

1. The wide binary is actually not genuine, but merely a chance alignment. As such the WB components would not be coeval. This is improbable here because of the stringent selection criteria in the source sample of EB21.
2. There can still be undetected multiplicity. This is likely the cause for most of the remaining deviations, especially for those WBs where one star rotates much faster than is expected from the other. An undiscovered planetary system (especially one hosting a Hot Jupiter) could also potentially be responsible.
3. Other possible, albeit rather very unlikely, scenarios include peculiar reddening that invalidates the color as good proxy for the mass and angular momentum transfer from chance encounters.

However, independently of whether any of those arguments can explain the nature of an outlier system, we argue that 9 remaining outlier systems out of 274 is a small enough fraction not to matter to the overall conclusion. It is certainly small enough not to undermine the core principles discussed here – the validity of gyrochronology for field stars and the coevality of wide binaries.

While none of the explanations given above are conclusive evidence for the deviations observed, they are good indications despite being somewhat circumstantial evidence. It could be argued that we have not offered a definitive criterion to separate rotationally well-behaved and ill-behaved systems. After all, many systems of class *S* (rotationally completely consistent) are also hierarchical (as discussed above). Nevertheless, we contend that whereas the single/binary nomenclature constitutes a strict dichotomy, the extent to which the rotation rates of components in a binary are influenced by separation, eccentricity, etc. could potentially lie on a continuum, with only *sufficiently isolated* components free to evolve rotationally as single stars. Certainly, the contours of that required isolation have not been mapped out to date. This thought is supported by the fact that open clusters also contain binaries – some of them agree and some of them disagree with the single star sequence.

In any case, the situation again highlights an important point – if one is to adopt a sample of stars for calibration or verification purposes, one cannot rely on the statistical dominance of well-behaved, non-pathological systems but has to scrutinize the nature (and data) of each and every star that is considered.

4.4.3 Systems outside the range of open clusters

Having established that WBs occupying regions of the color-period diagram covered by open clusters actually agree with the cluster sequences, we now turn to systems where one or both components have evolved beyond available open cluster ages or past the main sequence. We divide this into systems where both components are on the

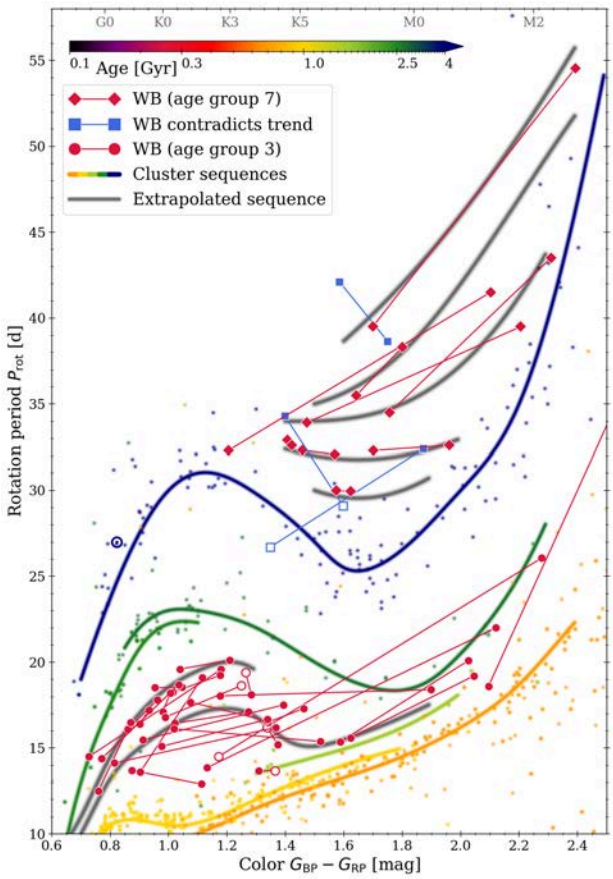

Figure 4.8: *Color-Period Diagram showing a possible interpretation of the wide binaries older than 4 Gyr and for those with ages 1 – 2.5 Gyr. The gray lines indicate a best-guess extrapolation/interpolation of the rotation sequences based on the wide binaries (red symbols) and adjacent cluster sequence (colored lines). The sun is shown with its usual symbol.*

main sequence, systems where one component is a giant or subgiant, and systems where one component is a white dwarf, with each category treated in its own sub-section below.

4.4.3a Systems beyond the cluster sequences

Unlike the situation with the intermediate age groups 3 and 5 where we can interpolate reasonably well between the cluster sequences to identify concordant and discordant behaviors, we cannot easily decide whether the binaries in age group 7 agree with the cluster predictions, given that those require extrapolation. As such, we have not classified them like the earlier cases. However, we can still compare them with age group 6 (4 Gyr), and examine their internal consistency. Fig. 4.8 shows the presumably older binaries of our sample in relation to the cluster predictions.

We notice the emergence of a certain trend from the distribution in group 7. The explicit downturn in rotation period around $G_{BP} - G_{RP} = 1.65$ mag for 4 Gyr seems to weaken slowly and eventually become a monotonic increase in period with color at even longer periods. We have drawn by eye possible extrapolated sequences in Fig. 4.8 to follow the stars in group 7.

Based on such extrapolation, we can identify three contradictory WBs at older ages (highlighted in blue in the figure). We find that two of these are hierarchical, with the hierarchical component apparently rejuvenated. Another one has a relatively large period error, and its mismatch could simply be a consequence of the generally large scatter in rotation periods observed in this long-period regime.

One detail regarding our sample in age group 7 is curious. It only contains stars in the redder regions of the cool star mass range. The earliest-type star is ∼K3 ($G_{BP} - G_{RP} = 1.2$ mag). This is likely a consequence of the difficulty of detecting rotation signals in G-type stars, rather than the absence of such stars altogether. We recall that the typical variability shown by the sun would not be detectable by *Kepler* at typical distances to stars in the *Kepler* field. However, we do know about the existence of G-type stars with periods (and independent age estimates) in the relevant region, such as HIP 102152 (8 Gyr old solar twin with $P = 35.7$ d, Lorenzo-Oliveira et al. (2020), see also Lorenzo-Oliveira et al. 2019) and 94 Aqr AB (see Sect. 4.4.4).

We attempt a similar artist's impression of the rotation sequences in age group 3 ($1 < t < 2.5$ Gyr, gray lines in Fig. 4.8). In this age range, the sinusoidal structure begins to emerge, and as it appears to move with increasing age like a wave from blue to red. However, the maximum of this wave appears to be redder than what is observed in the open clusters at 2.5 Gyr.

A similar estimate for age group 5 ($2.5 < t < 4$ Gyr) is not possible as the scatter of the wide binaries in this group is too great to be able to identify a suggestive picture. However, we note that the wide binaries are still consistent with a uniform (in a color-dependent sense) evolution between 2.5 and 4 Gyr.

4.4.3b Systems with a (sub-)giant component

Our sample contains a number of systems (21) that include (sub)giants as evolved components. The evolved star may or may not have a measured period itself. However, as the evolved component has changed its color due to its advanced state, has expanded beyond its main sequence radius, and has potentially experienced increased interaction with a planetary system, it is not expected to agree rotationally with the cluster predictions. One would need to invoke the mass directly for a meaningful comparison (as was done for M 67 by GBW23, see their Fig. 16), this, however, goes beyond the scope of this work.

We proceed with those stars analogously to our main sample, in that we consider the main sequence component as L component and assign it to an age group according to its period and color and then look up the position of T. However, this time it is the position in a color-magnitude diagram (CMD). In Fig. 4.9, we compare T's position to an isochrone whose age is determined by the gyro age of L. For this comparison we use (solar-metallicity) isochrones from the Padova and Trieste Stellar Evolutionary Code (PARSEC[15], Bressan et al. 2012; Chen et al. 2014,

[15] stev.oapd.inaf.it/cgi-bin/cmd

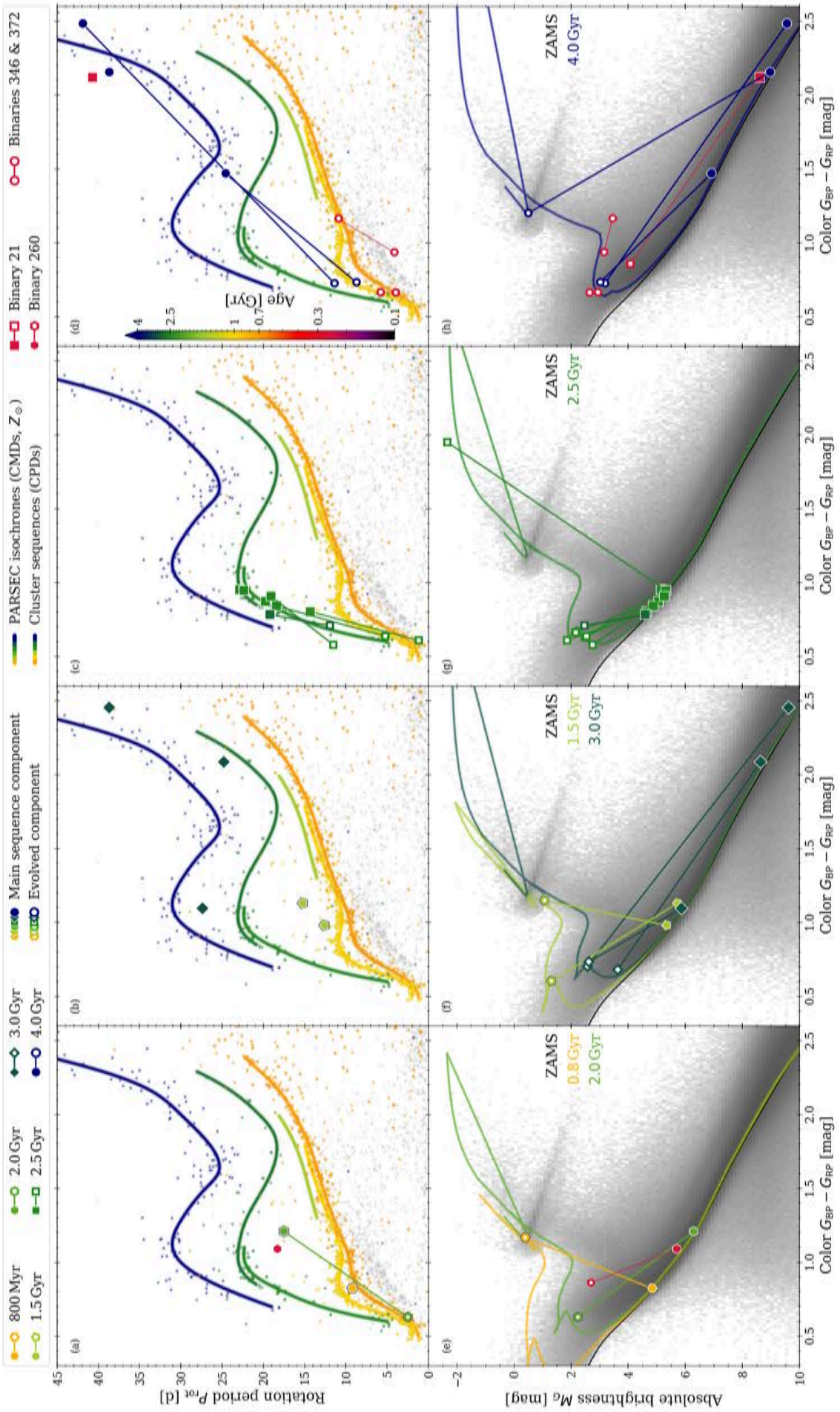
800 Myr
1.5 Gyr
2.0 Gyr
2.5 Gyr
3.0 Gyr
4.0 Gyr
Main sequence component
Evolved component
PARSEC isochrones (CMDs, $Z_\odot$)
Cluster sequences (CPDs)
Binary 21
Binary 260
Binaries 346 & 372
Rotation period P_{rot} [d]
Absolute brightness M_G [mag]
Color $G_{BP} - G_{RP}$ [mag]
Age [Gyr]
ZAMS
0.8 Gyr
2.0 Gyr
1.5 Gyr
3.0 Gyr
2.5 Gyr
4.0 Gyr

Figure 4.9: ◂ see figure on facing page
Color period diagram (CPD, panels a – d) and color magnitude diagrams (CMDs, panels e – h) for wide binaries containing an MS (filled symbols) and evolved star (open symbols) combination. The CPDs show the WBs in relation to the open cluster sample. We recall that not all evolved components have known rotation periods. In those cases, only a unconnected MS component will appear in the CPD. The CMDs show the WBs (binned by age and color-coded accordingly) against a background of the Gaia DR3 *parameters for the full El-Badry et al. (2021) sample (2.6M stars). The isochrones (*PARSEC*) are chosen to match the colors of the components of each binary. Four binaries are highlighted in red and individually identified in the legend. Those are the two WBs composed of two evolved stars (panel e), the one that does not have a consistent CMD position (panel b), and one that is arguably older than 4 Gyr. The separation of the CMD into four panels and the selection of the individual ages shown in them is for visibility purposes only. The CMD positions of binaries 21 and 346 suggest an age of ≈ 7 Gyr; however, no corresponding isochrone is shown for visibility reasons.*

2015). As can be seen, the agreement is striking. All WBs except for one contain evolved stars whose CMD positions are consistent. The outlier (binary 260, cf. panels (a) & (e) of Fig. 4.9) is highlighted in red in the figure. We note that this outlier follows the same pattern as the other outliers (cf. Sect. 4.4.2) in that the main sequence component appears rejuvenated (younger gyro age from faster rotation) as would be expected from the evolved component's CMD position[16]. For the others, all deviations are small and can easily be attributed to metallicity, reddening, some small amount of general scatter in the photometry. We also observe what was true for the main sample; this agreement holds throughout the age groups and for components of very different colors.

Our sample also contains two WBs (binaries 346 and 372, cf. panel (d) & (h) of Fig. 4.9) consisting each of two evolved stars with identified rotation periods. Both systems appear rather old and are, in a CMD context, consistent. However, their CPD positions are not helpful to our work here and we only list them for completeness.

Binary 21 appears to be older than even M 67, consistently in both the CPD and CMD (cf. panel (d) & (h) of Fig. 4.9).

4.4.3c Systems with a white dwarf component

Our sample provides an additional 68 binaries that contain a white dwarf (WD). It is always the MS star that has a measured rotation period; most WDs do not even have recorded light curves. While a comparison with WD ages is beyond the scope of this work, we can still inspect for superficial consistency. We know that WDs enter their sequence bright and hot and then slowly cool down, becoming fainter and redder with age. Fig. 4.10 generally shows the expected distribution with younger WDs (based on the main sequence star's gyro age) being higher up, and older ones further down the WD sequence. Investigating individual deviants from this behavior exceeds the scope of this work. However, we do know that some of the MS stars are binaries themselves (not separately indicated here), a fact which may skew their rotation rate and age (generally towards younger ages). This could explain the odd young WD further down the sequence. The older WDs further up the sequence do not contradict the expectations as they may be WDs from lower mass progenitors which have entered the WD phase later and have cooled down less.

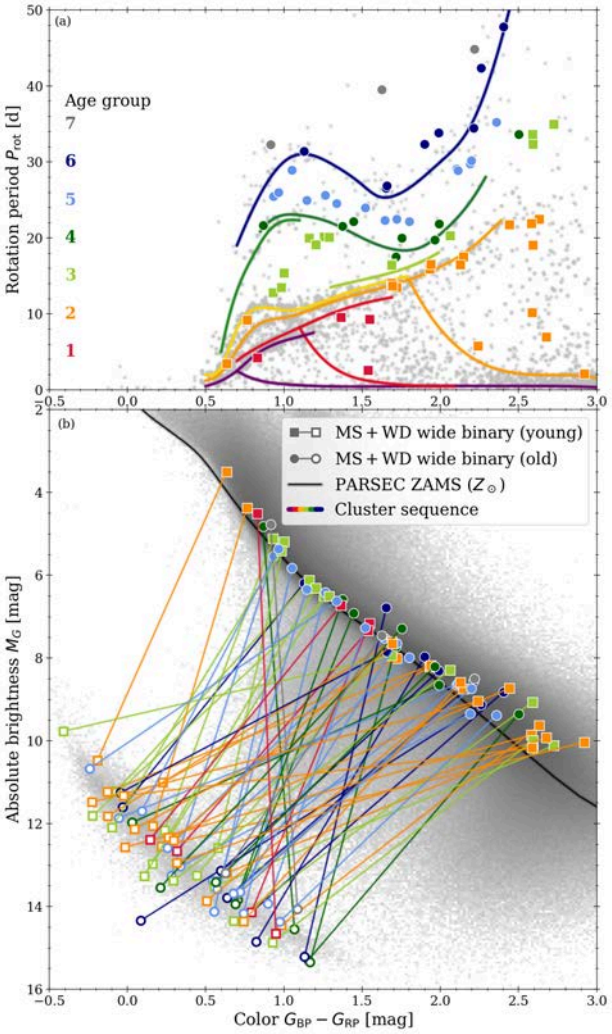

Figure 4.10: *Color period diagram (CPD) and color magnitude diagram (CMD) for all wide binaries containing white dwarfs (WD). The upper panel (a) shows the CPD of the MS components of the wide binaries color coded according to their age groups. The same sample of binaries is shown in the CMD in the lower panel (b), now connected to their WD companions (open symbols). The background gray scale distribution is of the 2.6M stars of the EB21 sample. MS stars with younger gyro ages (red-orange) show a slight preference to connect to the upper part of the WD sequence, while those with older gyro ages (green-blue) have a slight preference for the lower part of the WD sequence. Younger systems (age groups 1 – 3) and older systems (age groups 4 – 7) are shown with squares and circles, respectively.*

[16] An argument could be made that we have listed only the half-period for the MS star.

4.4.4 Revisiting well-known bright wide binaries

There are a number of familiar wide binaries that have been studied extensively in the past owing to their brightness. In particular these are some of the systems that have been considered in a rotational context by Barnes (2007), Mamajek & Hillenbrand (2008), Epstein & Pinsonneault (2014), and Otani et al. (2022). We have compiled them together in Table 4.3. Rotation periods are taken directly from the above-mentioned works, where they agree reasonably well when they overlap (see the individual references therein). We supplement the rotation data with GDR3 photometry and retrieve information regarding binarity from SIMBAD. These systems are not in our sample per se as they were not in the *Kepler* or *K2* fields of view. An exception to this is 16 Cyg which is in our sample but was rejected because of cross contamination between the two very bright stars.

Table 4.3: *Well-known bright wide binary systems.*

Binary	Component	$P_{\rm rot}$[a] [d]	$G_{\rm BP}-G_{\rm RP}$ [mag]	Notes[b]
16 Cyg	A	23.8	0.81	Double
	B	23.2	0.83	
36 Oph	A	20.7	1.06	
	B	21.1	1.06	
	C	18.0	1.41	
61 Cyg	A	35.0	1.46	
	B	38.0	1.72	
70 Oph	A	20.0	1.00	Double
	B	34.0	1.49	
94 Aqr	A	42.0	0.95	Double
	B	43.0	1.06	
alf Cen	A	28.0	0.84	Double
	B	36.7	1.02	
	C	83.0	3.80	
ksi Boo	A	6.3	1.46	
	B	11.9	1.52	

Notes.[a] *Rotation periods are adopted from Barnes (2007), Mamajek & Hillenbrand (2008), and references therein.* [b] Double *indicates that a component has itself been identified as a binary.*

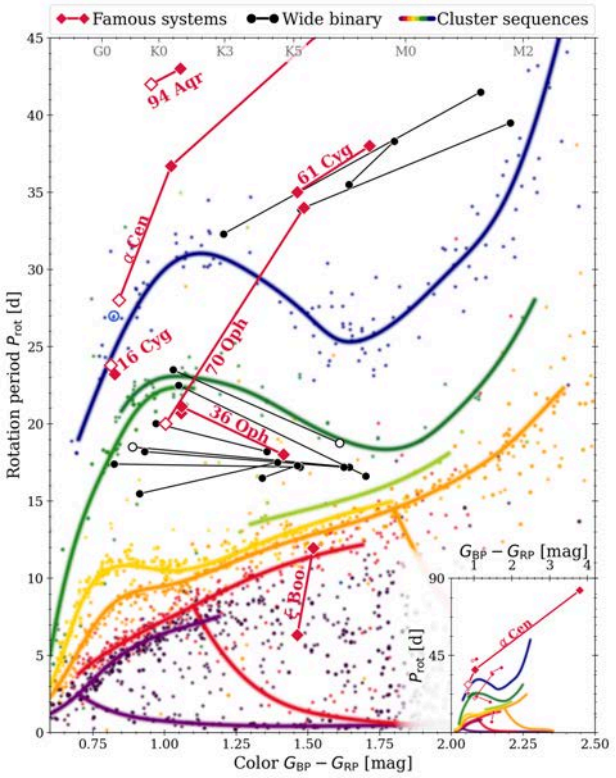

Figure 4.11: *Color-period diagram for some well-known wide binaries in the literature. These are shown in red and labeled individually (see Sect. 4.4.4 and Table 4.3.) Open cluster sequences are overplotted, together with a selection of wide binaries that follow comparable behaviors (where available) with the well-known ones. The inset shows the position of alf Cen C which extends far beyond all other systems discussed here. As before, open symbols denote* doubles*, i.e., WB components that are themselves binaries.*

Now we can compare these famous systems with our sample and the OC predictions. Figure 4.11 shows them in a combined CPD. We find significant changes in the picture since the above-mentioned work.

- ksi Boo is apparently the youngest among our sample of well-known systems. Barnes (2007) reported gyro ages of 187 and 265 Myr for the *A* and *B* components, respectively. Strassmeier & Steffen (2022) have recently reported a lithium abundance for ksi Boo B that is consistent with that of stars in M 34 (200 Myr), corroborating the system's youth. We find that the rotation periods of both components in this system fall consistently on the slow rotator sequence of the 300 Myr-old cluster NGC 3532.
- 36 Oph was anomalous in Barnes (2007) because while the *A* and *B* components are almost identical (and thus automatically rotationally consistent), *C* was found to rotate faster than expected (with gyro ages then of ∼1.5 and 0.5 Gyr, respectively for *A*/*B* and *C*). Curtis et al. (2020) pointed out that this system is rotationally parallel in the CPD with newly-obtained data for Ruprecht 147, and likely younger because it is below it. We agree with this evaluation based on comparison with the same cluster and with similarly situated WBs in our sample (in groups 3 and 4). Altogether, we find that all three stars of this system suggest a consistent age, likely around 2 Gyr.
- 16 Cyg is unaltered with respect to prior work. Both stars are very similar in multiple ways, including rotation periods. As such they are fully consistent with the M 67 cluster and WBs of 4 Gyr age, although it should be noted that the primary is somewhat evolved. Problems arise when one compares this (e.g., van Saders et al. 2016) with its astroseismic age, which appears to be of the order of 7 Gyr (e.g., Bazot 2020; Buldgen et al. 2022). However, since we are only concerned with its consistency with the OCs and WBs, which is the case, we do not engage any further with the system.
- 70 Oph was somewhat consistent with the old picture,

pointing towards an age of 1.8 Gyr, whereas at face value it is now inconsistent with what is seen for OCs. The *A* and *B* components indicate very different rotational ages. Knowing that the *A* component is a binary changes our perspective, and the system's age. Examining the system in the same way we did for all contradictory, hierarchical WBs, we find that the *A* component rotates too fast compared to the age set by the *B* component, which we estimate to be around 5 – 6 Gyr. We note that the rotation period of 70 Oph B is estimated from chromospheric activity. However, considering its similarity to 61 Cyg A in terms of color and activity and the measured rotation period of 61 Cyg A, we consider it relatively reliable. We also note that the identification of 70 Oph A as a binary is based on radial velocity variations (Halbwachs et al. 2018). Those, however, indicate an orbit of $\sim$ 88 yr, making it more likely to be the *A* - *B* orbit rather than a hypothetical *Aa* - *Ab* orbit.

- 61 Cyg is beyond the range populated by the OCs in the color-period diagram. It was always assumed consistent with itself, but its estimated age of 6 Gyr (Kervella et al. 2008) did not match its early gyro-age of 2 Gyr (Barnes 2007). Curtis et al. (2020) evolved the cluster sequence of Ruprecht 147 forward in time and found reasonably good agreement between its estimated age and its CPD position. From our current perspective – now also including results for M 67 and other WBs in the relevant region – we can confirm that the position of 61 Cyg in the CPD appears to be fully consistent with an age of about 6 Gyr.
- Alf Cen is also beyond the range populated by the OCs and our WBs. However, it gives an impression that the binarity of the *A* component again impacts its rotation rate, making it rotate faster than it otherwise would. It was consistent with being about solar age in the (now superceded) descriptions used by Barnes (2007) and Mamajek & Hillenbrand (2008), as well as the forward prediction by Curtis et al. (2020). Given that we do not know the evolution (especially of G-type stars) beyond solar age, it very well may still be consistent. There is a recent debate in the community (see e.g., Hall et al. 2021, and references therein) about how spindown behaves for sun-like stars older than solar age, but since we do not have clear indications from the open clusters, we do not engage in that discussion here. Alf Cen C, more famously referred to as Proxima Cen, is far beyond any region populated by the clusters, both in terms of color as well as period.
- 94 Aqr is likewise beyond the range populated by the OCs and the WBs. While its CPD position appears to be consistent it should be noted that the 94 Aqr A is a Hertzsprung-gap star. Thus, the CPD agreement is coincidental. Evaluating the system using methods described in Sect. 4.4.3b , we find that the CMD position of *A* suggests a younger age (3 – 4 Gyr) than B's CPD position ($\gg$ 4 Gyr).

What can we conclude from the details presented above? WBs that formerly were thought to be consistent (alf Cen, 70 Oph) are now not. These have also been found to be hierarchical systems, suggesting a possible resolution to their newly found inconsistencies with gyrochronology. Another system (36 Oph) is not known to be hierarchical other than the three resolved components which are confirmed to be consistent with gyrochronology. Similarly ksi Boo provides a consistent picture. The old age of 61 Cyg, that has sparked controversies in the past thanks to its much younger gyro age, is seen to be fully consistent. With that, no unexplained inconsistencies remain.

4.4.5 Metallicity effects

Theoretical considerations and observational indications suggest that a change in stellar metallicity changes the size of the convective zone, with consequent effects on the convective turn-over timescale and the amount of differential rotation, and thus ultimately on the stellar dynamo and activity (e.g., Karoff et al. 2018, and references therein). However, the extent to which metallicity, by a similar route, influences stellar rotation and rotational evolution has yet to be understood. Rotationally investigated open clusters have largely been of solar metallicity. (In fact, the available observational evidence suggests that all nearby clusters are in a band of near-solar metallicity, so that opportunities for related investigations are limited.) In principle, wide binaries, owing to their more diverse nature, offer a way past this. However, this means that we first require a handle on the stellar metallicity, which needs to be established individually for each binary.

To do so, we obtain metallicities from two different sources, GDR3 and the *TESS* Input Catalog (TIC 8.2, Stassun et al. 2019; Paegert et al. 2021). GDR3 metallicities are measured from a small spectral range and provided as [Fe/H] values. Regardless of their uncertainties, they at least have the virtue of being uniformly derived. TIC metallicities are compiled from a variety of spectroscopic surveys and are provided as [M/H] values.

To begin, we check each of these for consistency by comparing the metallicities of both WB components, where available. In principle, these should agree. However, as Fig. 4.12 shows, the result is sobering. While the 33 WBs with TIC values for the primary and secondary components at least display a correlation (coefficient $r = 0.65$), the 231 WBs with GDR3 values barely even correlate with each other. It is almost certain that the low correlation arises from uncertainties in the metallicity measurements rather than in the association of the wide binary components. Consequently, we are unable to use the metallicities for the individual systems in a reliable way.

However, we can make a more general observation. Although we may not know the individual metallicities very precisely it is likely that the binaries cover a much larger range. This is consistent with the fact that we are drawing our sample from both *Kepler* and *K2* data, simultaneously probing very different regions in the galaxy; the center and anti-center, in the galactic plane, above and below it, out to a distance of 1 kpc. The rotation periods have already shown that the ages of the systems considered are very diverse, ranging from tens of millions of years to more than

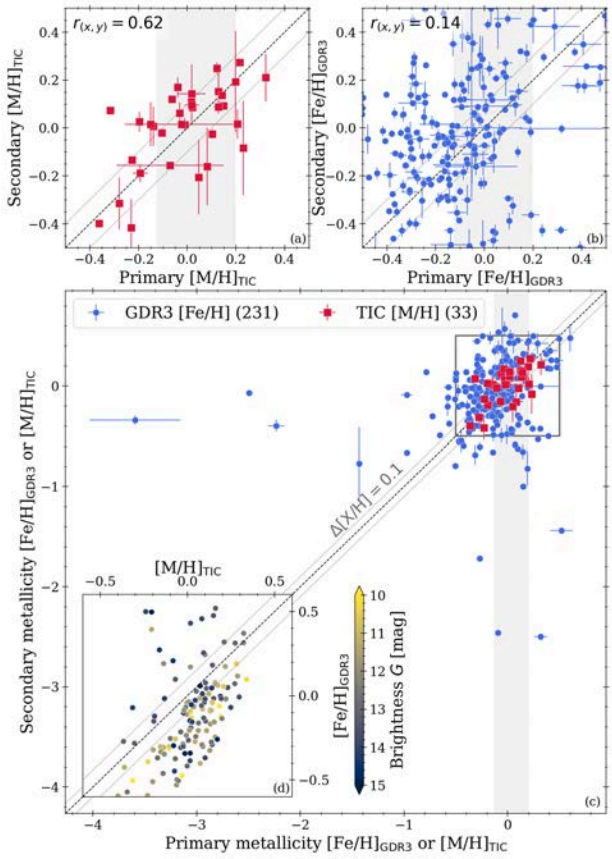

Figure 4.12: *Comparison between the metallicities of the WB components of our wide binary sample, as extracted from GDR3 (blue, [Fe/H]) and TIC (red, [M/H]). The highlighted region indicates the nominal metallicity range covered by the open cluster sample assembled in Table 4.1. The gray box in panel (c) indicates the range plotted in panels (a) and (b). Panels (a) and (b) display Pearson's r correlation coefficient (Galton 1877; Pearson 1895) between the primary and secondary's metallicities. Panel (d) compares the [Fe/H] and [M/H] measurements for all our sample stars where both are available.*

4 Gyr.

Despite that diversity in the sample, the rotation period data does not show significant deviations from the cluster predictions. Our sample contains binaries in all age groups with components of very different masses, but nearly all agree with the open clusters. This suggests to us that changes in metallicity do not impact stellar rotational evolution in a significant way. It could, however, be the case that a change in metallicity affects stars of different mass equally, meaning in our case, that both stars in the binary appear similarly displaced from their actual age in a CPD. In other words, a change in metallicity speeds up or slows down the spindown rate equally for stars of differing masses. This seems unlikely given that the spindown is strongly mass-dependent.

There is of course also the change in color with respect to a star of equal mass but different metallicity. Even a moderate variation in metallicity (Δ[Fe/H] $\sim$ 0.2) causes significant change in the relation between color and mass for a MS star. Since we do not see a change in spindown in color-period space, we would expect such in mass-period space. The explicit shape of this difference is unclear and beyond the scope of this work. It is, however, likely that the usage of color (or another photospheric parameter such as temperature) somewhat diminishes the impact of metallicity changes with respect to a systematic spindown. Thus, it is a better approximation than the alternatives to state that stars exist on a single surface in age - rotation period - *color* space. Further exploration of this will require a diverse sample of stars with well-constrained metallicities.

4.5 Conclusion

We have investigated the rotation rates of stars in wide binaries by direct comparison with those in open clusters to explore the viability of using stellar rotation as an age indicator outside clusters, perhaps even in field stars. To this end we have constructed a sample of wide binaries whose components were observed by the *Kepler* telescope during its primary and *K2* missions. After scrutinizing the relevant data, adopting only verified rotation periods, and eliminating all those that cannot be verified, we created a clean sample of 372 systems that shows remarkable agreement between the rotation rates of cluster stars and those of wide binary components.

We find 236 WBs where each contain 2 main sequence stars that agree right away with the cluster behavior. This includes WB pairs in all combinations of late-type main sequence stars, ranging from the Kraft break to the fully-convective boundary, and with ages ranging from tens of millions of years all the way to the age of M 67 (4 Gyr). The WBs in our sample follow the intricate mass-dependence of the rotation rate in open clusters, especially recently studied ones, including the flattening of the distribution around 1 Gyr and the sinusoidal shape in older clusters.

The sample also contains 19 wide binaries that contain one component that has evolved beyond the main sequence into the sub-giant and giant regions. For all but one of these we find the CMD position of the evolved component to be consistent with the main sequence star's gyro age. 68 additional WBs contain a white dwarf component and, generally speaking, their positions along the white dwarf sequence are consistent as well.

There are an additional 9 diversely-distributed WBs with dual MS components that are likely older than 4 Gyr, permitting a rough extrapolation of stellar spindown, providing hints of the dependencies of rotation beyond ages covered by open clusters available to date. Lastly, assuming that our wide binary sample consists of a group of stars that has some diversity in composition, we conclude that the impact of metallicity on stellar spindown is likely small.

A minority of MS wide binary pairs (38 in number) are positioned in discordant rotation/age configurations. Three quarters of these (29 in number) are shown to be hierarchical systems where angular momentum transfer has likely rejuvenated a component's rotation rate. This leaves us with only 9 genuinely unexplained outliers. This is similar to the fraction of outliers in the cluster sample (e.g.,

the few blue overly slow rotating stars in the Praesepe and NGC 6811 clusters, and the fast rotators in M 67).

Altogether, these results suggest that the placement of well-characterized wide binary systems in the color-period diagram is eminently comparable with open clusters of appropriate age. In fact, the components of clean wide binaries have the same rotational ages. Thus wide binaries appear to be fundamentally compatible with the usage of gyrochronology. This compatibility likely extends to suitable single field dwarfs.

The relative clarity of the results presented here is in contrast with the ambiguous results from prior work on wide binaries. We ascribe the difference to three factors: (1) Whereas prior work preferentially compared observations with models, ours is grounded in comparing observations with observations. Our ability to do the latter has been particularly enhanced by newly-available observations, especially in the older Ruprecht 147 and M 67 clusters. (2) The sample of rotation periods admitted into our sample, although larger, is likely more exclusive, informed by a greater scrutiny of the individual light curves and further recognition of the systematics and trending in *Kepler*/*K2* data. (3) The detailed investigation of outliers to identify disqualifying features such as components being binaries themselves. We also identify systems with evolved components and find that they are generally in agreement with conclusions based on the rotation of the unevolved component. Rotation periods of evolved stars, although some are available, are currently unsuitable for gyrochronology.

In conclusion, we find that the rotation of wide binary stars is demonstrably in agreement with open cluster stars where the latter are available, and broadly in agreement with expectations for more evolved systems, suggesting that gyrochronology can likely be used to obtain ages for well-characterized single field stars.

○ ○ ○

Appendix

The Appendix to this paper begins on page 127 as Appendix Sections H – J.

Acknowledgements

We are grateful to the anonymous referee for insightful comments and suggestions that helped to improve the quality of this paper.

Part 5 - Discussion

The results in context

In this thesis, I have explored the evolution of stellar rotation and the prospects of gyrochronology in old cluster stars and field stars of various ages. I have employed data that have been sitting untouched in the archives for several years, likely untouched due to the fact that they posed a significant challenge to reveal their secrets. However, they promised hitherto unparalleled insights into the rotational evolution of stars and one may paraphrase J. F. Kennedy's famous words in that *"[we] chose to [explore the rotation of old stars] and do the other things, not because they are easy, but because they are hard."*[1] Ultimately, the challenges posed by the data used in this thesis proved to be significant but not insurmountable.

This thesis (in papers I and II) details the work on *Kepler/K2* data of the open clusters Ruprecht 147 and M 67. For both, I was able to identify rotation periods after extensive data correction and systematic removal procedures. It was the first secure rotation period detection of K and M-stars for cluster stars older than 1 Gyr that showed a clear systematic behavior. It should be noted that somewhat in parallel others have worked on the same clusters (Curtis et al. (2020) on Ruprecht 147 and Dungee et al. (2022) on M 67), partially based on proprietary ground-based data, and arrived at similar conclusions to us. For paper III the focus moved toward a connection between open cluster and field stars. I used wide binaries as intermediaries between the two and investigated the intricate details of a diverse field star population. This comparison was only possible due to the open cluster data derived in papers I and II.

5.1 Answering the posed questions

This thesis aimed to answer questions regarding the rotational evolution of (old) stars, of field stars, and the prospects of gyrochronology. Let us recall those quickly:

1. *How do stars spin down beyond 1 Gyr?*
2. *Can we bridge the gap between cluster and field stars?*
3. *Can we address some of the conflicts and inconsistencies pointed out in prior work?*

After the work presented in prior sections, where are we in answering those questions? This section of the discussion is dedicated to an evaluation of the results in context.

5.1.1 How do stars spin down beyond the age of 1 Gyr?

We have explored stellar rotation in stars older than 1 Gyr in the open clusters Ruprecht 147 (2.7 Gyr) and M 67 (4 Gyr) and Fig. 5.1 shows how the new data extends on the prior knowledge of stellar rotation. Both cluster studies have used *Kepler/K2* data to accomplish this. The data, after a long road full of systematics and their corrections, revealed that even to the age of M 67 stars continue to live on a single surface in mass-rotation period-age space. This means that however the details may look like, the relation between age and rotation period (and its inversion) is a well-defined single-value function. Thus confirming that gyrochronology can be used for stars at least up to 4 Gyr.

We have, however, also seen that the shape of this surface differs widely from the (comparably simple) Skumanich-style $P_{\rm rot} \propto \sqrt{t}$ spindown. Instead of a continuous increase of the rotation period with color at a given age, we found that the distribution of Ruprecht 147 shows a flattening and suggests even a slight downturn towards redder stars. And while for Ruprecht 147, there are only a few stars with known rotation periods in this region, leaving the result somewhat speculative, our work on M 67 has eliminated any doubts about such a downturn in the distribution. Below in Sect. 5.3, I present an idea for an interpretation of the observed spindown behavior.

[1] Address on the Nation's Space Effort, Rice University, Houston, Texas on September 12, 1962.

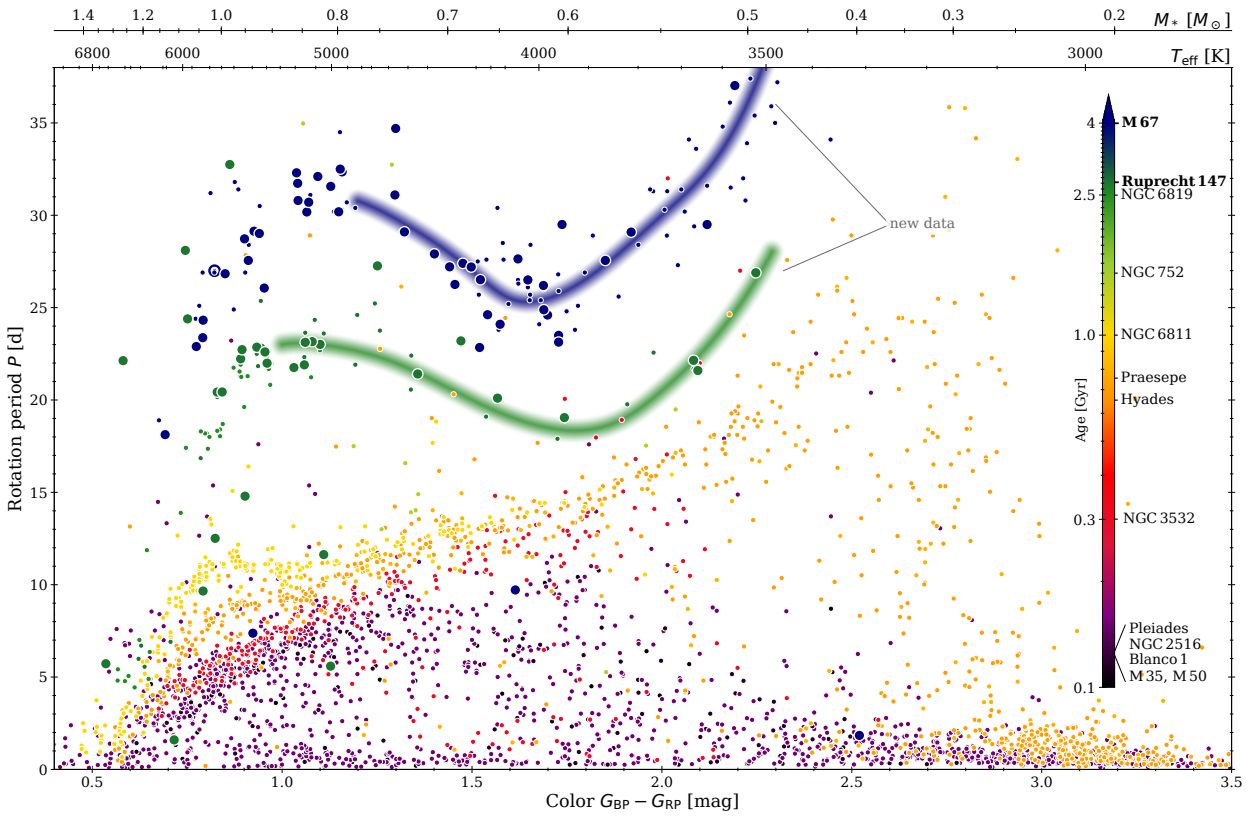

Figure 5.1: *Color-period diagram similar to Fig. 1.5 – now highlighting how the results obtained in paper I and II extend the current knowledge of stellar rotation to older and lower mass stars (green and blue shaded lines). The figure includes the data from Curtis et al. (2020) for Ruprecht 147 and Dungee et al. (2022) for M 67 which have been produced somewhat in parallel to the works presented here.*

The observed sinusoidal shape of the older clusters is in stark contrast to any assumption and model proposed for stellar spindown in the relevant region. Studies that have relied on these kinds of extrapolations often found a mismatch between prediction and observation. We have now shown that those models are not able to reproduce the clusters either, which renders their apparent inconsistencies when applied to field stars insubstantial.

An important detail for the application of gyrochronology is that the relationship between mass, period, and age is sufficiently unique to allow the estimate of a well-constrained age from a combination of mass and period. The clear separation between the cluster sequences of Ruprecht 147, M 67 and the younger clusters indicates that this is indeed fulfilled. However, we note one caveat on this assessment: it is done in color, not in mass. We have already noted in paper III that the fact that we do not see a metallicity dependence in color and the fact that there is a color difference between stars of the same but different metallicity hints at the fact that using color over mass mitigates the effect of metallicity.

A quick investigation reveals this to be true. If we estimate the masses of stars in Praesepe and in NGC 6811 from their CMD position and an isochrone of corresponding metallicity and plot the CPD but with mass instead of color, we see that the sequences of those two clusters overlap. Therefore, the often-cited statement that

"stars exist on a single surface in age - rotation period - mass space,"

has to be changed to *"Stars of the same metallicity exist [...]"*. However, given that color appears to mitigate some of these effects, we can state as a good approximation that

*"stars exist on a single surface in age - rotation period - **color** space."*

Further exploration will reveal the specific role of Z, how good this approximation[2] is, and whether there is a parameter that removes the metallicity dependency better or altogether. Such a parameter, if existent, is likely akin to something like the convective turnover timescale τ_C.

5.1.2 Do field stars behave the same way as cluster stars?

Fritzewski et al. (2020) and Cole-Kodikara et al. (2022b) have shown consistency between cluster stars of the same age

[2]One important detriment to the usage of color or temperature is that they change even during a star's main sequence lifetime. The change is not large but can become significant when comparing stars of very different ages and in regimes with a strongly mass-dependent spindown (for example in a *the-sun-in-time*-esque study).

(NGC 2516, Pleiades, Blanco 1, M 35, and NGC 6709 ; all $\sim$ 125 Myr), Cole-Kodikara et al. (2022a) has shown the same for NGC 6940 and the Hyades (both $\sim$ 650 Myr), and we (Gruner & Barnes 2020, paper I) demonstrated it for NGC 6819 and Ruprecht 147 (both $\sim$ 2.5 Gyr). This means spindown appears to be universal for cluster stars. Stars of the same age and mass (and metallicity) but from different clusters rotate at the same rate. In paper III, we have investigated the next logical step in such a comparison: whether or not this is true for field stars as well. Our cluster data (derived in papers I and II) reaches into hitherto unexplored parameter ranges, allowing us to omit (outdated) model descriptions and to perform a direct comparison between clusters and field stars spanning a wide range of ages and masses.

What did we find? To paraphrase Gertrude Stein, we can state that *"a star is a star is a star"*[3]. We found crucial evidence that it does not matter whether a particular one is associated with a cluster or not. Field stars and cluster stars spin down in the same way. Thus, gyrochronology calibrated on clusters can be applied to field stars. Using wide binaries from the *Kepler* and *K2* fields, we were able to show that their coeval components consistently agree with the rotation periods seen in open clusters.

Our comparison has shown that the environment of a star does not matter for its spindown behavior. This is, however, only true as long as the star is effectively single. Binarity can be considered an environmental condition as well and from the presented results it is clear that it has an impact. Stars that show signs of binarity tend to show rotation rates that are faster than what their ages (estimated from an association to other stars) suggest. The interpretation of this is that angular momentum in a binary system is transferred from the binary orbit to stellar rotation, spinning the star up in the process.

Stars have to be close by for this transfer to happen – tidal forces have to be significant. Means, this happens predominantly in tight (hard) binaries, and those have short ($\sim$ 1 d) orbital periods. In consequence, the faster orbit speeds up the rotation rate. Depending on the rate of angular momentum transfer, this may slow down or even halt the spindown altogether. This effect becomes more significant as the stars get older, as there is more time to transfer angular momentum and even small changes result in larger changes in the rotation period. A slowdown by the same means is possible but much less likely as it requires a very eccentric orbit[4]. The orbit has to be slow ($P_{\rm orb} > P_{\rm rot}$) but still involve close proximity between the binary components to allow angular momentum transfer.

5.1.3 Can we make some sense of the confusion created by works in recent years?

The results presented throughout all three papers are highly consistent among themselves and compared to prior and simultaneous studies by the community. We were able to conclude that stellar spindown remains systematic at least to 4 Gyr (and likely even beyond) and is universal for all late-type main sequence stars. This means gyrochronology is applicable for stars at least as old as 4 Gyr and to cluster stars and to field stars likewise. With that, it stands in some contrast to some interpretations that claim a breakdown of gyrochronology one way or the other. Where does this differing conclusion originate from?

Already Barnes et al. (2016a) noted that some stars are not appropriate for usage regarding gyrochronology and others have certain caveats to be mindful of. We found similar things here:

- Our Ruprecht 147 sample is relatively small but even there it is already notable. A CPD created from all stars with rotation periods causes confusion. However, if we remove stars that are not effectively single main sequence stars, the confusion is lifted and a clear systematic sequence emerges. This becomes even clearer in the M 67 sample, which allowed us to state that if a star shows signs of binarity, it is more likely than not that the rotation period of a star is adversely (regarding gyrochronology) affected.
- As was already stated in the previous section, stars of different metallicities show changes in their spindown behavior. However, the usage of color for the comparison mitigates this effect to some degree. Thus, metallicity is likely not the culprit for any observed discrepancies yet. This may change due an increased level of precision in the ages and rotation periods in future observations.
- Already stated in prior section but reiterated due to its importance: tidal interaction in binary systems may render a rotation period meaningless for gyrochronology.
- Stars that have reached the end of their main sequence lifetime undergo rather fast changes in their color and radius. This renders the color unsuitable as a proxy for the stellar mass and changes the angular momentum distribution within the star. Latter means that changes in a star's rotation rate are not only due to magnetic braking. In rare cases, it might even be possible that an expanding envelope of a star starting to cross the Hertzsprung-gap interacts with a companion star or a planetary system. Both will impact its angular momentum evolution.

This means stars need to be scrutinized whether they are usable for gyrochronology and the chosen parameters are meaningful. Ultimately, citing a discrepancy based on stars that are not exclusively effectively single main sequence stars is somewhat meaningless.

However, this vetting must also include the detected rotation period. As we have shown with our analysis of prior

[3] after *"A rose is a rose is a rose"*, *Sacred Emily*, Geography and Plays, Stein (1922)

[4] See the discussion of binary 297 in Sect. 4.4.2a for such a case.

work on M 67 in paper II and the re-derivation of *Kepler* and *K2* rotation periods in paper III – both originally derived without sufficient attention to the intricacies of data systematics and spot evolution – those are bound to produce unreliable results. Again, this is especially true for older, slower-rotating stars. As such, we can now state that, if one is to explore the ins and outs of stellar rotation and gyrochronology, it is imperative to scrutinize all aspects of the considered stars.

On the same note, I would like to point out that some confusion appears to be of a more linguistic origin. Originally, Barnes (2003) has coined the term *gyrochronology* in concordance with *dendrochronology* regarding its etymology and meaning. Gyrochronology, the way it was intended by Barnes (2003) and how it is also used by us here, refers to the process of age dating a star based on its observed rotation period and mass (or proxy thereof). In that, it is independent of the detailed relationship between the three involved parameters and it merely brands the concept of doing so. However, recent literature is filled with formulations akin to *"The breakdown of current gyrochronology [...]"* (taken from the title of Silva-Beyer et al. 2022). Here, the term "gyrochronology" seems to refer towards the actual dependence (as defined in a specific spindown description) of rotation period on mass and age[5]. While I agree on the shortcomings of such spindown descriptions, referring to them as (failing) gyrochronology is rather misleading.

5.2 Future prospects of gyrochronology

This thesis has expanded on the knowledge of stellar rotational evolution in open clusters and field stars. To evaluate the implications of the findings presented in the preceding chapters and section, let us summarizes all the findings and assertions made in this work in a compact form:

1. *Stars continue to exist on a single surface in age-rotation period-mass space at least until the age of M 67 (4 Gyr), likely even beyond that.*
2. *The spindown has a strong mass dependence that leads to a significant deviation from the classical Skumanich-style for K and M-stars.*
3. *Wide binary stars – which are coeval – are rotationally consistent.*
4. *A star that shows signs of (close) binarity – even just photometric – is likely to have undergone some angular momentum transfer which causes its rotation period to deviate from the normal spindown.*
5. *Field stars spin down in the same way as cluster stars.*
6. *Gyrochronology can be used to estimate the ages of field stars.*
7. *Inconsistencies found in prior work can largely be explained by insufficiently vetted samples.*
8. *The metallicity of a star is likely of minor concern when comparing stars of the same color.*
9. *Current spindown models fail to adequately reproduce the observed spindown behavior in stars older than 1 Gyr.*

Most importantly, we have brought forward critical evidence for the rotational consistency between cluster and field stars. This means systematic stellar spindown as a consequence of magnetic braking is very likely universal for late-type main sequence stars. This hurdle was crucial as we can now comfortably apply gyrochronology to field stars to obtain their ages, opening doors to widespread usage for, among others, Galactic Archaeology and Exoplanet work. Gyrochronology made a big step towards its ultimate goal: being a method for a reliable age estimate for individual stars. There may be many more questions to be answered before this application can be done for all relevant stars with the appropriate precision and reliability (see Sect. 5.2.1), but the universality of spindown is the fundamental requirement.

5.2.1 Questions, questions, questions

There are a number of questions awaiting an answer regarding the evolution of stellar rotation. Answers that largely exceed the scope of this thesis but will have to be addressed in the future.

How do stars older than 4 Gyr spin down? We have advanced the knowledge of stellar spindown to 4 Gyr of for stars from late-F to early-M. However, the sun remains the only star for which we have a certain age and rotation estimate beyond that. Given that this means we have explored less than 50 % of the main sequence life time of the sun and $\lesssim 20\,\%$ for an early M-dwarf. The continued exploration will not be easy (cf. Sect. 5.2.2), but is essential for the application of gyrochronology on timescales relevant to Galactic Archaeology and galaxy evolution.

What is the impact of metallicity? It is imperative to establish what impact the metallicity of a star has on its mass-dependent spindown. More important for the application of gyrochronology is whether we are able to identify a mass proxy that allows for mitigation of those effects and direct comparability.

[5] If however, the occurrence in the title is intended to be used in its original sense (the use of the word *"current"* suggests otherwise), then it is contradicted by the contents of the associated paper.

How do fully convective stars spin down? This question encompasses the thought of whether or not the disappearance of the tachocline has an impact on stellar spindown. From the M-dwarf samples with rotation periods, we know that they do spindown and we need to establish if they follow a different behavior than only partially convective stars.

What is the impact of stellar binarity and planetary systems of rotation? We have shown that close binarity impacts stellar rotation to the degree that it renders stars entirely unsuitable for gyrochronology. While this is not an essential question for the application of gyrochronology as we can always simple sort out stars with spurious behavior, it is still an interesting question which binary configuration lead to unusable rotation periods. And it will also inform us whether to believe a gyro age for a star in a binary system when there is no other way to evaluate its age.

How tight are cluster sequence? This question hints at the precision of gyrochronology age estimates. The scatter in rotation periods among stars of the same age and mass compared with the rate of stellar spindown will determine the precision with which an age can be determined. Judging from our comparison done in paper III, the precision currently reached is about 10 – 20 % for stars redder than the sun. Sun-like and earlier type stars have larger uncertainties.

These questions suggest that it is premature to try to explain stellar spindown in a holistic way just yet. Several of the question above can only be answered with new data and not with new models. We have seen throughout this thesis that models calibrated in certain regimes of the CPD generally fail when applied beyond that. One may speculate regarding the interpretation of stellar rotational evolution (as I do in Sect. 5.3) but only continued exploration can guide us towards a meaningful outcome. It is the rotation of stars older than the sun, of M-dwarfs, of stars of different metallicity, and stars of ages between the age mileposts we currently have that are of interest. Thus, the immediate future of work on stellar rotation should be an observational one – more exploration, less interpretation.

5.2.2 Future explorations of stellar rotation

Much of the exploration of stellar rotation and its evolution to this date has been done using open clusters. They are the obvious choice – they provide samples of stars with well-constrained ages and a variety of masses, they are typically sufficiently spatially confined to be observable as a whole with a single (but repeated) telescope pointing while simultaneously being not too crowded to allow the separation of individual stars. Ideally, we would continue to use them forever. However, we run into the fundamental limitation already pointed out in the opening remarks to this thesis: we can only observe what is provided to us by the universe. And in terms of nearby open clusters – especially towards older ages – almost all of them have been observed and added to the cluster skeleton that marks our rotational evolution mileposts.

Figure 5.2 illustrates the distribution of (nearby) open clusters based on the compilation by Dias et al. (2021). While

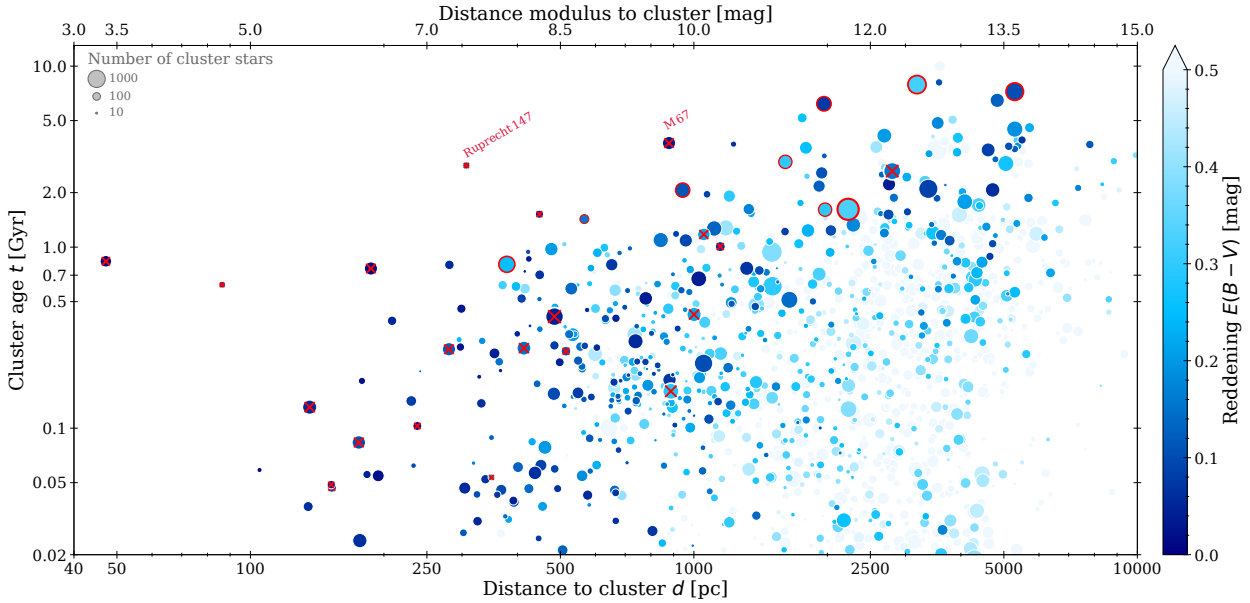

Figure 5.2: *Nearby open clusters. Each point represents an open cluster as listed in Dias et al. (2021) with their distances, reddening values, and ages taken adopted from there as well. Point size indicates the number of stars in a cluster and the reddening is color coded as indicated in the figure. Crossed in red are the clusters previously studied with respect to stellar rotation (essentially corresponding to Table 1.1). Ruprecht 147 and M 67 are individually identified. Encircled in red are likely valuable targets for future exploration (cf. Table 5.1).*

there are some inconsistencies in their data set[6], it gives a good overview of the sample we can draw from. Most well-populated clusters have been studied before, including the oldest at a given distance up to 1 kpc (indicated in red). The apparent lack of clusters > 5 kpc is not real but merely a consequence of the color coding in the figure (clusters have $E(B-V) \geqslant 0.5$ mag). A reddening of 0.3 mag corresponds to an extinction of about 1 mag. This means the cluster stars' brightnesses effectively correspond to a distance greater by a factor of 1.6. Furthermore, clusters with unusually large reddening (in comparison to their distance) tend to suffer from differential reddening. As such, those are generally disfavored.

As of this writing, NGC 6811 and NGC 6819 are the clusters with the greatest distances that have been studied. They give a good indication of what is possible with current data and in general. Both clusters were located in the *Kepler* field and observed for four years. Still, their distances severely limited the stars with detectable periods (cf. the reddest most stars in each, e.g., in Fig 1.5). Both clusters are not the first choices in their age ranges to be studied but they happened to be in the *Kepler* field[7] and we take what we can get.

Figure 5.2 marks a few clusters (encircled in yellow and listed in Table 5.1) that pose good opportunities for future investigations. Typically, they are relatively distant. Special among them is NGC 6791. It was located in the *Kepler* field as well, but at a distance of $d = 5.2$ kpc it will be challenging to extract meaningful data[8]. The other clusters are not observed in *Kepler* and thus require a dedicated observation each.

Table 5.1: *Selected clusters that may help progress gyrochronology. Cluster age, member count, distance, reddening, and metallicity are from Dias et al. (2021). The* Limit *column denotes the spectral type of main sequence star with $V \approx 20$ mag in the cluster, indicating a (rather optimistic) lower mass limit.*

Cluster	Age [Gyr]	N	$E(B-V)$ [mag]	d [pc]	[Fe/H]	Limit
Stock 2	0.8	1157	0.26	379	0.03	M3
NGC 6991	1.4	245	0.16	566	-0.08	M2.5
NGC 6939	1.6	656	0.30	1976	0.46	K5.5
NGC 7789	1.6	2981	0.33	2227	0.03	K5
IC 4651	2.1	812	0.11	943	0.12	M1
Ruprecht 171	3.0	660	0.30	1608	0.05	K6.5
NGC 188	6.2	860	0.08	1965	0.11	K7
NGC 6791	7.2	1520	0.10	5291	0.40	K1.5
Collinder 261	7.9	1706	0.32	3185	0.02	K3

Beyond that, however, there are hardly any more open clusters available that allow a continued exploration of spindown where it is needed. Clusters of relevant ages are further and further away, partially beyond current observing capabilities even if we would be able to invest the significant amounts of time required to obtain the data at sufficient quality. And thus far, we have not even mentioned obtaining them at a variety of metallicities. This means that ultimately, the expansion of the exploration of stellar rotation and gyrochronology to field stars is inevitable. A step that will come with its very own set of problems and opportunities.

Our wide binary sample has illustrated nicely the diversity in metallicities and ages we can achieve when we leave the cluster stars behind. However, employing field stars as calibrators requires a detailed characterization of the individual stars and outliers are much harder to identify. Wide binary stars are the preferential path forward due to their imposed consistency between both stars, albeit that they will require costly observations to be as usable as cluster stars. However, once we have a diverse sample, we will be able to address the many questions still surrounding stellar rotational evolution.

5.3 A semi-empirical interpretation of stellar spindown

Throughout this thesis, we have gained an unprecedented look at the observational constraints on stellar rotational evolution. Many aspects and details are yet unknown but our data allow us to rethink the observable evolution of stellar rotation. We discovered the sinusoidal shape of older open clusters in the CPD and that this behavior is shared between cluster and field stars. Taking this new information into account, I want to offer a semi-empirical interpretation of the observed spindown based on those findings. This section deviates a little from the rest of the thesis and represents the amalgamation of years of the author staring at CPDs, CMDs and light curves of various kinds. The interpretations offered here are speculative *"and can be proved or disproved on the anvil of experiment"*[9]. The experiment in this case is the continued exploration of stellar spindown as described in the preceding section.

[6] See for example the overestimation of the Hyades age – the closest, i.e., left-most cluster shown.

[7] This is a bit of hyperbole – many considerations went into the selection of the *Kepler* field, including the open clusters.

[8] We note that there was recent work on NGC 6791 by Sanjayan et al. (2022), who have also published rotation periods for stars in the cluster based on *Kepler* data. However, their results are problematic for various reasons: (1) judging from a CMD, the membership of the individual stars seems questionable. (2) The sample seemingly contains various types of stars in different stages of evolution, including post-MS stars. (3) there is only a very rudimentary description of how the rotation periods were obtained (aperture photometry on *Kepler* data) and no light curves are shown. (4) The reported rotation periods are in complete disagreement with everything that would be expected (all stars are rotationally younger than 2 Gyr) and are presented without comment. Given all these circumstances, it is safe to disregard the work by Sanjayan et al. (2022).

[9] from *Dragons of Eden*, Carl Sagan (1986)

Let us look at our data in a slightly different way than before. Figure 5.3 shows the temporal evolution of stellar rotation as demonstrated by the open clusters distinguished for stars of different colors. We can see directly (panels b – f) that spindown deviates strongly from the classical Skumanich-style for most stars. While we find a Skumanich-style spindown for sun-like stars, the picture differs widely when we move to lower-mass stars. From the classical $P_{\rm rot} \propto \sqrt{t}$ around early-G type stars ($G_{\rm BP} - G_{\rm RP} \approx 0.8$), it evolves to linear behavior around early-K ($G_{\rm BP} - G_{\rm RP} \approx 1.1$), and becomes somewhat exponential for early-M ($G_{\rm BP} - G_{\rm RP} \approx 2.0$)[10].

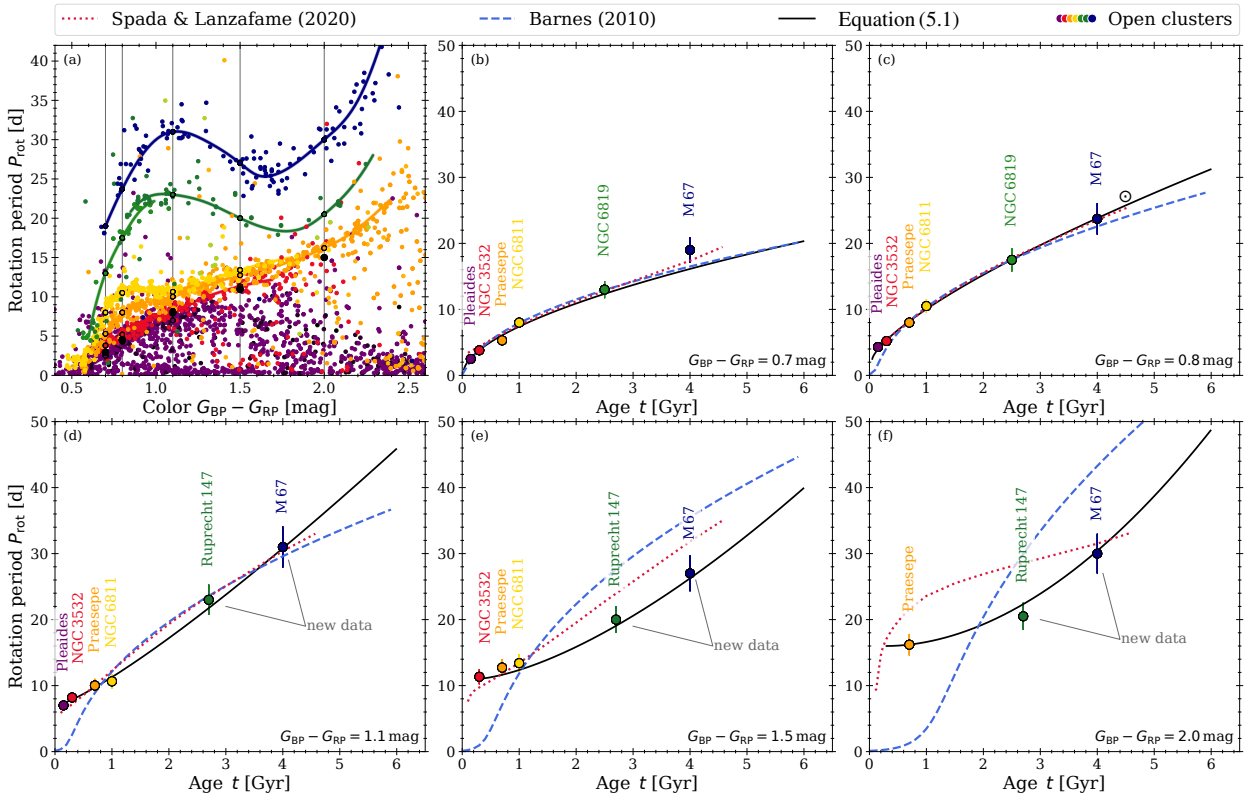

Figure 5.3: *A new interpretation of the evolution of stellar rotation. Panel (a) shows a color-period diagram, akin to many shown throughout this thesis and most closely related to Fig 4.3, including the color-coding regarding the age. Black vertical lines indicate the color slicing used for panels (b)–(f). Empirical open cluster sequences are overplotted in the corresponding colors. Points of intersection are highlighted. Panels (b)–(f) show the evolution of stellar rotation along the slicing defined in panel (a), with colored points indicating the cluster sequences. In each, the rotational evolution described by Barnes (2010, dotted blue line), Spada & Lanzafame (2020, dashed red line), and Eq. (5.1, solid black line) is overplotted.*

This emerging pattern of evolution is suggestive of a new interpretation of stellar spindown behavior that I want to present here. It seems that the Skumanich-style spindown needs to be modified by introducing an additional mass-dependence – we had indicated this before when comparing the found cluster sequences to models in Sects. 2.6 and 3.5.4. Given what we see in Fig. 5.3, we modify $P_{\rm rot} \propto \sqrt{t}$ to become $P_{\rm rot} \propto t^{\alpha}$ with a mass-dependent $\alpha = \alpha(M_*)$. However, this spindown does not seem to find its origin in a very fast rotation ($P_{\rm rot} \lesssim 3$ d) for all stars. It rather seems to follow an – again mass-dependent – onset point $P_0 = P_0(M_*)$. This P_0 appears to be steadily growing when going towards lower masses and it may be reaching break-up velocities at the Kraft-break. An educated guess can be made that $P_0(M_*)$ is created by connecting the red (i.e., low-mass) boundary of the converged slow rotator sequences. Let us call this point the *convergence point* for now.

At this point, we venture a bit into stellar evolution. Young clusters contain a significant amount of pre-main sequence stars. Similarly to the turn-off point, a cluster has a certain color/mass/temperature[11] beyond which all stars are not on the main sequence. Only in this case, it is all the stars with lower masses than this *turn on* point that are still PMS stars. There are many uncertainties in the PMS evolution and we only have a few cluster sequences defining this region, but it is likely no coincidence that there is some similarity between the time-dependence of our *convergence point* and this *turn on* point. With this in mind, it is opportune to identify $P_0(M_*)$ as some kind of *rotational ZAMS*.

Where are we now? We have interpreted the stellar spindown as beginning not near break-up velocity but in an advanced state $P_0(M_*)$ that is reached when a star has converged on the ZAMS. From there on, a star spins down

[10] Although it has to be emphasized that this color range is only defined by three ribs of our open cluster skeleton. Future observations should aim to get some more meat on those bones by exploring the inter-cluster gaps. A comparison to the wide binaries from paper III that fall into age groups 3 and 5 are likely helpful here to provide at least an additional indication for consistency.

[11] Although, one needs to be careful with a notation of color or temperature, as both change drastically during PMS evolution.

following a modified Skumanich-relation as $P_{\rm rot} \propto t^{\alpha(M_*)}$. Here, we have to keep another point in mind. Due to the fact of a star only beginning its systematic spindown on the ZAMS, the time it has spun down is not equal to the age of the cluster, but that reduced by the delay before converging onto the ZAMS. With that, it becomes $P_{\rm rot} \propto (t - t_0)^{\alpha}$, where t_0 is the (mass-dependent) time at which a star has converged onto the ZAMS, i.e., the length of its PMS evolution. The sinusoidal shape observed in open clusters (and its likely reversal beyond that) is now a consequence of the combination of a delayed start and a faster spindown for lower-mass stars.

5.3.1 Suggestions for a semi-empirical spindown description

Combining those thoughts, we arrive at a spindown that may be described in the form

$$P_{\rm rot}(t, M_*) = P_0(M_*) + g(M_*) \cdot (t - t_0(M_*))^{\alpha(M_*)}\,, \tag{5.1}$$

where $t_0(M_*)$ is the length of the PMS evolution, $P_0(M_*)$ the rotational ZAMS, and have introduced a mass-dependent scaling relation $g(M_*)$ as a separable function, inspired by the original interpretation by Barnes (2003). With that, spindown involves four mass-dependencies, whereas Barnes (2010) had two (which we certainly know to be not enough now) and Spada & Lanzafame (2020) had three. Although, an argument can be made that $P_0(M_*)$ and $t_0(M_*)$ are the same dependency or at least closely connected. The explicit forms of the components of Eq. (5.1) have to be found empirically but may also be motivated by theoretical considerations. Given that we strive for an easily applicable description it is opportune to express Eq. (5.1) in terms of color rather than mass, i.e., $P_{\rm rot}(t, M_*) \rightarrow P_{\rm rot}(t, x)$. with x being the color of our choosing. This choice is further supported by the fact that color seems to mitigate the effect of metallicity on spindown. Here, we select $x = G_{\rm BP} - G_{\rm RP}$ due to its wide availability. In Fig. 5.4 (panels a – d), we have displayed a possible shape of the components of $P_{\rm rot}(t, x)$ constructed in a purely empirical way. This is only meant as a proof of concept and not as an applicable relation to determine stellar ages. $\alpha(x)$, $t_0(x)$, $P_0(x)$, and $g(x)$ are constructed from a cubic spline interpolation to the points listed in Table 5.2. The color-dependent spindown resulting from this description is overplotted in panel (e) of Fig. 5.3.

$\alpha(x)$, $t_0(x)$, and $P_0(x)$ are monotonously increasing with color and can probably be described by simple relations. The *wiggles* seen in the figure for each are likely a consequence of the relation between color and a more intrinsic stellar parameter (e.g., mass or temperature). $g(x)$ shows a more complex shape with a maximum around solar-type stars after starting at zero at the Kraft break and falling to a somewhat constant level for redder stars. I cannot offer a compelling interpretation of this shape and for now, it is solely informed by numerical consideration.

There are a few shortcomings. Our description in its current form fails to adequately reproduce the Pleiades' slow rotator sequence. This is likely a consequence of uncertainty in (P_0, t_0) and further fine-tuning may help to overcome this. Furthermore, we have seen in paper III that the wide binaries arguably older than 4 Gyr indicate a flattening of the distribution around early-M stars – thereby changing the sinusoidal shape back to a monotonously increasing period distribution. This is not seen when we extrapolate $P_{\rm rot}(t, x)$ to ages > 4 Gyr. Lastly, the predicted shape for $1.0 < t < 2.5$ Gyr appears much flatter than the wide binaries in the corresponding age group (group 3, see Fig. 4.8) suggest.

Table 5.2: *Points used to create a cubic spline interpolation as a representation of Eq.* (5.1)*. The points and the created spline are shown in panels (a) – (d) of Fig. 5.4.*

$G_{\rm BP} - G_{\rm RP}$ [mag]	α	t_0 [Gyr]	g [d]	P_0 [d]
0.55	0.50	0.00	0.50	-2.00
0.80	0.73	0.05	7.82	2.50
1.00	1.06	0.11	5.88	6.00
1.50	1.50	0.25	2.10	11.00
2.00	1.90	0.30	1.20	16.00
2.50	2.30	0.40	0.80	24.00

5.3.2 Thoughts on the nature of fast rotators

With all four mass dependencies sufficiently constrained, the description culminating in Eq.(5.1) is able to reproduce our current knowledge of stellar rotation of slow rotators (cf. panels (e) – (i) in Fig 5.4)[12]. But what about fast rotators? So far, we have largely ignored the more complex shape formed of a combination of fast and slow rotators found in younger clusters. This dichotomy in stellar rotation has puzzled researchers since its first discovery. Here, I want to propose a likely controversial hypothesis: there is no fast rotator sequence, at least not in the classical sense.

The fast rotator sequence is thought to be occupied by rapidly rotating stars which – on timescales and for reasons we do not know yet – converge to the slow rotator sequence. Fast and slow rotators are, in this classical interpretation, two somewhat distinct stellar populations (in rotation). They are being separated from each other by a sparsely populated

[12] This is not too big of a surprise given that a function with four parameters can be tuned quite a lot to match the observations. We note, however, that the four mass dependencies are of a relatively simple form and partially physically motivated.

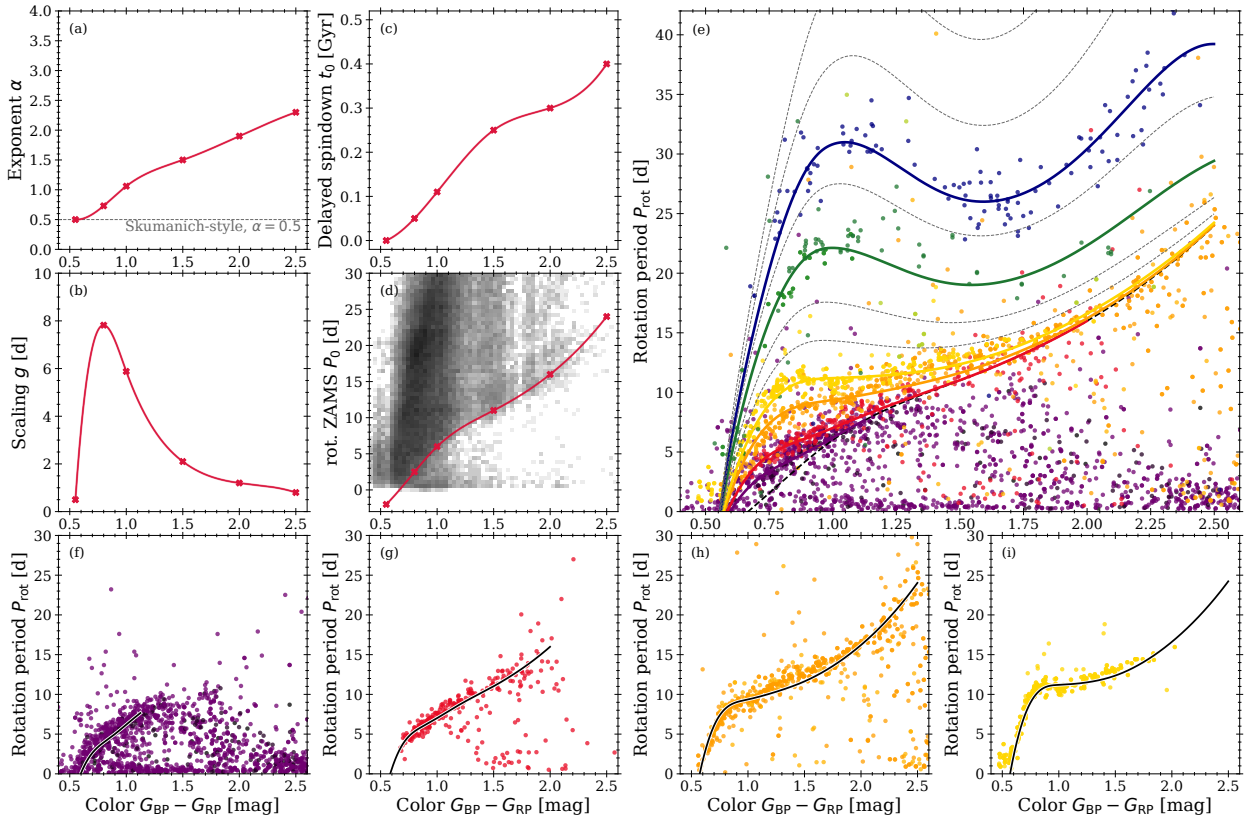

Figure 5.4: *Proof of concept of a spindown description represented by Eq.* (5.1)*. Panels (a)–(d) show the individual components of the equation and panel (e) shows an open cluster CPD and sequences of the corresponding ages overplotted. Dashed gray lines indicate the age steps of 1.5, 2, 3.5, 5, and 6 Gyr. The points in panels (a)–(d) correspond to Table 5.2 connected by a line from a cubic spline interpolation. Panels (f)–(i) show the sequences of the younger clusters (*$\leqslant 1$ *Gyr) individually for better visibility. Panel (d) shows a background histogram build from the combined* Kepler *field star samples described in Sect. 1.2.*

gap – populated by stars rapidly converging from slow to fast rotators. The fact that the stars populating the gap are rather randomly distributed suggests that the transition from fast to slow is not closely mass-dependent. The dashed lines in Fig. 1.3 indicate the slow rotator sequences following the description of Barnes (2003). But if we look closer at Figs. 1.3 or 5.4, is that really a sequence? It is certainly less populated than the slow rotator sequence in all clusters with available observations. In most clusters, the fast rotator sequences appear to be barely more than lower boundaries, admittedly a little denser populated than the gaps – but not by much.

This begs the question: what if we see the fast rotators not as somewhat separate, although coeval population, but rather as stars of delayed formation? We always assume clusters to be of a single age[13], but how good is this assumption? In young star forming regions age spreads are found (e.g., Hartmann 2001; Palla et al. 2005, 2007). This spread is significant compared to the age of a very young cluster (e.g., Jeffries & Oliveira (2005) found $\Delta t \leqslant 2$ Myr in the 9 Myr old cluster NGC 2547). However, already for Pleiades-age clusters such a spread is negligible. This cannot be it. Observations in older clusters show a broadening of the turn-off point and there are interpretations as to which an age spread is responsible for this (e.g., Goudfrooij et al. 2009, 2011b,a; Correnti et al. 2014; Goudfrooij et al. 2015)[14]. The corresponding spreads are significant, reaching $\sim 200-700$ Myr within a cluster[15]. The proposed idea to explain this spread in age is that cluster forms in an initial star formation burst (with a duration of a few million years, the spread seen in very young clusters) and the death of the first generation massive stars (after 10^6-10^8 yr) triggers a delayed formation of a second generation of stars. This is a debated hypothesis but let us take it at face value for now.

Looking back at Fig. 1.3 with this in mind, we see that we do not even need to go far from the lower boundary of this estimated age spread to encompass all stars in the gap and on the fast rotator sequence[16]. Furthermore, the delayed star formation only produces fewer stars than the original burst – perfectly resembled in the difference in population between slow and fast rotators. The difference (in mass, color, etc.) between the intersection of fast and slow rotator

[13] *simple stellar populations* (SSP)

[14] There are competing interpretations, e.g., arguing that differences in stellar rotation can mimic an age-spread widened turn-off (Niederhofer et al. 2015). However, this explanation only works for clusters whose turn-off point is blueward of the Kraft break. The systematic spindown would level the field in older clusters (as evidenced by all open clusters with ages > 1 Gyr).

[15] We recall our own uncertainties with setting ages for Ruprecht 147 (2.7–3.0 Gyr) and M 67 (3.6–4.1 Gyr) with isochrones – which might be indications of those clusters' age spreads.

[16] A Pleiades-age cluster would have stars spanning ages from formation to 125 Myr old.

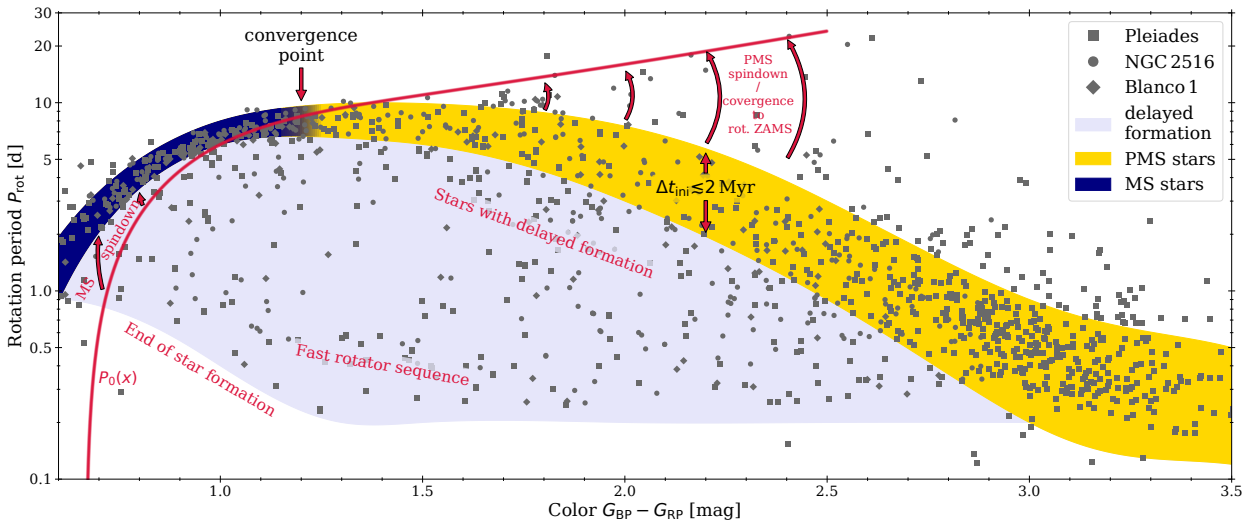

Figure 5.5: *Schematic illustration of the new interpretation of the fast rotators. The CPD shows the samples of the three ZAMS clusters NGC 2516, Blanco 1, and the Pleiades (gray symbols). The shaded areas distinguish between the different types of stars mentioned in the text. The dark blue shaded area marks the stars of the classical slow rotator sequence. Those are from the initial star formation burst, have converged to the rotational ZAMS P_0 (blue line) in the past, and are now spinning down as described in Eq.* (5.1)*. The yellow area marks the stars similarly from the initial formation burst and that are about to converge to the rot. ZAMS. Those are PMS stars and do not follow the spindown described by Eq.* (5.1)*. The width of the shaded areas (blue and yellow) indicate the spread in rotation periods that likely corresponds to some degree with the initial age spread of the cluster (i.e., the small spread, $\lesssim 2$ Myr, from the initial star formation burst) and is broadened further by the uncertainties of rotation period measurements. All stars in the pale blue-shaded area – which very much includes the stars identified as part of the fast rotator sequence – are from the longer delayed formation of the second generation.*

sequences and the red boundary of the rotation ZAMS is then an indicator of the age spread within a cluster. Figure 5.5 visualizes some of these concepts on the example of the ZAMS cluster.

There is another indication favoring this interpretation. Again, looking back at Fig. 1.3, we see that the Pleiades clusters contains a population of stars $B - V > 1.0$, i.e., redward of the converged slow rotator sequence, that mark a downturn in rotation period from 10 d to near break-up (this is especially visible in the logarithmic plot, see also yellow highlighted region in Fig. 5.5). It is likely that those stars are the ones formed in the initial burst and are now in the process of converging onto the rotational ZAMS.

Another clue in favor can be seen in our wide binary sample (cf. panel (a) and (b) of Fig. 4.3). Wide binaries should not be subject to such an age spread. Most F systems[17] are either composed of two stars that are fast rotators or combine a slow rotator and fast rotator that is located in the yellow highlighted region in Fig. 5.5. The systems that do not fall in this distinction are hierarchical (the fast rotator is a *double*; all are in age group 2). This means that the wide binary sample does not contain (non-hierarchical) systems with one star on the fast sequence and one star on the slow sequence (outside of the highlighted region)[18]; which is exactly what we would expect if there is no age difference between the components in the presented interpretation.

A way to explore whether there is substance to this interpretation is to compare stars of similar spectral type belonging to the fast and slow rotator sequences and to identify the state of other age indicators (the Li abundance would be an obvious choice) and whether they are consistent with an age spread. Work has been done in this regard, but was so far limited to very young systems (like the Orion Nebula Cluster, e.g., Palla et al. 2007; Jeffries 2007). Our limited knowledge of the evolution of PMS stars is certainly an issue in this exploration (e.g., Naylor 2009). Fritzewski et al. (2021) has shown a clear distinction between the activity levels of fast and slow rotators. Fast rotators are much more active, and a separation between the fast, slow, and gap population is seen in activity, too (see their Fig. 7). However, since activity is a consequence of the rotation rate, this is hardly supporting evidence.

5.3.3 Conclusions and open questions

The previous sections included a new interpretation of stellar spindown based on our recent observations of M 67, Ruprecht 147, and wide binaries derived as part of this thesis, as well as updated data on younger clusters from the literature. Let us summarize the ideas and conclusions regarding the proposed interpretation:

- The spindown has an additional mass dependence that causes an increasingly strong deviation from the Skumanich-style spindown for stars of lower masses.

[17] To recap: those are the ones that contain at least one fast rotator (green symbols in the figure).
[18] Or to phrase it differently: The sample does, e.g., not contain systems with two stars of very similar color but located on the different sequences.

- There exists a rotational ZAMS that somewhat coincides with the convergence of stars to the main sequence.
- The spindown before and after the rot. ZAMS is different.
- Stars of the same mass spindown in the same way, there is no distinction between fast and slow rotators. This means spindown is truly universal (neglecting the metallicity dependence for the moment).
- Fast rotators in clusters are formed later and thus have not spun down as much.
- The gradual disappearance of the fast rotator sequence is due to the reduced significance of the initial age spread at older ages.

Furthermore, we have demonstrated that the description presented in Eq. (5.1) can describe the observed slow rotator sequences based on four (three) relatively simple mass dependencies. However, a few questions remain to be answered but a more in-depth discussion goes beyond the scope of this work:

What about the evolution from $P \approx 1$ d to P_0? We have re-interpreted the fast rotator sequence not as a distinct population but as stars of delayed formation. This, however, only mitigates the problem. As we can see in Fig. 5.3, the spindown for $P < P_0$ and $t < t_0$ is incompatible with our description; a different behavior governs this episode of stellar evolution. We already pointed out the possible interpretation of (P_0, t_0) as the endpoint of PMS evolution of the star. Thus, it is not surprising that we find different behaviors of spin evolution before and after – now we need to quantify it. Despite having many more clusters explored in the relevant age range, the picture is not clear. Unlike for the evolution of the slow rotator sequence, changes in the stratification and processes within a star have a significant impact on the PMS evolution.

We note that the detailed shape of P_0 might be inferred from the large field star samples (cf. Sect. 1.2 and Fig. 1.4) and the apparent lower, diagonal boundary visible for them (cf. panel (d) of Fig. 5.4).

What are the physical interpretations of α and g? Unlike (P_0, t_0), which is interpreted as a consequence of PMS evolution, the nature of α and g are not immediately obvious. Both – in their own way – are likely a consequence of the internal structure of the star, the relative size of the convective envelope, and the coupling between core and envelope. Important in this discussion will be the impact of re-distribution of angular momentum within a star (the currently most successful description of spindown (Spada & Lanzafame 2020) indeed includes a mass-dependent coupling between core and envelope).

○ ○ ○

Part 6 – Conclusions

Closing remarks and future perspective

The results of this thesis push the boundary of the empirical exploration of the evolution of stellar rotation, partially to the edge of what is possible with currently available observations. It was a difficult but ultimately successful endeavor. Generally speaking, this thesis strengthens the case for gyrochronology while also highlighting that we have merely scratched the surface in the exploration of the intricate details of stellar rotational evolution.

The two open cluster studies on Ruprecht 147 and M 67 were motivated by more and more prevalent claims towards strange behaviors of the stellar spindown at older ages. However, it was all speculative. We have changed that. We have performed detailed investigations of *Kepler* data for both open clusters, with large efforts taken to address the intrinsic difficulties imposed by the all too familiar systematics in the *K2* data. But it was worth it as we were able to construct CPDs for both clusters, extending our knowledge into hitherto unknown regimes, age-wise and mass-wise. We have provided undeniable proof that the spindown of K and M-stars differs widely from their G-type counterparts. Cluster CPDs exhibit a sinusoidal shape which becomes more prevalent for older systems. With that, they deviate strongly from a classical Skumanich-style spindown. However, in all that we also showed that a fundamental requirement of gyrochronology is still fulfilled: Stars continue to exist on a single surface in age – rotation period – color space.

With us learning that old open clusters deviate strongly from our expectations, another fact became obvious. Every attempt to extend gyrochronology to field stars had failed. It was thought that this is an indication of the breakdown of gyrochronology, a fundamental disparity in the nature of stellar spindown. Yet, those attempts were based on a comparison between field stars, partially populating regions of the CPD which were at that time unexplored, and extrapolated models calibrated on younger stars. The models struggled to reproduce the very cluster stars they were calibrated on and they failed outright in comparison to our newly found knowledge thanks to our work on Ruprecht 147 and M 67. Thus, using them to evaluate the rotational consistency between clusters and field stars is without merit.

As long as the stellar spindown models – be they empirical, theoretical, or somewhere in-between – cannot satisfyingly explain the cluster observations, we have to proceed differently if we aim to expand gyrochronology to field stars. And this we did. Using the known open clusters as an empirical description of the spindown, we investigated wide binaries towards their agreement. And they do indeed agree. With the help of a thoroughly vetted sample of wide binary stars with rotation periods, we showed that they are not only rotationally consistent between the individual components, they also trace the open cluster sequence tightly – including the newly found sinusoidal shapes. With that we have, for the first time ever, successfully bridged the gap between the rotation of field and cluster stars.

In all this, another important aspect of this work has to be mentioned. We spend a significant time of the work on vetting our sample stars, validating the found rotation periods, and investigating literature results in the same way. In consequence, we were able to show that formerly confusion-causing results become fully consistent when scrutinized properly.

Our results have simultaneously closed and pushed the door wide open regarding the future exploration of stellar rotation. The door is wide open as we have shown that gyrochronology is valid across the entire parameter regime explored to date. Furthermore, we have shown that it is equally valid for field stars. In a more practical sense, however, the door is closed. Any further exploration of stellar spindown requires more and better observations. With our work on M 67, we have demonstrated the difficulties in obtaining reliable rotation periods in the relevant regimes.

The *Kepler* telescope is now retired for about four years, innumerable studies have been carried out based on its data, and still, we were able to harvest more scientifically valuable information from it. However, all good things must come to an end. Almost all data obtained by *Kepler* have now been gathered and evaluated. Yet, a few remain that will pose a challenge in obtaining results but promise results worth the effort. During the original *Kepler* mission, NGC 6791 ($\sim$ 6 Gyr), NGC 6819 (2.5 Gyr), and NGC 6811 (1 Gyr) were observed, partially with dedicated superstamps. Pre-

processed light curves for NGC 6811 and 6819 have been used successfully (i.e., all the data for these clusters used throughout this work). However, both clusters are very distant, so the light curves provided by the *Kepler* mission team are limited. In fact, barely any light curve data on the even more distant NGC 6791 is in the archive. A sophisticated approach using photometry directly on the obtain target pixel files or superstamps (similar to what we did for M 67) should be able to extract valuable information pushing the boundary even further. Alas, it will be a difficult endeavor[1].

At this point, I would like to include a few words to express my gratitude towards the *Kepler* mission team[2] – especially those responsible for its continued operation as part of its *K2* mission after several parts of the telescope ceased to function. While I have often cursed the systematics in *Kepler* data – mostly during the work on M 67 – it amounts to a miracle that the telescope continued its operation at all. Thank you, for all the dedication towards this wonderful instrument and its continued operation owing to some ingenious solutions on your part. Many works on gyrochronology, very much including everything in this thesis, would not have been possible without it.

With *Kepler* gone/harvested, what else is there that will pave the road to the future of gyrochronology? *Kepler*'s spiritual successor is the *TESS* mission. It is, however, doubtful that *TESS* will come even close to a legacy similar to *Kepler*'s. Although *TESS* is all-sky – in contrast to *Kepler*'s few patches – and is operated by many of the same people that already were involved with *Kepler*, any other mission parameter is detrimental to the pursuit of gyrochronology and stellar rotation in general. While the telescope observes all-sky, it does so only for 27 d at a time before moving to the next slice of the sky; potentially returning to the same region about 2 yr later. With that, *TESS* simply does not provide the observational baseline required for the detection of rotation periods longer than 15 d. There are a few regions of longer baseline – notably the ecliptic poles – but those are devoid of clusters. And even if this were not the case and *TESS* would observe a meaningful open cluster continuously for a year; it would still be difficult to analyze such crowded regions due to *TESS*' very low spatial resolution ($\sim 20''$ pixel). *TESS* is in operation since about 5 yr at the time of this writing, has observed the full sky twice, and there has yet to be a significant study on stellar rotation.

CoRot, *Kepler*, and *TESS* – all these missions were intended primarily for the hunt of exoplanets and stellar rotation work was merely piggy-back riding. Despite this, it is astonishing what the community was able to accomplish over the years. Now one can only imagine what would be possible with a more dedicated mission. The bad news is that there is no plan for dedicated missions to study stellar rotation. However, the good news is that there are plans for missions with different scientific focus but similar observational constraints. Asteroseismology, and the ever-increasing interest in it, may be the savior. While being marketed again as planet finder, *PLATO*[3] (Rauer et al. 2014) has significant dedication towards asteroseismology. The mission has certain similarities to the original *Kepler* program, in that it focuses for a prolonged time (2 –5 months) of observation on a specific field. A clear downside of the mission is again the large pixels ($\sim 15''$). *PLATO*'s launch is already on the horizon – planned for 2026.

Whereas *PLATO* focuses on a specific field, there are plans for a dedicated asteroseismology mission towards open and globular clusters. The *Haydn*[4] mission (Miglio et al. 2021) is still in very early planning steps but has passed some first hurdles towards the approval by ESA. *Haydn* is intended to carry out observation of stellar clusters, spending months on the individual targets. Next to some significant open clusters among the proposed targets (e.g., M 67), *Haydn* will also aim for globular clusters (e.g., 47 Tuc). To accomplish this, it will be geared towards a spatial resolution unparalleled in similar missions ($< 0.5''$ pixel). It is anything but certain that *Haydn* will eventually fly, and even if it does, it will take at least a decade until then. But if I were asked to design a mission dedicated to the exploration of stellar rotation in cluster stars, it would look akin to *Haydn*.

To summarize, the immediate future regarding the exploration of stellar rotation is dire, at least observation-wise. However, I am convinced that the creativity the community has shown facing the available data (and its issues) will last and allow us to squeeze every little bit of information and knowledge out of the data provided by *TESS*, *PLATO*, and – even still – *Kepler*. And in any case, there is always the possibility to return to ground-based observations. While they come with their very own set of problems, they are much more flexible and expeditious compared to space-based missions.

Observations aside, where is the field itself going? There are two different aspects to consider here: the exploration of stellar rotation and the application of gyrochronology. Let us start with the latter. There will be a flood of rotation periods for individual field stars. Similar to what we have seen for *Kepler* and *K2* will eventually happen for *TESS*, *PLATO*, and potentially even ground-based missions like ASAS. We can expect that over the coming years we will derive rotation periods for most faster rotating ($P_{\rm rot} < 15$ d) nearby stars. The current data is likely sufficient for that already and all that is missing is someone with the required time and dedication. This can be combined with a, as of yet lacking, consistent interpretation of stellar rotation in the relevant parameter regime. And even without

[1] The *Kepler* observations of NGC 6791 have concluded ten years ago and it is rather unlikely that the only reason no serious work on it has been published yet is just that everyone forgot it existed.

[2] `exoplanets.nasa.gov/news/1529/meet-the-kepler-mission-team/`

[3] **PLA**netary **T**ransits and **O**scillation of stars

[4] **H**igh-precision **A**steroseismolog**Y** of **D**e**N**se stellar fields

a working model, one can directly compare stars to the available cluster data, similar to what was done in paper III. Ultimately, this will provide a hitherto unprecedented view of the ages of stars in the solar neighborhood in the not-too-distant future. Gradually, gyrochronology will evolve from a matter of frontline research to a widely applicable and commonly used tool. This thesis has provided critical evidence for this in showing that gyrochronology relations calibrated on open clusters can be applied to field stars.

The other aspect is the frontline research, the continued exploration of the evolution of stellar rotation. And it faces a more substantial problem. As we have shown here, detecting rotation periods for stars as old as M 67 (~ 4 Gyr) is difficult. This comes from two different reasons. The first one is the reduced level of activity a star shows and the second is the required baseline to detect rotation periods unambiguously. The reduced activity comes with smaller and smaller star spots (or similarly traceable features, such as faculae). This means the imprint they leave in the light curve of a star becomes harder and harder to detect in the face of all other flux-altering processes and noise. Smaller spots have also shorter lifetimes, causing them to significantly evolve or even dissolve before a star has rotated even once. This means detecting rotation periods in old stars via their photometric signature becomes more and more a matter of luck; that just during the time we happen to observe it, a star exhibits a stronger feature that we can trace long enough to detect a period. In G-type stars around and beyond solar age we may have reached this limit already.

Again, asteroseismology may provide a solution to this problem. Asteroseismic rotation periods have the distinct advantages that they are independent of the current level of stellar activity and survival of starspots. It does, however, require an extended observational baseline to identify the relevant frequencies and the signal becomes smaller for slower rotation. In any way, any currently existing calibration issues facing asteroseismology on dwarf stars will likely be overcome in the coming years.

Another problem to be faced in the future is that of binaries. From a gyrochronology perspective, this one may be easy to assess: everything that has seen angular momentum transfer is unsuitable for an age estimate. It will, however, be interesting to establish what orbital configurations in a binary lead to impactful angular momentum transfer.

The exploration of stellar rotation in general and gyrochronology in particular has seen rapid evolution, growth, and lively debate in recent years. More and more studies adopt gyrochronology as a valid age estimation method. It marks the transition from a fringe methodology to a mainstream tool. For those of us who push the boundaries, explore new frontiers, and ultimately shape the tool presented to the astronomical community to be used, challenging times are ahead. Observational, interpretational, and theoretical obstacles have to be overcome to deliver a consistent concept of stellar rotational evolution. These obstacles include the aforementioned observational difficulties, the complex interplay of all involved parameters with metallicity, the impact of stellar binarity and tidal interactions, and the early evolution of stellar rotation – including the transition from fast to slow rotators.

As such, and despite all the progress, our work here is far from done. If anything, one can argue that all work up to this point was merely the confirmation that gyrochronology generally works and it is now time to explore all the intricate details. And in light of the recent discovery of the sinusoidal shape of sequences of older clusters; who can say what other traits and quirks of stellar rotational evolution we will encounter in this endeavor?

○ ○ ○

Acknowledgments

Some of the data presented in this paper were obtained from the Mikulski Archive for Space Telescopes (MAST). STScI is operated by the Association of Universities for Research in Astronomy, Inc., under NASA contract NAS5-26555. Support for MAST for non-HST data is provided by the NASA Office of Space Science via grant NNX09AF08G and by other grants and contracts.

This paper includes data collected by the *Kepler* mission and obtained from the MAST data archive at the Space Telescope Science Institute (STScI). Funding for the *Kepler* mission is provided by the NASA Science Mission Directorate. STScI is operated by the Association of Universities for Research in Astronomy, Inc., under NASA contract NAS 5-26555.

This publication makes use of data products from the Two Micron All Sky Survey, which is a joint project of the University of Massachusetts and the Infrared Processing and Analysis Center/California Institute of Technology, funded by the National Aeronautics and Space Administration and the National Science Foundation.

This work has made use of data from the European Space Agency (ESA) mission *Gaia* (`cosmos.esa.int/gaia`), processed by the *Gaia* Data Processing and Analysis Consortium (DPAC, `cosmos.esa.int/web/gaia/dpac/consortium`). Funding for the DPAC has been provided by national institutions, in particular the institutions participating in the *Gaia* Multilateral Agreement.

Based on photographic data obtained using The UK Schmidt Telescope. The UK Schmidt Telescope was operated by the Royal Observatory Edinburgh, with funding from the UK Science and Engineering Research Council, until 1988 June, and thereafter by the Anglo-Australian Observatory. Original plate material is copyright (c) of the Royal Observatory Edinburgh and the Anglo-Australian Observatory. The plates were processed into the present compressed digital form with their permission. The Digitized Sky Survey was produced at the Space Telescope Science Institute under US Government grant NAG W-2166.

The project has made use of public databases hosted by SIMBAD, maintained by CDS, Strasbourg, France (Wenger et al. 2000).

This research has made use of the VizieR catalogue access tool, CDS, Strasbourg, France. The original description of the VizieR service was published in Ochsenbein et al. (2000).

This research has made use of the WEBDA database, operated at the Department of Theoretical Physics and Astrophysics of the Masaryk University, Czech Republic.

This research has made use of the NASA Exoplanet Archive, which is operated by the California Institute of Technology, under contract with the National Aeronautics and Space Administration under the Exoplanet Exploration Program.

This work made use of the `python3` implementations of the `numpy` (Harris et al. 2020), `matplotlib` (Hunter 2007), `scipy` (Virtanen et al. 2020), `numba` (Lam et al. 2015), `scikit-learn` (Pedregosa et al. 2011), and `astropy` (Astropy Collaboration et al. 2018, 2022) libraries.

Bibliography

Abney, W. D. W. 1877, MNRAS, 37, 278

Abt, H. A. 2003, Biographical Memoirs National Academy of Sciences, 82, 1

Aerts, C., Christensen-Dalsgaard, J., & Kurtz, D. W. 2010, Asteroseismology (Springer Science)

Agüeros, M. A., Bowsher, E. C., Bochanski, J. J., et al. 2018, ApJ, 862, 33

Agüeros, M. A., Covey, K. R., Lemonias, J. J., et al. 2011, ApJ, 740, 110

Ahuir, J., Brun, A. S., & Strugarek, A. 2020, A&A, 635, A170

Aigrain, S., Hodgkin, S. T., Irwin, M. J., Lewis, J. R., & Roberts, S. J. 2015, MNRAS, 447, 2880

Aigrain, S., Parviainen, H., & Pope, B. J. S. 2016, MNRAS, 459, 2408

Alfvén, H. 1942, Arkiv for Matematik, Astronomi och Fysik, 28A, 1

Allain, S., Bouvier, J., Prosser, C., Marschall, L. A., & Laaksonen, B. D. 1996, A&A, 305, 498

Alter, G., Ruprecht, J., & Vanýsek, V. 1958, Catalogue of star clusters and associations (Prague, Pub. House of the Czechoslavak Academy of Sciences)

Amard, L., Palacios, A., Charbonnel, C., et al. 2019, A&A, 631, A77

Amelin, Y., Krot, A. N., Hutcheon, I. D., & Ulyanov, A. A. 2002, Science, 297, 1678

Anderson, C. M., Stoeckly, R., & Kraft, R. P. 1966, ApJ, 143, 299

Andrae, R., Fouesneau, M., Creevey, O., et al. 2018, A&A, 616, A8

Angus, R., Beane, A., Price-Whelan, A. M., et al. 2020, AJ, 160, 90

Arlt, R. 2009, Sol. Phys., 255, 143

Arlt, R. & Vaquero, J. M. 2020, Living Reviews in Solar Physics, 17, 1

Astropy Collaboration, Price-Whelan, A. M., Lim, P. L., et al. 2022, ApJ, 935, 167

Astropy Collaboration, Price-Whelan, A. M., Sipőcz, B. M., et al. 2018, AJ, 156, 123

Attridge, J. M. & Herbst, W. 1992, ApJ, 398, L61

Baglin, A., Auvergne, M., Boisnard, L., et al. 2006, in 36th COSPAR Scientific Assembly, Vol. 36, 3749

Baliunas, S., Sokoloff, D., & Soon, W. 1996, ApJ, 457, L99

Barnes, S. & Sofia, S. 1998, in American Astronomical Society Meeting Abstracts, Vol. 192, American Astronomical Society Meeting Abstracts #192, 67.01

Barnes, S. A. 2003, ApJ, 586, 464

Barnes, S. A. 2007, ApJ, 669, 1167

Barnes, S. A. 2010, ApJ, 722, 222

Barnes, S. A. & Kim, Y.-C. 2010, ApJ, 721, 675

Barnes, S. A., Sofia, S., Prosser, C. F., & Stauffer, J. R. 1999, ApJ, 516, 263

Barnes, S. A., Spada, F., & Weingrill, J. 2016a, Astronomische Nachrichten, 337, 810

Barnes, S. A., Weingrill, J., Fritzewski, D., Strassmeier, K. G., & Platais, I. 2016b, ApJ, 823, 16

Basri, G. 2021, An Introduction to Stellar Magnetic Activity (Institute of Physics Publishing)

Basri, G. & Nguyen, H. T. 2018, ApJ, 863, 190

Basu, S., Grundahl, F., Stello, D., et al. 2011, ApJ, 729, L10

Batalha, N. M., Borucki, W., Caldwell, D. A., et al. 2006, in American Astronomical Society Meeting Abstracts, Vol. 209, American Astronomical Society Meeting Abstracts, 210.08

Bazot, M. 2020, A&A, 635, A26

Beatty, T. G., Morley, C. V., Curtis, J. L., et al. 2018, AJ, 156, 168

Beck, P. G., Allende Prieto, C., Van Reeth, T., et al. 2016, A&A, 589, A27

Bedell, M., Bean, J. L., Meléndez, J., et al. 2018, ApJ, 865, 68

Bellini, A., Bedin, L. R., Piotto, G., et al. 2010, A&A, 513, A50

Binney, J. & Tremaine, S. 1987, Galactic dynamics (Princeton University Press)

Blaauw, A. 1964, ARA&A, 2, 213

Borucki, W. J., Koch, D., Basri, G., et al. 2010, Science, 327, 977

Bouma, L. G., Palumbo, E. K., & Hillenbrand, L. A. 2023, ApJ, 947, L3

Bouvier, J., Cabrit, S., Fernandez, M., Martin, E. L., & Matthews, J. M. 1993, A&A, 272, 176

Bouvier, J., Covino, E., Kovo, O., et al. 1995, A&A, 299, 89

Bragaglia, A., Fu, X., Mucciarelli, A., Andreuzzi, G., & Donati, P. 2018, A&A, 619, A176

Brandenburg, A. 2018, Journal of Plasma Physics, 84, 735840404

Brandt, J. C. 1966, ApJ, 144, 1221

Breger, M. 1986, ApJ, 309, 311

Bressan, A., Marigo, P., Girardi, L., et al. 2012, MNRAS, 427, 127

Brown, T. M. 2014, ApJ, 789, 101

Buldgen, G., Farnir, M., Eggenberger, P., et al. 2022, A&A, 661, A143

Cantat-Gaudin, T. & Anders, F. 2020, A&A, 633, A99

Cantat-Gaudin, T., Jordi, C., Vallenari, A., et al. 2018, A&A, 618, A93

Canto Martins, B. L., Gomes, R. L., Messias, Y. S., et al. 2020, ApJS, 250, 20

Cargile, P. A., James, D. J., Pepper, J., et al. 2014, ApJ, 782, 29

Carrera, R., Bragaglia, A., Cantat-Gaudin, T., et al. 2019, A&A, 623, A80

Casagrande, L., Schönrich, R., Asplund, M., et al. 2011, A&A, 530, A138

Casagrande, L. & VandenBerg, D. A. 2018, MNRAS, 479, L102

Casamiquela, L., Blanco-Cuaresma, S., Carrera, R., et al. 2019, MNRAS, 490, 1821

Casamiquela, L., Carrera, R., Blanco-Cuaresma, S., et al. 2017, MNRAS, 470, 4363

Chen, Y., Bressan, A., Girardi, L., et al. 2015, MNRAS, 452, 1068

Chen, Y., Girardi, L., Bressan, A., et al. 2014, MNRAS, 444, 2525

Cody, A. M., Barentsen, G., Hedges, C., Gully-Santiago, M., & Cardoso, J. V. d. M. 2018, Research Notes of the American Astronomical Society, 2, 25

Cole-Kodikara, E., Barnes, S., Weingrill, J., & Granzer, T. 2022a, in Cambridge Workshop on Cool Stars, Stellar Systems, and the Sun, Cambridge Workshop on Cool Stars, Stellar Systems, and the Sun, 100

Cole-Kodikara, E. M., Barnes, S. A., Weingrill, J., & Granzer, T. 2022b, arXiv e-prints, arXiv:2207.11063

Collins, M. 2000, Benjamin's Mountain, `https://www.oldradio.com/archives/stations/LA/mtwilson1.htm`, [Online; accessed 14-Feb-2023]

Conrad, C., Scholz, R. D., Kharchenko, N. V., et al. 2017, A&A, 600, A106

Conti, P. S. 1968, ApJ, 152, 657

Correnti, M., Goudfrooij, P., Kalirai, J. S., et al. 2014, ApJ, 793, 121

Cowan, J. J., Thielemann, F.-K., & Truran, J. W. 1991, ARA&A, 29, 447

Curtis, J. & Agüeros, M. 2018, in 20th Cambridge Workshop on Cool Stars, Stellar Systems and the Sun, 24

Curtis, J., Vanderburg, A., Montet, B., et al. 2016, in 19th Cambridge Workshop on Cool Stars, Stellar Systems, and the Sun (CS19), Cambridge Workshop on Cool Stars, Stellar Systems, and the Sun, 95

Curtis, J. L., Agüeros, M. A., Douglas, S. T., & Meibom, S. 2019, ApJ, 879, 49

Curtis, J. L., Agüeros, M. A., Matt, S. P., et al. 2020, ApJ, 904, 140

Curtis, J. L., Vanderburg, A., Torres, G., et al. 2018, AJ, 155, 173

Curtis, J. L., Wolfgang, A., Wright, J. T., Brewer, J. M., & Johnson, J. A. 2013, AJ, 145, 134

Cutri, R. M., Skrutskie, M. F., van Dyk, S., et al. 2003, VizieR Online Data Catalog, II/246

Dalrymple, G. 1991, The Age of the Earth (Stanford University Press)

Davenport, J. R. A. & Covey, K. R. 2018, ApJ, 868, 151

David, T. J., Angus, R., Curtis, J. L., et al. 2022, ApJ, 933, 114

Deacon, N. R. & Kraus, A. L. 2020, MNRAS, 496, 5176

Deacon, N. R., Kraus, A. L., Mann, A. W., et al. 2016, MNRAS, 455, 4212

Demarque, P., Green, E. M., & Guenther, D. B. 1992, AJ, 103, 151

Deming, D., Knutson, H., Kammer, J., et al. 2015, ApJ, 805, 132

Dhital, S., West, A. A., Stassun, K. G., & Law, N. M. 2013, Astronomische Nachrichten, 334, 14

Dias, W. S., Monteiro, H., Moitinho, A., et al. 2021, MNRAS, 504, 356

Distefano, E., Lanzafame, A. C., Brugaletta, E., et al. 2022, arXiv e-prints, arXiv:2206.05500

do Nascimento, J. D., J., García, R. A., Mathur, S., et al. 2014, ApJ, 790, L23

do Nascimento, J. D., J., Takeda, Y., Meléndez, J., et al. 2013, ApJ, 771, L31

Donor, J., Frinchaboy, P. M., Cunha, K., et al. 2020, AJ, 159, 199

Donor, J., Frinchaboy, P. M., Cunha, K., et al. 2018, AJ, 156, 142

Douglas, S. T., Agüeros, M. A., Covey, K. R., & Kraus, A. 2017, ApJ, 842, 83

Douglas, S. T., Curtis, J. L., Agüeros, M. A., et al. 2019, ApJ, 879, 100

Douglass, A. E. 1928, Carnegie Institution of Washington publication, Vol. no.289:v.2 (1928) (Washington Carnegie Institution of Washington), 204, https://www.biodiversitylibrary.org/bibliography/5800

Dreyer, J. L. E. 1888, MmRAS, 49, 1

Dungee, R., van Saders, J., Gaidos, E., et al. 2022, ApJ, 938, 118

Durney, B. R., De Young, D. S., & Roxburgh, I. W. 1993, Sol. Phys., 145, 207

Durney, B. R. & Latour, J. 1978, Geophysical and Astrophysical Fluid Dynamics, 9, 241

Edwards, S., Strom, S. E., Hartigan, P., et al. 1993, AJ, 106, 372

Eggenberger, P., Haemmerlé, L., Meynet, G., & Maeder, A. 2012, A&A, 539, A70

El-Badry, K., Rix, H.-W., & Heintz, T. M. 2021, MNRAS, 506, 2269

Endal, A. S. & Sofia, S. 1978, ApJ, 220, 279

Epstein, C. R. & Pinsonneault, M. H. 2014, ApJ, 780, 159

Esselstein, R., Aigrain, S., Vanderburg, A., et al. 2018, ApJ, 859, 167

Esselstein, R. A. 2018, PhD thesis, University of Oxford, UK

Evans, D. W., Riello, M., De Angeli, F., et al. 2018, A&A, 616, A4

Fridlund, M. 2007, COROT discovers its first exoplanet and catches scientists by surprise

Fritzewski, D. J., Barnes, S. A., James, D. J., & Strassmeier, K. G. 2020, A&A, 641, A51

Fritzewski, D. J., Barnes, S. A., James, D. J., & Strassmeier, K. G. 2021, A&A, 652, A60

Fruchter, A. S., Stinebring, D. R., & Taylor, J. H. 1988, Nature, 333, 237

Gaia Collaboration. 2020, VizieR Online Data Catalog, I/350

Gaia Collaboration. 2022, VizieR Online Data Catalog, I/355

Gaia Collaboration, Babusiaux, C., van Leeuwen, F., et al. 2018a, A&A, 616, A10

Gaia Collaboration, Brown, A. G. A., Vallenari, A., et al. 2018b, A&A, 616, A1

Gaia Collaboration, Prusti, T., de Bruijne, J. H. J., et al. 2016, A&A, 595, A1

Gaia Collaboration, Vallenari, A., Brown, A. G. A., et al. 2022, arXiv e-prints, arXiv:2208.00211

Galton, F. 1877, Nature, 15, 492

Garraffo, C., Drake, J. J., Dotter, A., et al. 2018, ApJ, 862, 90

Gehrig, L. & Vorobyov, E. I. 2023, A&A, 673, A54

Geller, A. M., Latham, D. W., & Mathieu, R. D. 2015, AJ, 150, 97

Geller, A. M., Mathieu, R. D., Latham, D. W., et al. 2021, AJ, 161, 190

Gillen, E., Briegal, J. T., Hodgkin, S. T., et al. 2020, MNRAS, 492, 1008

Gonzalez, G. 2016a, MNRAS, 463, 3513

Gonzalez, G. 2016b, MNRAS, 459, 1060

Gordon, T. A., Davenport, J. R. A., Angus, R., et al. 2021, ApJ, 913, 70

Goudfrooij, P., Girardi, L., Rosenfield, P., et al. 2015, MNRAS, 450, 1693

Goudfrooij, P., Puzia, T. H., Chandar, R., & Kozhurina-Platais, V. 2011a, ApJ, 737, 4

Goudfrooij, P., Puzia, T. H., Kozhurina-Platais, V., & Chandar, R. 2009, AJ, 137, 4988

Goudfrooij, P., Puzia, T. H., Kozhurina-Platais, V., & Chandar, R. 2011b, ApJ, 737, 3

Greisen, E. W. & Calabretta, M. R. 2002, A&A, 395, 1061

Gruner, D. & Barnes, S. A. 2020, A&A, 644, A16

Gruner, D., Barnes, S. A., & Weingrill, J. 2023, A&A, 672, A159

Halbwachs, J. L., Mayor, M., & Udry, S. 2018, A&A, 619, A81

Halko, N., Martinsson, P.-G., & Tropp, J. A. 2009, arXiv e-prints, arXiv:0909.4061

Hall, O. J., Davies, G. R., van Saders, J., et al. 2021, Nature Astronomy, 5, 707

Harris, C. R., Millman, K. J., van der Walt, S. J., et al. 2020, Nature, 585, 357

Hartmann, L. 2001, AJ, 121, 1030

Henry, G. W., Kane, S. R., Wang, S. X., et al. 2013, ApJ, 768, 155

Herschel, J. F. W. 1833, Philosophical Transactions of the Royal Society of London Series I, 123, 359

Herschel, J. F. W. 1863, Proceedings of the Royal Society of London Series I, 13, 1

Howell, S. B., Sobeck, C., Haas, M., et al. 2014, PASP, 126, 398

Huber, D., Bryson, S. T., & et al. 2017, VizieR Online Data Catalog, IV/34

Hunter, J. D. 2007, Computing in Science & Engineering, 9, 90

Irwin, J., Aigrain, S., Bouvier, J., et al. 2009, MNRAS, 392, 1456

Irwin, J., Aigrain, S., Hodgkin, S., et al. 2006, MNRAS, 370, 954

James, D. J., Barnes, S. A., Meibom, S., et al. 2010, A&A, 515, A100

Janes, K. 2018, in 20th Cambridge Workshop on Cool Stars, Stellar Systems and the Sun, Cambridge Workshop on Cool Stars, Stellar Systems, and the Sun, 85

Janes, K. 2019, in American Astronomical Society Meeting Abstracts, Vol. 233, American Astronomical Society Meeting Abstracts #233, 259.36

Janes, K. A. 2017, ApJ, 835, 75

Jansen, F., Lumb, D., Altieri, B., et al. 2001, A&A, 365, L1

Jeffries, R. D. 2007, MNRAS, 381, 1169

Jeffries, R. D. & Oliveira, J. M. 2005, MNRAS, 358, 13

Jofré, P., Jackson, H., & Tucci Maia, M. 2020, A&A, 633, L9

Johnson, H. L. 1968, Interstellar Extinction (University of Chicago Press), 167

Johnson, H. L. & Sandage, A. R. 1955, ApJ, 121, 616

Joner, M. D., Taylor, B. J., Laney, C. D., & van Wyk, F. 2006, AJ, 132, 111

Karoff, C., Metcalfe, T. S., Santos, Â. R. G., et al. 2018, ApJ, 852, 46

Kawaler, S. D. 1988, ApJ, 333, 236

Kepler Mission Team. 2009, VizieR Online Data Catalog, V/133

Kervella, P., Mérand, A., Pichon, B., et al. 2008, A&A, 488, 667

Kharchenko, N. V., Piskunov, A. E., Röser, S., Schilbach, E., & Scholz, R. D. 2005, A&A, 438, 1163

Kiraga, M. 2012, Acta Astron., 62, 67

Kjurkchieva, D., Vasileva, D., & Atanasova, T. 2017, AJ, 154, 105

Koenigl, A. 1991, ApJ, 370, L39

Kraft, R. P. 1965, ApJ, 142, 681

Kraft, R. P. 1967, ApJ, 150, 551

Kraft, R. P. & Wrubel, M. H. 1965, ApJ, 142, 703

Krijgsman, W., Hilgen, F. J., Raffi, I., Sierro, F. J., & Wil-

son, D. S. 1999, Nature, 400, 652

Krishnamurthi, A., Terndrup, D. M., Pinsonneault, M. H., et al. 1998, ApJ, 493, 914

Kron, G. E. 1947, PASP, 59, 261

Lam, S. K., Pitrou, A., & Seibert, S. 2015, in Proceedings of the Second Workshop on the LLVM Compiler Infrastructure in HPC, LLVM '15 (New York, NY, USA: Association for Computing Machinery)

Lanzafame, A. C., Distefano, E., Messina, S., et al. 2018, A&A, 616, A16

Lasker, B. M., Lattanzi, M. G., McLean, B. J., et al. 2008, AJ, 136, 735

Lejeune, T., Cuisinier, F., & Buser, R. 1997, A&AS, 125, 229

Lejeune, T., Cuisinier, F., & Buser, R. 1998, A&AS, 130, 65

Lindegren, L., Hernández, J., Bombrun, A., et al. 2018, A&A, 616, A2

Lockwood, G. W., Skiff, B. A., Henry, G. W., et al. 2007, ApJS, 171, 260

Lomb, N. R. 1976, Ap&SS, 39, 447

Lorenzo-Oliveira, D., Meléndez, J., Ponte, G., & Galarza, J. Y. 2020, MNRAS

Lorenzo-Oliveira, D., Meléndez, J., Yana Galarza, J., et al. 2019, MNRAS, 485, L68

Lu, Y. L., Curtis, J. L., Angus, R., David, T. J., & Hattori, S. 2022, AJ, 164, 251

Ludwig, H. G., Caffau, E., Steffen, M., Bonifacio, P., & Sbordone, L. 2010, A&A, 509, A84

Luger, R., Agol, E., Kruse, E., et al. 2016, AJ, 152, 100

Luger, R., Kruse, E., Foreman-Mackey, D., Agol, E., & Saunders, N. 2018, AJ, 156, 99

Lynga, G. & Palous, J. 1987, A&A, 188, 35

MacGregor, K. B. & Brenner, M. 1991, ApJ, 376, 204

Maeder, A. & Meynet, G. 2000, ARA&A, 38, 143

Mallonn, M., Herrero, E., Juvan, I. G., et al. 2018, A&A, 614, A35

Mamajek, E. E. & Hillenbrand, L. A. 2008, ApJ, 687, 1264

Marigo, P., Girardi, L., Bressan, A., et al. 2017, ApJ, 835, 77

Marrese, P. M., Marinoni, S., Fabrizio, M., & Altavilla, G. 2019, A&A, 621, A144

Martin, P. G. & Whittet, D. C. B. 1990, ApJ, 357, 113

Matt, S. & Pudritz, R. E. 2005, ApJ, 632, L135

Matt, S. P., Brun, A. S., Baraffe, I., Bouvier, J., & Chabrier, G. 2015, ApJ, 799, L23

Mayor, M. & Queloz, D. 1995, Nature, 378, 355

McQuillan, A., Aigrain, S., & Mazeh, T. 2013, MNRAS, 432, 1203

McQuillan, A., Mazeh, T., & Aigrain, S. 2014, ApJS, 211, 24

Meibom, S., Barnes, S. A., Latham, D. W., et al. 2011a, ApJ, 733, L9

Meibom, S., Barnes, S. A., Platais, I., et al. 2015, Nature, 517, 589

Meibom, S., Mathieu, R. D., & Stassun, K. G. 2009, ApJ, 695, 679

Meibom, S., Mathieu, R. D., Stassun, K. G., Liebesny, P., & Saar, S. H. 2011b, ApJ, 733, 115

Messina, S., Nardiello, D., Desidera, S., et al. 2022, A&A, 657, L3

Metcalfe, T. S. & Egeland, R. 2019, ApJ, 871, 39

Metcalfe, T. S., Finley, A. J., Kochukhov, O., et al. 2022, ApJ, 933, L17

Metcalfe, T. S., Kochukhov, O., Ilyin, I. V., et al. 2019, ApJ, 887, L38

Meusinger, H., Reimann, H. G., & Stecklum, B. 1991, A&A, 245, 57

Miglio, A., Girardi, L., Grundahl, F., et al. 2021, Experimental Astronomy, 51, 963

Mihalas, D. & Binney, J. 1981, Galactic astronomy. Structure and kinematics

Monet, D. G., Levine, S. E., Canzian, B., et al. 2003, AJ, 125, 984

Nardiello, D. 2020, MNRAS, 498, 5972

Nardiello, D., Borsato, L., Piotto, G., et al. 2019, MNRAS, 490, 3806

Nardiello, D., Deleuil, M., Mantovan, G., et al. 2021, MNRAS, 505, 3767

Naylor, T. 2009, MNRAS, 399, 432

Netopil, M., Paunzen, E., Heiter, U., & Soubiran, C. 2016, A&A, 585, A150

Newton, E. R., Irwin, J., Charbonneau, D., et al. 2016, ApJ, 821, 93

Niederhofer, F., Georgy, C., Bastian, N., & Ekström, S. 2015, MNRAS, 453, 2070

Nissen, P. E. 2015, A&A, 579, A52

Nordström, B., Mayor, M., Andersen, J., et al. 2004, A&A, 418, 989

Nowak, G., Palle, E., Gandolfi, D., et al. 2017, AJ, 153, 131

Noyes, R. W., Hartmann, L. W., Baliunas, S. L., Duncan, D. K., & Vaughan, A. H. 1984, ApJ, 279, 763

Ochsenbein, F., Bauer, P., & Marcout, J. 2000, A&AS, 143, 23

Olivares, J., Bouy, H., Sarro, L. M., et al. 2019, A&A, 625, A115

Oswalt, T. D., Buzasi, D. L., & Otani, T. 2017, in American Astronomical Society Meeting Abstracts, Vol. 229, American Astronomical Society Meeting Abstracts #229, 240.26

Otani, T., von Hippel, T., Buzasi, D., et al. 2022, ApJ, 930, 36

Pablo, H., Whittaker, G. N., Popowicz, A., et al. 2016, PASP, 128, 125001

Paegert, M., Stassun, K. G., Collins, K. A., et al. 2021, arXiv e-prints, arXiv:2108.04778

Paegert, M., Stassun, K. G., Collins, K. A., et al. 2022,

VizieR Online Data Catalog, IV/39

Palla, F., Randich, S., Flaccomio, E., & Pallavicini, R. 2005, ApJ, 626, L49

Palla, F., Randich, S., Pavlenko, Y. V., Flaccomio, E., & Pallavicini, R. 2007, ApJ, 659, L41

Pallavicini, R., Golub, L., Rosner, R., et al. 1981, ApJ, 248, 279

Parker, E. N. 1958, ApJ, 128, 664

Pass, E. K., Charbonneau, D., Irwin, J. M., & Winters, J. G. 2022, ApJ, 936, 109

Pastorelli, G., Marigo, P., Girardi, L., et al. 2019, MNRAS, 485, 5666

Patten, B. M. & Simon, T. 1996, ApJS, 106, 489

Patterson, C. 1956, Geochim. Cosmochim. Acta, 10, 230

Pearson, K. 1895, Proceedings of the Royal Society of London Series I, 58, 240

Pecaut, M. J. & Mamajek, E. E. 2013, ApJS, 208, 9

Pedregosa, F., Varoquaux, G., Gramfort, A., et al. 2011, Journal of Machine Learning Research, 12, 2825

Perrin, M. N., Hejlesen, P. M., Cayrel de Strobel, G., & Cayrel, R. 1977, A&A, 54, 779

Pinsonneault, M. H., Kawaler, S. D., Sofia, S., & Demarque, P. 1989, ApJ, 338, 424

Platais, I., Gosnell, N. M., Meibom, S., et al. 2013, AJ, 146, 43

Predehl, P., Andritschke, R., Böhringer, H., et al. 2010, in Society of Photo-Optical Instrumentation Engineers (SPIE) Conference Series, Vol. 7732, Space Telescopes and Instrumentation 2010: Ultraviolet to Gamma Ray, ed. M. Arnaud, S. S. Murray, & T. Takahashi, 77320U

Prosser, C. F. & Grankin, K. N. 1997, Rotation Periods of Open Cluster Stars. IV., Center for Astrophysics Preprint Series No. 4539, 12 pages

Prosser, C. F., Shetrone, M. D., Dasgupta, A., et al. 1995, PASP, 107, 211

Prosser, C. F., Shetrone, M. D., Marilli, E., et al. 1993, PASP, 105, 1407

Queloz, D., Allain, S., Mermilliod, J. C., Bouvier, J., & Mayor, M. 1998, A&A, 335, 183

Racine, R. 1971, ApJ, 168, 393

Radick, R. R., Lockwood, G. W., Henry, G. W., Hall, J. C., & Pevtsov, A. A. 2018, ApJ, 855, 75

Radick, R. R., Skiff, B. A., & Lockwood, G. W. 1990, ApJ, 353, 524

Radick, R. R., Thompson, D. T., Lockwood, G. W., Duncan, D. K., & Baggett, W. E. 1987, ApJ, 321, 459

Rampalli, R., Agüeros, M. A., Curtis, J. L., et al. 2021, ApJ, 921, 167

Randich, S., Schmitt, J. H. M. M., Prosser, C. F., & Stauffer, J. R. 1996, A&A, 305, 785

Rauer, H., Catala, C., Aerts, C., et al. 2014, Experimental Astronomy, 38, 249

Rebull, L. M., Stauffer, J. R., Bouvier, J., et al. 2016, AJ, 152, 113

Reinhold, T., Bell, K. J., Kuszlewicz, J., Hekker, S., & Shapiro, A. I. 2019, A&A, 621, A21

Reinhold, T. & Hekker, S. 2020, A&A, 635, A43

Ricker, G. R., Winn, J. N., Vanderspek, R., et al. 2014, in Society of Photo-Optical Instrumentation Engineers (SPIE) Conference Series, Vol. 9143, Space Telescopes and Instrumentation 2014: Optical, Infrared, and Millimeter Wave, ed. J. Oschmann, Jacobus M., M. Clampin, G. G. Fazio, & H. A. MacEwen, 914320

Roberts, D. H., Lehar, J., & Dreher, J. W. 1987, AJ, 93, 968

Rucinski, S., Carroll, K., Kuschnig, R., Matthews, J., & Stibrany, P. 2003, Advances in Space Research, 31, 371

Ruprecht, J. 1966, Bulletin of the Astronomical Institutes of Czechoslovakia, 17, 33

Sagan, C. 1986, Dragons of Eden: Speculations on the Evolution of Human Intelligence (Random House Publishing Group)

Sahlholdt, C. L. & Lindegren, L. 2021, MNRAS, 502, 845

Salaris, M. 2009, in The Ages of Stars, ed. E. E. Mamajek, D. R. Soderblom, & R. F. G. Wyse, Vol. 258, 287–298

Sandage, A. 1957, ApJ, 126, 326

Sanjayan, S., Baran, A. S., Németh, P., et al. 2022, Acta Astron., 72, 77

Santos, A. R. G., Breton, S. N., Mathur, S., & García, R. A. 2021, ApJS, 255, 17

Santos, A. R. G., García, R. A., Mathur, S., et al. 2019, ApJS, 244, 21

Scargle, J. D. 1982, ApJ, 263, 835

Schmitt, J. H. M. M. & Mittag, M. 2020, Astronomische Nachrichten, 341, 497

Silva-Beyer, J., Godoy-Rivera, D., & Chanamé, J. 2022, arXiv e-prints, arXiv:2210.01137

Skrutskie, M. F., Cutri, R. M., Stiening, R., et al. 2006, AJ, 131, 1163

Skumanich, A. 1972, ApJ, 171, 565

Smith, J. C., Stumpe, M. C., Jenkins, J. M., et al. 2020, Kepler Data Processing Handbook: Presearch Data Conditioning, Kepler Science Document KSCI-19081-003, id. 8. Edited by Jon M. Jenkins.

Soderblom, D. R. 2010, ARA&A, 48, 581

Soderblom, D. R., Stauffer, J. R., Hudon, J. D., & Jones, B. F. 1993a, ApJS, 85, 315

Soderblom, D. R., Stauffer, J. R., MacGregor, K. B., & Jones, B. F. 1993b, ApJ, 409, 624

Spada, F., Demarque, P., Kim, Y. C., Boyajian, T. S., & Brewer, J. M. 2017, ApJ, 838, 161

Spada, F. & Lanzafame, A. C. 2020, A&A, 636, A76

Stassun, K. G., Oelkers, R. J., Paegert, M., et al. 2019, AJ, 158, 138

Stauffer, J. R., Hartmann, L., Soderblom, D. R., & Burnham, N. 1984, ApJ, 280, 202

Stauffer, J. R. & Hartmann, L. W. 1987, ApJ, 318, 337

Stauffer, J. R., Hartmann, L. W., & Latham, D. W. 1987, ApJ, 320, L51

Stein, G. 1922, Geography and Plays (University of Wis-

consin Press)
Stellingwerf, R. F. 1978, ApJ, 224, 953
Strassmeier, K. G., Hall, D. S., & Henry, G. W. 1994, A&A, 282, 535
Strassmeier, K. G. & Steffen, M. 2022, Astronomische Nachrichten, 343, e20220036
Strassmeier, K. G., Weber, M., Gruner, D., et al. 2023, A&A, 671, A7
Tan, J. & Basri, G. 2020, Astronomische Nachrichten, 341, 513
Tang, J., Bressan, A., Rosenfield, P., et al. 2014, MNRAS, 445, 4287
Tatsumoto, M., Knight, R. J., & Allegre, C. J. 1973, Science, 180, 1279
Taylor, B. J. 2007, AJ, 133, 370
Torres, G., Curtis, J. L., Vanderburg, A., Kraus, A. L., & Rizzuto, A. 2018, ApJ, 866, 67
Torres, G., Vanderburg, A., Curtis, J. L., et al. 2019, ApJ, 887, 109
Torres, G., Vanderburg, A., Curtis, J. L., et al. 2020, ApJ, 896, 162
Ulrich, R. K. 1986, ApJ, 306, L37
Van Cleve, J. E., Howell, S. B., Smith, J. C., et al. 2016, PASP, 128, 075002
van den Heuvel, E. P. J. & Conti, P. S. 1971, Science, 171, 895
van Leeuwen, F. & Alphenaar, P. 1982, The Messenger, 28, 15
van Leeuwen, F., Alphenaar, P., & Meys, J. J. M. 1987, A&AS, 67, 483
van Saders, J. L., Ceillier, T., Metcalfe, T. S., et al. 2016, Nature, 529, 181
VanderPlas, J., Connolly, A. J., Ivezic, Z., & Gray, A. 2012, in Proceedings of Conference on Intelligent Data Understanding (CIDU, 47–54
VanderPlas, J. T. & Ivezić, Ž. 2015, ApJ, 812, 18
Vaughan, A. H. 1980, PASP, 92, 392
Vaughan, A. H. & Preston, G. W. 1980, PASP, 92, 385
Virtanen, P., Gommers, R., Oliphant, T. E., et al. 2020, Nature Methods, 17, 261
Weber, E. J. & Davis, Jr., L. 1967, ApJ, 148, 217
Weiler, M. 2018, A&A, 617, A138
Weiss, W. W., Moffat, A. F. J., Schwarzenberg-Czerny, A., et al. 2014, in Precision Asteroseismology, ed. J. A. Guzik, W. J. Chaplin, G. Handler, & A. Pigulski, Vol. 301, 67–68
Weisskopf, M. C., Tananbaum, H. D., Van Speybroeck, L. P., & O'Dell, S. L. 2000, in Society of Photo-Optical Instrumentation Engineers (SPIE) Conference Series, Vol. 4012, X-Ray Optics, Instruments, and Missions III, ed. J. E. Truemper & B. Aschenbach, 2–16
Wenger, M., Ochsenbein, F., Egret, D., et al. 2000, A&AS, 143, 9
Wilson, O. & Woolley, R. 1970, MNRAS, 148, 463
Wilson, O. C. 1963, ApJ, 138, 832
Wilson, O. C. 1978, ApJ, 226, 379
Wilson, O. C. & Vainu Bappu, M. K. 1957, ApJ, 125, 661
Wood, F. B. 1946, Contributions from the Princeton University Observatory, 21, 1
Yeh, F. C., Carraro, G., Montalto, M., & Seleznev, A. F. 2019, AJ, 157, 115
Zacharias, N., Finch, C. T., Girard, T. M., et al. 2012, VizieR Online Data Catalog, I/322A
Zhao, J.-L. 2005, Progress in Astronomy, 23, 346

Appendix to Paper I

A Relationship between *Gaia* $G_{\rm BP} - G_{\rm RP}$ and Johnson $B - V$

In this section of the Appendix, we present our empirical color transformation between $G_{\rm BP} - G_{\rm RP}$ and $B - V$. The necessity for an easy way to transform between those two colors systems was mentioned above. However, a reliable transformation has yet to be established. Evans et al. (2018) does not provide a direct transformation between the colors. It is possible to use the combination of two relations given there to construct a transformation. But this not only introduces additional uncertainties, a closer inspection reveals that it also fails for stars redder than $B - V = 1.2$. Therefore we decide to derive an empirical relation from observed stars in both color systems

We obtain photometric data for Hyades and Pleiades stars from the WEBDA cluster data base[1]. We use the photoelectric $B - V$ colors and V-band magnitudes, match the stars to the list of identifiers based on their internal reference number, query those in SIMBAD[2], retrieve the *Gaia* DR2 crossmatch from there, and lookup them up in the *Gaia* DR2 catalog to obtain $G_{\rm BP} - G_{\rm RP}$, G, and their parallaxes. This procedure leaves us with 401 and 135 unique stars respectively representing 1044 and 324 magnitudes for the Hyades and Pleiades. We retain all instances of multiple occurrences of the same star. To those, we add the table of Pecaut & Mamajek (2013) to cover redder colors. This provides an independent perspective, given that that relationship is constructed using field stars rather than those of clusters. We complement those with our Ruprecht 147 sample that have *K2* counterparts.

To obtain the intrinsic colors and absolute brightnesses, we deredden the Hyades data. Here we use

$$E_{\rm Hyades}(B-V) = 0.027$$
$$E_{\rm Pleiades}(B-V) = 0.04$$

from Joner et al. (2006) and Breger (1986), respectively. Extinction is calculated as

$$A_V = R_V \cdot E(B-V)$$

with $R_V = 3.1$ for the Johnson colors and magnitudes and

$$E(G_{\rm BP} - G_{\rm RP}) = k \cdot E(B-V) \tag{7.1}$$

and

$$A_G = R_G \cdot E_(G_{\rm BP} - G_{\rm RP})$$

with $k = 1.339$ (using the mean extinction coefficients from Casagrande & VandenBerg 2018, ; their Table 2) and $R_G = 2.0$ (as found in Sect.2.2.3 and Fig. 2.3) for the *Gaia* colors and magnitudes.

The distribution of stars in a Color-Color diagram (cf. panel (a) and (b) in Fig. 7.1) shows that the relation between both color is complex. Despite this complexity, we find very good agreement between the Hyades, Pleiades, the averages of local dwarfs in PM13, and our sample of Ruprecht 147 members, together providing confidence in the applicability of our analytical description. However, given the complexity of the relation, it cannot easily be represented with a simple polynomial approximation.

A.1 Forward transformation

Hence, we decide to use a function with multiple components, each itself a polynomial with a different range of validity. The goal is a one-to-one function

$$f(B-V) = G_{\rm BP} - G_{\rm RP} \tag{7.2}$$

that can be used piece-wise, depending on how red one needs to go, and is both continuous and continuously differentiable, even at join points. For brevity, we substitute $x = B-V$ and $y = G_{\rm BP} - G_{\rm RP}$ in the following. It turns out that we are not able to describe the observed distribution with only one or two polynomials sufficiently[3]. However, we can describe the distribution sufficiently with four polynomials f_i such that, symbolically,

$$y = f(x) = f_1(x) + f_2(x) + f_3(x) + f_4(x),$$

with successive terms added as required when the desired color is redder. We tested various combinations of functions to reproduce the observed distribution and the aforementioned combination provided the best and most simple result we could find. We tested polynomials of different orders, logarithmic-, exponential-, and trigonometric functions. We find that the combination of 4th-order polynomials results in the best description of the observed distribution without invoking too many parameters.

$$f(x) = f_1 + \begin{cases} 0 & x \leqslant 1.11 \\ f_2 & 1.11 < x \leqslant 1.52 \\ f_2 + f_3 & 1.52 < x \leqslant 2.04 \\ f_2 + f_3 + f_4 & x > 2.04 \end{cases} \tag{7.3}$$

where

$$f_1(x') = m_{4,1} \cdot x'^4 + m_{3,1} \cdot x'^3 + m_{2,1} \cdot x^2 + m_{1,1} \cdot x',$$
$$f_2(x') = m_{4,2} \cdot x'^4 + m_{2,2} \cdot x'^2,$$
$$f_3(x') = m_{4,3} \cdot x'^4 + m_{2,3} \cdot x'^2,$$
$$f_4(X) = m_{4,4} \cdot x'^4 + m_{2,4} \cdot x'^2,$$

with

$$x' = s_i \cdot (x - x_{0,i})$$

and the coefficients given in Table 7.1. The resulting curve is displayed in panel (a) in Fig 7.1. Panel (c) shows the residual of the fit.

To ensure continuity of the function and its slope, we restrict the fit to the parts of the polynomial with even exponents (with the exception of f_1) and use only a shift x_0 and re-scaling s in x and no shift in y. This creates a function that, at each breaking point in Eq. (7.3), is a combination of the ones before plus a function whose value and slope are 0.

[1] webda.physics.muni.cz
[2] simbad.u-strasbg.fr/simbad
[3] Testing up to 12th order.

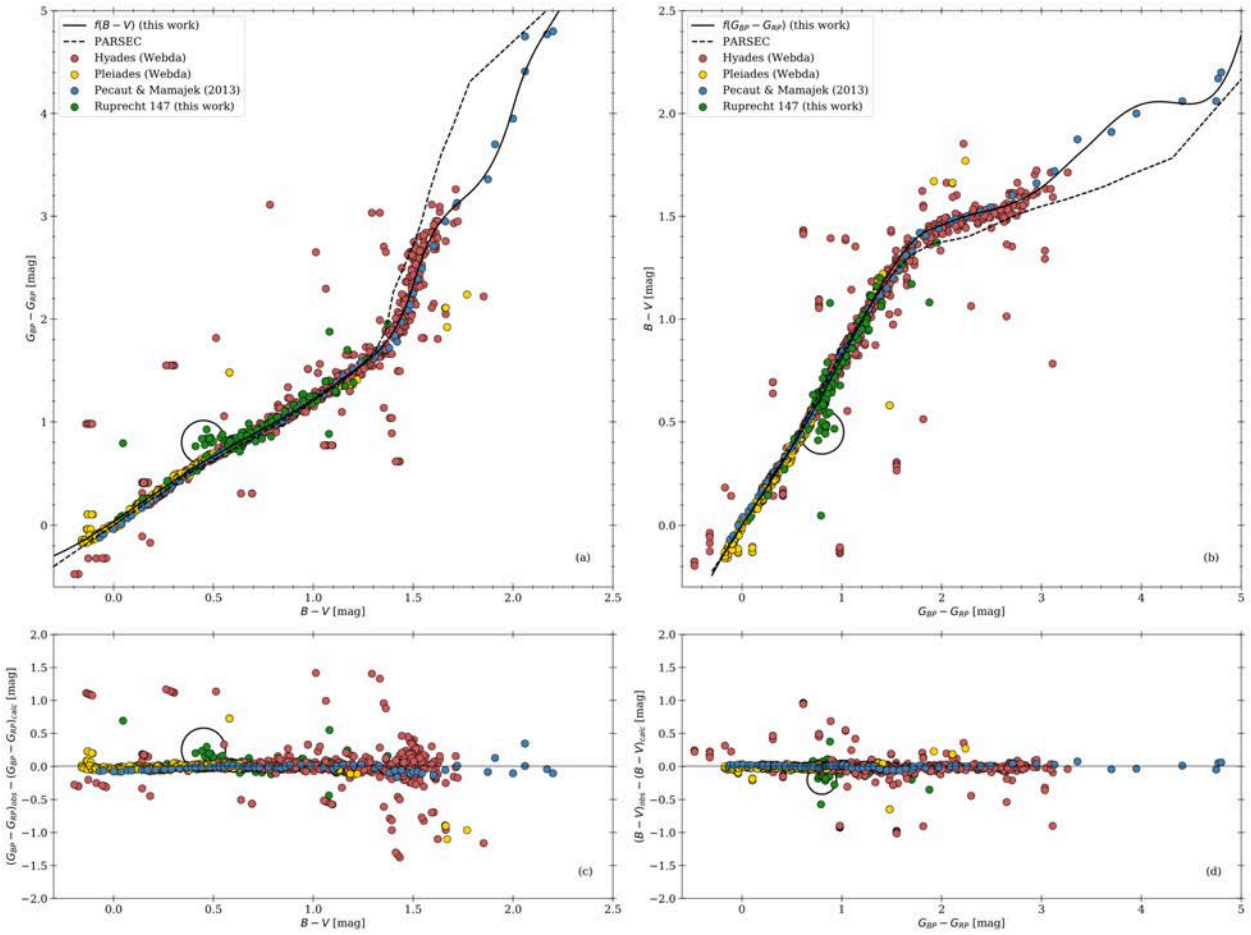

Figure 7.1: *Calibration of the color transformations from $B-V$ to $G_{\rm BP}-G_{\rm RP}$ in Eq.* (7.3) *and vice versa in Eq.* (7.4)*. Panel (a) shows a Color-Color diagram for the Hyades (red), the Pleiades (yellow), and the calibration by PM13 (blue). The same Color-Color diagram, but with switched axes, is shown in panel (b). Overplotted are the relationsships between the two colors as derived. Panels (c) and (d) show the residual between the calculated and measured color for both transformations each. The subgiants of Ruprecht 147 (encircled) do not follow the same relation, as expected. We note that the small horizontal structures in in panel (a), and their equivalents in the other panels, originate from stars with multiple entries in WEBDA.*

A.2 Inverse transformation

We do not only want to have a transformation from $B-V$ to $G_{\rm BP}-G_{\rm RP}$ but also the back transformation. Given the complex shape of $f(x)$ it is not practical to calculate its inverse. It is also not very convenient to solve $f(x)$ numerically for this purpose every time. We decide to derive a completely independent transformation $g(G_{\rm BP}-G_{\rm RP}) = B-V$ in the same way as before. We find the following representation:

$$g(y) = g_1 + \begin{cases} 0 & x \leqslant 1.88 \\ g_2 & 1.88 < x \leqslant 2.67 \\ g_2+g_3 & 1.88 < x \leqslant 3.04 \\ g_2+g_3+g_4 & x > 3.40 \end{cases} \quad (7.4)$$

where

$$\begin{aligned} g_1(y) &= n_{4,1}\cdot y'^4 + n_{3,1}\cdot y'^3 + n_{2,1}\cdot y'^2 + n_{1,1}\cdot y', \\ g_2(y) &= n_{4,2}\cdot y'^4 + n_{2,2}\cdot y'^2, \\ g_3(y) &= n_{4,3}\cdot y'^4 + n_{2,3}\cdot y'^2, \\ g_4(y) &= n_{4,4}\cdot y'^4 + n_{2,4}\cdot y'^2, \end{aligned}$$

with

$$y' = s\cdot(y-y_0)$$

and the coefficients given in Table 7.1. The resulting curve is displayed in panel (b) in Fig 7.1. Panel (d) shows the residual of the fit.

Because the two transformations are not inverses in a mathematical sense, a forward-and-reverse transformation will not generally yield the initial color perfectly again. Given the limited range of colors covered by the stars we used for a fit here, parts of the relation are speculative (and prone to overfitting) and have to be adopted carefully. The stars merit confidence in the relationship described here for

$$0.0 \leqslant B-V \leqslant 1.6 \quad \& \quad 0.0 \leqslant G_{\rm BP}-G_{\rm RP} \leqslant 3.0.$$

We note further that the here found relation is only calibrated on dwarf stars, it may look different for (sub-)giants or white dwarfs. This can be seen for the few (sub-)giants in the Ruprecht 147 sample in Fig. 7.1. However, blue stragglers follow the here found relation.

Additionally to a color transformation, we also need one for the brightnesses to create a CMD. We adopt the same

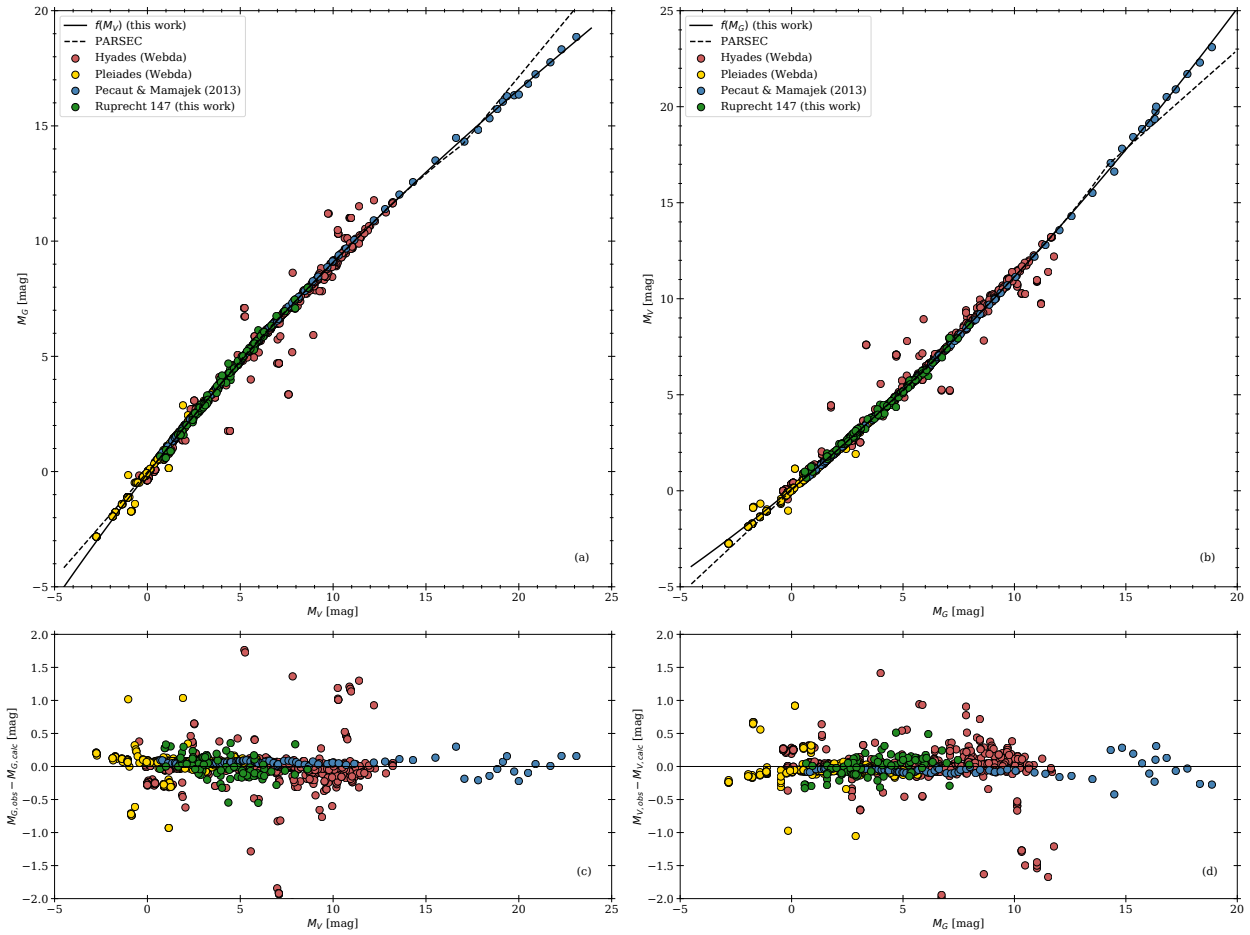

Figure 7.2: *Calibration of the brightness transformations from M_V to M_G in Eq. (7.5) and vice verse in Eq. (7.6). Panel (a) shows a magnitude-magnitude diagram for the Hyades (red), the Pleiades (yellow), and the calibration by PM13 (blue). The same magnitude-magnitude diagram, but with switched axes, is shown in panel (b). Overplotted are the found relation between the two magnitudes each. Panels (c) and (d) show the residual between the calculated and measured magnitudes for both transformations each.*

Table 7.1: *Coefficients used to construct the color transformation from $B - V$ to $G_{\rm BP} - G_{\rm RP}$ in Eq. (7.3) and vice verse in Eq. (7.4).*

	m_4	m_3	m_2	m_1	x_0	s
f_1	0.55	−0.97	0.33	1.27	0.0	1.0
f_2	20.94	–	−2.70	–	1.11	1.00
f_3	−8.62	–	−23.44	–	1.51	1.36
f_4	5.19	–	−11.90	–	2.00	1.79
	n_4	n_3	n_2	n_1	y_0	s
g_1	−0.12	0.29	−0.11	0.74	0.0	1.0
g_2	8.06	—	4.68	—	1.88	0.52
g_3	−28.70	—	−2.05	—	2.67	0.45
g_4	16.26	—	3.5	—	3.40	0.53

	$f(M_V)$	M_G
m_3	0.00017	−0.0001
m_2	−0.01339	0.01684
m_1	1.03269	0.9465
b	−0.07834	0.09871

Table 7.2: *Coefficients used to construct the transformation from M_V to M_G in Eq. (7.5) and vice verse in Eq. (7.6).*

sample as above and use the Gaia parallaxes to calculate absolute magnitudes. As can be seen in Fig. 7.2 (panels a and b), the relation between M_V and M_G is much simpler and can be described with simple polynomials:

$$M_G = f(M_V) = m_3 \cdot M_V^3 + m_2 \cdot M_V^2 + m_1 \cdot M_V + b \quad (7.5)$$

and

$$M_V = g(M_G) = m_3 \cdot M_G^3 + m_2 \cdot M_G^2 + m_1 \cdot M_G + b \quad (7.6)$$

and the coefficients m_i and n_i given in Table 7.2.

We note that there are two approaches to the comparison: (1) on absolute brightnesses and intrinsic colors, or (2) on apparent colors and brightnesses. The latter is intrinsically more correct for the cluster it is calibrated on, since the spectral energy distribution (SED) of a star is reddened prior to the filter. However this limits any relation found to stars with the same reddening and is therefore impratical for an easy comparison. We decided in favor of the former approach, one which may introduce an additional error, but can be applied to every cluster independently of its particular reddening. The introduced error becomes larger for greater reddening. However, this problem can be overcome when the stellar SED is taken into account for the dereddening. Casagrande & VandenBerg (2018) derived extinction parameters that depend on the stellar parameters ($T_{\rm eff}$ and [Fe/H]) and those can be used to describe a

color-dependend reddening. The reddening of the Hyades is small and a uniform extinction is a good approxmiation.

B Details of the Principal Component Analysis

The basic idea of Principal Component Analysis (PCA) is a reduction in data dimensionality by identifying common patterns in the data and creating a new set of k m-dimensional basis vectors $\vec{v}_j$ (PCA components) from the data a with k m-dimensional datapoints a_i. Each datapoint a_i can then be described by a new k-dimensional coordinate $\vec{b}_i$ with $a_i = \sum_j^k b_{i,j} \cdot \vec{v}_j$ in this new basis. The basis is created by k-times successively finding the vector that explains the largest variation in the data (in principle the minimization of the average distance) and removing its contribution to the data. At this point, the dimensionality has changed from m to k, generally not a reduction. The reduction in dimensionality is achieved by simply truncating the dimensionality (from k) in the calculation of a datapoint in the new basis, based on the assumption that the first few components provide a reasonably good approximation of the data.

In our case, each light curve is an m-dimensional datapoint, with $m = 4043$ being the number of points in each light curve[4]. Trend correction with PCA is based on the assumption that trends in the data are visible in a large number or all lightcurves and are therefore represented in the first few components. This means that when calculating a light curve from the new basis using the first components (typically 2-5), only the data systematics, but not the individual variability that changes from lightcurve to lightcurve, is reproduced. The observed light curve is then corrected by its (purposefully incomplete) reconstruction and the residual is the detrended lightcurve.

Unfortunately, reality is almost always more complex. The $\vec{v}_j$ are not individual components of the systematics, with each representing one kind of trending, but averages of the data as a whole. This also means that other effects such as noise and pulsations can intrude into the first few components. Additional difficulties arise when the data systematics themselves show variations. Both of these problems are present in the Ruprecht 147 data. The challenge is to find the correct number of PCA components for the reconstruction to account for (enough of) the systematics present, while also not including the intrinsic stellar variability that is our signal, and which we obviously would like to retain. There is no metric to choose the number of components necessary for a given light curve in our case because those instrumental characteristics vary across the field, CCD, channel, etc. Consequently, the procedure becomes intrinsically somewhat subjective.

We believe that we have been able to bound these problems for a significant number of stars of interest. Numerous lightcurves show variations that clearly originate in stellar pulsations, with remnants of this behavior finding their way into the prominent components. Similar effects can be observed for starspot induced variations. This can lead to over-fitting and the introduction of high frequency variations. We cross-checked by eliminating the pulsating stars from the sample and redoing the PCA; the problematic components disappeared as expected. This issue could not be resolved by omitting those components from the reconstruction because those still carry parts of the global trends necessary for the elimination of systematics.

Therefore, we use a different procedure. We select a subset of our *full sample* by omitting all lightcurves that clearly show pulsations, spot induced variation, artifacts, such as sudden jumps, or eclipses. Furthermore, we eliminate very noisy lightcurves from our sample. Moderately noisy data are retained, but we smooth all lightcurves with 1 d binning. This does not affect our analysis because variations on this timescale are irrelevant for our work. The smoothing is only applied for the purposes of PCA; the final lightcurves are provided on the original sampling corrected by the smoothed PCA solution. At this point, we are left with $k \approx 3000$ lightcurves as the basis for the PCA.

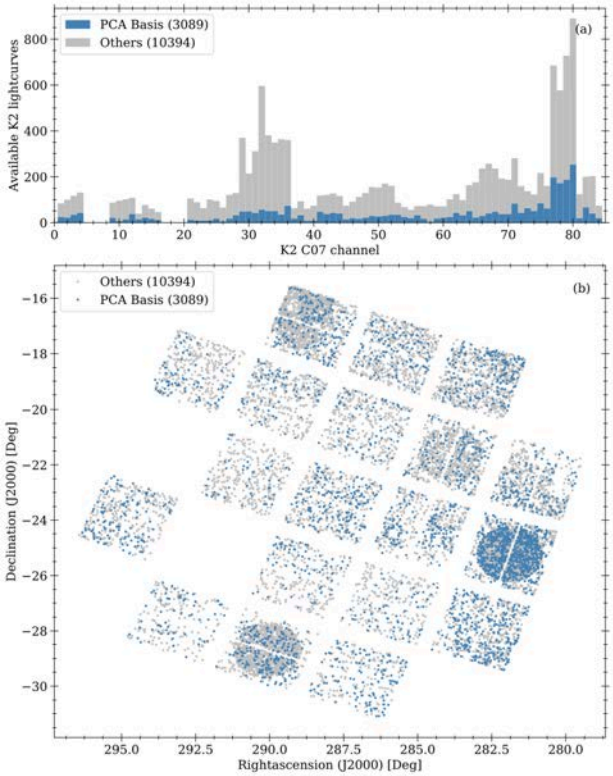

Figure 7.3: *Selection of the ($\approx$ 3000) lightcurves for the PCA basis. Panel (a) shows histograms of lightcurves available (gray), and those taken for the PCA basis (blue), as distributed over the* K2 *channels. Panel (b) shows the spatial distribution across the entire* K2 *C07 field.*

As can be seen in Fig. 7.3, our selection of lightcurves for the PCA basis is more or less evenly distributed across the C07 field of view and across the CCD channels, at least to the extent that the *K2* target selection allows. Furthermore, it can be seen that the basis is not biased with respect to the position of the Target Pixel Files (TPFs) inside a *Kepler* module and channel. Finally, the boundaries of the

[4]The sampling rate of the light curves is irrelevant as long as all are sampled in the same way

lightcurve must be addressed. The PCA and the smoothing can introduce artifacts at the beginning and end of the data stream. To eliminate those effects, we censor the first and last 80 data points from each lightcurve for the purposes of period analysis.

PCA requires a set of identically sampled light curves. We also work with light curves that are normalized to their respective medians. Each of the relevant *K2* light curves contains 4043 data points, but not all of these have meaningful values stored. For instance there are both outliers and NaNs. Luger et al. (2016) provide a mask that lists outliers for each data set. These are virtually identical for all datasets, but the NaNs are not. To perform the PCA we replace both the NaNs and masked values by a linear interpolation using neighboring data points. If these are unavailable, that is, at the beginning or the end of the data, we set the flux to unity. The interpolations occur on time scales ($\leqslant 0.5$ d) that are irrelevant to our expected periodicity timescales of many days. This procedure provides a set of identically sampled lightcurves for the PCA.

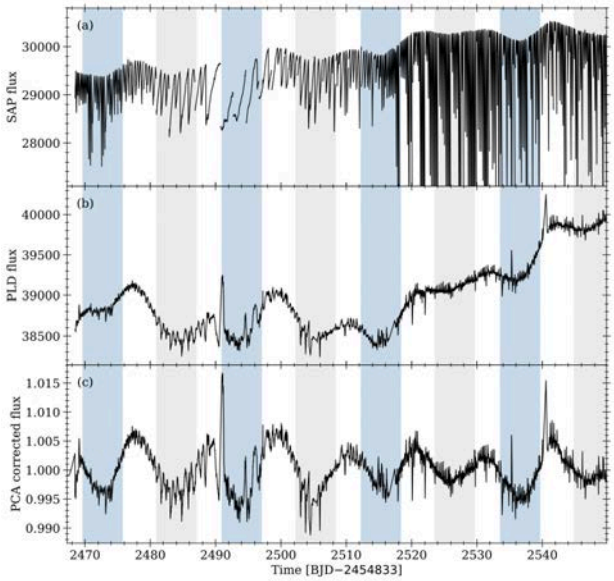

Figure 7.4: *Example of the lightcurve correction process using EPIC 219722781. Panel (a) shows the original* K2 *lightcurve from simple aperture photomerty (SAP). Panel (b) shows the* `Everest` *lightcurve after the pixel level de-correlation (PLD). Panel (c) displays the lightcurve after both normalization and principal component analysis (PCA). In all panels, the colored regions mark identified flux variations assigned to two different spots with a phase shift of 0.47 and a period of 21.3 d.*

We perform the PCA for each lightcurve individually by comparing the relevant lightcurve with the basis, as constructed above. The prominent components determined by PCA on just the basis, as compared with the basis plus one lightcurve, are virtually identical. The calculation is performed using the `python` implemetation in the `sklearn` package, which itself is based on the method outlined in Halko et al. (2009). Figure 7.4 displays a comparison of three lightcurves for the same object, EPIC 219722781, (a), from the *Kepler* archive based on simple aperture photometry, (b), the `Everest` lightcurves, and (c), our detrended lightcurve. Flux dips identified as belonging to two different starspots are marked with their periodic re-occurrence. As can be seen, these features are visible to the experienced eye in all stages of the processed lightcurve.

The degree of reproduction from the PCA is crucial for our final lightcurves and the derived results. If only a small number of components is used, the reproduction is clearly insufficient in suppressing observable trends. If too many components are used, we risk overfitting, and destroy clear signals from stellar variation. As can be seen, the lightcurve trends occur on the same timescale (10 d to 40 d) as the spot-induced variability. This complicates the identification of stellar flux variations. The slowest rotators tend to be impacted more by this, given their low amplitude of brightness variation.

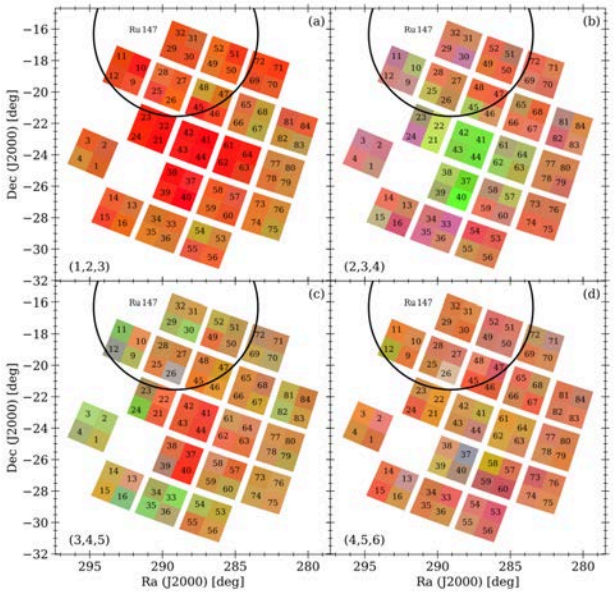

Figure 7.5: *Spatial distribution of the observed trending in the EVEREST lightcurves of* K2 *C07. Each colored patch represents a channel with the corresponding number labeled. The color of each patch is based on the contribution of individual components. Here, the calculation works as follows: For each color, three components are adopted with their scaling factors from the PCA as RGB values. The numbers for each color are normalized to their maximum to guarantee a color range of 0 – 1. This is calculated for each lightcurve that is part of our basic sample (see text, Sect. B). We calculate a mean color and mean position of all lightcurves from each channel, which is then plotted. The channel number is plotted at the mean position. The difference between the individual panels are the components used for the RGB color. In panel (a), red is given by component one, green by component two and blue by component three. For (b), (c), and (d), the components used are* $(2, 3, 4)$, $(3, 4, 5)$, *and* $(4, 5, 6)$, *respectively. The position of Ruprecht 147 is indicated.*

We have compared the contribution of the components for the individual lightcurves to their origin on the *Kepler*/*K2* CCD and have not found any correlation with the channel, module, or location in each channel. However, there appears to be a correlation with the location in the *K2* C07 field itself; see Fig. 7.5. The further away from the center of the *K2* field a lightcurve was extracted, the more that extraction shifts the contribution from the first to the

second and third components. When one considers higher components, this trend is reversed.

As a consequence of the foregoing considerations, we adjust the number of components used for each star individually. We require that a variation that is adopted as a spot-induced feature has to be visible in the original light curve as well as for a PCA corrected with a high number of components. Its specific form may vary because of the presence of data systematics or overfitting, but it will still be visible. It turns out that 5 to 8 components are usually used for the reconstruction. We do not skip individual components up the selected one, that is, all components of lower order than the final number are used. The resulting (de-trended) light curves are subjected to periodicity analysis, as described in the main text in Sect. 2.3.3.

C Lightcurves and phase diagrams

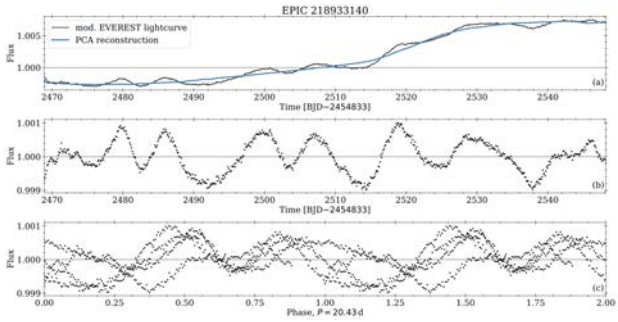

Figure 7.6: *Light curve, PCA correction and phase plot for sample stars. Panel (a) shows the modified EVEREST light curve (black) and the reconstruction from the PCA (blue). The modifications for the PCA are applied as outlined Sect. 2.3.2. Panel (b) shows the corrected lightcurve and panel (c) the phase plot. For visibility reasons all data are displayed with a 0.1 d binning.*

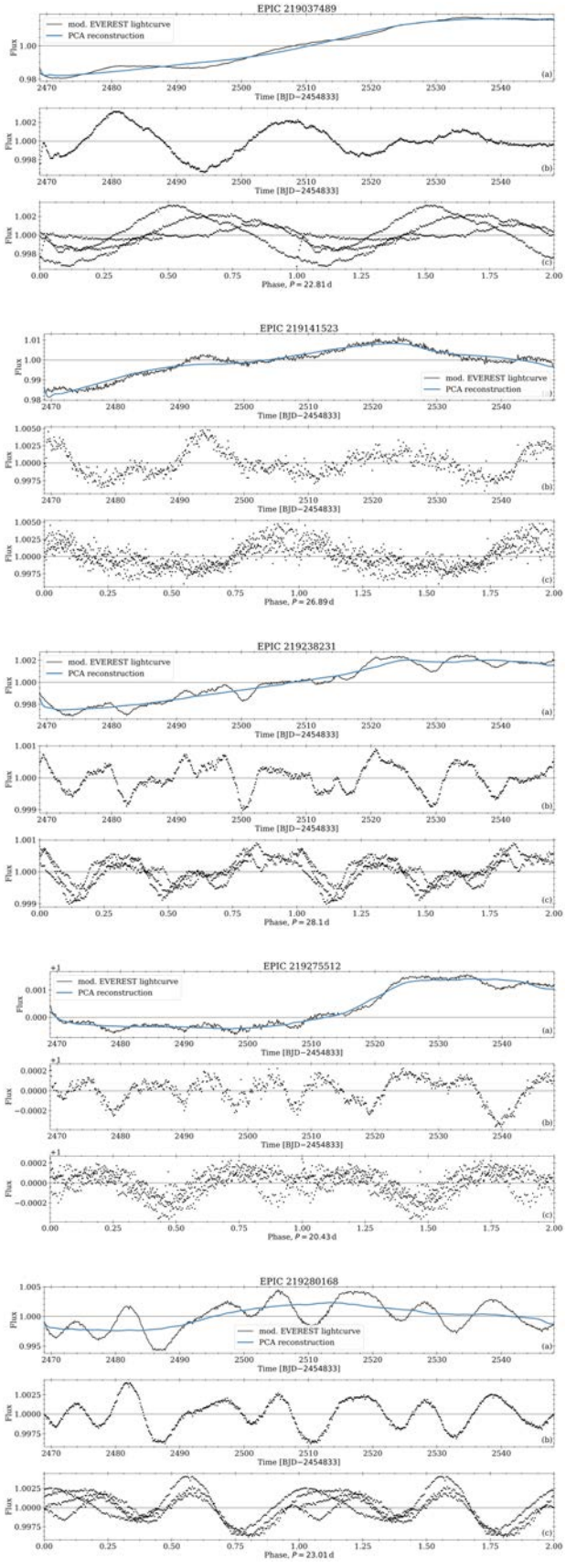

Figure 7.6: *continued.*

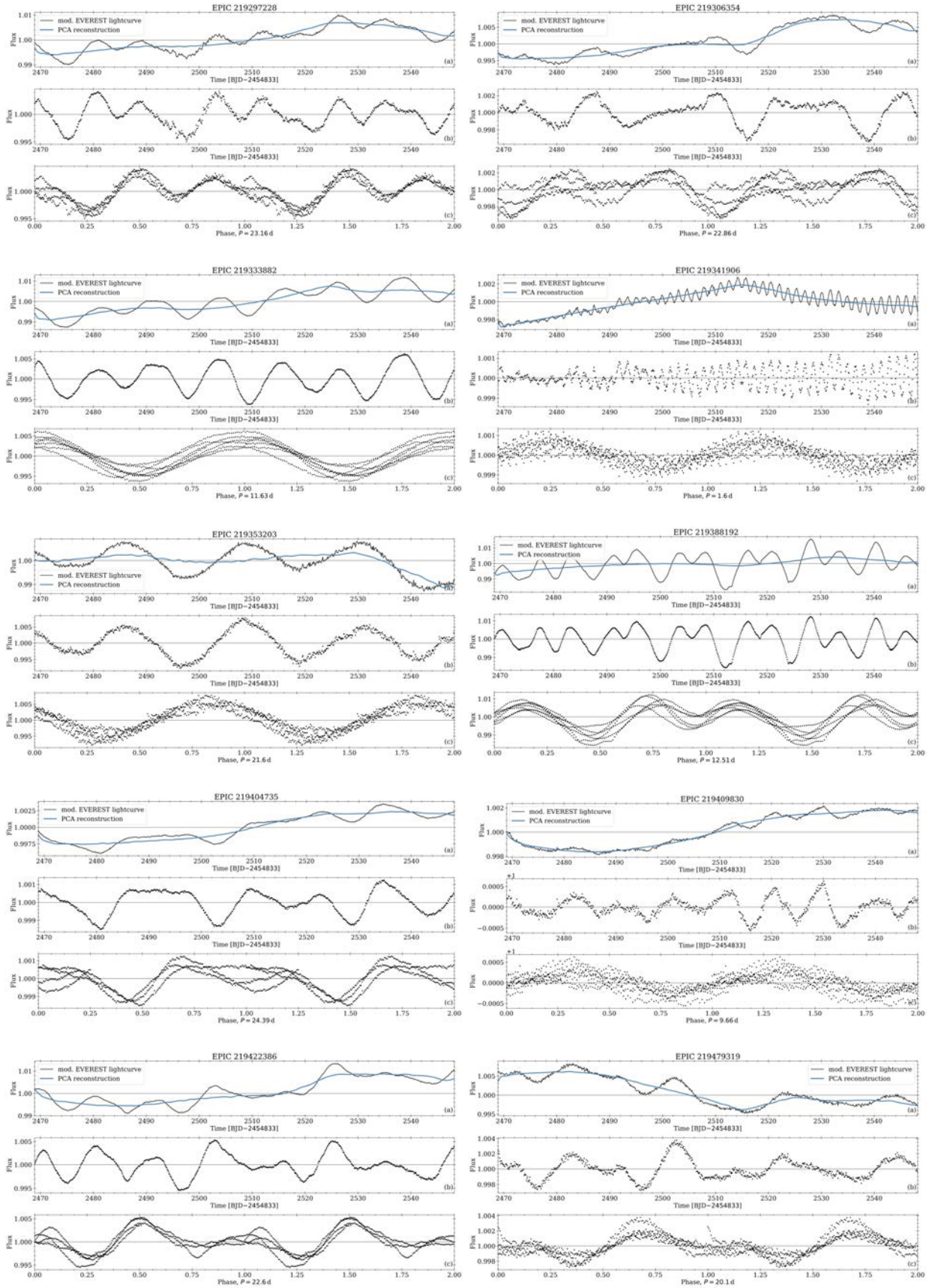

Figure 7.6: *continued.*

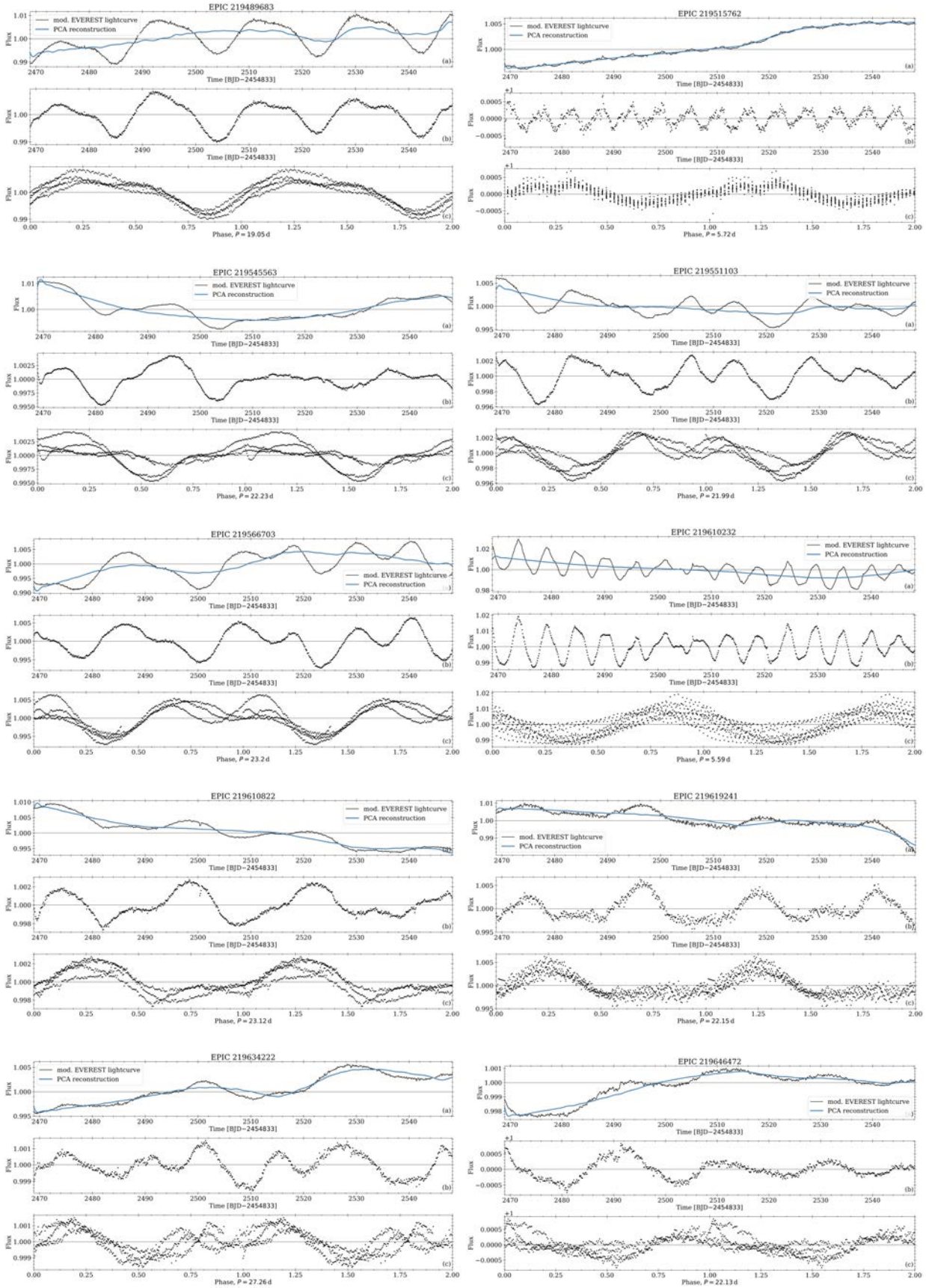

Figure 7.6: *continued.*

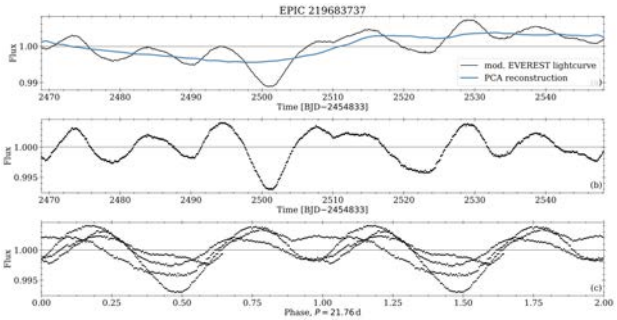

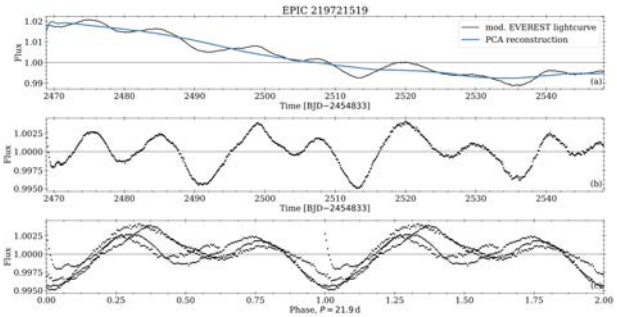

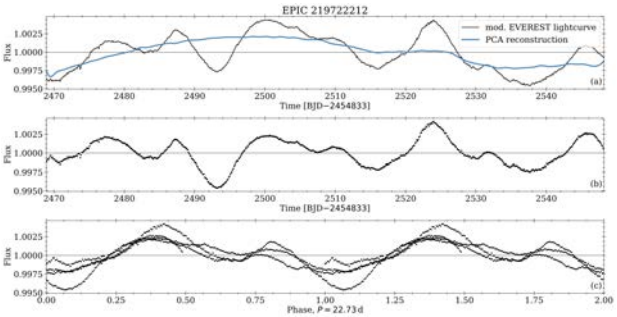

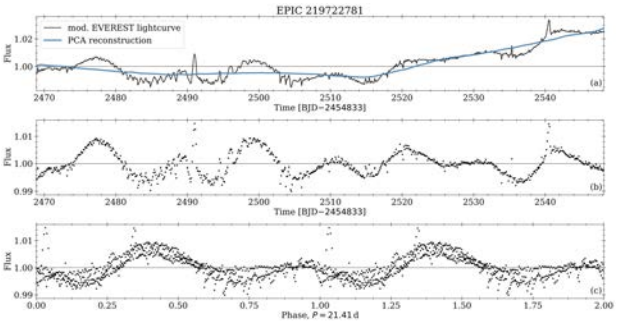

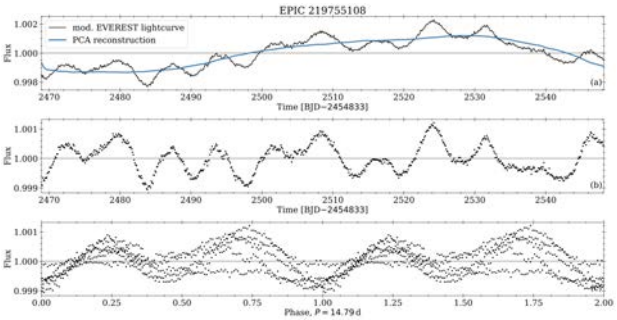

Figure 7.6: *continued.*

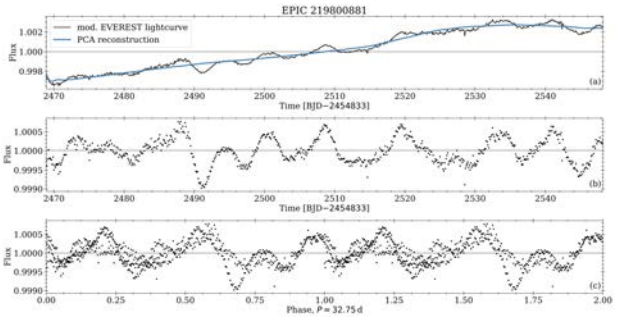

Figure 7.6: *continued.*

D Sample table

Table 7.3: *Identifiers and basic information for the 32 periodic Ruprecht 147 stars.* Notes:
(a) Reddening and extinction adopted from closeby source
(b) Y = member, P = likely member, N = no member, Cu13 = Curtis et al. (2013)
(c) Y = member, GC18 =Gaia Collaboration et al. (2018a)
(d) Membership probability, DANCe = Olivares et al. (2019), CC18 = Cantat-Gaudin et al. (2018)

Gaia	EPIC	2MASS	G [mag]	$(G_{\rm BP}-G_{\rm RP})_0$ [mag]	Plx [mas]	M_G [mag]	B [mag]	V [mag]	J [mas]	H [mag]	K [mag]	Cu13[b]	GC18[c]	CC18[d]	Ol19[d]
4084645500601105536	218933140	19180938-1752498	12.36	0.87	3.31	4.91	13.28	12.52	11.11	10.82	10.74	-	-	1.0	0.35
4087622153460553216	219037489	19144383-1739427	13.03	0.99	3.32	5.59	14.13	13.22	11.63	11.28	11.15	-	Y	1.0	0.99
4087725262729508736	219141523	19153691-1726070	16.56	2.27	3.46	9.21	-	-	13.91	13.31	13.1	-	Y	0.7	0.31
4087736159069458304	219238231	19163672-1713101	12.09	0.78	3.25	4.6	13.37	12.3	10.95	10.68	10.62	Y	Y	1.0	0.81
4087748833503644800	219275512	19155912-1708032	11.86	0.88	3.3	4.4	12.54	11.87	10.61	10.28	10.19	-	Y	1.0	0.0
4087714409360276864	219280168	19133741-1707261	13.33	1.15	3.35	5.9	14.58	13.57	11.77	11.27	11.17	-	Y	0.7	0.92
4087799655867454720	219297228	19152010-1705038	13.61	1.13	3.2	6.08	14.47	13.45	12.11	11.62	11.56	-	Y	1.0	0.92
4087762371240557696	219306354	19172705-1703472	13.03	0.98	3.2	5.5	-	13.2	11.66	11.29	11.21	-	Y	1.0	0.99
4087769075699852416	219333882	19173541-1659580	13.56	1.16	3.03	5.92	14.88	13.89	11.96	11.47	11.37	-	-	0.7	0.95
4180839161574392704	219341906	19193373-1658514	9.76	0.75	3.29	2.3	10.48	9.85	8.68	8.4	8.33	Y	-	-	-
4087770239621640704	219353203	19173100-1657159	16.24	2.1	3.3	8.78	-	-	13.75	13.09	12.84	-	-	1.0	0.99
4087782677845919744	219388192	19173402-1652177	12.36	0.86	3.25	4.87	13.28	12.53	11.07	10.73	10.67	P	Y	1.0	0.93
4087786874044570880	219404735	19170954-1649540	11.48	0.79	3.45	4.12	12.3	11.61	10.34	10.05	9.97	-	Y	0.8	0.0
4088004611707768320	219409830	19134334-1649109	12.28	0.83	3.19	4.75	13.07	12.35	11.13	10.77	10.72	P	Y	1.0	1.0
4183850105448920576	219422386	19182218-1647232	13.17	1.01	3.16	5.62	14.26	13.4	11.79	11.4	11.31	-	Y	1.0	0.98
4087838104415873920	219479319	19164975-1638577	14.94	1.6	3.19	7.41	16.59	15.42	12.9	12.32	12.13	-	Y	1.0	0.98
4183867079159884672	219489683	19175045-1637260	15.38	1.78	3.31	7.92	17.11	16.03	13.18	12.51	12.32	-	Y	1.0	0.97
4183915388953023616	219515762	19172865-1633313	9.99	0.57	3.17	2.44	10.62	10.16	9.11	8.97	8.9	Y	-	-	-
4088042888457322624	219545563	19135496-1628553	12.79	0.93	3.22	5.28	13.79	13.01	11.52	11.12	11.05	-	Y	1.0	0.97
4088034161083427968	219551103	19123785-1628037	13.03	1.0	3.2	5.51	14.1	13.24	11.63	11.21	11.16	-	Y	1.0	1.0
4087858819031214336	219566703	19153354-1625368	14.46	1.51	3.17	6.91	16.17	14.9	12.52	11.89	11.74	Y	Y	1.0	0.93
4088060686802235392	219610232	19133109-1618401	13.32	1.17	3.2	5.8	14.65	13.7	11.63	11.13	11.01	-	-	1.0	0.98
4088051783318575488	219610822	19144049-1618344	13.52	1.11	3.16	5.97	14.72	13.7	12.0	11.57	11.42	-	Y	1.0	0.99
4088060892960421248	219619241	19133215-1617120	16.22	2.11	3.36	8.8	-	-	13.77	13.08	12.84	-	Y	1.0	0.99
4183930777809206656	219634222	19181352-1614496	13.64	1.29	3.46	6.28	15.04	13.98	11.87	11.32	11.2	N	Y	1.0	0.96
4183942670575016320	219646472	19172382-1612488	9.99	0.61	3.23	2.48	10.66	10.03	9.26	8.9	8.82	P	Y	0.7	0.78
4183968401721906048	219683737	19175075-1606406	13.31	1.07	3.27	5.84	14.53	13.54	11.84	11.41	11.31	-	Y	1.0	0.99
4184140406570650496	219721519	19161757-1600177	13.08	1.1	3.93	6.0	14.27	13.31	11.52	11.07	10.94	P	-	-	-
4184146900561610880	219722212	19152141-1600107	12.77	0.94	3.11	5.18	13.72	12.9	11.43	11.09	11.05	Y	Y	1.0	0.98
4184140994996369152	219722781	19163732-1600050	13.89	1.39	4.01	6.86	-	-	12.02	11.45	11.35	Y	-	-	0.64
4184200501759138688	219755108	19141294-1554291	11.95	0.94	3.2	4.42	12.96	12.14	10.61	10.25	10.17	Y	-	-	-
4184182737768311296	219800881	19162203-1546159	12.56	0.9	3.09	4.96	13.5	12.71	11.29	11.0	10.86	Y	Y	1.0	0.45

Appendix to Paper II

E M 67 cluster membership

In this section we describe the process that we used to determine cluster membership. For this, we use the stellar photometry (G and $G - G_{\rm RP}$), proper motions ($\mu_{\rm Ra}$ and $\mu_{\rm Dec}$), parallax ϖ, and radial velocity $v_{\rm rad}$ to the extent available in the sample. Based on a comparison with the cluster parameters (cf. Table 3.1), each star is then classified as either a *member*, *candidate*, or a *field star* in each of these parameter categories. Stars that lack a particular parameter are designated as *unknown*. Those individual designations are then combined into a single membership assessment.

For parallax and radial velocity, we define a range around the cluster value in which each star is designated a *member* when the measured value overlaps with that range within its error. A second, larger range is defined in similar fashion for the designation of *candidate* status (see below). For proper motions, we use a circular area around the cluster that is compared with the error ellipse spanned by the proper motion errors in the same way. The ranges around the cluster are defined as

$$\mu_{\rm M67} \pm 2.5\,\text{mas/yr for } \textit{member}, \tag{7.7}$$
$$\mu_{\rm M67} \pm 3.5\,\text{mas/yr for } \textit{candidate}, \tag{7.8}$$
$$v_{\rm rad,M67} \pm 10\,\text{km/s for } \textit{member}, \tag{7.9}$$
$$v_{\rm rad,M67} \pm 15\,\text{km/s for } \textit{candidate}, \tag{7.10}$$
$$\varpi_{\rm M67} \pm 0.2\,\text{mas for } \textit{member}, \text{ and} \tag{7.11}$$
$$\varpi_{\rm M67} \pm 0.3\,\text{mas for } \textit{candidate}. \tag{7.12}$$

An additional constraint for the parallax criterion is that the parallax needs to exceed its error by a factor > 3. Furthermore, we limit the proper motion offset to ± 8 mas/yr. Table 7.4 provides an overview of the sample sizes in each category determined by this process.

Table 7.4: *Membership overview. For each parameter involved in the membership designation and merged result, we list the number of stars falling into the categories described in the text.*

Status	phot.	PM	plx	$v_{\rm rad}$	M 67
Member	1226	913	856	1226	873
Candidate	186	18	63	186	–
Field star	549	1082	877	549	1140
Unknown	52	0	217	52	–

Because a cluster follows a complex sequence in the color-magnitude diagram (instead of being approximately represented by a single point), we need a more sophisticated approach. Instead, for each star we calculate the χ^2 distance to a cluster isochrone. We use a PARSEC isochrone corresponding to the age and metallicity of M 67 and apply dilution, extinction, and reddening according to Table 3.1. Similar to all other parameters, this χ^2 is then used to evaluate the photometric cluster membership.

Following the assessment as described above, we have evaluated four individual membership criteria. Figure 7.7 shows the assigned category to the sample for each parameter. To combine them into a single, general membership designation, we assign a numeric value to each category. Here, *member* counts as 1.0, *candidate* as 0.5, and *field star* as 0.0. Those values are then added up for each star and divided by the number of available criteria for each star. If the resulting fraction for a star evaluates to a value $\geqslant 0.5$, we designate that star as a *member*, wheras stars with lower values are designated as *field stars*. The result of this combination is displayed in the final column named *M67* in Table 7.4 and plotted accordingly in Fig. 3.2. Stars with fewer than two criteria available are treated as field stars. This is only relevant for stars with $G > 20$ mag, for which photometry is often the only available parameter.

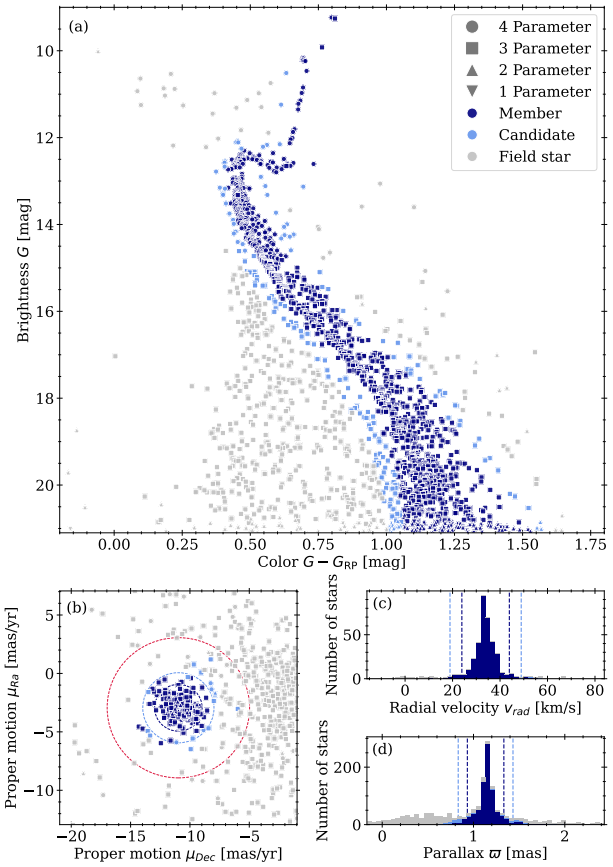

Figure 7.7: *M 67 cluster membership evaluation. The panels (a) to (d) show the individual parameters used for our membership analysis: photometry, proper motions, radial velocity and parallax, respectively. Each point in panels (a) and (b) is a* Gaia *DR3 target in the field of view. Panels (c) and (d) show histograms (gray) of the sample. The parameter numbering in the legend refers to the number of parameters that are available per star. The color coding indicates the assigned membership status. We note that this refers solely to the membership on the respective parameter of panel, not on the total membership. For an overview of the total membership, see Fig. 3.2. The dashed lines in panels (b), (c), and (d) indicate the parameter ranges for* member *and* candidate *designations based on Eqs.* (7.7) *to* (7.12) *(dark and light blue, respectively). The red circle in panel (b) indicates the 8 mas/yr cutoff.*

F K2 systematics correction

In this section, we describe the steps that were taken to extract and correct light curves from the *K2* superstamp. In Sect. 3.3 have we already introduced the notation regarding *intrinsic variability*, *instrumental systematics*, and *trending* which we will continue to use here. The method for correcting the instrumental systematics was iterative, following the understanding of their nature and an exploration of different ways of approaching the problems present. Below we describe the approach that provided the best results. The method involves a detailed understanding of the systematics present in the data. We illustrate the process on the example of the sample star *Gaia DR3 604895948360165888*[5].

F.1 General description of the systematics

We begin with a description of the systematics because their precise characteristics arise from multiple sources, not apparent immediately. However, those details are crucial to obtaining good results.

As noted before, during the *K2* mission several parts of the *Kepler* telescope ceased to function. Among those were the reaction wheels, crucial for the stability of the telescope's pointing. Their malfunction caused the telescope to drift and to lose its pointing on the sky. This drift was then regularly corrected with the telescope thruster, pointing the telescope back to its intended location. The drift was small and firings were frequent to prevent targets from moving out of the field of view (aside from objects on the edges).

However, this constant motion away and back caused an object to meander across the detector. While the drift itself is slow and the stars do not leave visible trails on the images, they still fall on slightly different clusters of pixels on the detector. Figure 7.8 shows the visible difference in the stellar positions on the detector between two different cadences. This shift is small; a little more than two pixels in a diagonal motion (at least for the *K2* superstamp data). With the large pixels of *Kepler* ($4''$), however, this motion spans $\approx 10''$ a significant amount in crowded regions, especially when one considers the overlap of the individual point spread functions (PSF).

While motion alone could probably be corrected relatively easily, an additional effect introduces further complexity; the sensitivity of the detector is not constant across its surface. To be more precise, even on a subpixel scale, two areas of the CCD record different fluxes despite being illuminated by the same amount.

Considering both the constant drift and varying sensitivity, this means that the recorded flux of an intrinsically constant star is different depending on the epoch of observation. And since the individual regions of the detector are largely independent of each other, those changes in flux are different from position to position (and with that from star to star) on the CCD. Their systematic changes can be small and barely noticeable in a particular star while causing flux differences exceeding 15 % for others. Applications that seek to identify variations in the mmag range are therefore difficult.

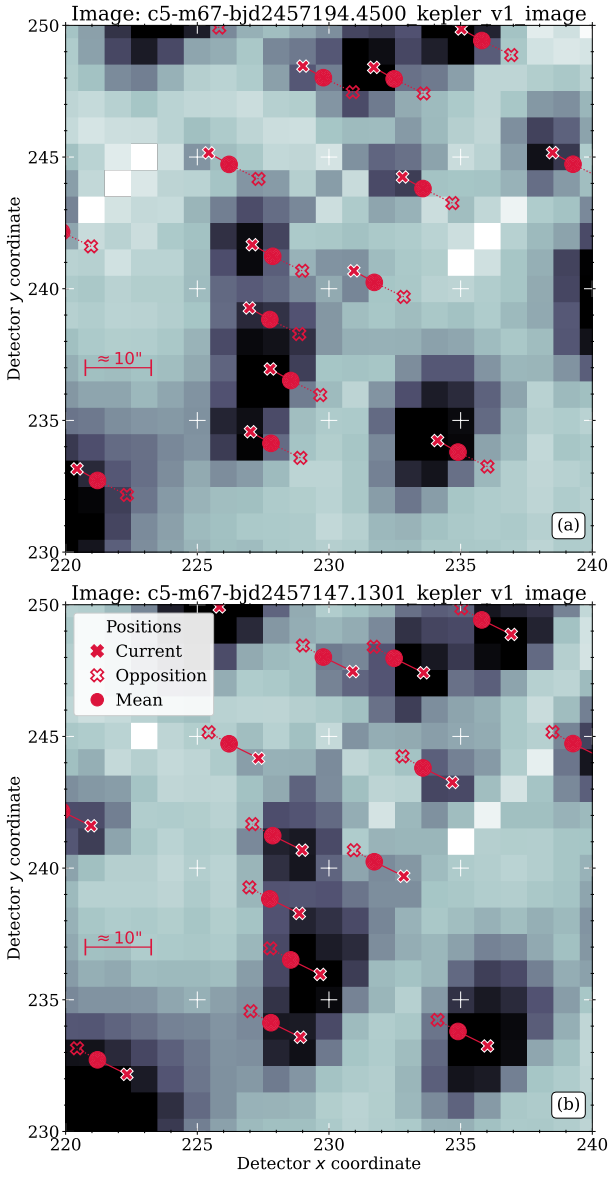

Figure 7.8: *Visualization of the two most extreme positions of the telescope drift during C05. Upper and lower panel both show superstamp images ($\Delta t \approx 47\,d$) indicating the peak-to-peak positional variation, that is, the minimal and maximal x coordinate of a star. The CCD pixel range is identical in both images. The red dots represent the mean position of a star throughout the observing run, and the filled red crosses connected to them mark the position at the time of the image. Red outlines crosses indicate the extreme opposite positions of a star. The white crosses indicate identical pixel coordinates in both panels to help to visualize the magnitude of the positional changes.*

We are fortunately seeking stars that are not very variable and which change only over the course of tens of days, whereas the systematics occur of time scales of a few hours. As such, we can assume that our targets of interest are constant during a single drift, with only a small change in flux occurring from one drift to another.

However, the motion is more complicated than the description so far; it changes over the course of the cam-

[5] $G = 16.3\,\mathrm{mag}$ and $G_{\mathrm{BP}} - G_{\mathrm{RP}} = 1.58\,\mathrm{mag}$

paign, drifts are unequal in length and amplitude, and there are jumps in the pointing. Therefore, we cannot adopt a mean flux from each drift; more precautions have to be taken to obtain reasonable light curves. Fortunately, the motions do allow us to identify common patterns which are then transferred into chunk-wise processing of the light curves. Images taken during the thruster firing (where the motion during the exposure is significant) exist, but those are fortunately rare (and only one or two at a time) and are consequently simply omitted by us. We also note that the sensitivity changes across the CCD are sufficiently well behaved to allow us to model them with a polynomial function, simplifying the problem.

We use aperture photometry for this work. Photometry that models the point spread function (PSF) generally allows disentangling stars in crowded regions to a certain extent, but there are two problems with the application of PSF photomtery to *K2* data. The low spatial sampling and large FOV introduce complicated PSF shapes that vary across the detector, and even vary strongly depending on where a star is located on a subpixel scale. This alone can be solved with a sufficiently detailed empirical PSF, for example, see the PATHOS project (Nardiello et al. 2019; Nardiello 2020; Nardiello et al. 2021; Messina et al. 2022) that operates this way on *TESS* data.

However, given the special problems of *K2* as described above we also face the issue that the PSF changes for a star from image to image, while also being essentially unique for each star in a particular image. The nominal strength of PSF fitting, the assumption that stars have similar PSF shapes despite differing in their fluxes, is not valid for these data.

F.2 Details of telescope drift

To obtain the information about the motion of the star across the detector, we utilize the world coordinate system (WCS) for each image provided by Cody et al. (2018). This allows us to calculate the position $p_0(t) = (x_0(t), y_0(t))$ of a star in each image. While we use the GDR3 ICRS coordinates for this, it would, however, not be a problem to use J2000 (or other) coordinates instead since we are only interested in relative changes.

For simplicity going forward, we will always refer to the telescope drift from the viewpoint of the star moving across the detector. As already noted, the motion of stars is not as simple as a straightforward back-and-forth motion. It is shown in Fig. 7.9 for one example. The majority of the motion is in a diagonal direction, with an additional slow drift perpendicular to that, the latter jumping with some regularity. These jumps force us to divide the light curve into individual chunks of similar behavior. Since these are all on the same detector, the emerging patterns arethe same for each star, allowing us to construct one mask that works for all.

The first step is to simplify this motion by transforming the underlying coordinate system (x, y) to one where the majority of the motion is along one coordinate axis. For that we determine the gradients m_i between two consecutive cadences ($p(t_{i-1})$ and $p(t_i)$) as

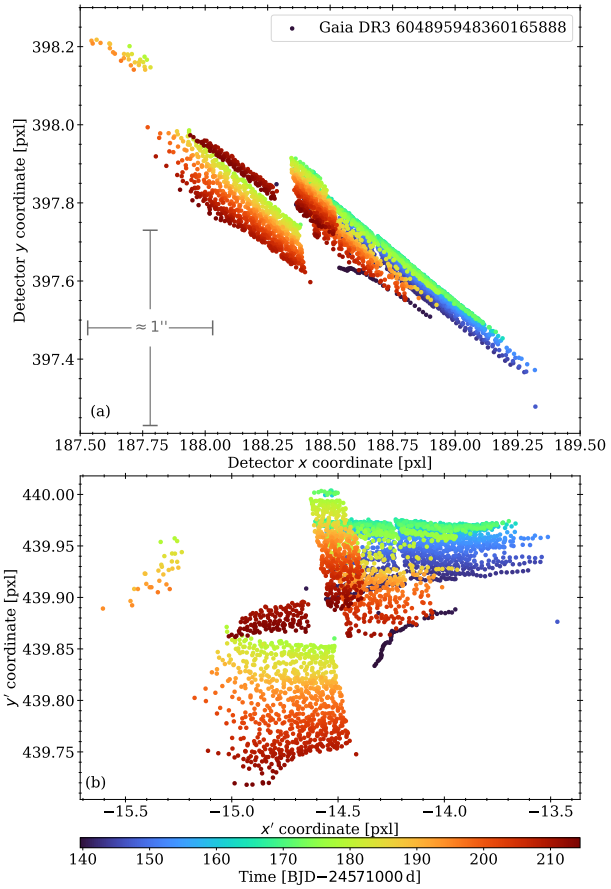

Figure 7.9: *Motion of the sample star* Gaia DR3 604895948360165888 *across the detector during C05. Each point represents the central position in one image color coded with the time of observation. Panel (a) gives the original detector coordinates and panel (b) those after the rotation applied. The extent of 1″ on-sky is indicated. We note the difference in scaling between the x and y coordinate axes, and the change from (a) to (b).*

$$m_i = \frac{y(t_i) - y(t_{i-1})}{x(t_i) - x(t_{i-1})} \qquad \text{with } i \in \{1, \ldots, 3620\}$$

and take the respective median $\bar{m}$. We note that we purposefully do not take the mean value or use a linear fit to the data. Both of those approaches fail to provide good approximations of the motion due to the frequent jumps in the data. We then rotate the coordinate system around the angle $\theta = \arctan \bar{m}$ such that

$$\begin{pmatrix} x'(t) \\ y'(t) \end{pmatrix} = \Psi \begin{pmatrix} x_0(t) \\ y_0(t) \end{pmatrix} \text{ with } \Psi = \begin{pmatrix} \cos\theta & \sin\theta \\ -\sin\theta & \cos\theta \end{pmatrix}$$

creates a new set of coordinates $p' = (x'(t), y'(t))$. Figure 7.9 shows the new coordinates for same target. Note the differing scaling for y' and x' in the plot. The motions clearly follow patterns within certain segments of the data in both coordinates. This becomes even more obvious when we plot x' and y' over time as shown in Fig. 7.10. It turns out that these individual segments of similar behavior are impossible to process together because their individual motion patterns are still too distinctive. Following this, we mask the segments and identify regions of

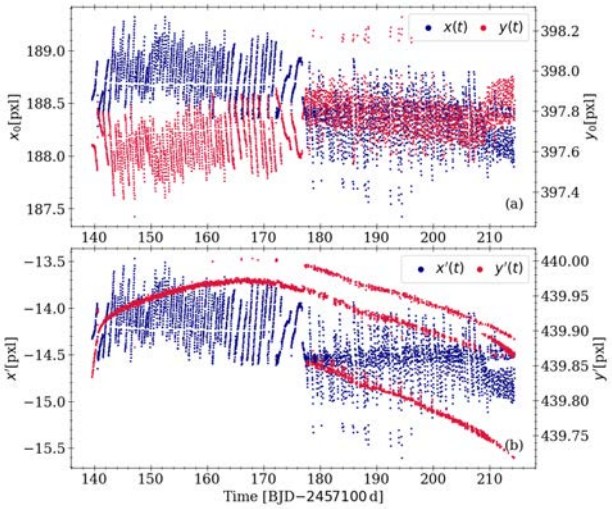

Figure 7.10: *Detector coordinates of the sample star* Gaia DR3 604895948360165888 *over the course of C05. Panel (a) shows the x and y coordinates while panel (b) shows x' and y' after the rotation. Note that significantly smaller scale for y' compared with x'.*

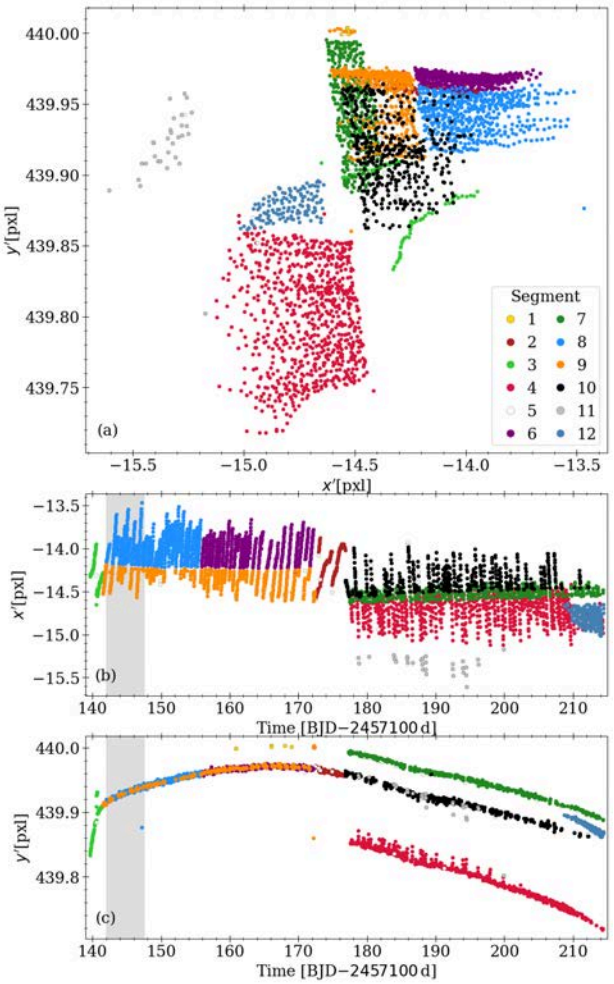

Figure 7.11: *Motion of the sample star* Gaia DR3 604895948360165888 *across the detector during C05. The correspondence of each point with the segments is color coded. The gray shaded area is inspected more closely in Fig 7.14 below.*

similar behavior for collective processing. Based on the patterns, we mark 12 different groups of pixel behavior which we will henceforth refer to as *segments*. As can be seen in Fig. 7.11, the individual segments are neither identical in size nor are they distinct in time. The latter fact will be advantageous for us below.

This pattern of behavior is indeed real and traceable in the image and not, for example, an artifact of the creation of the WCS. One can easily show this by combining the superstamp images into a movie, with the position of a star according to the WCS indicated and then observe the changes in the observable PSF of the star. These match one another, indicating that the WCS solution is an accurate representation of the positions (and therefore of the motion) of the stars.

There is one potential assumption we have not talked about yet which, if valid, would allow for an additional simplification or validation of our results. It is reasonable to assume that when a star falls two times on a very similar position, the detector response should be identical. With that, all observed flux variations between those two individual cadences should be free of the instrumental systematics, that means only composed of trending and the intrinsic signal. A closer inspection of Fig. 7.11 shows that the distribution of positions of a star would allow this for at least some cadences (upper right region of the figure). However, upon further investigation, we notice that this assumption is not valid in most cases. This can be shown by selecting a star where the photometric noise is negligible and that exhibits a clear signal of variation (e.g., a M67 giant branch star). When we now compare the fluxes of two similar locations and compare those to the overall behavior of the raw light curve, we find that they do not match. We can identify the reason for that. Figure 7.11 shows that most the of cadence pairs that we can use for this are made of cadences from different segments. If we limit ourselves to cadence pairs that are only from one segment, the assumption does indeed hold. However, there are too few of those available to be a significant help in the reduction process. At this point we have to look back at the origin of the detector coordinates. They come from the superstamp, which was created from the individual TPFs. Thus they are not necessarily connected to the actual physical pixel coordinates of the detector and may be shifted (by integer multiples of pixels). Judging from what we see, it is reasonable to assume that the distinction into the segments we see finds its origin in a jump in actual pixel coordinates and is not reflected in the superstamp coordinates. It may be possible to verify this assumption from the telescope telemetry itself or the individual TPFs. However, this verification (or rebuttal thereof) does not provide any additional value given that the segments are obvious in the data and therefore, we do not pursue this line of inquiry any further.

Table 7.5 shows the extent of the individual segments. Within those segments, we can now express the flux f as a function of the coordinate x' short of one more technical detail we will address below. However, we first need to describe the flux extraction from the superstamp images,

because it also needs to be performed segment-wise.

Table 7.5: *The different masks used on the lightcurves.* Segments *refers to identification used in the text.* Cadences *and* Slices *list the number of each included in each segment. The* comment *denotes whether a segment is adopted for the final light curve.*

Segment	Cadences	Block	Slices	Comment
1	6	E	3	cut
2	211	A	8	take
3	92	E	4	cut
4	796	C	110	take
5	98	E	19	cut
6	505	B	29	take
7	390	A	103	take
8	519	B	32	take
9	414	A	49	take
10	432	A	68	take
11	30	D	13	cut
12	127	C	19	take

F.3 Flux extraction from the full frame images

The FFI underwent background subtraction in the *K2* pipeline. We see no reason to revisit this, and accept it as is. However, we will introduce an additional background subtraction to reduce the impact of the light from bright stars surrounding a particular target (as detailed below).

As described in Sect. 3.3, we use aperture photometry with an individually defined pixelmask rather than a fixed aperture or PSF photometry. A fixed circular or elliptical aperture differs too much from the very non-gaussian PSF present in the FFI. Furthermore, taking only fractions of the flux stored in a given pixel based on the degree of aperture coverage introduces additional artefacts in the recorded flux.

As described in Sect. 3.3, we use aperture photometry with an individually defined pixelmask rather than a fixed aperture or PSF photometry. A fixed circular or elliptical aperture differs too much from the very non-Gaussian PSF present in the FFI. Furthermore, taking only fractions of the flux stored in a given pixel based on the degree of aperture coverage introduces additional artifacts in the recorded flux.

To include all the relevant flux of the star, we need to account for the motion of the star as well. The peak to peak motion covers more than two pixels. In a situation where the PSF of a star of intermediate brightness roughly covers a cluster of 5×5 pixel, this is a significant effect and cannot be neglected. The brightest stars have PSFs about three times this size, whereas the faintest stars can be adequately covered by 2×2 pixel. Thus we need to account for the motion in the design of the aperture mask. For stars that are isolated, this does not present a problem as the aperture can just be designed large enough to cover all eventualities, though that would accumulate unnecessary noise. For stars in crowded regions, this is not a valid approach since the apertures begin to overlap and flux from neighboring stars is recorded.

Thus, we need an aperture that moves with the star. As already stated above, taking only fractions of the flux from a pixel introduces additional unwanted effects. Thus, we cannot have the pixelmask gradually moving with the star. Another approach that adds and removes entire pixel to and from the mask based on the current position of the star fails due to similar problems. Given the originally diagonal motion of the star and the fact that our determined segments separate mostly perpendicular to this motion, we use the following approach: we design different pixelmasks for different segments. It is, however, not necessary to design different pixelmasks for every segment. The coordinates allow different segments to share the same pixelmask. We refer to this grouping as a *block*, denoted with the letters A to E, for the five groups we found. Table 7.5 includes the block designation in the column of the same name. We note that the blocks D and E only contain regions that will be cut due to the peculiar motion during the involved segments. Therefore, we focus on the blocks A – C from here on. The raw flux is extracted in D and E with a copy of the pixelmask for A.

We go on to design a pixelmask for each star, based on its visible shape in an image that averages all superstamp FFIs belonging to a certain *block*. This design is performed manually and iteratively. We endeavor to create a pixelmask for each star in each block that includes most of the flux of a star while simultaneously excluding flux from surrounding stars. This is, however, not always possible and so there are stars for which it is impossible to define a pixelmask that allows good extraction of the flux. We discard those from the sample. The design is iterative because the work showed that an incomplete pixelmask *may* leave strong imprints on the extracted flux that cannot be corrected. Thus, we iterate between pixelmask design and flux correction until we achieve light curves for the individual stars that are appropriate for our science case. In Figure 7.12, we show the pixelmask for the example star in block A together with a comparison to a high resolution image from the *Digitized Sky Survey 2* (DSS2[6]).

Given the extent of manual work on each target in the FOV, we limit ourselves to targets of interest and a certain number of additional stars to verify the method. At this point we also discard all stars which cannot be separated well-enough from neighboring stars.

F.4 Extraction of the lightcurve and background subtraction

We can now extract the raw flux $f_{\mathrm{raw}}(t)$ based on the pixelmasks found by simply adding the flux from all included pixels for each cadence. Before doing so, we create a mean image for each block and determine all pixels fainter than the median in each. We assume that those pixels constitute the background. However, we do not use all those pixels for each star. From this selection, we use the ones closest to the extracted star. Here we sort the pixels by their distances to the mean position of the star in the block, exclude a potential overlap with the pixelmask itself, and

[6] `archive.eso.org/dss/dss`

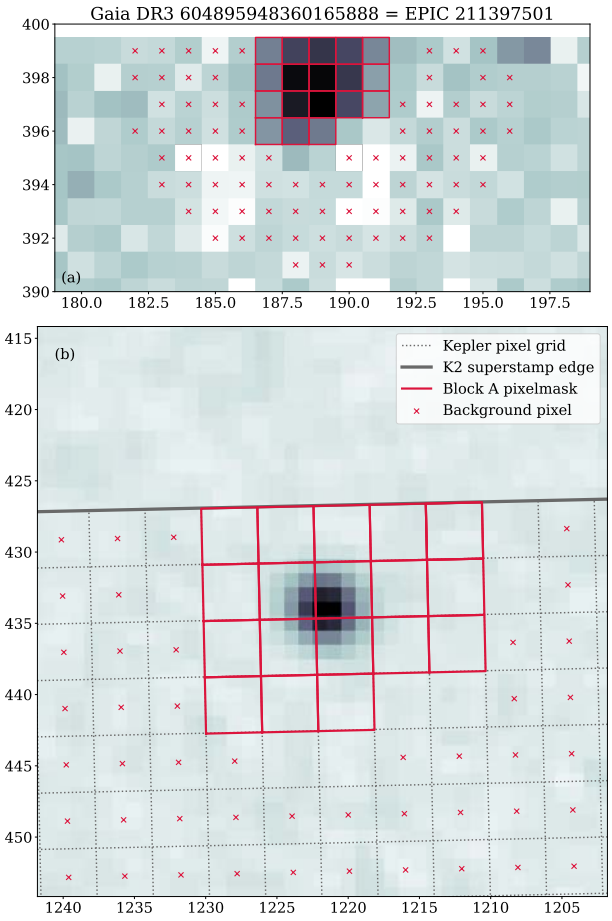

Figure 7.12: *Pixelmask and background selection for* Gaia DR3 604895948360165888 *in block A. Panel (a) shows an averaged* K2 *superstamp image around the target. Panel (b) shows a comparison with a DSS2 (red channel) image of the same region.* K2 *pixels outlined in red mark the chosen pixelmasks pixels selected for the background estimate are marked with an X. The DSS2 mage has the* K2 *pixelgrid indicated by the dotted lines and the solid line marks the edge of the superstamp.*

include all pixels until we have at least three times as many background pixels as we have in the pixelmask. We then use the median of those pixels as the background and subtract it, weighted by the number of pixels included. This procedure allows the removal of stray light from stars in the vicinity. The number of pixels included and the use of the median are based on extensive testing of different variations and the final procedure presented appears to provide the best result overall. This provides us with the raw light curve $f_{\rm raw}(t)$ which is shown in Fig. 7.13 for our example star. The typical systematic patterns due to the telescope motion are obvious. We note that due to differently shaped pixelmasks, the individual segments are generally not as well aligned as seen in Fig. 7.13 but show offsets (cf. Fig. 7.22). Those are eliminated when the light curves are realigned (see below).

F.5 Correction of instrumental systematics

With the raw, but background subtracted light curves $f_{\rm raw}(t)$ at hand, we can now proceed to correct the instrumental systematics. This process continues to be on a star-by-star basis and is also carried out segment-by-segment. When we investigate the position dependency of the flux $f_{\rm raw}(x')$ (see Fig. 7.15) we see that the correlations are well-behaved enough to be modeled with a low order polynomial. To a large degree, the trends are almost linear but even a slight curvature can have a significant impact. We find that a 5th-order polynomial s the best compromise for the fit and use it to reproduce $f_{\rm raw}(x')$ for each segment. However, one more difficulty has to be accounted for before doing so. When we directly fit a polynomial to $f_{\rm raw}(x')$, it is very dependent on the range covered in x' and the number of points responsible for said coverage.

At this point we introduce the a third (and last) masking variable which we will refer to as a *slice*. A slice is a short section of the light curve which covers one continuous episode of motion between two jumps. In Figure 7.10, each apparent upward (or downward) stripe for x' is distinguished as a slice. (There are jumps and gaps that are not apparent in the plot, causing the number of slices to be higher than obvious.) By virtue of the design of the process, each slice in its entirety is part of only one segment. Figure 7.14 provides a zoomed-in view of the light curve in Fig. 7.11, with the slices distinguished by the color coding. Slices vary strongly in their extent for all involved parameters (x', t, number of cadences). They typically cover 5 to 15 cadences, with the smallest containing only one individual cadence. Table 7.5 includes a column that lists the number of slices in each segment.

We now utilize the slices that were introduced above. All slices of one segment exhibit the same systematic behavior (cf. Fig. 7.15). However, given the fact that they are spread over several days (the segments cover typically about half the baseline of the light curve), even slow variations in the light curve leave their imprints in the mean flux of a slice. Furthermore, the individual *slices* have a different degree of coverage in x'. This complicates a polynomial fit to the data. We need an additional technical step to proceed.

We designate the one *slice* which has the most extensive coverage in x' in each segment as the *prime slice*. Each *slice* is then rescaled to this prime slice. We proceed to fit a 5th-order polynomial $p_5(x')$ to the resulting distribution of fluxes, and apply it as a correction to the individual *slice* (their unscaled fluxes!) as

$$f_{\rm cor1,slice}(x') = f_{\rm raw,slice}(x')/p_5(x') \cdot \overline{f_{\rm raw,seg}(x')}$$

to create the first step in the correction process $f_{\rm cor1}$. We multiply with the average flux of segment $\overline{f_{\rm raw,seg}(x')}$ because the polynomial normalizes the fluxes to the *segment* mean. The result can be seen for a few selected slices in Fig. 7.15. This processes is carried out for all *slices* in a *segment* and for all *segments*. We note that this process conserves long term flux changes and differences between individual *slices*. The resulting light curve for our example star *Gaia DR3 604895948360165888* is shown in Fig. 7.16.

This process reveals that two regions of the light curve cannot be processed in this way. The first $\approx$ 3 d and a central part ($t \approx 172-177$ d) correspond to exceedingly

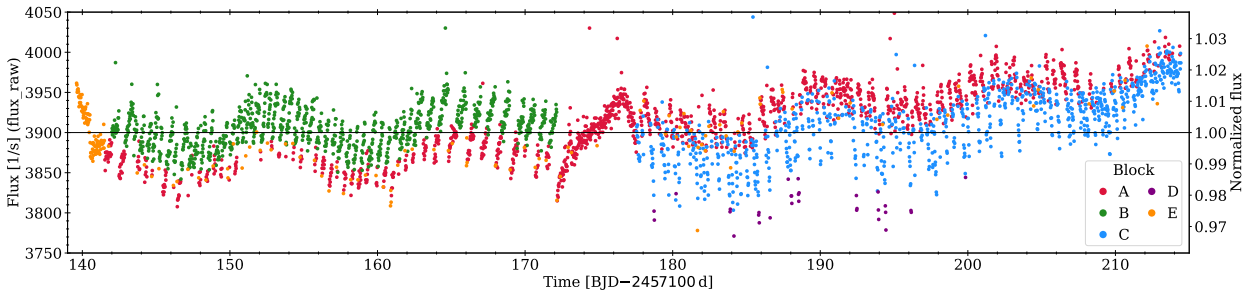

Figure 7.13: *Raw lightcurve $f_{raw}(t)$ of* Gaia DR3 604895948360165888.

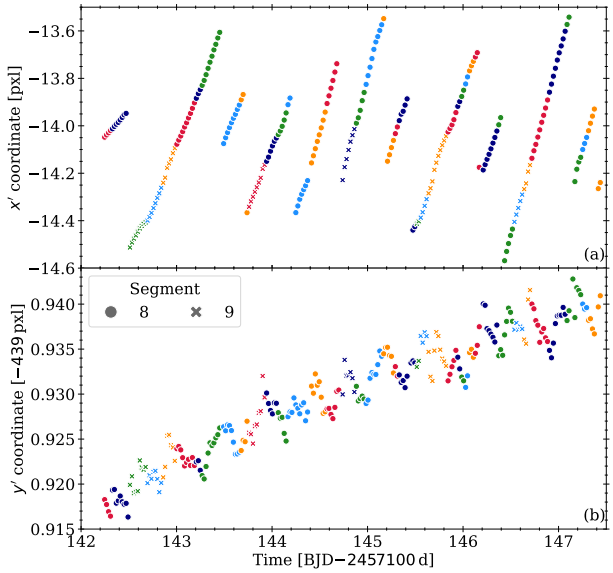

Figure 7.14: *Designation of the slices in a short light curve segment. Panels (a) and (b) show the time dependency of $x'(t)$ and $y'(t)$, respectively. The alternating color coding distinguishes individual slices and different symbols refer to different segments as indicated in panel (b). Only a small cutout from the full light curve is shown, corresponding to the shaded area in Fig. 7.11. It contains 40* slices *for the sample star* Gaia DR3 604895948360165888.

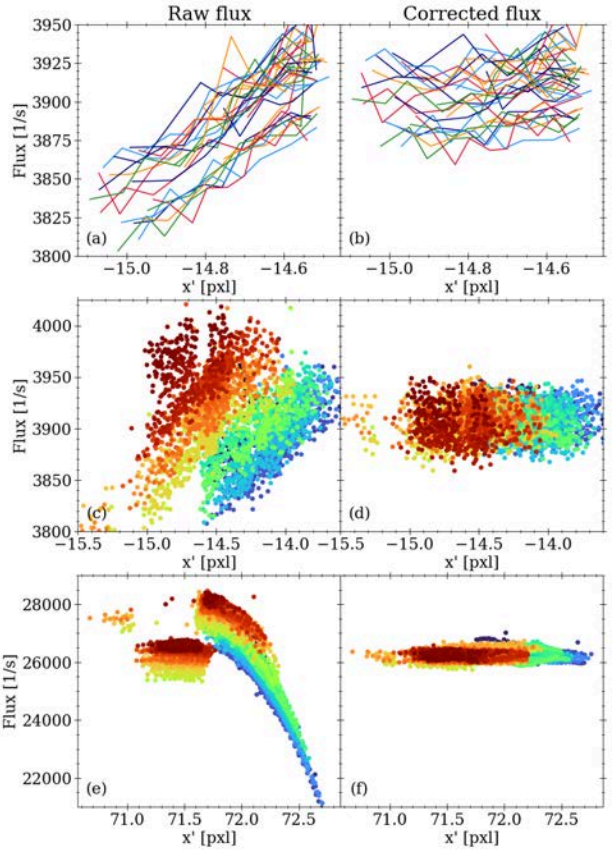

Figure 7.15: *Position dependence of the recorded raw flux $f_{raw}(x')$ and the correction thereof. Panel (a) shows the raw flux from* Gaia DR3 604895948360165888 *as a function of the detector coordinate and clearly shows the linear dependence. Flux values are plotted for the same* slices *as in Fig. 7.14. Each line represents one* slice. *Panel (b) shows the same* slices *but with the flux after the correction is applied. Panels (c) + (d) are similar to (a) + (b), only for the full light curve of* Gaia DR3 604895948360165888 *and the color coding representing the time as in Fig. 7.9. Panels (e) + (f) are the same as (c) + (d) but for* Gaia DR3 604917629355039360 *for which the position dependency becomes nonlinear.*

long *slices* that exhibit behaviors that cannot be found anywhere else and therefore those regions cannot be corrected this way (cf. the same regions in Fig. 7.11). We mask those regions and cut them from the final light curves. Furthermore, there are individual cadences in the light curve from times of fast telescope motion (thruster firing). Those cannot be processed as well. We mask them in the correction step and later, when all other *segments* are processed, recreate those points from a linear interpolation in the corrected light curve. Those regions are entirely part of the *blocks* D and E (cf. the comment column Tab. 7.5).

Thanks to the processing described above, the relative fluxes between the individual slices is conserved and the (fragmented) light curve of a *segment* may act as a valid light curve all by itself. However, this is not true when we compare the fluxes of the individual segments. They are not aligned. This is, however, not a result of our processing but a consequence of the instrumental systematics and different pixel masks that gives each segment a slightly different recorded average flux (cf. Fig. 7.13). To align those fluxes, we merge the segments successively with a scaling to the chronologically first sector. The scaling factor is determined by minimizing the average standard deviation in the merged light curve for a series of windows 15 cadences wide along the light curve. This rescaling provides us with the next level of correction f_{cor2} which is shown for example star in Fig. 7.17. For the chronologically first segment we set $f_{\mathrm{cor2}} = f_{\mathrm{cor1}}$.

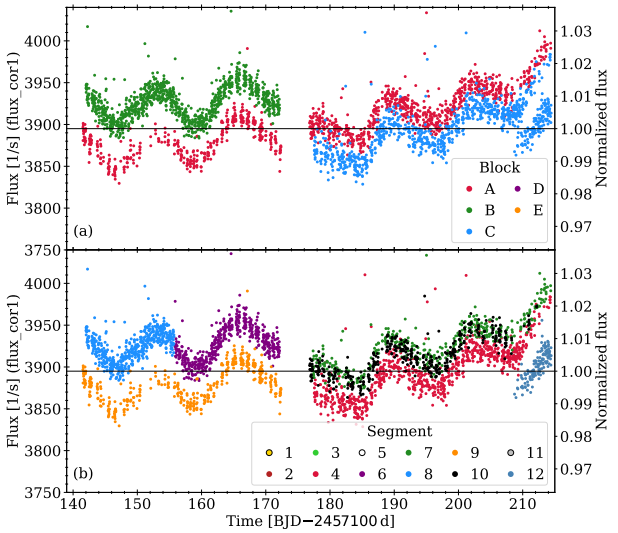

Figure 7.16: *Lightcurve of* Gaia DR3 604895948360165888 *after the application of the first correction for the instrumental systematics. Both panels show the same lightcurve. The color coding in the upper panel indicates the block as in Fig. 7.12. In the lower panel, the colors indicate the segments as in Fig 7.11.*

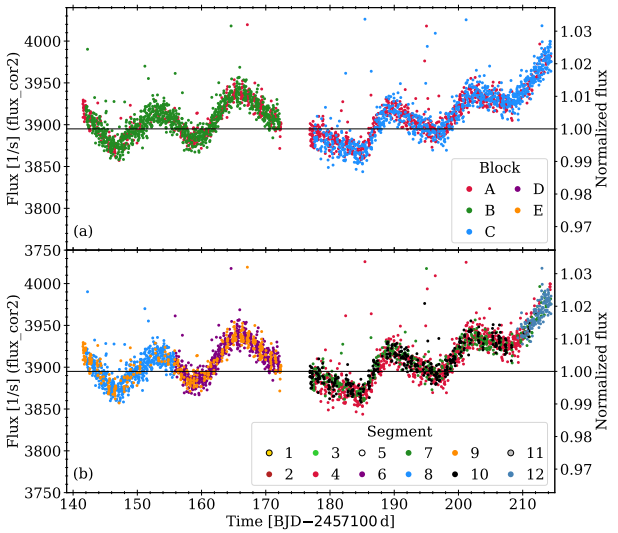

Figure 7.17: *Light curve of* Gaia DR3 604895948360165888 *after the application of the second correction, the realignment of the segments. Both panels show the same light curve. The color coding in the upper panel indicates the* block. *In the lower panel, the colors indicate the segments as in Fig 7.11. We emphasize that the flux axis is identical between the Figs. 7.13, 7.16, and this one.*

The corrected and realigned flux f_{cor2} now represents the light curve in which we have removed all instrumental systematics. However, this is not fully true for all light curves. A polynomial fit can only do so much and an insufficient pixelmask may introduce effects that cannot be corrected. As such, the process fails for stars in very crowded regions and on the edges of the superstamp. The slices generally cover a few hours. Intrinsic variations that occur on the same timescale may be misidentified by the polynomial. However, such rapidly varying targets are not of interest to us here, allowing us to ignore this problem. Despite this, we note that rapid signals are generally still visible reasonably well in the final light curves, thanks to their large amplitudes.

F.6 Cleaning the data

From this point onward, there is no further separation into blocks, segments, or slices, and the light curves are always treated as a whole. In the next step we apply σ-clipping to the data to clean it of outliers. This is done only at this stage, because the instrumental systematics may create or hide actual flux outliers and a σ estimate is dominated by it. For each point along the light curve we calculate the mean and standard deviation in a 1 d window around the point and replace it with a linear interpolation between its neighbors if it exceeds a 3σ deviation from the mean. We note that this may create artifacts for fast transients like transits or flares. However, since we are not interested in such phenomena, we elect to ignore those issues.

At this point we have constructed light curves for target stars that are corrected for instrumental systematics and cleaned of outliers. The light curves exhibit a gap of a few days around the middle and still include long term trending effects. The removal of the latter will be performed using Principal Component Analysis (PCA).

F.7 Principal Component Analysis

PCA is performed in a very similar manner to the light curve processing for Ruprecht 147 (from *K2* C07, see Gruner & Barnes 2020, Appendix B). However, we modify the process slightly and describe the deviations below.

Because we do not have a large number of ($\sim$ 10k) light curves from the entire campaign for this dataset, we select stars for the PCA basis from our processed sample. We identify 769 stars for the said basis, covering a large range of brightnesses, colors, and locations on the detector (cf. Fig. 7.18). From this basis, it becomes obvious that the trending signal is not universal for all stars. It shows a strong brightness dependence and a weak location dependence. We therefore limit the PCA basis applied for each target to stars of similar brightness and location. This means we take only the 125 nearest stars on the FFI within $\Delta G \pm 1$ mag. Both of these choices are the result of testing different parameter combinations; these particular ones provided the best results throughout the sample. We note that, depending on the brightness, there could be fewer than 125 stars overall in the brightness range and the PCA basis for such stars is correspondingly smaller.

We smooth the light curves before entering them into the PCA to remove the impact of the noise from the analysis. This smoothing is done by replacing each flux value by the mean of a 1 d wide window around this point. We note that this smoothing is only in place to create the PCA correction and is not used beyond that. Furthermore, we normalize all light curves to their respective means before entering them into the PCA. This smoothing removes rapid-trending signals from the PCA input. This means that such signals are not accounted for in the PCA correction and thus remain in the final light curve. However, their impact is small with respect to our purposes and as

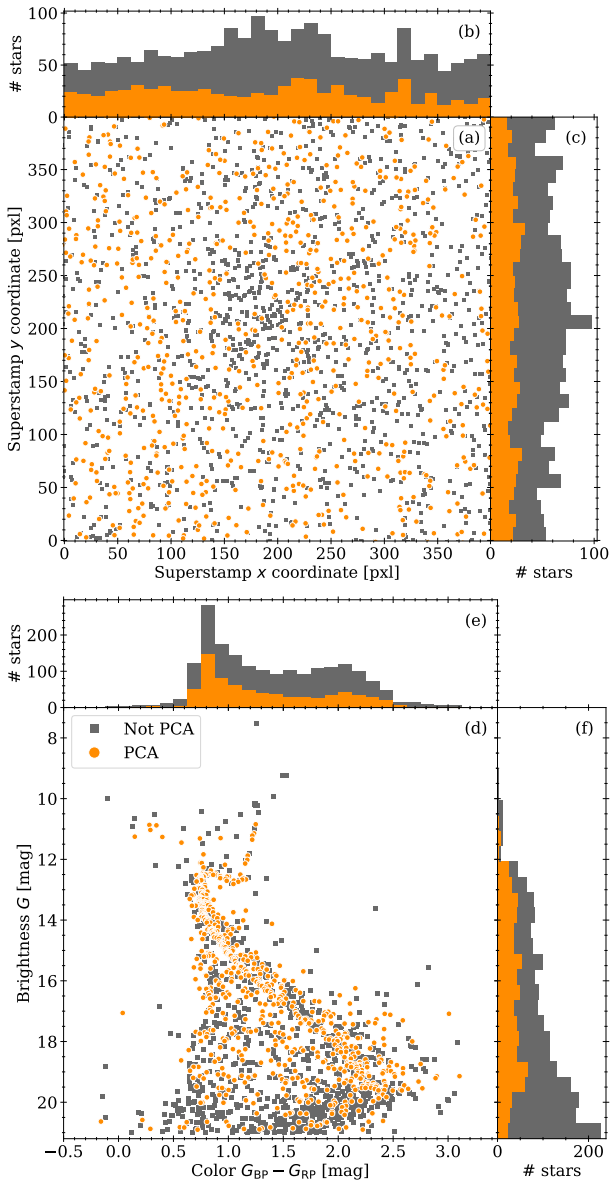

Figure 7.18: *Star selection for the Principal Component Analysis, indicating those used and those not used.*

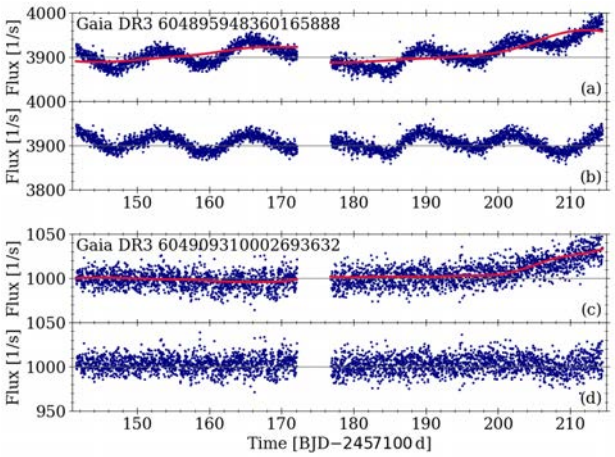

Figure 7.19: *Application of the PCA correction to the example star* Gaia DR3 604895948360165888 *(panels a and b), and the fainter and essentially constant star* Gaia DR3 604909310002693632 *(panels c and d). Panels (a) and (c) each show the result of the instrumental systematics correction (blue) and the PCA correction (red) whereas panels (b) and (d) show the final light curve after the PCA correction was applied.*

such we do not address them any further. Traces of this can be seen in the light curve plots in Fig. 7.28 and are generally of two different types:

1. A very rapid fluctuation, as seen for instance, between $t = 150\,\mathrm{d}$ and $t = 160\,\mathrm{d}$ for *Gaia DR3 604914880575997056* and
2. A distinct short term signal, as seen for instance, between $t = 150\,\mathrm{d}$ and $t = 170\,\mathrm{d}$ for *Gaia DR3 604915773929008384*.

The (long-term) trending signals are dominant and the PCA can identify their different shapes relatively easily. We use only two components for the reconstruction; this is enough to remove the trending signals adequately. This is a consequence of the limited PCA basis (brightness and position), which preremoves very different trending signals from the basis. Figure 7.19 shows the application of the PCA correction on the example star and on an essentially constant star.

At this point we are in possession of the final light curves f_{fin} which are corrected for instrumental systematics, cleaned for outliers, and are free of trending. Figure 3.4 summarizes the individual steps for the example star. This process is by no means perfect, and does not work for all targets. We only use a carefully selected subsample of all potential targets, and remove all light curves where residuals of the systematics or trending cause uncertainties. Most removed light curves suffer from an insufficient pixelmasking (mostly due to being in a crowded area in the superstamp FFI) or because the corresponding star coincides with a region of bad pixels. Both problems make corrections nearly impossible. Only for a few stars does the correction itself directly fail. For those, the flux does not behave well enough to be adequately modeled with a polynomial. However, their numbers are small enough not to merit the effort required for an adjusted correction procedure.

The above-described process is specifically designed for the *K2* C05 superstamp around M67. However, it should be possible to adapt it for other parts of the *K2* survey as well. The principal idea should hold and, assuming that the detector variability stays similar in its magnitude, provide good results without modifying the core components. The parts that would need to be modified are those that are fine-tuned to the superstamp. The pixelmasks for the individual targets are the first among these. Secondly, the masking (block, segment, slice) would also need to be adjusted to a different campaign. However, we can reasonably assume that our masks work for other regions of C05 without modification. Caveats such as the difficulties with rapidly varying stars and crowded regions do, of course, remain. A precondition for such work is the existence of a reference for the telescope motion, and with that of motion of the stars on the detector. The *K2* TPFs do not provide this, but some of the other superstamps created by Cody et al. (2018) do. We note that the SPICE kernels for

the *K2* mission only include position and velocity of the telescope but not its orientation, a necessity to be able to leverage those products.

F.8 Performance of the reduction

The correction process described above works well for stars that are isolated and whose PSF does not exceed the FFI range, that is, stars for which we can define a pixel-mask that includes all of the stellar flux and none from surrounding sources. This condition is not fulfilled on the edges of the superstamp, and especially in the central region of the cluster. Figure 7.20 highlights some details that show the performance and limitations of our corrections.

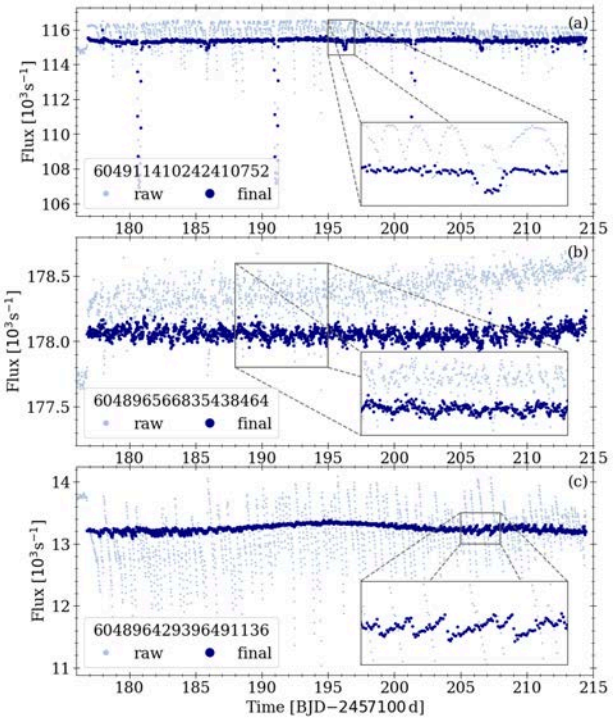

Figure 7.20: *Example light curves illustrating the capabilities and limitations of our correction process. Panel (a) shows the light curve of an eclipsing binary with a significant primary eclipse and a secondary eclipse that only becomes really apparent after the correction was carried out. Panel (b) shows a star where the instrumental systematics completely obscure the intrinsic signal despite their being of comparable amplitude. Panel (c) shows the light curve of a star located at the edge of the superstamp and which suffers from artifacts created by the correction process as a consequence. Each panel includes highlighted regions to show the details of the relevant effects.*

Whenever the pixelmask cannot, for whatever reason, be created in a way that includes all the stellar flux the recorded raw flux f_{raw} includes a second systematic effect. This effect invalidates the original assumption we had to make, that the raw flux only changes because of variations in detector sensitivity, and is otherwise somewhat constant on short time scales. With that, it very much depends on the individual star's location on the detector whether our correction still works or whether we under- or over-correct the apparent systematics. The star we used as an example for the correction process is located on the edge of the superstamp (c.f. Fig. 7.12) but is well-behaved enough to allow a good correction process. Meanwhile, *Gaia DR3 6048964293964911136*, whose light curve is depicted in panel (c) of Fig. 7.20, shows remnants of an over-correction in the highlighted area due to proximity to the superstamp edges and subsequent loss of flux.

F.9 Comparing our results with K2SC, SAP, EVEREST

We validate our light curves by comparing them with those produced as part of the original survey and from two commonly used works that implemented a systemtatics correction, K2SC, and EVEREST. This comparison again highlights one important fact that supports our approach with creating our own light curves – not many light curves are available for targets within the superstamp. Figure 7.21 shows the distribution of stars with available light curves. Only 96 are within the field of view of the superstamp, as compared with GDR3 listing ∼2000 sources. This most likely originates from the differing nature of the superstamp as compared with the normal TPFs. The latter are typically associated with a proposed star and therefore are automatically processed. This is not true for the superstamp. As far as we are aware, all other projects that dealt with the *K2* systematics only operate on the same sample. Therefore, other extant work does not venture outside this 96-star sample.

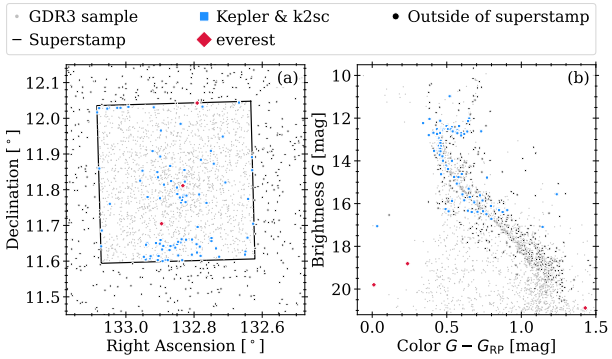

Figure 7.21: *Spatial distribution of stars with available light curves in the archives for different data products. Panel (a) shows a map centered on M67 with the extent of the superstamp indicated (black box). Targets with archived light curves within (red and blue) and outside (black) of superstamp are overplotted. Panel (b) shows the same stars in a CMD.*

We extracted the 96 light curves in the FOV of the superstamp from the *Kepler* archive[7]. These include the light curves based on simple aperture photometry (SAP, f_{SAP}) on the TPFs and corrected light curves that resulted from the Presearch Data Conditioning (PDC, f_{PDCSAP}) module of the *Kepler* pipeline (Smith et al. 2020). The PDC is employed to remove data systematics and trending while retaining astrophysical signals. This generally works reasonably well but leaves traces of both artifacts. In some cases the trend correction removes astrophysical signal. For our comparison we employ the SAP flux as well as

[7] archive.stsci.edu/k2/data_products.html

the PDCSAP with the aim of comparing the most similar products from each. For the former we compare with our raw extracted flux. However, we generally do not expect a large agreement in the shape of the raw light curves on short term scales due to the differently shaped aperture mask used. Long term effects are expected to be the same. The PDCSAP flux f_{PDCSAP} is compared with our final light curve f_{fin} (lower panel of Fig. 7.22) as both have the same level of processing (systematics and trend removal), whereas the SAP flux f_{SAP} is equivalent to our raw flux f_{raw} (upper panel of Fig. 7.22).

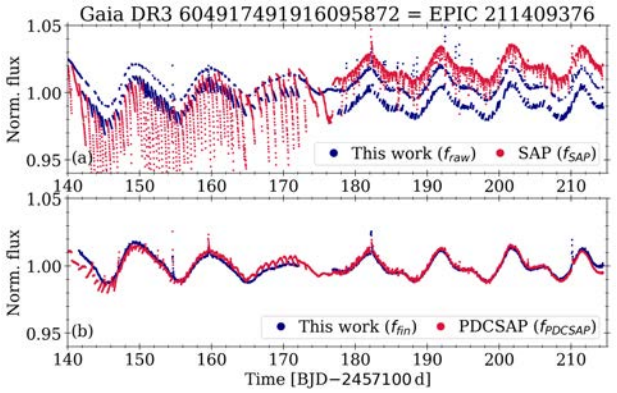

Figure 7.22: *Comparison between the* Kepler *PDCSAP light curves and the ones created by us. In both panels, our light curves are shown in blue and the archival light curves are shown in red. Panel (a) shows the uncorrected aperture photometry fluxes (*`flux_raw` *from ours and* `SAP_FLUX` *for theirs). Panel (b) shows the final light curve product –* `flux_fin` *from ours and* `PDCSAP_FLUX` *for theirs.*

We can see that, as expected, the raw light curves generally do not agree with respect to the short-term systematics while having the same long-term behavior. However, after the correction is applied, we find very good agreement between the *Kepler* and our pipeline results. Despite our relatively simple approach for an empirical correction, we not only do match the quality of the official product but partially exceed it. Generally, our approach is slightly better in the removal of the *instrumental systematics*.

The *K2 Systematics Correction* (K2SC) pipeline implements Gaussian processes to correct for the telescope jitter (Aigrain et al. 2015, 2016). It is geared toward exoplanet detection; as such the pipeline is set up in a way that also removes the astrophysical signal from the final product f_{k2sc}. However, they provide the removed systematics as part of their data product, differentiated in a position-dependent f_{posi} and a time-dependent part f_{time}. Long term variability is retained in the time-dependent part, together with trending. Recombining their final light curve with both those parts yields back the PDCSAP light curve ($f_{\mathrm{PDCSAP}} = f_{\mathrm{k2sc}} \cdot f_{\mathrm{time}} \cdot f_{\mathrm{posi}}$) which was the starting point for the K2SC pipeline. Thus, the K2SC light curves benefit from the long-term trend correction in the *Kepler* PDC pipeline. Technically, with their procedure they also implement a correction for instrumental systematics twice. To obtain a light curve that is corrected to a similar degree as our final product, we recombine the final flux and the time-dependent trending part. Figure 7.23 shows the comparison. The additional systematics removal pays off, as the light curves are improved as compared with PDCSAP, and reach a fidelity similar to, or perhaps are even superior to ours. All 96 PDCSAP light curves are processed with K2SC. The final K2SC light curve (f_{k2sc}) is not comparable to any other, as it blatantly removes any long term signal, including physical ones (cf. upper panel of Fig. 7.23). A comparison makes sense between our light curves before the PCA (f_{cor2}) and the K2SC one with the time-dependent signal included ($f_{\mathrm{k2sc}} \cdot f_{\mathrm{time}}$, cf. lower panel of Fig. 7.23).

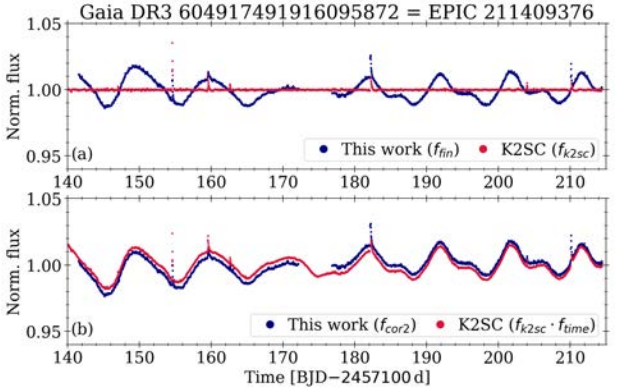

Figure 7.23: *Same as Fig. 7.22 but for the comparison between the* K2SC *light curve of* Gaia DR3 6049174919160958 72 *and the ones created by us.*

The *EPIC Variability Extraction and Removal for Exoplanet Science Targets* (EVEREST) light curves (Luger et al. 2016, 2018) use a pixel-level decorrelation (PLD) method that operates on pixel level light curves and, since its update to v2.0, includes the telescope motion for the correction. They are, as far as we know, the best available light curves based on *K2* data and the study of variability longer than a few days. Only long-term trending is a remaining issue; such trends are generally more pronounced than in other light curves. However, with those retained, there is also no problem with accidentally removed astrophysical signal. We have worked successfully with them in the past (Gruner & Barnes 2020). However, they are even more limited in their availability regarding the superstamp region. Only three stars in the FOV of the superstamp have an EVEREST light curve. And all three of those stars are very faint. Two are white dwarfs, while the third is a very faint red dwarf at the brightness limit of *Gaia* (cf. panel (d) of Fig. 7.21). All three stars are nearly constant in their light curves, and dominated by noise and some weak long-term trending. We use the red dwarf for the comparison in Fig. 7.24. The extent to which we can correct for instrumental systematics is similar in both products, however, EVEREST reaches a slightly higher photometric precision. PDCSAP and K2SC fail to fully remove either trends or systematics, and their photometric precision is lower compared with ours or EVEREST for the faint stars.

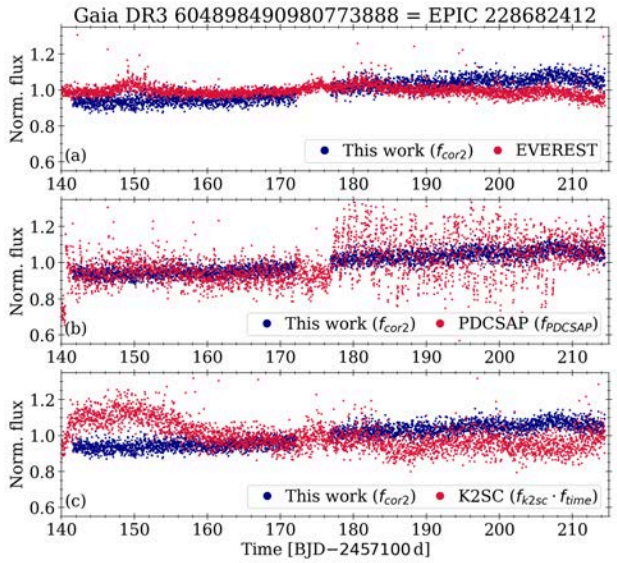

Figure 7.24: *Same as Fig. 7.22 but for the comparison between the* EVEREST, *PDCSAP, and* K2SC *light curves of* Gaia DR3 604898490980773888 *(panels a, b, and c, respectively) and the ones created by us.*

G Supplements

G.1 Supplementary tables

Table 7.6: *Datapoints for the empirical cluster sequences. The manually drawn sequences used in the CPDs throughout this work are plotted from cubic interpolation between the listed colors and periods. The subscript to the period label indicates the corresponding age in Gyr.*

$G-G_{\rm RP}$ [mag]	$G_{\rm BP}-G_{\rm RP}$ [mag]	$B-V$ [d]	$V-K$ [d]	P_1 [d]	$P_{2.5}$ [d]	P_4 [d]
0.32	0.50	0.38	0.99	1.5	nan	nan
0.38	0.61	0.46	1.20	2.0	5.0	nan
0.40	0.65	0.49	1.28	3.0	8.0	14.0
0.45	0.74	0.58	1.44	8.5	15.0	22.0
0.50	0.83	0.67	1.64	11.0	19.0	26.0
0.55	0.93	0.76	1.84	11.0	22.0	29.0
0.60	1.03	0.85	2.09	10.5	23.0	31.0
0.65	1.14	0.93	2.32	11.0	nan	31.0
0.70	1.25	1.02	2.57	12.0	23.0	nan
0.75	1.37	1.11	2.83	12.5	nan	29.5
0.80	1.48	1.19	3.08	13.0	20.2	26.0
0.85	1.61	1.27	3.32	13.8	nan	nan
0.90	1.74	1.33	3.55	14.3	18.0	25.5
0.95	1.87	1.37	3.79	15.0	nan	nan
1.00	2.02	1.39	4.03	nan	22.0	32.0
1.10	2.33	1.44	4.55	nan	30.0	41.0

Table 7.7: *Selected stars from the Gonzalez (2016b,a) sample. Only those stars from the Gonzalez (2016b,a) sample that have been classified by us as having reliable periods and subsequently adopted in this study.*

Gaia DR3	P [d]	$P_{\rm err}$ [d]	$(G-G_{\rm RP})_0$ [mag]	binary
604907454576711040	27.2	0.5	0.42	
598689411379091328	24.9	0.5	0.42	
605000024007420416	12.1	0.5	0.43	PB
598692675554477056	22.6	0.5	0.48	
604960235430488960	26.8	0.5	0.53	
598901788922041728	32.4	0.9	0.58	
604949961868553856	32.6	0.8	0.58	
598689926775182208	29.4	0.5	0.59	
604895325589137920	31.5	0.5	0.61	
598902716634970240	30.4	0.5	0.66	
604987139105593344	28.9	1.0	0.68	
604898731498904704	29.0	0.5	0.71	
604964010706281856	32.4	0.6	0.74	
604901239759778176	26.3	0.5	0.76	
604965178937376512	29.0	0.5	0.76	
604704633336193152	30.8	0.5	0.77	
598955729416267264	27.3	0.7	0.79	
604895948360165888	12.4	0.5	0.81	PB
604946693397490816	28.8	0.5	0.83	
598889213257785984	29.5	0.8	0.83	
604899448757770624	13.5	0.5	0.83	
604894535315152512	28.6	0.5	0.84	
605000058367154176	13.7	0.5	0.85	
604901686436367232	25.6	0.5	0.85	
604980713834545664	15.6	0.5	0.85	PB
598903128951834496	29.2	0.5	0.88	PB
604930509961364352	26.8	0.5	0.88	
604930445537379712	23.3	0.5	0.90	
598956485330513536	24.7	0.5	0.91	
604966518966784256	21.3	0.7	0.92	
604713669947377024	22.0	0.5	0.93	
598901995079871744	24.0	0.5	0.98	PB
604926043198690176	23.9	0.5	1.04	PB

Table 7.8: *Results of the period analysis. For convenience, we have limited the sample shown here to data used to create Fig. 3.9.* HPS *indicates whether are star is found on the half-period sequence. A star indicated as such is listed here with its period doubled, that being assumed to be the actual period. EPIC ids in italics denote stars for which a PDCSAP light curve is available.*

Gaia DR3	EPIC	P [d]	P_{err} [d]	G [mag]	$(G-G_{\mathrm{RP}})_0$ [mag]	$(G_{\mathrm{BP}}-G_{\mathrm{RP}})_0$ [mag]	$(B-V)_0$ [mag]	$(V-K)_0$ [mag]	HPS
598903678707639296	*211398541*	32.4	1.3	15.93	0.65	1.16	0.94	2.27	
604896498115959296		23.5	1.5	17.50	0.88	1.73	1.43	3.27	
604896635554924672	*211397512*	32.5	1.4	15.87	0.65	1.15	0.96	2.26	
604897558972113024	*211400106*	29.1	2.6	14.75	0.55	0.93	0.69	1.86	
604897833850019328	*211400500*	24.3	1.6	14.37	0.48	0.79	0.58	1.50	
604898490980772352		27.4	2.1	16.61	0.79	1.48	1.20	2.93	
604899831010539904		18.1	0.4	13.29	0.42	0.69	0.42	1.42	x
604900071528704128		34.7	2.5	16.18	0.73	1.30	1.04	2.61	
604900651348634240		23.1	2.1	17.60	0.88	1.73	1.38	3.56	
604903331408222208		29.5	1.6	18.46	1.02	2.12	1.50	3.84	
604903438783070208		37.0	3.0	18.64	1.02	2.19	1.61	4.17	
604906840397139584		29.1	1.1	17.76	0.95	1.92	1.47	3.80	x
604907046555568896		27.2	1.4	16.84	0.79	1.50	1.27	2.93	
604908004332577152	*211400002*	22.9	2.2	14.31	0.47	0.77	0.55	1.52	
604909206923484160		27.6	1.1	17.23	0.83	1.62	1.30	3.31	x
604909756679296640		30.2	2.2	15.65	0.61	1.06	0.90	2.17	
604911204083987584		7.37	0.14	15.08	0.55	0.92	0.78	1.89	
604913540546033024		31.1	1.5	16.31	0.70	1.30	1.05	2.45	
604913952863073920		26.5	2.2	16.82	0.80	1.52	1.24	3.05	
604914880575997056		29.1	1.8	16.37	0.72	1.32	1.08	2.60	
604915773929008384		29.0	0.5	15.16	0.55	0.94	0.77	1.84	
604916117526551680	211405832	23.4	1.5	14.42	0.48	0.79	0.55	1.62	
604917148318674816		30.8	2.7	15.49	0.60	1.04	0.95	1.98	
604919587860083328		29.5	2.6	17.42	0.88	1.74	1.39	3.34	
604920549932807296		24.6	1.4	17.33	0.87	1.70	nan	nan	
604920549932809344		26.1	1.6	15.16	0.56	0.95	0.81	1.83	
604922130480588544		27.2	2.0	16.73	0.77	1.44	1.21	2.89	
604922229264424448		9.72	0.25	17.07	0.84	1.61	1.27	3.19	
604922817675316096		27.6	3.2	14.97	0.54	0.91	0.77	1.71	
604923333071376512		32.1	2.5	15.66	0.62	1.09	0.94	2.22	
604923848467470976		26.2	2.3	17.37	0.87	1.69	1.40	3.44	
604930681760054656		27.6	2.3	17.73	0.92	1.85	nan	nan	
604943674036665472	211418998	26.8	2.6	14.60	0.51	0.85	0.49	1.82	
604944120713062784		31.7	2.7	15.47	0.60	1.04	0.83	2.15	
604963362166649856		22.8	1.4	16.78	0.80	1.52	1.14	3.07	
604969061592133376		1.84	0.01	19.57	1.11	2.52	nan	nan	
604969237681908480		26.3	2.0	16.78	0.78	1.46	1.13	2.96	
604969267746267520		26.5	1.2	17.24	0.85	1.65	1.22	3.34	
604969267746269696		30.7	2.2	15.56	0.61	1.07	0.89	2.13	
604969306401373824		30.2	1.1	15.87	0.65	1.15	0.96	2.33	
604969306401373952		24.6	1.7	16.93	0.81	1.54	1.26	3.08	
604969336465748352		24.9	1.7	17.28	0.87	1.69	1.43	3.36	
604970131035099008		24.1	2.3	16.98	0.81	1.57	1.18	3.12	
604971466769552128		27.9	2.0	16.51	0.75	1.40	1.06	2.94	
604972467498966400		32.3	1.5	15.53	0.60	1.04	0.97	1.92	
604973979325779328		28.7	1.1	14.88	0.53	0.90	0.71	1.76	x
604974151124482944		31.6	2.9	15.81	0.64	1.13	0.88	2.23	

G.2 The data provided

Table 7.8 gives an overview of the most relevant sample of the stars for which we found periodic signals. As a supplement to this work we provide the extend version containing all 136 stars with additional columns in machine-readable form. The columns included are described in Table 7.9. Additionally, we provide the light curves, including, raw fluxes, the intermediate steps, the PCA, and all masking.

Table 7.9: *Sample table overview. Measured and derived values such as photometry, astrometry, and the rotation period have an additional column with a* `e_` *prefix which denote the associated errors. Those are not listed here separately.*

Column	Unit	Description
`Star`		Running catalog number
`Sample`		=`Y` if in M 67 single MS star sample
`Gaia DR3`		Gaia DR3 identifier
`EPIC`		EPIC identifier
`2MASS`		2MASS identifier
`period`	[d]	derived period
`Xmag`	[mag]	X-band magnitude for $X \in \{B, V, R, I, J, H, K, G, G_{\rm BP}, G_{\rm RP}\}$
`M67`		member `M`, candidate `C`, field star `F`
`M67_pmu`		proper motions cluster member
`M67_plx`		parallax cluster member
`M67_vrad`		radial velocity cluster member
`M67_phot`		photometric cluster member
`G_RP`	[mag]	$G - G_{\rm RP}$ color
`G_RP_0`	[mag]	$(G - G_{\rm RP})_0$ color
`BP_RP`	[mag]	$G_{\rm BP} - G_{\rm RP}$ color
`BP_RP_0`	[mag]	$(G_{\rm BP} - G_{\rm RP})_0$ color
`B_V`	[mag]	$B - V$ color
`B_V_0`	[mag]	$(B - V)_0$ color
`V_K`	[mag]	$V - K$ color
`V_K_0`	[mag]	$(V - K)_0$ color
`ra_icrs`	[°]	GDR3 Right Ascension α
`de_icrs`	[°]	GDR3 Declination δ
`plx`	[mas]	GDR3 parallax ϖ
`pmra`	[mas/yr]	GDR3 proper motion $\mu_{\rm RA}$
`pmde`	[mas/yr]	GDR3 proper motion $\mu_{\rm Dec}$
`vrad`	[km/s]	radial velocity $v_{\rm rad}$
`otype`		Simbad object type
`sptype`		Simbad spectral type
`binary`		=`Y` if binary/multiple
`phot_bin`		=`Y` if photometric binary
`MS`		=`Y` if star is main sequence
`HPS`		=`Y` if star is half-period sequence
`DD`		=`Y` if star shows ¿1 spot
`x_stamp`	[pxl]	mean x coordinate on the superstamp
`y_stamp`	[pxl]	mean y coordinate on the superstamp
`kepler`		=`Y` if star has Kepler light curve
`k2sc`		=`Y` if star has K2SC light curve
`everest`		=`Y` if star has EVEREST light curve

G.3 Supplementary figures

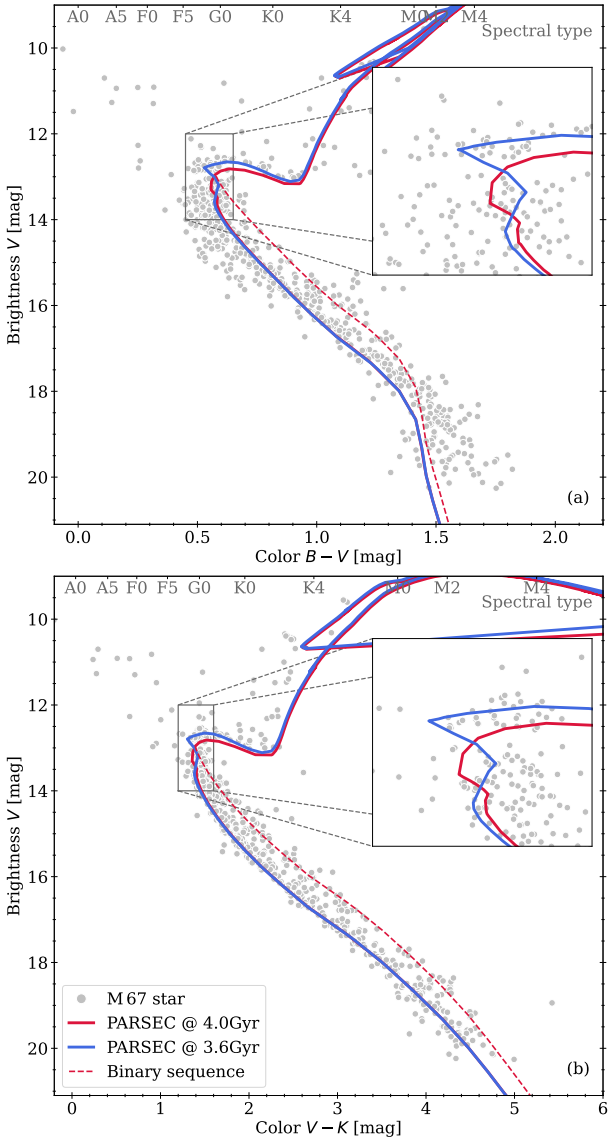

Figure 7.25: *Same as Fig. 3.3 but for $B-V$ and $V-K$ colors.*

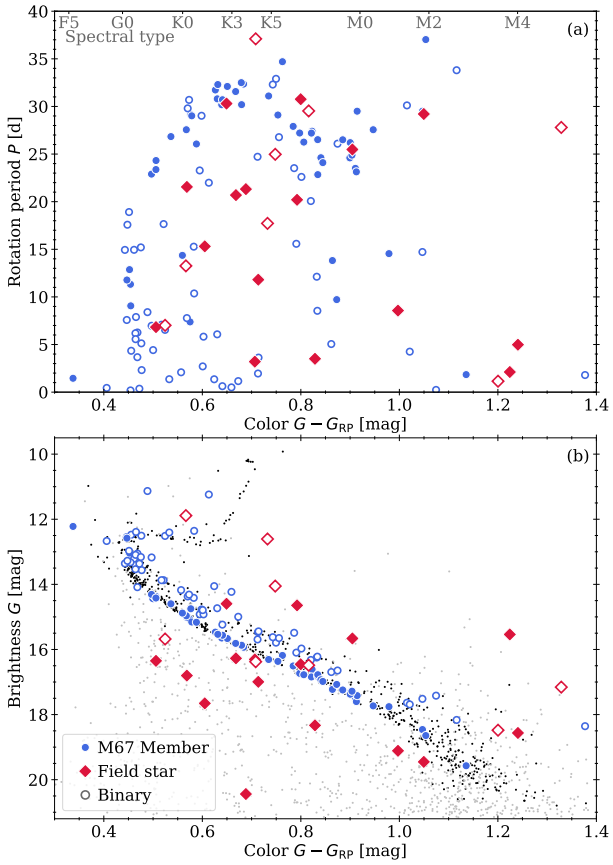

Figure 7.26: *Color-period diagram (CPD, panel a) and color-magnitude diagram (CMD, panel b) of the complete superstamp sample. Blue symbols indicate the M 67 members as discussed above. Overplotted in red are the field stars for which we found a periodic signal. Note that the colors here are not reddening corrected. Open symbols denote binaries.*

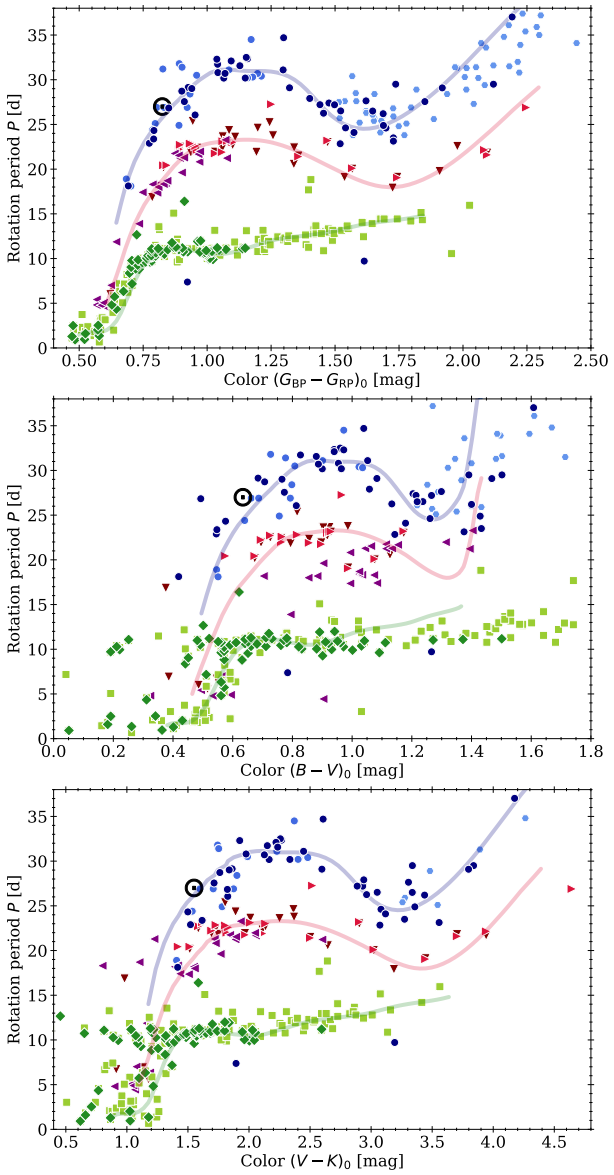

Figure 7.27: *Same as Fig. 3.15 but for* $(G_{\rm BP} - G_{\rm RP})_0$, $(B - V)_0$, *and* $(V - K)_0$ *colors.*

G.4 Sample light curves

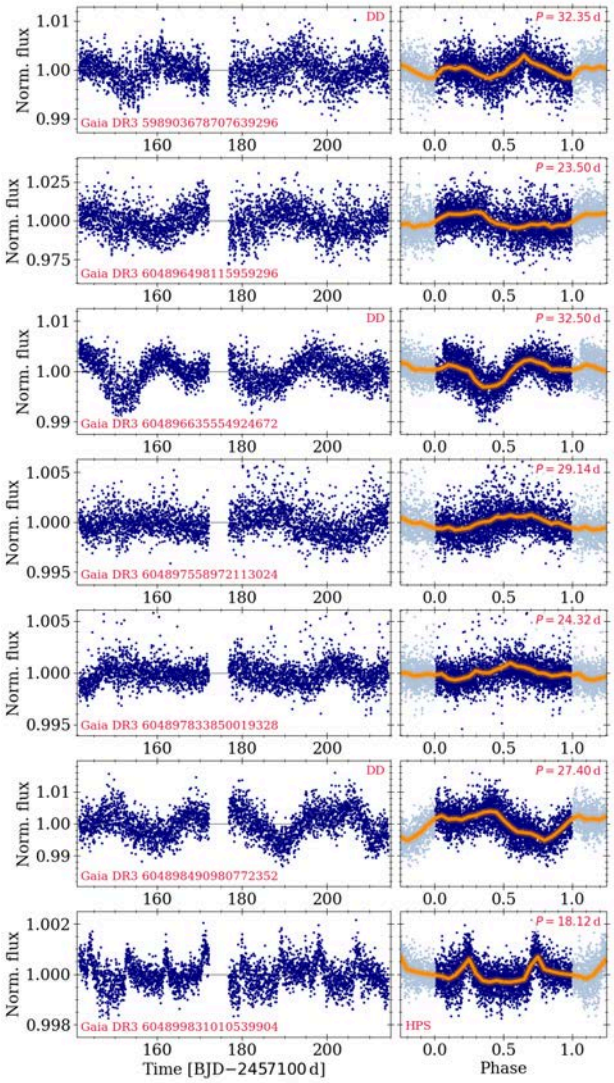

Figure 7.28: *Light curves for our sample stars. Each row in the figure is a star, with the name indicated. The left panel shows the light curve, the right panel their phase folded counterparts. The period used for the phase folding is shown in the upper right. The light curve panel displays the* Gaia *DR3 id in the lower left corner. Additional labels indicate whether a star's light curve exhibits multiple spot features, i.e., is* double dipping *(DD, upper right corner in the left panel) or is a member of the* half-period sequence *(HPS, lower left corner of the right panel). The orange line indicates a 0.01 binning. Note that double dipping refers to all stars whose light curves exhibit signs of more than one spot. Stars are sorted as in Table 7.8, by their* Gaia *Id.*

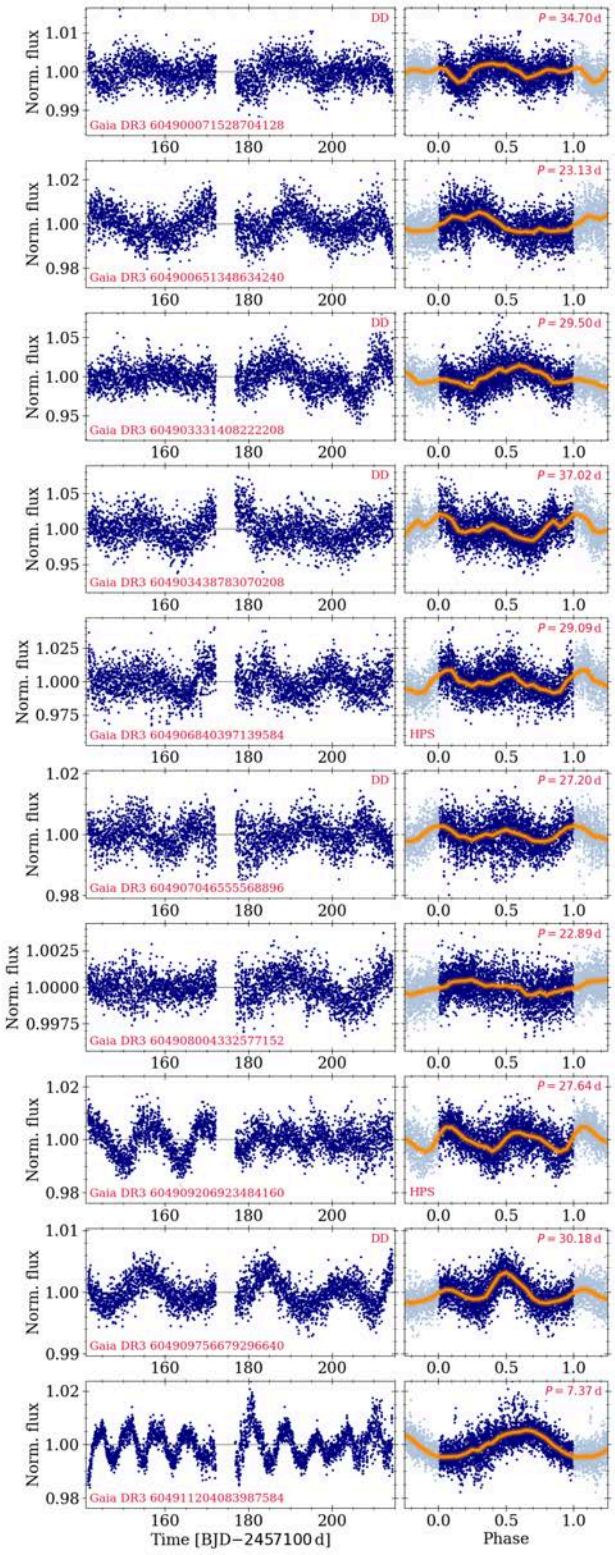

Figure 7.28: *continued.*

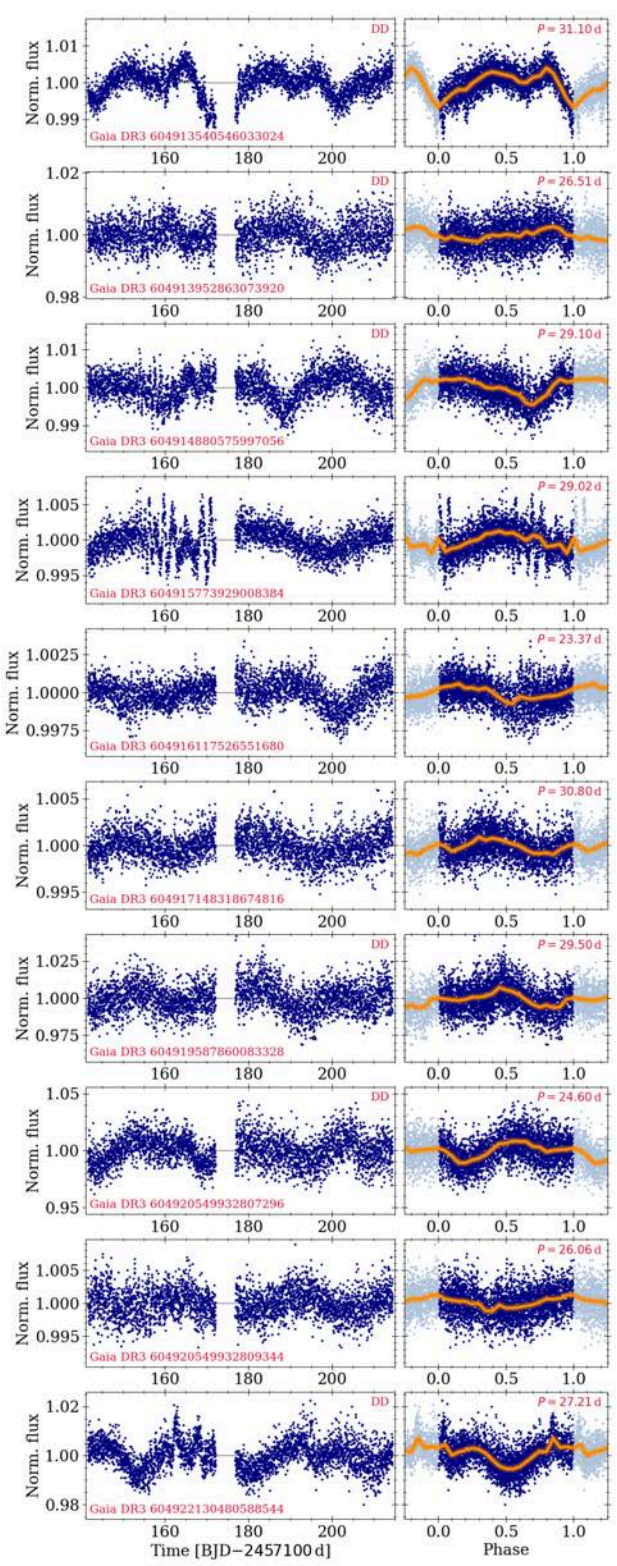

Figure 7.28: *continued.*

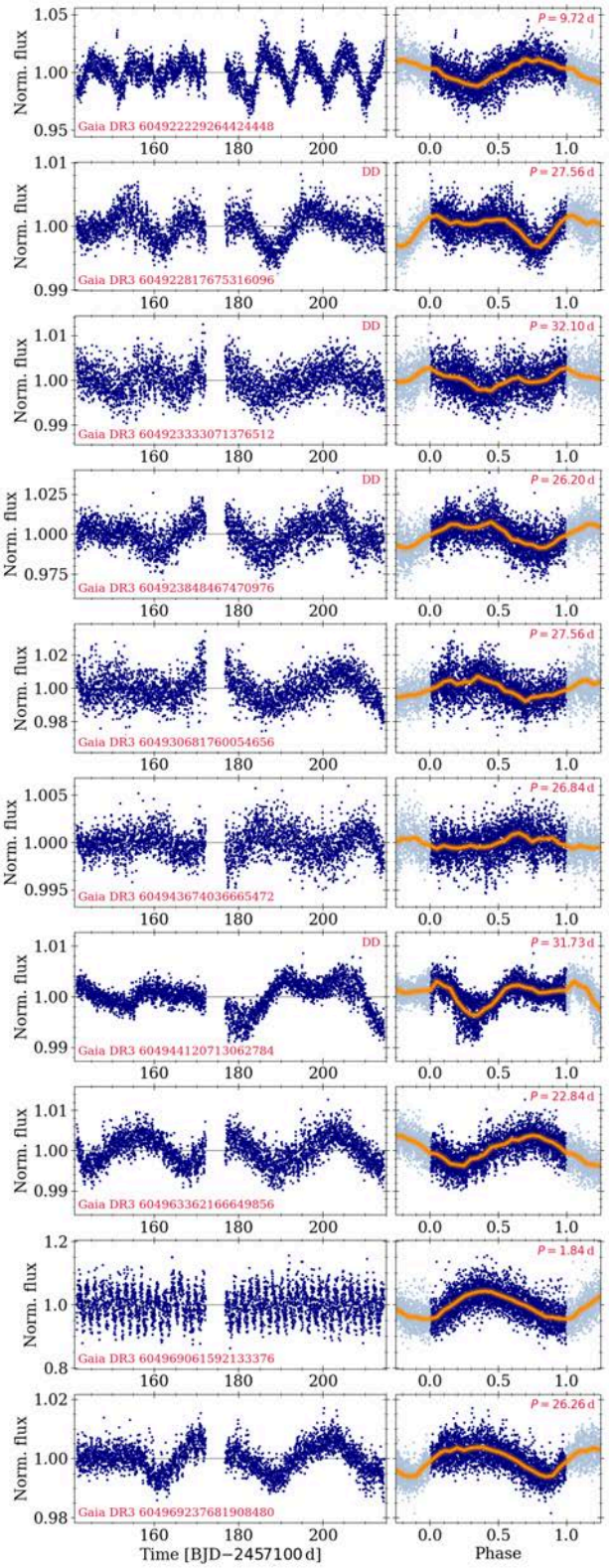

Figure 7.28: *continued.*

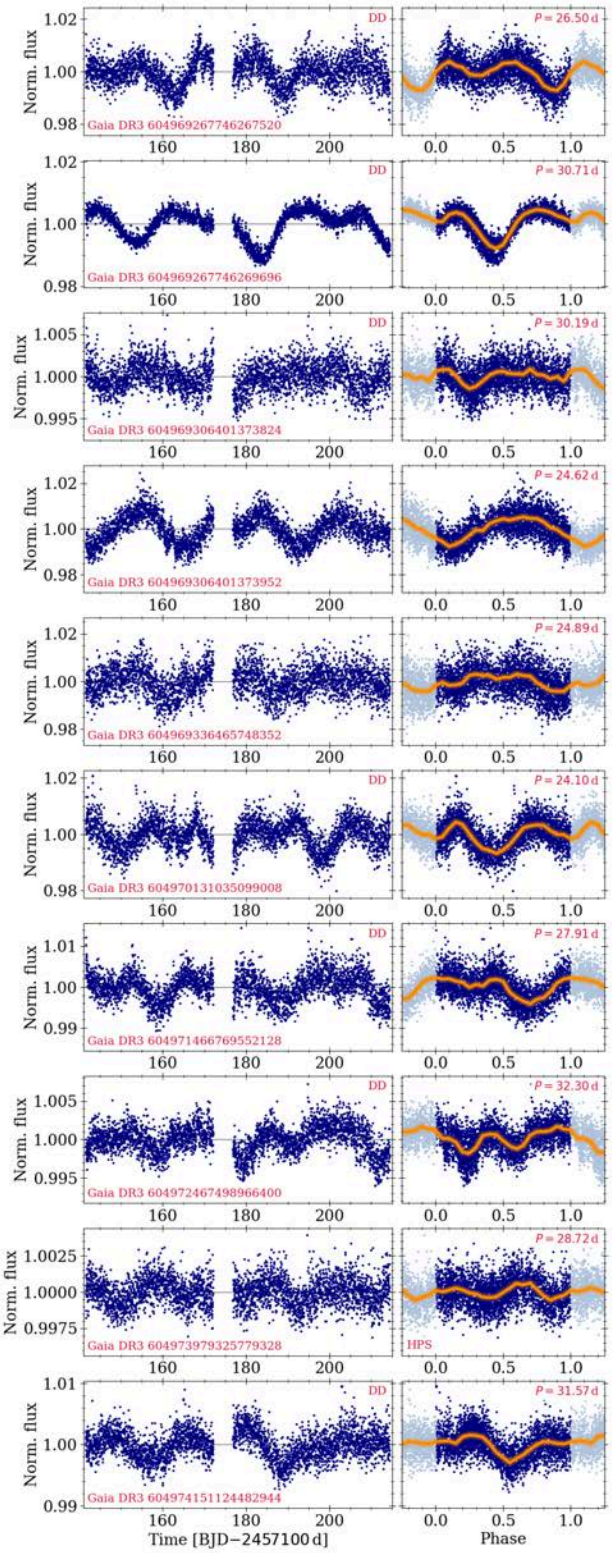

Figure 7.28: *continued.*

Appendix to Paper III

H Issues in the period sample

To create our sample of wide binaries, we have matched the El-Badry et al. (2021) catalog of wide binaries to KIC and EPIC targets with known periods from MQ14 and RH20, respectively. However, there are a few issues regarding this matching, with the light curve data and with the derived periods. We will illustrate these issues here in a little more detail.

H.1 Light curve cross-contamination

The spatial resolution of GDR3 (and also of 2MASS) exceeds the spatial resolution of the *Kepler* telescope CCDs. For a large number of sources with near neighbors, the point-spread functions (PSF) of the stars overlap and the aperture masks for each star include flux from the other. The light curves need to be checked for signs of this contamination.

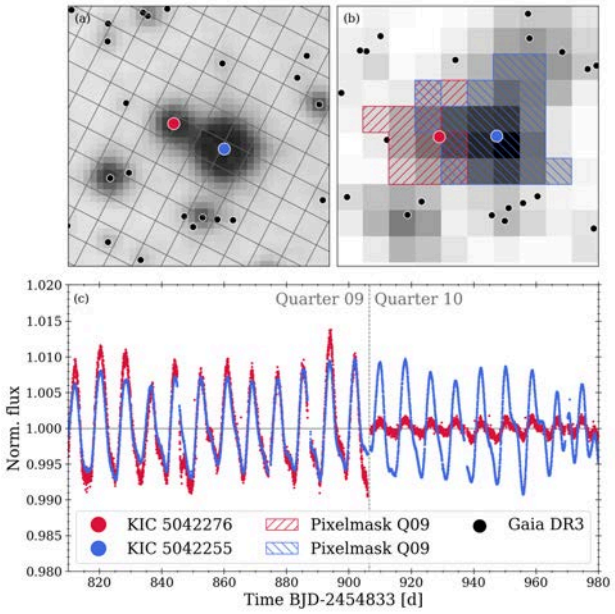

Figure 7.29: *Example of light curve contamination. Panel (a) shows a DSS2 (red) image around one of our wide binaries (KIC Ids given in the legend of panel c). The positions of the two WB stars (red and blue dots) are indicated, along with those of other sources recognized by GDR3. The overlaid grid shows the* Kepler *pixels that sample the region. Panel (b) shows a cutout from a* Kepler *full frame image of the same region (with a somewhat similar orientation and size). The field of view in panels (a) and (b) is about* $40'' \times 40''$*. The overplotted hatched areas indicate the pixelmask for Quarter 9 as reported in the auxiliary data to the light curves. Panel (c) shows the light curves of the component stars. They are focused on the end of Quarter 9 and the beginning of Quarter 10. The similarity in both behaviors is readily visible. This, and similar systems, are discarded from our sample.*

We find 131 wide binaries that suffer from this kind of cross contamination. Often times, it is the components of the WB themselves which affect each others' light curves. If we were to put them in a color period diagram, those systems are rather obvious as they have essentially the same rotation period and form horizontal structures. Figure 7.29 illustrates the light curves for one such system. It is clearly visible that both light curves exhibit the same behavior. The reported periods of the stars in MQ14 are (as expected) essentially identical: 8.161 d and 8.198 d for KIC 5042276 and KIC 5042255, respectively. The pixelmasks show the reason for this – the PSFs of the two components are too close to be separated. In this particular example, it is likely that the brighter star, KIC 5042255, is the origin of the observed variability and that the pixelmask of the secondary records parts of the primary's flux. The transition between Quarters 9 and 10 involves a rotation of the telescope and rather large change in the aperture mask for each star. The latter causes the changes between the recorded light curves for each star between the quarters. We note that the pixelmasks used in the *Kepler* mission are created by a sophisticated algorithm that combines a stellar catalog with an estimate for the point spread function of a star to set an aperture. As the figure shows, this process is not (and cannot be) always fully successful. We reject all 131 wide binaries that show signs of such contamination.

An issue related to the cross-contamination due to overlapping pixelmasks is one pixelmask capturing the flux of two stars. There are typically two cases: (1) The flux from a bright star located some distance away is incorporated into the pixelmask for a fainter star. We observe this for e.g., EPIC 220668834, whose K-giant HD 8412 companion ($P_{\rm rot} = 15.9$ d, Kiraga 2012, based on ASAS data) creates a false periodic signal observed in the ≈ 11 mag fainter M-dwarf's light curve. (2) The pixelmask for a brighter star encompasses another star that is fainter but still bright enough to cast doubt on the origin of the observed signal. A good example is EPIC 212694561 (and its faint companion Gaia DR3 3625200307631332864, both a pair in our WB sample), whose light curve (see Fig. 7.30) shows two distinct signals, one with about 14 d and one with about 1.8 d. RH20 reported a rotation period of $P_{\rm rot} = 13.8$ d, the stronger signal, for EPIC 212694561. We could, in principle, make an educated guess regarding which period corresponds to which star. However, this runs the risk of prejudging the outcome, and thus we elect to proceed without introducing sample systems whose distribution would be informed by our prior assumptions. Accordingly we reject such systems from our sample.

H.2 Period identification

The problems caused by systematics and trends in *Kepler* data (especially for *K2*) have been described extensively elsewhere (e.g., Howell et al. 2014). They impact period detections in *Kepler* light curves and as such we need to be aware of their existence and how they may impact the periods identified. Without going into too much detail here, the important problem is that trends can mimic

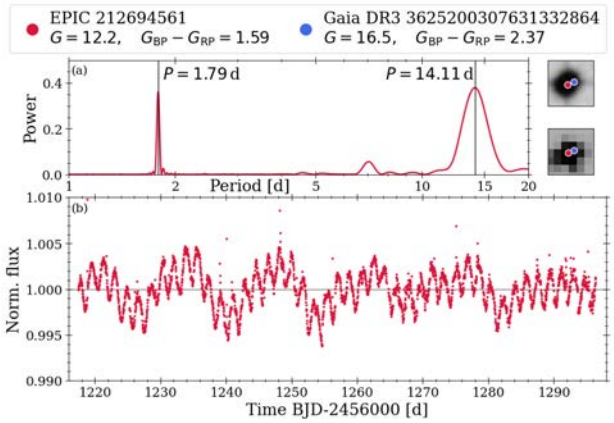

Figure 7.30: K2 *light curve and power spectrum for EPIC 212694561, showing the superposition of two periodic signals. Panel (a) shows the power spectra based on a Lomb-Scargle periodogram indicating the two periodic signals. Panel (b) shows the recorded light curve from* K2 *C06. The small postage stamps in the upper right show DSS2 (upper) and Kepler (lower) images around the recorded stars. The positions of the primary EPIC 212694561 and the secondary Gaia DR3 3625200307631332864 are indicated.*

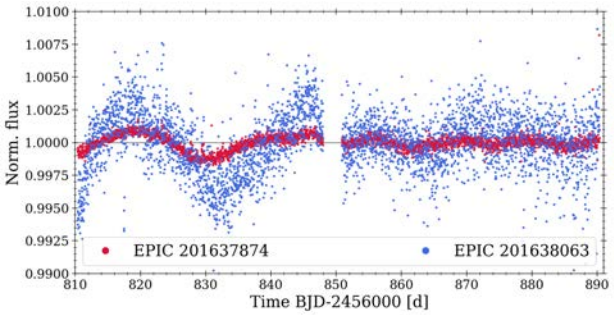

Figure 7.31: K2 *light curves for two stars belonging to the same wide binary. Both show the same trending behavior, albeit with different relative amplitudes. The variation seen is apparently not from intrinsic variability of the star (for instance from a spot), but arises from trending, hence is an artifact.*

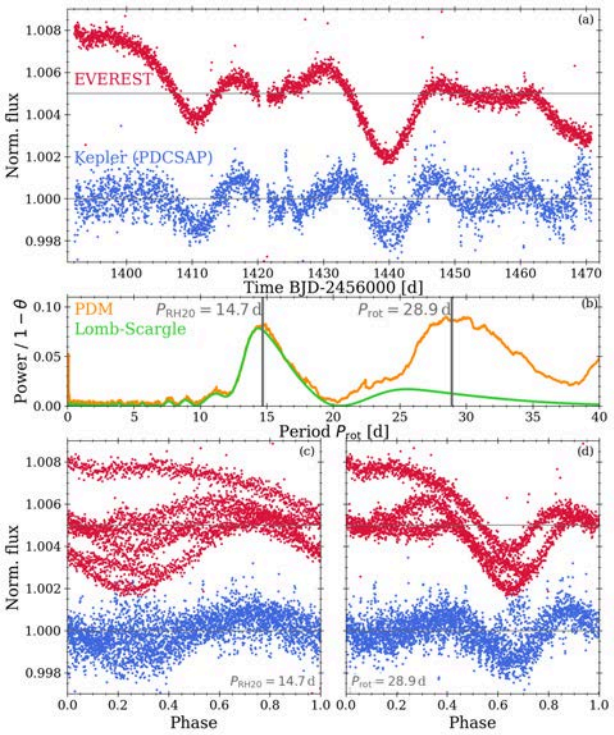

Figure 7.32: *Light curve and period analysis for the sample star EPIC 220332155. Panel (a) shows the* K2 *C08 (blue) and the* `Everest` *(red) light curve. It shows a clear double-dipping signal. The power spectra in panel (b) are calculated from a phase dispersion minimization (PDM, orange, displayed as* $1 - \theta$*) and a Lomb-Scargle periodogram (green). The rotation periods identified by RH20 (14.7 d) and us (28.9 d) are both indicated. Panels (c) and (d) show phase folded plots based on the RH20 period and ours, respectively. In (a), (c), and (d), we have shifted the* `Everest` *data vertically by 0.005 units for visibility reasons. Typically, trending is pronounced in* `Everest` *data, here in the shape of a downward slope.*

or obfuscate an intrinsic stellar signal. Their problems intensify when the light curve only has a short baseline ($\lesssim 3P_{\rm rot}$). Automated period finding algorithms (as employed by MQ14 and RH20) struggle to identify the right rotation period especially for slower rotating stars, those with small amplitudes, multiple spots, and spot evolution. This was highlighted by, e.g., GBW23 (see their Sect. 5.1) in an evaluation of rotation period work on M 67.

In space-based photometric timeseries data (such as we have here from *Kepler*), which is both well-sampled and almost exactly regularly sampled, a rotation period is typically visually evident. However, it needs to be vetted against the adverse effects mentioned above. If carefully done, a manually set period is generally more reliable than an automatically derived one, albeit at the cost of being much more labor intensive. We strive for reliability in our sample and, therefore, manually re-derive the rotation periods for our sample stars based on an evaluation of the phase-folded light curves, while accounting for spot evolution and also considering the impact of data systematics (based on knowledge from light curves of similarly situated sources). Error ranges for the periods are set, similarly manually, by investigating how the phase folded light curve behaves under changes of the assumed period.

As expected, we do encounter stars for which the reported periods by MQ14 and RH20 do not reflect what we observe in their light curves. The problems are of three kinds:

1. The reported period incorrectly identifies either somewhat random intrinsic variations of the light curve, systematic trending, or a combination of both as a periodic signal where there is none present. We reject the corresponding 65 stars from our sample. Figure 7.31 shows an example of trending being identified as a rotation signal. Here, both stars are from the same wide binary, making the detection straight-forward; typically one needs to involve other stars in such assessments. It is readily apparent that both stars exhibit the same (artificial) patterns, with both misidentified as periodic signals. And indeed RH20 identified the same period of about 23 d for both stars. We note that this similarity in the light curves is not an issue of contamination as described above. Both stars are sufficiently far apart to be unproblematic with respect

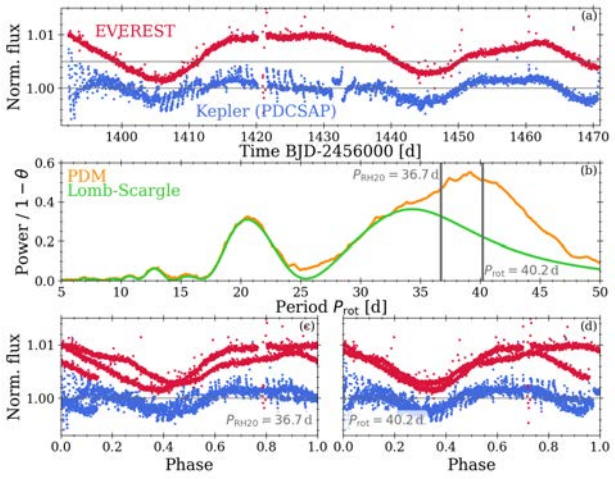

Figure 7.33: *Same as Fig. 7.32, but for the sample star EPIC 220652177. Panel (a) shows the* K2 *C08 (blue) and the* `Everest` *(red) light curve. It shows a clear double-dipping signal. The power spectra in panel (b) are calculated from a phase dispersion minimization (PDM, orange, displayed as* $1 - \theta$*) and a Lomb-Scargle periodogram (green). The rotation periods identified by RH20 (36.7 d) and us (40.2 d) are both indicated. Panels (c) and (d) show phase folded plots based on RH20 and our period, respectively. In (a), (c), and (d), we have shifted the* `Everest` *data vertically by 0.005 units for visibility reasons.*

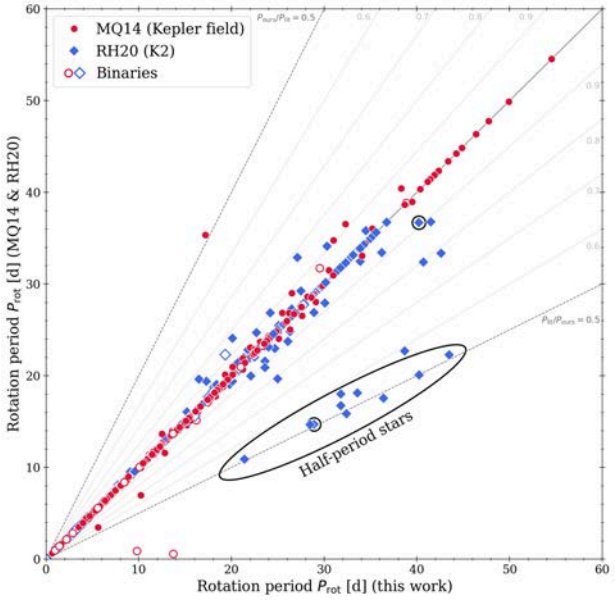

Figure 7.34: *Comparison between the periods reported in MQ14 (red) for the wide binaries in the* Kepler *mission and in RH20 (blue) from* K2 *and our adopted and vetted periods. Overplotted gray lines indicate the size of the offsets between our and their periods as labeled. Open symbols denote stars with signs of binarity. The black ellipse marks double-dipping stars that were detected with their half-period. The two highlighted stars are the ones displayed in Figs. 7.32 and 7.33.*

to the low spatial resolution of *Kepler*.

2. The periodicity assigned was half the true periodicity. Tan & Basri (2020, see also Basri & Nguyen 2018) have shown that longer period stars especially tend to exhibit multiple spot features in the their light curve. These *double-dipping* stars can then be identified with only half their real period as the two spot signals are interpreted as the same. Figure 7.32 shows an obvious example of such a case. We find 18 such stars in our sample.
3. The star exhibits a clear periodic signal but the reported period is somewhat different from our preferred period. This occurs at times when the light curve exhibits strong signs of multiple spots and spot evolution that causes one spot to vanish and result in an erroneous association between variability features. Typically, the difference between them is well within the error estimate (which is large as a result of a relatively bad fit, given the changes in the light curve behavior). Figure 7.33 shows an obvious example of such a case. We choose to adopt our modified periods (and error) for these stars.

Despite those issues, we find that the vast majority of stars ($> 90\,\%$) are actually reported with the correct periods.

H.3 Period comparison

Figure 7.34 shows a comparison between our final sample of periods and the values reported in MQ14 and RH20. As can be seen, the majority of the values are in agreement. However, we had to revise a significant number of periods, especially those for *K2* stars. The changes are typically of the order of $10-20\,\%$. There are 18 stars for which we find that RH20 has only reported half the period of a double-dipping star. In the one case where it appears that we have adopted the half-period of a MQ14 star it seems that they have identified the period including a large-scale systematic, ignoring the weaker but more consistent signal throughout the rest of the light curve. The other outliers where we have identified ≈ 10 d periods, we are unable to understand what has led MQ14 to adopt periods of only ≈ 1 d. We also believe that the errors reported in RH20 for stars with slower rotation ($\gtrsim 20$ d) are highly overestimated (e.g., ≈ 10 d for stars with $P_{\rm rot} = 30$ d).

I `gyrointerp` (Bouma et al. 2023)

Bouma et al. (2023, BPH23 hereafter) have created an interpolation on the empirical sequences of selected open clusters using Bayesian statistics to estimate an age probability distribution for a star of given effective temperature $T_{\rm eff}$ and rotation period $P_{\rm rot}$. In this section we apply their algorithm (`gyrointerp`[8]) to our WB sample. We proceed as follows:

1. We select all WB from the age groups $1-5$ falling into the classes *S*, *F*, and *C*.
2. For each star, we obtain $T_{\rm eff}$ from GDR3 $G_{\rm BP} - G_{\rm RP}$ via the empirical color-temperature relation from Curtis et al. (2020, see their Table 4).
3. We assume a flat $T_{\rm eff}$ error of 100 K for each star for the calculation.
4. The calculation is executed on an age grid between $t = 0$ and 4 Gyr and with $\Delta t = 0.01$ Gyr.

Not all stars can be processed this way; the bluest and

[8] `github.com/lgbouma/gyro-interp`

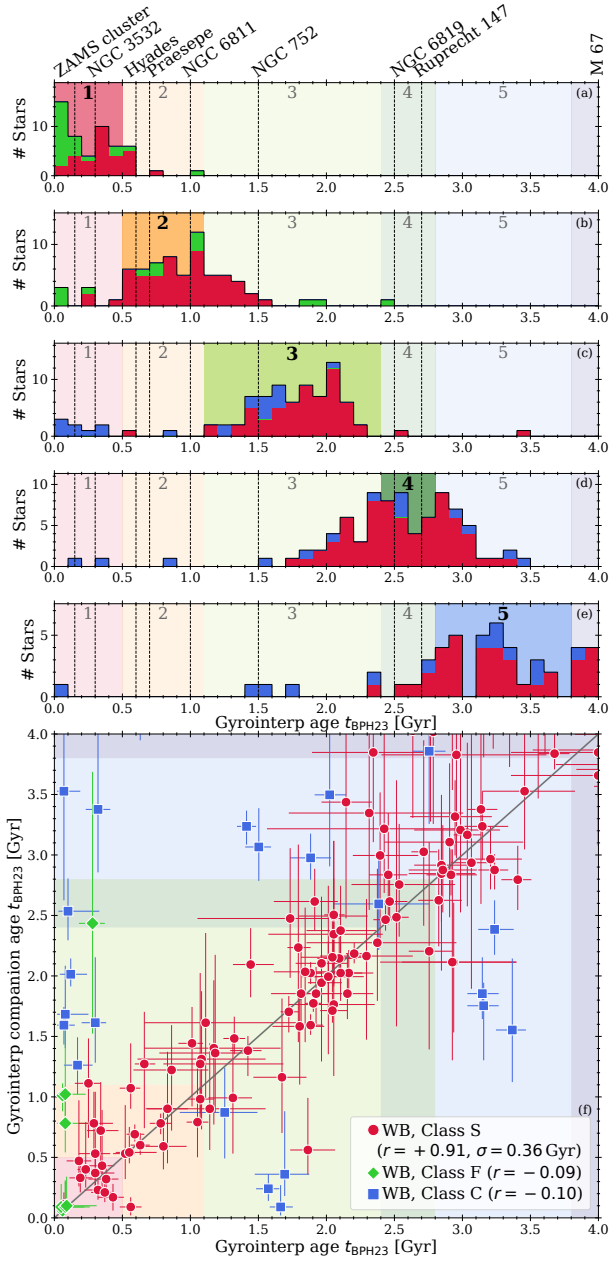

Figure 7.35: *Comparison with ages from* `gyrointerp`*. Panels (a) to (e) shows histograms of the ages sorted into our age groups 1 – 5. The background color coding shows the rough extent of the individual groups with the relevant one highlighted. Panel (f) shows the age of the WB component with larger age uncertainty against the one with smaller uncertainty. In all plots, the color coding refers to classification of the WB systems.*

reddest stars of our sample are beyond the interpolation range of `gyrointerp`. We only obtain results for stars with $0.7 \leqslant G_{\rm BP} - G_{\rm RP} \leqslant 2.0$ (3800 – 6200 K). As they have done, the median of the distribution is adopted as the age $t_{\rm BPH23}$.

In Fig. 7.35, we illustrate the results of the calculation. As we do not have a precise age estimated from our procedure, we compare the calculated ages $t_{\rm BPH23}$ to the extent of the corresponding age groups. Panels (a) – (e) in the figure show histograms of the resulting age distributions, distinguished by class. Each panel focuses on a different age group and the histograms only show stars that we have assigned to the particular (highlighted) group. Panel (f) shows a comparison between the WB components for all systems where we have an age estimate for both.

Generally speaking, the agreement is good, although a significant number of stars (especially in groups 2 and 4) lie beyond our nominal group limits. This is somewhat reflected in the age uncertainties which are of course not seen in the histograms. The largest discrepancies arise for the bluest stars. This is a consequence of the strong mass-dependence of the spindown in that region. Although BPH23 is cautious about age estimates beyond 2.6 Gyr (as there are boundary effects from interpolation with only M 67 as an older anchor point), we find that `gyrointerp` does a reasonable job for the stars in that age range. The best agreement is achieved for stars (and systems) that fall into the range (color and rotation period wise) that we have used to mainly draw the *L* component in Sect. 4.3 from. We note that `gyrointerp` appears to underestimate ages for fast rotators redder than the sun. This hints at an underlying issue with the distinction between slow and fast rotator sequences at a given age and the sparsely populated gap between them (a non-trivial problem). The class *C* systems contain one star that rotates too fast for its assigned age, and that is reflected in the scatter in all plots.

We consider `gyrointerp` to be a good first step towards obtaining model-independent rotational ages. Its current limitations arise mainly from the availability of open cluster data. We agree with BPH23 that future endeavors should focus on expanding the age range and closing gaps. A short-term improvement in the usability may be achieved by estimating ages directly using (dereddened) colors rather than $T_{\rm eff}$ values, e.g., by having `gyrointerp` calculate $T_{\rm eff}$ on the fly from provided colors. This would make it fully empirical and also more accessible as photometric colors are typically far more extensively available than $T_{\rm eff}$.

J Sample table

Table 7.10: see table on facing page ▸

Excerpt of the wide binary sample. The table lists the individual stars and groups them into the individual binaries. The stars listed are those shown in Fig. 4.4 with two more examples of wide binaries that contain an evolved component (see Sect. 4.4.3a). The Binary ID *column refers to the enumeration we have introduced for our sample of 372 WBs, the* Age group *column refers to the assignment performed in Sect. 4.3, the* WB Class *column refers to the classification from the same section (see table footnote (a) for details), the* System Issue *column lists the potential explanation for an inconsistent system, and the* Notes on components *column lists any peculiarities of a (component) star, such as signs of (close) binarity or an evolved state. The complete table, also including additional columns containing e.g., astrometry, is available in electronic form.* [a]*The* Class *column contains the classification in Sect. 4.3 and is as follows: S =* L *component and* T *component on slow rotator sequence; F = at least one of the components is a fast rotator; C =* T *component contradicts* L *component; E = binary contains a (sub)giant; W = binary contains a white dwarf*

Binary ID	Age group	WB Class[a]	System Issue	Gaia DR3	2MASS	EPIC	KIC	$P_{\rm rot}$ [d]	$P_{\rm err}$ [d]	$G_{\rm BP}-G_{\rm RP}$ [mag]	G [mag]	Notes on components
37	1	*F*		2119651091691155712	J18500021+4735070	–	10386229	7.72	0.02	0.96	11.8	
				2119667691742387456	J18491928+4743299	–	10515986	0.75	0.01	2.33	15.5	
68	4	*C*	hierarchical	2101369172560195840	J19181006+4027333	–	5267544	23.8	0.7	0.97	15.1	
				2101369172560194816	J19180995+4027289	–	5267541	17.2	1.2	1.22	15.3	Double
133	1	*F*		2082192658985723264	J20030145+4529233	–	9118981	1.51	0.01	0.94	13.7	
				2082191765632529664	J20031048+4527271	–	9119108	0.65	0.01	1.22	14.9	
148	2	*F*		2551656808041899136	J00523879+0337462	220346755	–	21.4	2.4	2.53	15.5	
				2551656808041898880	J00523729+0337516	220346833	–	1.51	0.01	2.99	16.6	
156	4	*C*	hierarchical	2554578725832963840	J00412128+0529399	220440269	–	21.8	1.5	1.02	13.4	
				2554578691473225600	J00412782+0529419	220440299	–	4.44	0.01	1.47	14.9	Double
183	4	*S*		2077301275348100352	J19362795+4040518	–	5456319	23.5	2.5	1.03	14.6	
				2077300759952080896	J19362346+4038341	–	5456253	18.8	0.3	1.61	15.8	Double
186	4	*S*		2107342716152550272	J18582249+4626591	–	9696358	15.6	1.5	0.72	11.7	
				2107336874997022464	J18581799+4626119	–	9696331	22.6	2.2	0.98	14.3	
189	4	*C*	hierarchical	2077605840068347904	J19343327+4137114	–	6290800	20.9	4.6	0.99	13.3	
				2077605840068352768	J19343395+4137235	–	6290811	2.83	0.01	2.19	15.4	Double
201	6	*S*		3798679053239405824	J11261592+0142258	201578138	–	28.2	1.5	0.95	11.1	
				3798679053239406080	J11261688+0142237	201578098	–	27.6	2.5	1.43	12.5	
220	6	*S*		2075134756418822272	J19561853+4108112	–	5905418	30.5	1.5	1.07	12.3	
				2075134962577250176	J19561703+4108289	–	5905382	34.1	1.5	2.27	15.6	
225	4	*S*		3584374199647645056	J12204839-0647402	228799745	–	23.6	2.5	0.93	12.2	
				3584374203942504448	J12204894-0647371	228799765	–	19.3	2.8	1.68	14.0	Double
246	4	*S*		3596051051789926528	J12005429-0513184	201153090	–	23.6	2.3	1.19	12.6	
				3596051086149665280	J12005483-0512490	201153439	–	25.0	2.0	2.1	15.0	
292	4	*E*		2052430769006849792	J19365340+3928181	–	4375408	1.18	0.01	0.61	10.0	Subgiant
				2052430769006846720	J19365272+3928089	–	4375393	14.4	0.1	0.8	12.8	
299	3	*W*		2053584770878226304	–	–	–	–	–	-0.1	17.9	White Dwarf
				2053585565450552960	J19284890+4100216	–	5792108	13.6	0.1	0.98	11.3	
…	…	…	…	…	…	…	…	…	…	…	…	…